Issue 2 2021 | Volume 17

The Journal on Advanced Studies in Theoretical and Experimental Physics, including Related Themes from Mathematics

PROGRESS IN PHYSICS

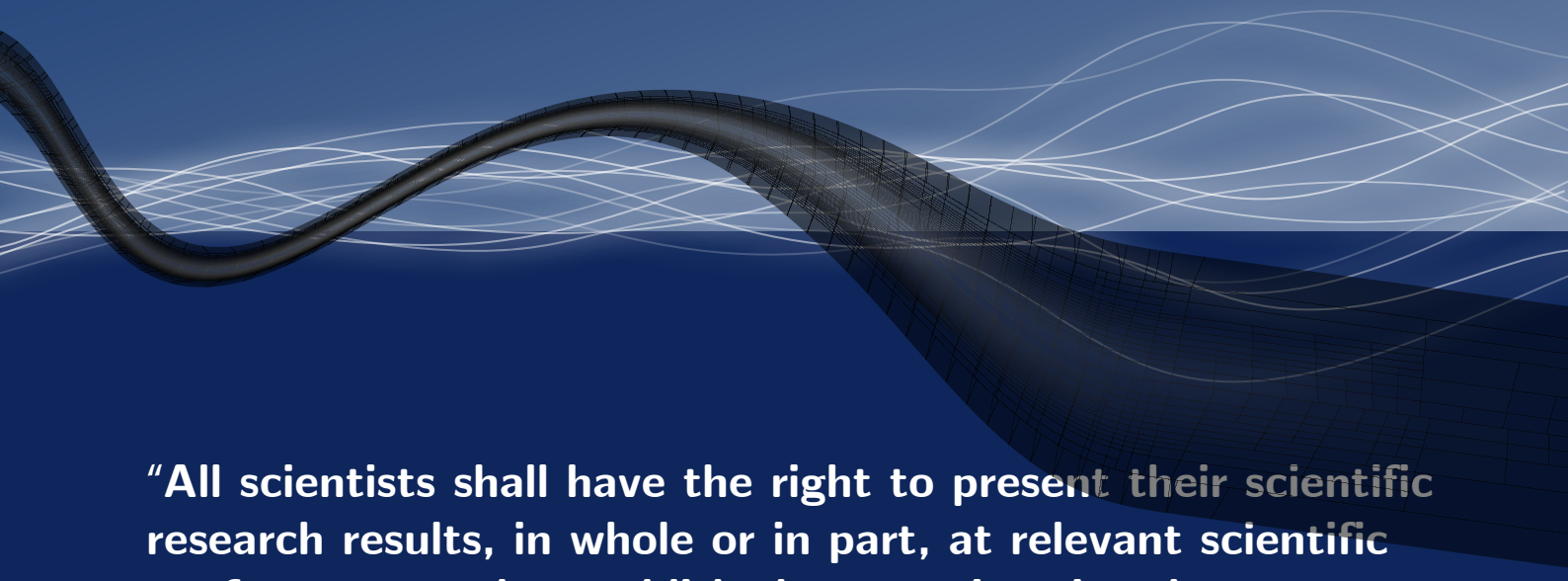

"All scientists shall have the right to present their scientific research results, in whole or in part, at relevant scientific conferences, and to publish the same in printed scientific journals, electronic archives, and any other media." — Declaration of Academic Freedom, Article 8

ISSN 1555-5534

The Journal on Advanced Studies in Theoretical and Experimental Physics, including Related Themes from Mathematics

PROGRESS IN PHYSICS

A quarterly issue scientific journal, registered with the Library of Congress (DC, USA). This journal is peer reviewed and included in the abstracting and indexing coverage of: Mathematical Reviews and MathSciNet (AMS, USA), DOAJ of Lund University (Sweden), Scientific Commons of the University of St. Gallen (Switzerland), Open-J-Gate (India), Referativnyi Zhurnal VINITI (Russia), etc.

Electronic version of this journal:
http://www.ptep-online.com

Postal Address

Department of Mathematics and Science,
University of New Mexico,
705 Gurley Ave., Gallup, NM 87301, USA

ISSN: 1555-5534 (print)
ISSN: 1555-5615 (online)

Standard Address Number: 297-5092
Printed in the United States of America

October 2021 **Vol. 17, Issue 2**

CONTENTS

Marquet P. The Exact Gödel Metric 133

Meng X. A Statistical Approach to Two-particle Bell Tests 139

Zhong Y. C. A Quantitative Description of Atmospheric Absorption and Radiation at Equilibrium Surface Temperature 151

Kritov A. Explicit Values for Gravitational and Hubble Constants from Cosmological Entropy Bound and Alpha-Quantization of Particle Masses 158

Müller H. Physics of Transcendental Numbers Determines Star Distribution 164

Greaves E. D., Bracho C., Gift S., Rodriguez A. M. A Solution to the Pioneer Anomalous Annual and Diurnal Residuals 168

Zhang T. Gamow Theory for Transmission and Decay of Unbound Diprotons 185

Müller H., Baccara R., Hofmann R. L., Lonero G., Muratori S., Papa G., Santoni F., Todesco L., Zanellati F., Khosravi L. Entropy Analysis of the Bioelectrical Activity of Plants 189

Danilov V. I. Ocean Currents and Tidal Movements: The Real Causes 194

Consa O. Searching for the Feynman Diagram IIc 198

Reshma P., Prasanth P., Udayanandan K. M. The Curse of Dimensionality in Physics 203

Noh Y. J. Anomalous Magnetic Moment in Discrete Time 207

Santilli R. M. Representation of the Anomalous Magnetic Moment of the Muons via the Einstein-Podolsky-Rosen Completion of Quantum into Hadronic Mechanics . . 210

Millette P. A. On Eddington's Temperature of Interstellar Space and the Cosmic Microwave Background Radiation 216

Rabounski D. In Memoriam of Simon Shnoll (1930–2021) 218

Müller H. Physics of Transcendental Numbers on the Origin of Astrogeophysical Cycles 225

Information for Authors

Progress in Physics has been created for rapid publications on advanced studies in theoretical and experimental physics, including related themes from mathematics and astronomy. All submitted papers should be professional, in good English, containing a brief review of a problem and obtained results.

All submissions should be designed in LaTeX format using *Progress in Physics* template. This template can be downloaded from *Progress in Physics* home page http://www.ptep-online.com

Preliminary, authors may submit papers in PDF format. If the paper is accepted, authors can manage LaTeXtyping. Do not send MS Word documents, please: we do not use this software, so unable to read this file format. Incorrectly formatted papers (i.e. not LaTeXwith the template) will not be accepted for publication. Those authors who are unable to prepare their submissions in LaTeXformat can apply to a third-party payable service for LaTeX typing. Our personnel work voluntarily. Authors must assist by conforming to this policy, to make the publication process as easy and fast as possible.

Abstract and the necessary information about author(s) should be included into the papers. To submit a paper, mail the file(s) to the Editor-in-Chief.

All submitted papers should be as brief as possible. Short articles are preferable. Large papers can also be considered. Letters related to the publications in the journal or to the events among the science community can be applied to the section *Letters to Progress in Physics*.

All that has been accepted for the online issue of *Progress in Physics* is printed in the paper version of the journal. To order printed issues, contact the Editors.

Authors retain their rights to use their papers published in *Progress in Physics* as a whole or any part of it in any other publications and in any way they see fit. This copyright agreement shall remain valid even if the authors transfer copyright of their published papers to another party.

Electronic copies of all papers published in *Progress in Physics* are available for free download, copying, and re-distribution, according to the copyright agreement printed on the titlepage of each issue of the journal. This copyright agreement follows the *Budapest Open Initiative* and the *Creative Commons Attribution-Noncommercial-No Derivative Works 2.5 License* declaring that electronic copies of such books and journals should always be accessed for reading, download, and copying for any person, and free of charge.

Consideration and review process does not require any payment from the side of the submitters. Nevertheless the authors of accepted papers are requested to pay the page charges. *Progress in Physics* is a non-profit/academic journal: money collected from the authors cover the cost of printing and distribution of the annual volumes of the journal along the major academic/university libraries of the world. (Look for the current author fee in the online version of *Progress in Physics*.)

The Exact Gödel Metric

Patrick Marquet
Calais, France. E-mail: patrick.marquet6@wanadoo.fr

We demonstrate that Gödel's metric does not represent a model of universe as it is usually accepted in the standard literature. In fact, a close inspection shows that this metric as it stands is a very special case of a broader metric. Introducing a simple conformal transformation readily induces a pressure term on the right hand side of the Einstein's field equations which actually describe a peculiar perfect fluid. This term was wrongly interpreted by Gödel as the *ad hoc* cosmological constant required to sustain his model. Gödel's space-time can be thus regarded as a real physical system with no cosmological implication and it is relegated to the class of ordinary metrics. The emergence of the related closed time-like curves is not bound to a rotating universe as stated in all classical treatments and this fact naturally sheds new light on time travel feasibility considerations.

Notations

Space-time greek indices run from: α,β: 0, 1, 2, 3.
Space-time signature: -2.
$\varkappa$ is the Einstein constant.
We adopt here: $c = 1$.

1 The Gödel universe

1.1 General

In his original paper [1], Kurt Gödel has derived an exact solution to Einstein's field equations in which the matter takes the form of a shear/pressure free fluid (dust solution).

This universe is homogeneous but non-isotropic and it exhibits a specific rotational symmetry which allows for the existence of *close timelike curves* (*CTCs*). The Gödel space-time has a five dimensional group of isometries (G5) which is transitive. (An action of a group is transitive on a manifold (M,$\boldsymbol{g}$), if it can map any point of the manifold into any other points of M).

It admits a five dimensional *Lie algebra* of *Killing vector fields* generated by a time translation ∂_{x_0}, two spatial translations ∂_{x_1}, ∂_{x_2}, plus two further Killing vector fields:

$$\partial_{x_3} - x_2\partial_{x_2} \quad \text{and} \quad 2\mathrm{e}^{x_1}\partial_{x_0} + x_2\partial_{x_3} + \left(\mathrm{e}^{2x_1} - \frac{1}{2}\,{x_2}^2\partial_{x_2}\right).$$

The *Weyl tensor* of the *standard* Gödel solution has Petrov type D:

$$C^{\alpha\beta}{}_{\mu\nu} = R^{\alpha\beta}{}_{\mu\nu} + \frac{R}{3}\,\delta^{\alpha}{}_{[\mu}\delta_{\nu]}{}^{\beta} + 2\delta^{[\alpha}{}_{[\mu}R_{\nu]}{}^{\beta]}.$$

The presence of the non-vanishing Weyl tensor prevents the Gödel metric from being *Euclidean* whatever the coordinates transformations.

This is in contrast to the Friedmann-Lemaître-Robertson-Walker metric which can be shown to reduce to a conformal Euclidean metric, implying that its Weyl tensor is zero [2].

The Gödel universe is often dismissed because it implies a non zero cosmological term and also since its rotation would conflict with observational data.

In what follows, we are able to relax our demand that the Gödel metric be a description of an actual universe. This is achieved through a specific transformation which makes Gödel space-time an "ordinary" metric just as any other metrics currently derived in physics.

1.2 The basic theory

The classical Gödel line element is generically given by the interval

$$ds^2 = a^2\left[{dx_0}^2 - {dx_1}^2 + {dx_2}^2\frac{1}{2}\,\mathrm{e}^{2x_1} - {dx_3}^2 + 2\mathrm{e}^{x_1}(dx_0\,dx_2)\right], \quad (1.1)$$

or equivalently:

$$ds^2 = a^2\left[-{dx_1}^2 - {dx_3}^2 - {dx_2}^2\frac{1}{2}\,\mathrm{e}^{2x_1} + (\mathrm{e}^{x_1}dx_2 + dx_0)^2\right]. \quad (1.2)$$

$a > 0$ is a constant.

The components of the metric tensor are:

$$(g_{\mu\nu})_{\mathrm{G}} = \begin{pmatrix} a^2 & 0 & a^2\mathrm{e}^{x_1} & 0 \\ 0 & -a^2 & 0 & 0 \\ a^2\mathrm{e}^{x_1} & 0 & a^2\frac{1}{2}\mathrm{e}^{2x_1} & 0 \\ 0 & 0 & 0 & -a^2 \end{pmatrix},$$

$$(g^{\mu\nu})_{\mathrm{G}} = \begin{pmatrix} -a^2 & 0 & -a^{-2}2\mathrm{e}^{-x_1} & 0 \\ 0 & -a^2 & 0 & 0 \\ -a^{-2}2\mathrm{e}^{-x_1} & 0 & -a^{-2}2\mathrm{e}^{-2x_1} & 0 \\ 0 & 0 & 0 & -a^2 \end{pmatrix}.$$

In this particular case, since only $\partial_1(g_{22})_{\mathrm{G}} \neq 0$ and $\partial_1(g_{02})_{\mathrm{G}} \neq 0$, the non-zero connection components are:

$$\Gamma^0{}_{01} = 1 \qquad \Gamma^0{}_{12} = \Gamma^1{}_{02} = \frac{1}{2}\,\mathrm{e}^{x_1}$$

$$\Gamma^1{}_{22} = \frac{1}{2}\,\mathrm{e}^{2x_1} \qquad \Gamma^2{}_{01} = -\mathrm{e}^{-x_1}$$

Those greatly simplify the Ricci tensor: $R_{\beta\gamma} = \partial_1\Gamma^1{}_{\beta\gamma} + \Gamma^1{}_{\beta\gamma} - \Gamma^{\delta}{}_{\alpha\beta}\Gamma^{\alpha}{}_{\delta\gamma}$ whose components reduce to:

$$R_{00} = 1, \qquad R_{22} = \mathrm{e}^{2x_1}$$

$$R_{02} = R_{20} = \mathrm{e}^{x_1}$$

The Gödel *unit vector* $\boldsymbol{u}$ of matter in the direction of the x_0 lines has the following components:

$$(u^\mu)_{\mathrm{G}} = (a^{-1},\, 0,\, 0,\, 0), \tag{1.3}$$

$$\left(u_\mu\right)_{\mathrm{G}} = (a,\, 0,\, a\mathrm{e}^{x_1},\, 0), \tag{1.4}$$

hence:

$$R_{\mu\nu} = \left(u_\mu u_\nu\right)_{\mathrm{G}}\, a^{-2}, \tag{1.5}$$

$$R = \left(u^\mu u_\mu\right)_{\mathrm{G}} = a^{-2}. \tag{1.6}$$

In order to make his metric a compatible solution to Einstein's field equations, Gödel is led to introduce a cosmological constant Λ as:

$$R_{\mu\nu} - \frac{1}{2} g_{\mu\nu} R = \varkappa\rho u_\mu u_\nu + g_{\mu\nu}\Lambda. \tag{1.7}$$

To achieve this compatibility, he then further sets:

$$a^{-2} = \varkappa\rho, \tag{1.8}$$

$$\Lambda = -\frac{1}{2}R = -\frac{1}{2a^2} = -\frac{1}{2}\varkappa\rho. \tag{1.9}$$

As primarily claimed by Gödel, its stationary space-time is homogeneous.

For every point A of the manifold $(\mathrm{M}, \boldsymbol{g}_{\mathrm{G}})$, there exists a one-parameter group of transformations of M carrying A into itself.

This means that $(\mathrm{M}, \boldsymbol{g}_{\mathrm{G}})$ has a rotational symmetry and matter rotates everywhere with a constant rotation velocity magnitude $\boldsymbol{\omega}_{\mathrm{G}}$ orthogonal to $\boldsymbol{u}_{\mathrm{G}}$.

Using the contravariant components:

$$(\omega^\alpha)_{\mathrm{G}} = \left(0,\, 0,\, 0,\, \frac{\sqrt{2}}{a^2}\right), \tag{1.10}$$

one finds:

$$\boldsymbol{\omega}_{\mathrm{G}} = (g_{a\mu}\omega^\alpha\omega^\mu)_{\mathrm{G}}{}^{1/2} = \frac{a}{\sqrt{2}}. \tag{1.11}$$

With (1.8) this magnitude is:

$$\boldsymbol{\omega}_{\mathrm{G}} = \left(\frac{1}{2}\,\varkappa\rho\right)^{1/2}. \tag{1.12}$$

A first glance at these constraints, readily reveals a fairly high degree of arbitrariness in the theory.

Finetuning the hypothetical constant Λ with the density of the universe (and the Ricci scalar) appears indeed as a somewhat dubious physical argument.

We shall see that those ill-defined assumptions are not required in order for the basic model to satisfy the field equations.

2 Gödel's model defined as a homogenous perfect fluid

2.1 Reformulation of Gödel's metric

We now make the assumption that a is slightly space-time variable and we set:

$$a^2 = \mathrm{e}^{2U}. \tag{2.1}$$

The positive scalar $U(x_\mu) > 0$ will be explicited below.

The Gödel metric tensor components (1.2) are related to the fundamental metric tensor $\boldsymbol{g}$ by:

$$(g_{\mu\nu})_{\mathrm{G}} = \mathrm{e}^{2U} g_{\mu\nu}, \tag{2.2}$$

$$(g^{\mu\nu})_{\mathrm{G}} = \mathrm{e}^{-2U} g^{\mu\nu}, \tag{2.2 bis}$$

This means that the Gödel metric is now conformal:

$$ds^2 = \mathrm{e}^{2U}\left[dx_0{}^2 - dx_1{}^2 + dx_2{}^2\frac{1}{2}\,\mathrm{e}^{2x_1} - dx_3{}^2 + 2\mathrm{e}^{x_1}(dx_0 dx_2)\right]. \tag{2.3}$$

We are now going to see how the substitution (2.1) drastically changes the meaning of Gödel's limited theory.

2.2 Relativistic analysis of a neutral homogeneous perfect fluid

2.2.1 The geodesic differential system

Let us consider the manifold $(\mathrm{M}, \boldsymbol{g})$, on which is defined a vector tangent to the curve C in local coordinates:

$$\dot{x}^\alpha = \frac{dx^\alpha}{d\zeta}, \quad \text{where } \zeta \text{ is an affine parameter.}$$

In these coordinates we consider the scalar valued function $f(x^\alpha, \dot{x}^\alpha)$ which is homogeneous and of first degree with respect to $\dot{x}^\alpha$.

To the curve C joining the point x_1 to x_2, one can always associate the integral $\mathcal{A}$ such that

$$\mathcal{A} = \int_{\zeta_1}^{\zeta_2} f(x^\alpha, \dot{x}^\alpha)\, d\zeta = \int_{x_1}^{x_2} f(x^\alpha, \dot{x}^\alpha)\, dx^\alpha. \tag{2.4}$$

We now want to evaluate the variation of $\mathcal{A}$ with respect to the points ζ_1 and ζ_2:

$$\delta\mathcal{A} = f\delta_{\zeta_2} - f\delta_{\zeta_1} - \int_{\zeta_1}^{\zeta_2} \delta f\, d\zeta.$$

Classically we know that:

$$\int_{\zeta_1}^{\zeta_2} \delta f\, d\zeta = \left[\frac{\partial f}{\partial \dot{x}^\alpha}\,\delta x^\alpha\right] - \int_{\zeta_1}^{\zeta_2} E_\alpha\, \delta x^\alpha\, d\zeta,$$

where E_α is the first member of the *Euler equations* associated with the function f.

With E_α as the components of $\boldsymbol{E}$, we infer the expression

$$\delta\mathcal{A} = [w(\delta)]_{x_2} - [w(\delta)]_{x_1} - \int_{\zeta_1}^{\zeta_2} \boldsymbol{E}\,\delta x\, d\zeta, \tag{2.5}$$

where $[w(\delta)]$ has the form:

$$[w(\delta)] = \left(\frac{\partial f}{\partial \dot{x}^\alpha}\right)\delta x^\alpha - \left(x^\alpha \frac{\partial f}{\partial \dot{x}^\alpha} - f\right)\delta\zeta.$$

Due to the homogeneity of f, it reduces to:

$$w(\delta) = \left(\frac{\partial f}{\partial \dot{x}^\alpha}\right)\delta x^\alpha.$$

Let us apply the above results to the function

$$f = \mathrm{e}^U \frac{ds}{d\zeta} = \mathrm{e}^U\left(g_{\alpha\beta}\dot{x}^\alpha \dot{x}^\beta\right)^{1/2},$$

where e^U is defined everywhere on $(\mathrm{M}, \boldsymbol{g})$.

Between two points x_1 and x_2, of $(\mathrm{M}, \boldsymbol{g})$ connected by a time-like curve we have the correspondence:

$$s' = \int_{x_1}^{x_2} \mathrm{e}^U ds = \int_{x_1}^{x_2} \mathrm{e}^U\left(g_{\alpha\beta}\dot{x}^\alpha \dot{x}^\beta\right)^{1/2}. \tag{2.6}$$

We first differentiate $f^2 = \mathrm{e}^{2U}\left(g_{\alpha\beta}\dot{x}^\alpha \dot{x}^\beta\right)$ with respect to $\dot{x}^\alpha$ and x^α:

$$f\frac{\partial f}{\partial \dot{x}^\alpha} = \mathrm{e}^{2U} g_{\alpha\beta}\dot{x}^\beta, \tag{2.7}$$

$$f\frac{\partial f}{\partial x^\alpha} = \mathrm{e}^U\left(g_{\beta\mu}\dot{x}^\beta \dot{x}^\mu\right)^{1/2} \times \left[\partial_\alpha \mathrm{e}^U\left(g_{\beta\mu}\dot{x}^\beta \dot{x}^\mu\right)^{1/2} + \frac{1}{2}\,\mathrm{e}^U \partial_\alpha\left(g_{\beta\mu}\dot{x}^\beta \dot{x}^\mu\right)\right]. \tag{2.8}$$

We now choose s as the affine parameter ζ of the curve C, so the vector $\dot{x}^\beta$ is here regarded as the unit vector u^β tangent to C.

Equations (2.7) and (2.8) then reduce to the following:

$$\frac{df}{d\dot{x}^\beta} = \mathrm{e}^U u_\beta, \tag{2.9}$$

$$\frac{df}{dx^\beta} = \partial_\beta \mathrm{e}^U + \frac{1}{2}\,\mathrm{e}^U \partial_\beta(g_{\alpha\mu})u^\alpha u^\mu,$$

$$\frac{df}{dx^\beta} = \partial_\beta \mathrm{e}^U + \mathrm{e}^U \Gamma_{\alpha\beta,\mu} u^\alpha u^\mu. \tag{2.10}$$

The $\Gamma_{\alpha\beta,\mu}$ are here the Christoffel symbols of the first kind.

Expliciting the Euler equations $f(x^\alpha, du^\alpha)$:

$$E_\beta = \frac{d}{ds}\frac{\partial f}{\partial u^\beta} - \frac{\partial f}{\partial x^\beta}, \tag{2.11}$$

we get:

$$E_\beta = \frac{d}{ds}\left(\mathrm{e}^U u_\beta\right) - \mathrm{e}^U\left(\Gamma_{\alpha\beta,\mu} u^\alpha u^\mu\right) - \partial_\beta \mathrm{e}^U,$$

$$E_\beta = \mathrm{e}^U\left(u^\mu \partial_\mu u_\beta - \Gamma_{\alpha\beta,\mu} u^\alpha u^\mu\right) - \partial_\alpha \mathrm{e}^U\left(\delta_\beta{}^\alpha - u^\alpha u_\beta\right),$$

$$E_\beta = \mathrm{e}^U\left[\left(u^\mu \nabla_\mu u_\beta\right) - \partial_\beta U - \partial_\alpha U\left(\delta_\beta{}^\alpha - u^\alpha u_\beta\right)\right]. \tag{2.12}$$

Equation (2.5) becomes:

$$\delta\mathcal{A} = [w(\delta)]_{x_2} - [w(\delta)]_{x_1} - \int_{x_1}^{x_2} \langle \boldsymbol{E}\delta x\rangle ds, \tag{2.13}$$

where locally: $w(\delta) = \mathrm{e}^U u_\alpha dx^\alpha$.

When the curve C varies between two *fixed* points x_1 and x_2 the local variations $[w(\delta)]_{x_2}$ and $[w(\delta)]_{x_1}$ vanish. Therefore applying the variational principle to (2.13) simply leads to:

$$\delta\mathcal{A} = -\int_{x_1}^{x_2} \langle \boldsymbol{E}\delta x\rangle ds = 0, \tag{2.14}$$

from which we infer $\boldsymbol{E} = 0$, i.e., from (2.12):

$$u^\mu \nabla_\mu u_\beta - \partial_\alpha U\left(\delta_\beta{}^\alpha - u^\alpha u_\beta\right) = 0 \qquad (\text{since } \mathrm{e}^U \neq 0). \tag{2.15}$$

The equation (2.15) is formally identical to the differential system obeyed by the flow lines of a perfect fluid of density ρ with an equation of state $\rho = f(P)$ (*see Appendix*):

$$T_{\mu\beta} = (\rho + P)u_\mu u_\beta - P g_{\mu\beta}. \tag{2.16}$$

These flow lines are thus timelike geodesics of the conformal metric to $(\mathrm{M}, \boldsymbol{g})$ according to (2.6):

$$s' = \int_{s_1}^{s_2} \mathrm{e}^U ds, \tag{2.17}$$

with

$$U = \int_{P_1}^{P_2} \frac{dP}{\rho + P}. \tag{2.18}$$

All along the curve segment (s'), the pressure is varying between two endpoints s_1 and s_2 which correspond to the values P_1 and P_2.

One can find similar conclusions in [3, 4].

The positive scalar e^U accounts for the *relativistic fluid index* [5].

2.2.2 The Gödel interpretation

The tensor (2.16) can be equivalently written:

$$T_{\mu\beta} = \rho u_\mu u_\beta - P h_{\mu\beta}, \tag{2.19}$$

with the *projection tensor*:

$$h_{\mu\beta} = g_{\mu\beta} - u_\mu u_\beta. \tag{2.20}$$

The cosmological term can then be re-introduced by setting

$$P = -\frac{\Lambda}{\varkappa}, \tag{2.21}$$

yielding the model which Gödel simply focused on.

Finally, by letting a be a *conformal factor*, we see that Gödel's metric (2.3) is simply the solution of the field equations with a variable pressure term as per:

$$R_{\mu\nu} - \frac{1}{2}\, g_{\mu\nu} R = \varkappa\left(\rho u_\mu u_\beta - P h_{\mu\beta}\right). \tag{2.21bis}$$

The cosmological "constant" Λ is thus no longer this arbitrary ingredient required to sustain the Gödel model and so are the constraints (1.8) and (1.9).

2.3 The Gödel rotation

2.3.1 Vorticity of the fluid

We just showed that Gödel space-time should be likened to a perfect fluid.

The time-like 4-vector u_α is everywhere tangent to the flow lines of this fluid.

The covariant derivative $u_{\alpha;\mu}$ may be expressed in a invariant manner in terms of tensor fields which describe the kinematics of the congruence of curves generated by u^α.

In Gödel's case, the *shear tensor* $\sigma_{\alpha\mu}$ vanishes:

$$\sigma_{\alpha\mu} = u_{(\alpha;\mu)} - \frac{1}{3}\,\theta h_{\alpha\mu} + \mathring{u}_{(\alpha}u_{\mu)} = 0, \tag{2.22}$$

where θ is the *expansion scalar*:

$$\theta = u^{\alpha}{}_{;\alpha}. \tag{2.22bis}$$

$\mathring{u}_\alpha$ is the *acceleration vector* of the flow lines:

$$\mathring{u}_\alpha = u_{\alpha;\mu}u^\mu. \tag{2.22ter}$$

For a perfect fluid, this acceleration is shown to be (*see Appendix*):

$$\mathring{u}_\alpha = \partial_\alpha U. \tag{2.23}$$

Besides $\mathring{u}_\alpha$ and θ, the shearless fluid is characterized by the *vorticity tensor*:

$$\omega_{\alpha\mu} = h_\alpha{}^\sigma h_\mu{}^\nu u_{[\sigma;\nu]} = u_{[\alpha;\mu]} + \mathring{u}_{[\alpha}u_{\mu]}, \tag{2.24}$$

from which is derived the vorticity *4-vector* $\boldsymbol{\omega}$ of the flow lines of the fluid.

The $\boldsymbol{\omega}$-components are known to be: [6]

$$\omega^\beta = \frac{1}{2}\,\eta^{\beta\gamma\sigma\rho}u_\gamma\omega_{\sigma\rho}, \tag{2.25}$$

with the Levi-Civita tensor: $\eta^{\beta\gamma\sigma\rho} = -g^{-1/2}\cdot\varepsilon^{\beta\gamma\sigma\rho}$.

The kinematic quantities $\omega_{\alpha\mu}$ and ω_α are completely orthogonal to u^μ , i.e.,

$$\omega_{\alpha\mu}u^\mu = 0, \quad \mathring{u}_\alpha u^\mu = \omega_\alpha u^\mu = 0.$$

(Shear free flows of a perfect fluid associated with the Weyl tensor have been extensively investigated by A. Barnes, Classical General Relativity. proc. Cambridge, 1984).

2.3.2 Conformal transformations

All above results can be easily extended to the conformal manifold $(\mathrm{M}, \boldsymbol{g}')$ by applying the covariant derivative $(\nabla_\mu)'$ formed with the *conformal connection coefficients*:

$$\left(\Gamma^\gamma{}_{\alpha\beta}\right)' = \Gamma^\gamma{}_{\alpha\beta} + 2\delta^\gamma{}_{(\alpha}U_{,\beta)} - g_{\alpha\beta}U^{\cdot\gamma}. \tag{2.26}$$

One also defines the unit 4-vector $\boldsymbol{w}$ of the fluid on the conformal metric $(ds^2)'$ as:

$$w^\mu = \mathrm{e}^U u^\mu, \tag{2.27}$$

$$w_\beta = \mathrm{e}^{-U}u_\beta. \tag{2.28}$$

In this case, the differential system of the flow lines w^μ admits the *relative integral invariant* in the sense of Poincaré [7]:

$$\int \Omega = \int w_\beta \delta x^\beta. \tag{2.29}$$

Denoting by $d\Omega$ the exterior differential of the form Ω, we have in local coordinates:

$$d\Omega = dw_\beta \wedge dx^\beta = \frac{1}{2}\Big[\partial_\beta w_\alpha - \partial_\alpha w_\beta\Big]dx^\beta \wedge dx^\alpha. \tag{2.30}$$

To the form $d\Omega$ is associated the antisymmetric tensor of components:

$$\omega_{\beta\alpha} = \partial_\beta w_\alpha - \partial_\alpha w_\beta. \tag{2.31}$$

It is easy to verify that these components coincide with the vorticity tensor components defined by (2.24). Unlike the vorticity tensor $\omega_{\beta\alpha}$, the vorticity vector ω^β does not remains the same upon the conformal transformations (2.27)–(2.28).

2.3.3 Application to the Gödel model

On the modified Gödel manifold $(\mathrm{M}, \boldsymbol{g}_\mathrm{G})$, the components of the unit 4-vector $\boldsymbol{w}_\mathrm{G}$ tangent to world lines of matter (1.3) (1.4) are here:

$$(w^\mu)_\mathrm{G} = \mathrm{e}^U(u^\mu)_\mathrm{G} = \mathrm{e}^U(1,0,0,0), \tag{2.32}$$

$$\Big(w_\beta\Big)_\mathrm{G} = \mathrm{e}^U\Big(u_\beta\Big)_\mathrm{G} = \mathrm{e}^{-U}(1,0,\mathrm{e}^{x_1},0). \tag{2.33}$$

Notice that the contravariant components $(u^\mu)_\mathrm{G}$ are all constant.

In this *particular case*, according to (2.23), one has

$$(\mathring{u}_\alpha)_\mathrm{G} = \partial_\alpha U = 0, \quad \text{i.e., } U \text{ is constant.}$$

By concatenation, the conformal factor $\exp U$ reduces to a constant and coincides with Gödel's choice $a = const$.

So the vorticity magnitude of the fluid's matter remains as in the initial theory:

$$\boldsymbol{\omega}_\mathrm{G} = \Big(g_{\alpha\mu}\omega^\alpha\omega^\mu\Big)_\mathrm{G}^{1/2} = \frac{a}{\sqrt{2}}. \tag{2.34}$$

On the other hand, we note that the covariant components of the velocity $(u_\beta)_\mathrm{G}$ are not all constant.

This means that the conformal geodesics principle holds within our theory.

In other words, we clearly see that Gödel's proposed solution is only a (very limited) special case (contravariant velocity components) which therefore reveals a patent lack of generality.

Therefore, Gödel's theory ought to be embedded in a broader scheme implying a conformal metric $\left(ds^2\right)'$ as we inferred above.

Note: one of the *Kretschmann scalar* is an invariant only for $\omega_{\mathrm{G}} : R_{\alpha\beta\gamma\delta}T^{\alpha\beta\gamma\delta} = 12{\omega_{\mathrm{G}}}^4$.

2.4 Chronal horizon

With Gödel one defines new (cylindrical) coordinates (t,r,ϕ,y) by setting:

$$\mathrm{e}^{x_1} = \cosh 2r + \cos\phi \sinh 2r, \tag{2.35}$$

$$x_2 \mathrm{e}^{x_1} = \sqrt{2}\sin\phi \sinh 2r, \tag{2.36}$$

$$\tan\frac{1}{2}\left[\phi + \frac{x-2t}{\sqrt{2}}\right] = \mathrm{e}^{-2r}\tan\frac{\phi}{2}, \tag{2.37}$$

$$2z = x_3. \tag{2.38}$$

Within the framework of our theory, these coordinates lead to the line element:

$$ds^2 = 4\mathrm{e}^{2U}(x)\Big[dt^2 - dr^2 - dz^2 + \\ + \left(\sinh^4 r - \sinh^2 r\right)d\phi^2 + 2\sqrt{2}\sinh^2 r\, d\phi\, dt\Big]. \tag{2.39}$$

This metric still exhibits the rotational symmetry of the solution about the axis $r = 0$, since we clearly see that the components of the metric tensor do not depend on ϕ.

For $r \geqslant 0$, we have: $0 \leqslant \phi \leqslant 2\pi$. If a curve r_{G} is defined by: $\sinh^4 r = 1$, that is

$$r_{\mathrm{G}} = \ln\left(1 + \sqrt{2}\right), \tag{2.40}$$

then any curve $r > \ln(1 + \sqrt{2})$, i.e. $(\sinh^4 r - \sinh^2 r) > 0$ materialized in the "plane" $t = const.$ (or zero t), is a *closed timelike curve*.

The radius r_{G} referred to as the *Gödel radius* induces a *light-like curve* or *closed null curve*, where the light cones are tangential to the plane of constant (or zero) t.

The photons trajectories reaching this radius are closing up, therefore r_{G} constitutes a *chronal horizon* beyond which an observer located at the origin ($r = 0$) cannot detect them.

With increasing $r > r_{\mathrm{G}}$ the light cones continue to keel over and their opening angles widen until their future parts reach the negative values of t.

In this *achronal domain*, any trajectory is a closed time-like curve and s' is extended over a full cycle.

As a result, the integral U performed over the closed path has no endpoints and is thus expressed in the form:

$$U = \int\left[\frac{dP}{\rho + P}\right] + const. \tag{2.41}$$

However, the pressure P which is fluctuating along the closed path remains at the same averaged value for the whole cycle and may be then regarded as globally constant.

In this case, the first term in the r.h.s. of (2.35) vanishes implies $U = const.$, and the conformal factor $(\exp U)$ may coincide again with Gödel's choice $a = const.$

Therefore, for $r > r_{\mathrm{G}}$, the acceleration of flow lines of matter is always zero whatever the components of w_{G}. Because of this, all closed timelike curves can no longer be derived from the geodesic principle calculation developed above.

By introducing the pressure in the Gödel model, we clearly put in evidence the difference between the geodesics and the closed time-like curves.

This was mathematically outlined in [8] but no explanation was provided as *why* this difference arises.

Conclusion

When Gödel wrote down his metric he was led to introduce a distinctive constant factor a in order to re-transcript the field equations with a cosmological constant along with additional constraints.

Our theory is free of all these constraints and moreover it provides a physical meaning to the a term. Inspection shows that by substituting a conformal factor to the constant a induces the field equations with a pressure like term which was wrongly interpreted by Gödel as the cosmological constant of the universe.

In fact, he empirically assembled the pieces of the constant matter density and curvature scalar in order to conveniently cope with the field equations precisely written with the cosmological constant.

In contrast, the reconstructed Gödel metric is here a straightforward solution to these equations and as such it can be reproduced like any other metric without referring to any cosmological model whatsoever.

The metric still exhibits a rotation which allows for the existence of *close timelike curves (CTCs)* since the light cone opens up and tips over, as the Gödel's circular coordinate radius increases within the cylindrical coordinates representation.

It seems that the first model exhibiting this property was pioneered by the German mathematician C. Lanczos in 1924 [9], and later rediscovered in a new form by the dutch physicist W. J. Van Stockum in 1937 [10].

However, the existence of *CTCs* satisfying the Einstein's equations remained so far a stumbling block for most of physicists because it should imply the possibility to travel back and forth in time.

The time travel possibility, was quoted as a pure mathematical "exercise" unrealistic in nature because it was deemed to describe a hypothetical universe contradicting the standard model in expansion as we observe it. Moreover, defining an absolute time is not readily applicable in Gödel space-time.

In here, the cards are now somewhat reshuffled: the Gödel model does not describe any sort of universe and the relevant metric can be applied as any other metrics like for example the Schwarzschild, the Kerr or the Alcubierre's ones.

Under these circumstances, why not considering the Gödel model as a potential time machine?

A typical example of such possible time machine is given by the cylinder system elaborated by the American physicist F. J. Tipler in 1974 [11].

It describes an infinitely long massive cylinder spinning along its longitudinal axis which gives rise to the "frame dragging" effect. If the rotation rate is fast enough the light cones of objects in cylinder's vicinity become tilted. Tipler suggested that a finite cylinder might also produce *CTCs* which was objected by Hawking who argued that any finite region containing *CTCs* would require negative energy density produced by a so-called "exotic matter" which violates all *energy conditions* [12].

The same kind of negative energy is needed to sustain a coupled system of *Lorentzian wormholes* designed to create a time machine as suggested in [13].

In all cases, feasibility and related causality paradoxes seemed to have been killed once for good by Hawking through a specific vacuum fluctuations mechanism that impedes any attempt to travel in the past [14].

Several authors have however recently challenged if not rejected this statement [15, 16].

These constraints do not apply in the present theory.

For a thorough study covering *CTCs* questions one can refer to [17, 18].

Submitted on May 24, 2021

References

1. Gödel K. An example of a New Type of Cosmological Solutions of Einstein's Field Equations of Gravitation. *Review of Modern Physics*, 1949, v.21(3).
2. Marquet P. Gödel's Universe Revisited. *Progress in Physics*, 2014, v.10, 259–262.
3. Eisenhart L.P. *Trans. Americ. Math. Soc.*, 1924, v.26, 205–220.
4. Synge J.L. *Proc. London Math. Soc.*, 1937, v.43, 37–416.
5. Lichnerowicz A. Les Théories Relativistes de la Gravitation et de l'Electromagnétisme. Masson et Cie, Paris, 1955.
6. Kramer D., Stephani H., Herlt E., Mac Callum M. Exact Solutions of Einstein's Field Equations. Cambridge University Press, Cambridge, 1982.
7. Cartan E. Leçons sur les invariants intégraux. A. Hermann, Paris, 1922.
8. Chandrasekhar S., Wright J.P. The geodesics in Gödels's universe. *Proc. of the National Academy of Sciences*, 1961, v.47(3), 341–347.
9. Lanczos C. Über eine Stationäre Kosmolologie im Sinne der Einsteinischer Gravitationstheorie. *Zeitschrift für Physik*, 1924, Bd.21, 73.
10. Van Stockum W. J. The gravitational field of a distribution of particles rotating around an axis of symmetry. *Proc. Roy. Soc. Edinburgh*, 1937, v.A57, 135.
11. Tipler F.J. Rotating cylinders and the possibility of global causality violation. *Phys. Rev. D.*, 1974, 9(8), 2203–2206.
12. Marquet P. Exotic Matter: A New Perspective. *Progress in Physics*, 2017, v.13, 174–179.
13. Morris M. S., Thorne K. S., Yurtsever U. Wormholes, Time machine and the weak energy condition. *Physical Rev. Letters*, 1988, v.61(13), 1446–1449.
14. Hawking S. W. Chronology protection conjecture. *Phys. Rev. D.*, 1991, v.46(2), 603–610.
15. Kim Sung Won, Thorne K. S. Do vacuum fluctuations prevent the creation of closed time-like curves? *Physical Review D*, 1991, v.43(12), 3929–3947.
16. Li Li-Xin. Must time machine be unstable against vacuum fluctuations? 2006, arXiv: gr-qc/9703024.
17. Friedmann J., Morris M.S., Novikov I., Echeverria F., Klinkhammer G., Thorne K.S., Yurtsever U. Cauchy problem in space-times with closed timelike curves. *Physical Rev. D*, 1990, v.42(6), 1915.
18. Thorne K. S. Closed Timelike Curves. Caltech, 1993, GRP-340.
19. Hawking S.W., Ellis G.F.R. The Large Scale Structure of Space-Time. Cambridge University Press, Cambridge, 1987.

Appendix

In a *holonomic frame* defined on (M,$\boldsymbol{g}$), the unit vectors are normalized so that:

$$g_{\mu\nu}u^\mu u^\nu = g^{\mu\nu}u_\mu u_\nu = 1. \tag{A.1}$$

By differentiating we get:

$$u^\mu \nabla_\nu u_\mu = 0. \tag{A.2}$$

Let us consider the following tensor which describes a homogeneous perfect fluid with density ρ and with pressure P:

$$T_{\mu\nu} = (\rho + P)u_\mu u_\nu - P g_{\mu\nu}. \tag{A.3}$$

The conservation equations are written:

$$\nabla_\mu[(\rho + P)u^\mu u_\nu] = \nabla_\mu\Big(P\delta_\nu^{\ \mu}\Big). \tag{A.4}$$

Setting the vector K_ν such that

$$(\rho - P)K_\nu = \nabla_\mu\Big(P\delta_\nu^{\ \mu}\Big), \tag{A.5}$$

$$\nabla_\mu[(\rho - P)u^\mu u_\nu] = (\rho + P)K_\nu, \tag{A.6}$$

$$\nabla_\mu[(\rho + P)u^\mu]u_\nu + (\rho + P)u^\mu\nabla_\mu u_\nu = (\rho + P)K_\nu. \tag{A.7}$$

Multiplying through with u^ν, and taking into account (A.2), we obtain after dividing by $(\rho + P)$:

$$u^\mu\nabla_\mu u_\nu = \Big(g_{\mu\nu} - u_\mu u_\nu\Big)K^\mu = h_{\mu\nu}K^\mu. \tag{A.8}$$

The flowlines everywhere tangent to the vector u^μ are determined by the differential equations (A.8).

K^μ only depends on x^μ and since: $h_{\mu\nu}K^\mu = K_\nu = \partial_\nu\dfrac{P}{\rho - P}$, we set

$$K_\nu = \partial_\nu U, \tag{A.9}$$

with

$$U = \int \frac{dP}{\rho + P}. \tag{A.10}$$

When the fluid pressure is function of the density, the 4-vector $\partial_\nu U$ is regarded as the *4-acceleration vector* $\mathring{u}_\nu$ of the flow lines given by the pressure gradient orthogonal to those lines [19, p.70].

A Statistical Approach to Two-particle Bell Tests

Xianming Meng

Research School of Physics, Australian National University, Canberra, ACT2601. E-mail: xianming.meng@anu.edu.au

Extensive experimental tests of the Bell inequality have been conducted over time and the test results are viewed as a testimony to quantum mechanics. In considering the close tie between quantum mechanics and statistical theory, this paper identifies the mistake in previous statistical explanation and uses an elegant statistical approach to derive general formulas for two-particle Bell tests, without invoking any wavefunctions. The results show that, for the special case where the spins/polarizations are in the same, opposite, or perpendicular directions, the general formulas derived in this paper convert to quantum predictions, which are confirmed by numerous experiments. The paper also investigates the linkages between the statistical and quantum predictions and finds that vector decomposition and probability law are at the heart of both approaches. Based on this finding, the paper explains statistically why the local hidden variable theory fails the Bell tests. The paper has important implications for quantum computing, quantum theory in general, and the role of randomness and realism in physics.

1 Introduction

The extensive study on Bell tests originated from the 1935 paper by Einstein *et al* [1], which claimed that physical reality can be predicted with certainty and that the uncertain nature of quantum prediction is due to incomplete information or the act of local hidden variables. Bohm [2] proposed a thought experiment to test the local hidden variable (LHV) theory and quantum mechanism, but this thought experiment was impractical to implement. In 1964, John Bell [3] developed the Bell inequality from the LHV theory as a testing tool: if the inequality is violated, the LHV theory is disproved. In 1969 Clauser *et al* [4] extended the Bell inequality to an experimentally testable version. Freedman and Clauser [38], Aspect [5, 6] and many others used this version to test the inequality and convincingly rejected it. Numerous experiments on Bell tests [7–21] have been conducted to close the "loopholes" in testing. Since almost all testing results are consistent with the quantum mechanical prediction, they are viewed as a testimony to quantum mechanism.

It is well known that quantum mechanics has a close tie with probability theory. The author suspects that both quantum mechanics and statistics mechanics may essentially be the same in the case of the Bell tests, and therefore identified the mistakes in previous statistical explanation and derived a statistical prediction for two-particle Bell tests. It is revealed that the quantum prediction of the Bell test results is a special case of the statistical prediction. By comparing the statistical and quantum derivations, the author further demonstrates that the essence of quantum prediction is probability law, and that quantum entanglement in two-particle Bell tests is nothing mysterious but an alternative expression for statistical correlation (i.e. there is no difference between statistical and quantum correlations). When the correlated particles are separated and facing different conditions (e.g. polarizers of different orientations), probability law can still maintain their correlation.

The paper is organized as follows: Section 2 demonstrates the deterministic or uncorrelated nature of the Bell inequality and reveals the mistakes in the previous statistical approach. Based on a general case of spin or polarization, Section 3 derives a statistical prediction for Bell tests for all possible uncorrelated and correlated particle pairs. Section 4 explores the linkage between the quantum and statistical predictions, while Section 5 uses the statistical approach to explain the results of representative two-particle Bell tests. Section 6 concludes the paper.

2 Deterministic or uncorrelated nature of the Bell inequality

Realism and localism play a key role in deriving the Bell inequality. The usual assumption for derivation is that at location A, a setting a (e.g. the direction of the spin/polarization analyser) leads to an experimental outcome $A(a)$, while setting b at location B leads to outcome $B(b)$, with the joint outcome being $E(a,b) = A(a)\,B(b)$. Since a setting leads to an outcome with certainty, the outcome is predetermined by the settings. This fits with the idea of determinism or realism. Moreover, the outcome at a location is determined only by the setting at that location, e.g. $A(a)$ is determined by local setting a at location A, not by setting b at location B. This is localism.

If settings a and b can be changed to a' and b', respectively, we can have joint outcomes:

$$E(a,b') = A(a)\,B(b')$$
$$E(a',b) = A(a')\,B(b)$$
$$E(a',b') = A(a')\,B(b')\,.$$

We further assume that the detected outcome at any setting is between -1 and +1, namely $|A| \leq 1$, $|B| \leq 1$. With these

assumptions, we can have:

$$\begin{aligned} E(a,b) - E(a,b') &= A(a)\,B(b) - A(a)\,B(b') \\ &= A(a)\,B(b) - A(a)\,B(b') + [A(a)\,B(b)][A(a')\,B(b')] \\ &- [A(a)\,B(b)][A(a')\,B(b')] \end{aligned}$$

or

$$\begin{aligned} E(a,b) - E(a,b') \quad &= A(a)\,B(b)\,[1 + A(a')\,B(b')] - \\ &- A(a)\,B(b')\,[1 + A(a')\,B(b)]\,. \end{aligned} \tag{1}$$

In absolute value, we can write:

$$\begin{aligned} \left|E(a,b) - E(a,b')\right| \quad &\le |A(a)\,B(b)| * |1 + A(a')\,B(b')| \; + \\ &+ |A(a)\,B(b')| * |1 + A(a')\,B(b)|\,. \end{aligned} \tag{2}$$

We have changed the negative sign on the right-hand side of (1) to a positive sign in (2) because $A(a)\,B(b')$ can be negative. Since the values of $A(a)$, $B(b)$, $A(a')$, and $B(b')$ are all between -1 and 1, we have:

$$|A(a)\,B(b)| \le 1 \quad \text{and} \quad \left|A(a)\,B(b')\right| \le 1\,.$$

As such, the inequality can be written as:

$$\begin{aligned} \left|E(a,b) - E(a,b')\right| &\le \left|1 + A(a')\,B(b')\right| + \left|1 + A(a')\,B(b)\right| \\ &= 2 \pm \left|A(a')\,B(b') + A(a')\,B(b)\right| \end{aligned}$$

or

$$\left|E(a,b) - E(a,b')\right| \le 2 \pm \left|E(a',b') + E(a',b)\right|\,. \tag{3}$$

On the right-hand side of (3), we used the "±" sign because both $A(a')\,B(b')$ and $A(a')\,B(b)$ can be negative (leading to negative sign) or positive (leading to positive sign). There are two boundaries in the above inequality. If the lower boundary is satisfied, the inequality holds, so we have arrived at the Bell inequality:

$$\left|E(a,b) + E(a',b') + E(a'b) - E(a,b')\right| \le 2\,. \tag{4}$$

To incorporate a hidden variable into the inequality, most researchers introduced a random variable. For example, Bell [3,22] and Clauser *et al* [4] added to the experiments a hidden variable λ, which has a normalized probability distribution:

$$\int_{-\infty}^{\infty} p(\lambda)\,d\lambda = 1\,.$$

With the added hidden variable, Bell [3,22] expressed the expected values of coincidence at the different settings a, a', b and b' as follows:

$$E(a,b) = \int_{-\infty}^{\infty} A(a,\lambda)\,B(b,\lambda)\,p(\lambda)\,d\lambda \tag{5}$$

$$E(a,b') = \int_{-\infty}^{\infty} A(a,\lambda)\,B(b',\lambda)\,p(\lambda)\,d\lambda \tag{6}$$

$$E(a',b) = \int_{-\infty}^{\infty} A(a',\lambda)\,B(b,\lambda)\,p(\lambda)\,d\lambda \tag{7}$$

$$E(a',b') = \int_{-\infty}^{\infty} A(a',\lambda)\,B(b',\lambda)\,p(\lambda)\,d\lambda\,. \tag{8}$$

Using the same procedure that was used to derive the Bell inequality for (3) – the deterministic case, Bell ([22, pp. 178–179]) derived (the notations are slightly changed for contemporary readers):

$$\begin{aligned} &E(a,b) - E(a,b') \;= \\ &= \textstyle\int_{-\infty}^{\infty} A(a,\lambda)\,B(b,\lambda)\,p(\lambda)\,d\lambda - \\ &- \textstyle\int_{-\infty}^{\infty} A(a,\lambda)\,B(b',\lambda)\,p(\lambda)\,d\lambda \\ &= \textstyle\int_{-\infty}^{\infty} [A(a,\lambda)\,B(b,\lambda) - A(a,\lambda)\,B(b',\lambda) + \\ &+ A(a,\lambda)\,B(b,\lambda)\,A(a',\lambda)\,B(b',\lambda) - \\ &- A(a,\lambda)\,B(b,\lambda)\,A(a',\lambda)\,B(b',\lambda)]\,p(\lambda)\,d\lambda \\ &= \textstyle\int_{-\infty}^{\infty} A(a,\lambda)\,B(b,\lambda)\,[1 + A(a',\lambda)\,B(b',\lambda)]\,p(\lambda)\,d\lambda - \\ &- \textstyle\int_{-\infty}^{\infty} A(a,\lambda)\,B(b',\lambda)\,[1 + A(a',\lambda)\,B(b,\lambda)]\,p(\lambda)\,d\lambda\,. \end{aligned} \tag{9}$$

In terms of absolute value, we have:

$$\begin{aligned} &|E(a,b) - E(a,b')| \\ &\le \left|\int_{-\infty}^{\infty} A(a,\lambda)\,B(b,\lambda)\,[1 + A(a',\lambda)\,B(b',\lambda)]\,p(\lambda)\,d\lambda\right| \\ &+ \left|\int_{-\infty}^{\infty} A(a,\lambda)\,B(b',\lambda)\,[1 + A(a',\lambda)\,B(b,\lambda)]\,p(\lambda)\,d\lambda\right| \\ &\le \left|\int_{-\infty}^{\infty} [1 + A(a',\lambda)\,B(b',\lambda)]\,p(\lambda)\,d\lambda\right| \\ &+ \left|\int_{-\infty}^{\infty} [1 + A(a',\lambda)\,B(b,\lambda)]\,p(\lambda)\,d\lambda\right| \\ &= 2 \pm |E(a',b') + E(a',b)|\,. \end{aligned}$$

Rearranging the above inequality as before, we can obtain the same inequality as (4).

From the above derivation, one may notice that the same term $\int_{-\infty}^{\infty} p(\lambda)\,d\lambda$ is added to outcomes of the different settings and then this term is filtered out in the end by the definition of expected values in (7) and (8). As such, the added hidden variable and probability are only additional statistical noise, which does not change the deterministic nature of the resulting inequality.

Later, Bell and others [28–30] moved on to a version of the Bell inequality based on joint and conditional probabilities. However, they used the same assumption that the distribution of hidden variable λ is UNRELATED to local settings. This assumption apparently contradicts the concept of a local variable. Ironically, the assumption is often regarded as a feature of a local variable. Myrvold *et al* [23] used a different approach. Instead of concerning the probability distributions of λ conditioned on settings, they conditioned the experimental outcomes on hidden variable λ. Since they assigned no

statistical property to λ, its behaviour is unknown, so its role in their derivation is negligible, or not essential at least.

To present a genuine statistical event, one should allow the probability density λ to vary with the local settings. In other words, the probability of value λ must be conditioned on the settings, i.e. for settings a and b, we have the probability $p(\lambda\,|\,a)$ and $p(\lambda\,|\,b)$, respectively. The probability of the joint outcome of settings a and b should be $p(\lambda\,|\,a,b)$. Similarly, we have $p(\lambda\,|\,a,b')$, $p(\lambda\,|\,a',b)$, $p(\lambda\,|\,a',b')$ for other joint settings. As such, the expected joint detection should be:

$$E(a,b) = \int_{-\infty}^{\infty} A(a,\lambda)\,B(b,\lambda)\,p(\lambda\mid a,b)\,d\lambda$$

$$E(a,b') = \int_{-\infty}^{\infty} A(a,\lambda)\,B(b',\lambda)\,p(\lambda\mid a,b')\,d\lambda$$

$$E(a',b) = \int_{-\infty}^{\infty} A(a',\lambda)\,B(b,\lambda)\,p(\lambda\mid a',b)\,d\lambda$$

$$E(a',b') = \int_{-\infty}^{\infty} A(a',\lambda)\,B(b',\lambda)\,p(\lambda\mid a',b')\,d\lambda\,.$$

Using this new definition of expected values, the terms for the probability of λ are different for each joint setting and thus cannot be filtered out. As a result, the Bell inequality cannot be derived.

However, one may further assume that the joint probability of outcome at joint setting a and b is the multiplication of probabilities of outcomes at each setting, namely:

$$p(\lambda\,|\,a,b) = p(\lambda\,|\,a)\,p(\lambda\,|\,b) \tag{10}$$

where $0 \le p(\lambda\,|\,a) < 1$; $0 \le p(\lambda\,|\,b) < 1$; $\int_{-\infty}^{\infty} p(\lambda\,|\,a)\,d\lambda = 1$; and $\int_{-\infty}^{\infty} p(\lambda\,|\,b)\,d\lambda = 1$.

Applying the same method for joint settings a and b', a' and b, and a' and b', we have:

$$p(\lambda\,|\,a,b') = p(\lambda\,|\,a)\,p(\lambda\,|\,b')$$

$$p(\lambda\,|\,a',b) = p(\lambda\,|\,a')\,p(\lambda\,|\,b)$$

$$p(\lambda\,|\,a',b') = p(\lambda\,|\,a')\,p(\lambda\,|\,b')\,.$$

Based on the above joint probabilities, we can calculate $E(a,b)$, $E(a,b')$, $E(a',b)$ and $E(a',b')$. Following the same procedure as in deriving (9), we can derive the Bell inequality (4).

As we see, (10) is crucial for deriving the Bell inequality from a statistical point of view. However, the expression of joint probability as a product of the probability of outcome of two experiments is not without a condition. The well-known but often neglected condition is that the two experiments involved in the joint probability calculation in (10) must be totally unrelated, i.e. independent random experiments. Applying this condition to the Bell tests, the requirement is that the probabilities of outcomes at different locations/settings are independent of each other, so "local" means "uncorrelated". This interpretation gives the alternative condition for the Bell inequality. That is, if the outcomes are not deterministic, the outcomes at two different settings should not be correlated.

The common wisdom is that, during a Bell test, the experiments at different locations A and B are apparently independent because the orientations of the polarizers at A and B are changed independently and randomly. However, the independence of settings are not the full condition for independent experiments because local settings are only one element of the polarization experiments. The other element is the light source. In fact, correlated source particles are used in all Bell tests conducted so far, so the experiments conducted at different locations are not independent. Since the experiments based on different settings are correlated by source particles, the joint probability in a Bell test should be calculated based on conditional probability:

$$p_{a,b} = p_a * p_{b|a}$$

or

$$p_{a,b} = p_b * p_{a|b}\,.$$

Similar mistakes are also commonly made in treating the expected value of joint events as being the multiplication of the expected values of separate events. Due to the statistical nature of the polarization experiments, we need to allow one setting to generate different results, e.g. experiments based on setting a can have results $A_1(a), A_2(a), \ldots A_n(a)$, so the expected value for results of setting a can be expressed as:

$$E(a) = \frac{1}{n}\sum_i A_i(a)\,. \tag{11}$$

We can also write the expected value for results of setting b as:

$$E(b) = \frac{1}{n}\sum_i B_i(b)\,. \tag{12}$$

Indeed, Bell [22, p. 178] realized the importance of introducing (11) and (12) for $E(a)$ and $E(b)$. However, with no precondition being specified, he assumed the following equality as the base for deriving the Bell inequality:

$$E(a,b) = E(a) * E(b)\,. \tag{13}$$

The above equation is used by numerous researchers on Bell tests, but the equation is not unconditional. Statistically, we can expand the expected values as:

$$E(a,b) = \frac{1}{n}\sum_i A_i(a)\,B_i(b) \tag{14}$$

$$E(a) * E(b) = \frac{1}{n^2}\sum_i A_i(a)\sum_i B_i(b)\,. \tag{15}$$

Apparently, $E(a,b) \neq E(a) * E(b)$ in general cases. A special statistical case where $E(a,b) = E(a) * E(b)$ holds is

when the outcomes of $A_i(a)$ are independent of (or not correlated to) the outcomes of $B_i(b)$. In this special case, the Bell inequality will hold. If $E(a)$ and $E(b)$ are correlated, we must use the conditional expected values that reflect the correlations between two experiments.

From the above discussion, we can conclude that the Bell inequality does not allow for a probabilistic nature (or correlation, to be exact) because it is based on determinism or realism. To allow for the Bell inequality in a statistical experiment, one must satisfy the condition for (13), which in turn requires that there is no correlation between $A_i(a)$ and $B_i(b)$. In terms of quantum mechanics terminology, if particles 1 and 2 are in separable (uncorrelated) states, the Bell inequality is valid, otherwise (if particles 1 and 2 are in entangled states), the Bell inequality will be violated.

3 A statistical interpretation of spin/polarization correlation

A statistical presentation of Bell tests seems to be complicated because it involves many random settings, such as random directions of polarizers and random polarization of light or spins of particles. Moreover, spins and polarizations have different features. After trying a number of methods, the author has arrived at a remarkably simple and elegant approach for deriving the statistical prediction.

The difference between polarization and spin is that spins in opposite directions have different values while polarizations in the opposite directions are viewed as being the same. In other words, the spin direction in a plane can have a 360° variation while the polarization direction varies only within 180°, so the case of polarization is a reduced case of spin. For generality, this section focuses on deriving the results for the case of spin, and then shows how the results can be applied to the case of polarization.

There are various types of spin analyzer/detector [24–27], but all spin detectors rely on a differing scattering cross section for spin polarized particles. During spin detection, the travel direction of the particle and the detector orientation form a plane, in which the particles are reflected and detected [25]. The spin polarized particles will cause asymmetric reflection, and the asymmetric results indicate the detected spin direction. Essentially, a spin analyser works similarly to a polarizer for light, but the analyser can identify the spin direction along the given detection orientation. Consequently, we use a polarizer with an arrow (a vector) to represent a spin analyzer.

Fig. 1 shows a general case where the particles of the different spin directions are measured by the two spin analyzers in a Bell test experiment. Two spins, s_1 and s_2, and two spin analyzers, A and B, are positioned in different directions. The spin directions of particles 1 and 2 form an angle of θ_1 and θ_2, respectively, with the x-axis. For simplicity, we assume that s_1 and s_2 are unit vectors, and that spin analyzer A is placed

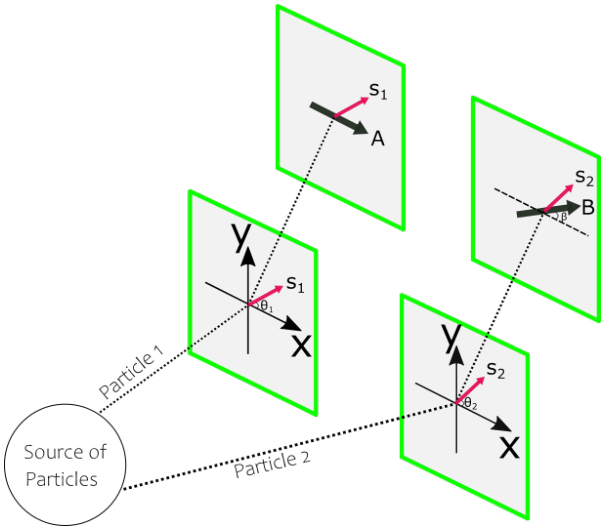

Fig. 1: Measuring spin directions

in the direction of the x-axis while spin analyzer B forms an angle of β with the x-axis. Given this setting, the component of s_1 detected by A is $E(A) = \cos\theta_1$. Similarly, the angle between s_2 and the spin analyzer B is $\theta_2 - \beta$, so the component of s_2 detected by B is $E(B) = \cos(\theta_2 - \beta)$.

There are two types of correlation measurement in the Bell tests. One is the joint detection counts normalized on the separate detection counts at each setting. The other is the joint detection rate normalized on the emission rate at the particle source. We address them in turn.

3.1 Correlation normalized on outcomes at each setting

This measurement fits with the standard definition of correlation, so we can calculate the expected value, variance and covariance and then obtain correlation. Since the source emits particles of random spin directions, the expected values and variances can be obtained by integrating $E(A)$ and $E(B)$ over the spin angles θ_1 and θ_2 in the range of $0 - 2\pi$ for particles 1 and 2.

$$\langle E(A)\rangle = \frac{\int_0^{2\pi} E(A)\, d\theta_1}{\int_0^{2\pi} d\theta_1} = \frac{\int_0^{2\pi} \cos\theta_1\, d\theta_1}{\int_0^{2\pi} d\theta_1} = \frac{\sin\theta_1}{\theta_1}\Big|_0^{2\pi} = 0$$

$$\begin{aligned}\mathrm{var}(A) &= \frac{\int_0^{2\pi} [\cos\theta_1 - \langle E(A)\rangle]^2\, d\theta_1}{\int_0^{2\pi} d\theta_1} \\ &= \frac{1}{2\pi}\int_0^{2\pi} \cos^2\theta_1\, d\theta_1 \\ &= \frac{1}{2\pi}\int_0^{2\pi} 0.5\,(\cos 2\theta_1 + 1)\, d\theta_1 = 0.5\end{aligned}$$

$$\langle E(B)\rangle = \frac{\int_0^{2\pi} E(B)\, d\theta_2}{\int_0^{2\pi} d\theta_2} = \frac{\int_0^{2\pi} \cos(\theta_2 - \beta)\, d\theta_2}{\int_0^{2\pi} d\theta_2} = 0$$

$$\begin{aligned}\mathrm{var}(B) &= \frac{\int_0^{2\pi}[\cos(\theta_2-\beta)-\langle E(B)\rangle]^2\,d\theta_2}{\int_0^{2\pi}d\theta_2}\\ &= \frac{1}{2\pi}\int_0^{2\pi}\cos^2(\theta_2-\beta)\,d\theta_2\\ &= \frac{1}{2\pi}\int_0^{2\pi}0.5\,[\cos 2(\theta_2-\beta)+1]\,d\theta_2 = 0.5\,.\end{aligned}$$

If the two particles are uncorrelated, θ_1 and θ_2 can vary independently, so the covariance can be calculated through a double integral:

$$\begin{aligned}&\mathrm{cov}(A,B) =\\ &= \frac{\iint_0^{2\pi}[\cos\theta_1-\langle E(A)\rangle][\cos(\theta_2-\beta)-\langle E(B)\rangle]\,d\theta_1\,d\theta_2}{\iint_0^{2\pi}d\theta_1\,d\theta_2}\\ &= \frac{1}{(2\pi)^2}\int_0^{2\pi}\cos\theta_1\,d\theta_1\int_0^{2\pi}\cos(\theta_2-\beta)\,d\theta_2 = 0\,.\end{aligned}$$

The zero covariance is expected because of the uncorrelated nature of s_1 and s_2 — the positive and negative joint detection counts will be largely cancelled out. If the two spins are correlated, θ_1 and θ_2 can still change randomly, but these two angles must keep the same difference, i.e. $\theta_2 = \theta_1 + \theta_0$, where θ_0 is the fixed relative angle between two spin directions. In this case, the covariance can be calculated by an integration over θ_1 (or θ_2):

$$\begin{aligned}&\mathrm{cov}(A,B) =\\ &= \frac{\int_0^{2\pi}[\cos\theta_1-\langle E(A)\rangle][\cos(\theta_1+\theta_0-\beta)-\langle E(B)\rangle]\,d\theta_1}{\int_0^{2\pi}d\theta_1}\\ &= \frac{1}{2\pi}\int_0^{2\pi}0.5\,[\cos(2\theta_1+\theta_0-\beta)+\cos(\beta-\theta_0)]\,d\theta_1\\ &= 0.5\cos(\beta-\theta_0)\,.\end{aligned}$$

As such, we have the following spin correlation:

$$\begin{aligned}E(A,B) &= \frac{\mathrm{cov}(A,B)}{[\mathrm{var}(A)]^{1/2}[\mathrm{var}(B)]^{1/2}}\\ &= \frac{0.5\cos(\beta-\theta_0)}{0.5^{0.5}*0.5^{0.5}} = \cos(\beta-\theta_0)\,.\end{aligned}\qquad(16)$$

Eq. (16) is a general result for joint detection for any given orientations of spin detectors. The application of this equation for special occasions can produce quantum predictions. For example, if two particles have the same spin, i.e. entangled particles of the same phase, we have $\theta_0 = 0$, $E(A,B) = \cos\beta$. If two particles have the opposite spin, i.e., negatively correlated particles, we have $\theta_0 = \pi$, $E(A,B) = -\cos\beta$. If the two spin vectors are perpendicular, $\theta_0 = \pi/2$, $E(A,B) = \cos(\pi/2-\beta) = \sin\beta$.

It is worth mentioning that some researchers used light intensity correlation instead of the expected-value correlation for polarization Bell test. For example, Ou and Mandel [31] and Rarity and Tapster [35] regarded the joint detection probability of photons as being proportional to the intensity correlation of light. This approach is misplaced. For polarization experiments, one or more photons (assuming perfect detection for the simplicity of an argument) pass through the polarizer, a positive detection will be recorded, so the intensity is not an appropriate measurement. One may argue that intensity is the square of amplitude so intensity can be used as the proxy of probability of photons passing through the polarizer, based on which the joint probability can be calculated. However, as explained in Section 2, the joint probability cannot be calculated through the multiplication of probabilities of separate detections because of the correlated particles in a Bell test. Since probability measures the average of the squared detection values, the intensity (or probability) correlation approach will produce totally different result from that in this paper. This can be shown in the following expression:

$$p_{AB} = p_A\,p_B = \langle E(A)^2\rangle\,\langle E(B)^2\rangle \neq \langle E(A)\,E(B)\rangle^2 = E(A,B)^2\,.$$

3.2 Correlation normalized on emissions at the source

For a Bell test, one needs to measure many pairs of particles of different spin directions with varied detector orientations. In this case, the joint detection rate is generally normalized on the emission rate at the source and the correlation is calculated based on the fixed axes.

Referring to Fig. 1, if the correlation is calculated based on x and y axes, the component detected by analyzer A and B needs to be further decomposed on the x-axis and y-axis:

$$E_{Ax} = E(A) = \cos\theta_1 \text{ and } E_{Ay} = 0$$

$$E_{Bx} = E(B)\cos\beta = \cos(\theta_2-\beta)\cos\beta$$

$$E_{By} = E(B)\sin\beta = \cos(\theta_2-\beta)\sin\beta\,.$$

Since no component on the y-axis is detected by analyzer A, the correlation (joint detection) on the y-axis is zero. On the other hand, both analyzers detect values on the x-axis, so the joint detection value is:

$$E_{AB} = E_{Ax}\,E_{Bx} = \cos\theta_1\cos(\theta_2-\beta)\cos\beta\,.$$

Since the correlation is based on the emissions at source, which are 100% detected (assuming all particles come to and are detected by either detector A or B), the variances are one and thus the correlation is equivalent to co-variance. If particles 1 and 2 are uncorrelated, the joint detection rate will be the value of E_{AB} integrated over both θ_1 and θ_2:

$$p_{AB} = \frac{\iint_0^{2\pi}E_{AB}\,d\theta_1\,d\theta_2}{\iint_0^{2\pi}d\theta_1\,d\theta_2}$$

$$= \frac{\iint_0^{2\pi} \cos\theta_1 \cos(\theta_2 - \beta) \cos\beta \, d\theta_1 \, d\theta_2}{\iint_0^{2\pi} d\theta_1 \, d\theta_2}$$
$$= \frac{\cos\beta}{(2\pi)^2} \int_0^{2\pi} \cos\theta_1 \, d\theta_1 \int_0^{2\pi} \cos(\theta_2 - \beta) \, d\theta_2 = 0 \, .$$

The above result indicates that for uncorrelated particles, the joint detection rate is zero. This makes sense. Due to the uncorrelated random nature, the different detection counts will be washed out by the independent random changes in θ_1 and θ_2.

If two particles are correlated, i.e. $\theta_2 = \theta_1 + \theta_0$, we can obtain correlation by integrating E_{AB} over θ_1 (or θ_2) in range $0 - 2\pi$:

$$\begin{aligned} p_{AB} &= \frac{\int_0^{2\pi} E_{AB} \, d\theta_1}{\int_0^{2\pi} d\theta_1} \\ &= \frac{\int_0^{2\pi} \cos\theta_1 \cos(\theta_1 + \theta_0 - \beta) \cos\beta \, d\theta_1}{\int_0^{2\pi} d\theta_1} \\ &= \frac{\cos\beta}{2\pi} \int_0^{2\pi} 0.5 \left[\cos(2\theta_1 + \theta_0 - \beta) + \cos(\beta - \theta_0)\right] d\theta_1 \\ &= 0.5 \, \cos(\beta - \theta_0) \cos\beta \, . \end{aligned} \tag{17}$$

The above result shows that when the two spin vectors are correlated, i.e., the value of θ_0 is fixed, the joint detection rate is determined only by correlation phase θ_0 and the angle β formed by the orientations of two spin detectors.

Eqs. (16) and (17) can also be applied to light polarization experiments. In the case of polarized light, it is tricky to derive the joint detection because the detected values have to be non-negative and thus are not consistent with the cosine functions for $E(A)$ and $E(B)$. The common approach (e.g. Aspect *et al* [4, 5]) is to define the result of no-detection as -1, instead of 0. In other words, when the light polarization is perpendicular to the orientation of detector, most likely no photon will be detected and thus a result of -1 with a 90° will be recorded. With this definition, all angles in (16) and (17) should be halved, and then the equation is equally applicable to the Bell tests with polarized light.

Where the two spin vectors are in the same directions (i.e. $\theta_0 = 0$), (17) becomes:

$$p_{AB} = 0.5 \cos^2\beta = 0.25 \, (\cos 2\beta + 1) \, . \tag{18}$$

In this special case, the joint detection rate can also be derived without integration, as shown in Fig. 2.

To present three random directions (i.e. the same direction of spin of the two particles, and the directions of the two spin analyzers A and B), we can fix one of them because only the relative angles between them matter. For convenience of presentation, we assume the spin vector $\overrightarrow{OV}$ to be a unit vector pointing to $\mathrm{V}(a_x/\sqrt{2}, a_y/\sqrt{2})$, where a_x and a_y are unit vectors at x and y directions, respectively.

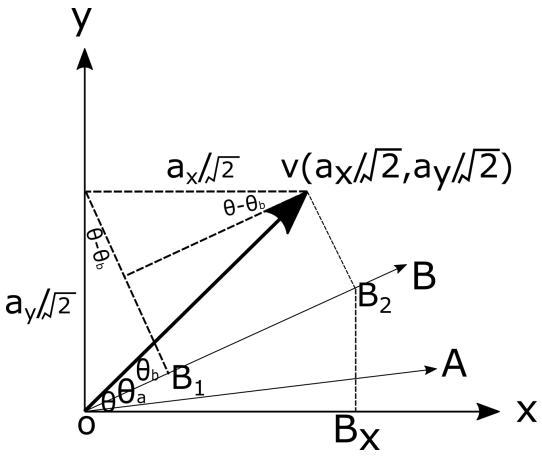

Fig. 2: Measuring the correlation of a particle pair of the same spin

The projection of the spin vector $\overrightarrow{OV}$ onto the B axis in Fig. 2 is:

$$\overrightarrow{OB_2} = \overrightarrow{B_1B_2} + \overrightarrow{OB_1} = \left[\vec{a_x}\cos(\theta - \theta_b) + \vec{a_y}\sin(\theta - \theta_b)\right] / \sqrt{2} \, .$$

This projection can be further projected onto the x-axis and y-axis and thus decomposed to two components $\overrightarrow{OB_x}$ and $\overrightarrow{OB_y}$, respectively ($\overrightarrow{OB_y}$ is not shown in Fig. 2 so as not to complicate the graph):

$$\overrightarrow{OB_x} = \cos(\theta - \theta_b) \left[\vec{a_x}\cos(\theta - \theta_b) + \vec{a_y}\sin(\theta - \theta_b)\right] / \sqrt{2} \tag{19}$$

$$\overrightarrow{OB_y} = \sin(\theta - \theta_b) \left[\vec{a_x}\cos(\theta - \theta_b) + \vec{a_y}\sin(\theta - \theta_b)\right] / \sqrt{2} \, . \tag{20}$$

Similarly, the projection of $\overrightarrow{OV}$ onto the A-axis can be decomposed into the x and y components of $\overrightarrow{OA_x}$ and $\overrightarrow{OA_y}$ respectively (not shown in Fig. 2):

$$\overrightarrow{OA_x} = \cos(\theta - \theta_a) \left[\vec{a_x}\cos(\theta - \theta_a) + \vec{a_y}\sin(\theta - \theta_a)\right] / \sqrt{2}$$

$$\overrightarrow{OA_y} = \sin(\theta - \theta_a) \left[\vec{a_x}\cos(\theta - \theta_a) + \vec{a_y}\sin(\theta - \theta_a)\right] / \sqrt{2} \, .$$

As such, the joint detection rate can be calculated as:

$$\begin{aligned} p_{AB} &= \overrightarrow{OA_x}\overrightarrow{OB_x} + \overrightarrow{OA_y}\overrightarrow{OB_y} \\ &= \cos(\theta - \theta_b) \left[\vec{a_x}\cos(\theta - \theta_b) + \vec{a_y}\sin(\theta - \theta_b)\right] / \sqrt{2} \\ &\times \cos(\theta - \theta_a) \left[\vec{a_x}\cos(\theta - \theta_a) + \vec{a_y}\sin(\theta - \theta_a)\right] / \sqrt{2} \\ &+ \sin(\theta - \theta_b) \left[\vec{a_x}\cos(\theta - \theta_b) + \vec{a_y}\sin(\theta - \theta_b)\right] / \sqrt{2} \\ &\times \sin(\theta - \theta_a) \left[\vec{a_x}\cos(\theta - \theta_a) + \vec{a_y}\sin(\theta - \theta_a)\right] / \sqrt{2} \\ &= 0.5 \left[\vec{a_x}\cos(\theta - \theta_b) + \vec{a_y}\sin(\theta - \theta_b)\right] \\ &\times \left[\vec{a_x}\cos(\theta - \theta_a) + \vec{a_y}\sin(\theta - \theta_a)\right] \cos(\theta_a - \theta_b) \\ &= 0.5 \cos^2(\theta_a - \theta_b) \end{aligned}$$

or

$$p_{AB} = 0.25\,[\cos 2(\theta_a - \theta_b) + 1]\,. \tag{21}$$

Noting that $(\theta_a - \theta_b)$ is the angle formed by the orientations of two detectors A and B, we find that the above result is the same as (18). This joint probability of detection is exactly the same as the coincidence rate derived from quantum mechanics. The experiment by Aspect [5] confirmed this result.

The correlation function (16) and the joint detection rate (17) derived in this section are general results that are applicable to both uncorrelated or correlated polarization/spin of any phase differences. The results can be tested experimentally using the current Bell test techniques. The only change needed is to add a randomly controlled source polarizer for each of the two beams after the collimation lenses, but before the traditional Bell test polarizers. If the pair of source polarizers are randomly and separately controlled, i.e. their relative angle of polarization θ_0 varies randomly, the source particles are uncorrelated, so the joint detection rate will be zero for a large sample size. If the pair of source polarizers are controlled randomly but jointly, i.e. the relative polarization angle of the pair is fixed at any given value, the joint detection rate should be determined by the relative angle (θ_0) of the first pair of (source) polarizers and that (β) of the second pair, with the quantitative relations determined by (16) and (17).

4 Linkage between the statistical approach and quantum mechanics

From the previous section, we see that the simple statistical approach gives equivalent but more general results when they are compared with the predictions from quantum mechanics (QM). This is not a coincidence. This section shows that the statistical approach is at the heart of quantum mechanical prediction on Bell tests.

QM uses wavefunctions to represent the different states. For example, a wavefunction of a spin-up (or +1) state can be written in Dirac notation as $|0\rangle$, while spin-down (or -1) can be written as $|1\rangle$. The spin states can be projected to (or measured on) different axes and may result in different results. If Alice measures a spin state of $|0\rangle$ on the A-axis while Bob measures $|1\rangle$ on the B-axis, we can express this spin state as $|0\rangle \otimes |1\rangle$, or simply $|01\rangle$. A wavefunction $|01\rangle + |10\rangle$ indicates that the measurement on the A-axis is always opposite to the measured results on the B-axis, i.e. the measured results are negatively correlated. Similarly, the states in wavefunction $|00\rangle + |11\rangle$ are positively correlated. The states in this type of wavefunctions are called entangled states. On the other hand, a wavefunction of $|01\rangle + |00\rangle$ shows that while Alice's measurement is always $|0\rangle$, Bob's measurement can be either $|0\rangle$ or $|1\rangle$, so there is no correlation between the two measurement results. The states in this wavefunction are called separable states. In short, the entangled states are the QM expression for correlation.

Now we consider a normalized wavefunction of the positively entangled states: $\psi = (|00\rangle + |11\rangle)/\sqrt{2}$. If the states are measured by Alice on the A or x axis (both axes coincide, shown in Fig. 3), the possible outcome will be $\langle 0|\sigma^A|0\rangle = +1$ or $\langle 1|\sigma^A|1\rangle = -1$. Similarly, if the state is measured by Bob on the B-axis, the possible outcome will be $\langle 0|\sigma^B|0\rangle = +1$ or $\langle 1|\sigma^B|1\rangle = -1$. Since this is a wavefunction of positively entangled states, Alice and Bob will always obtain the same (positive or negative) measurement outcome. Bob's measurement can be decomposed to two components on the x-axis and y-axis: $\sigma^B = \sigma_x^B \cos\beta + \sigma_y^B \sin\beta$. Alternatively, we can write: $\langle 0|\sigma_x^B|0\rangle = \cos\beta$, $\langle 1|\sigma_x^B|1\rangle = -\cos\beta$, $\langle 0|\sigma_y^B|0\rangle = \sin\beta$, $\langle 1|\sigma_y^B|1\rangle = -\sin\beta$. Since Alice's measurement is on the x-axis, we have $\sigma^A = \sigma_x^A$.

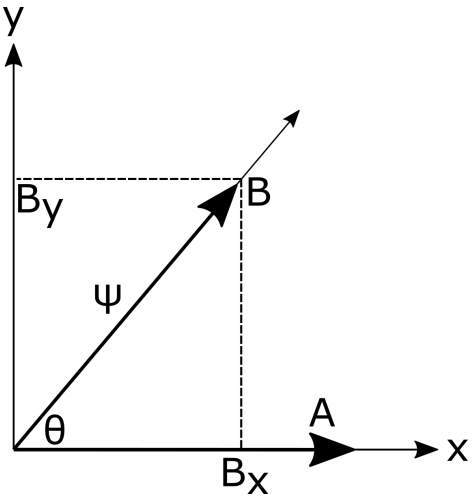

Fig. 3: Spin measurement for positively entangled particles

The correlation between the measurements of Alice and Bob can be calculated by the expected value of joint measurements: $\langle \sigma^A \sigma^B \rangle$. The QM calculation result is as follows:

$$\begin{aligned}
&\langle \sigma^A \sigma^B \rangle = \langle \psi\,|\,\sigma^A \otimes \sigma^B\,|\,\psi \rangle \\
&= 0.5\,(\langle 00|\,+\langle 11|\,)\sigma^A \otimes \sigma^B(|\,00\rangle + |\,11\rangle) \\
&= 0.5\,(\langle 00|\,\sigma^A \otimes \sigma^B\,|\,00\rangle + \langle 11|\,\sigma^A \otimes \sigma^B\,|\,00\rangle) \\
&+ \langle 00|\,\sigma^A \otimes \sigma^B\,|\,11\rangle + \langle 11|\,\sigma^A \otimes \sigma^B\,|\,11\rangle) \\
&= 0.5\,(\langle 0|\,\sigma^A\,|\,0\rangle\langle 0|\,\sigma^B\,|\,0\rangle + \langle 1|\,\sigma^A\,|\,0\rangle\langle 1|\,\sigma^B\,|\,0\rangle) \\
&+ \langle 0|\,\sigma^A\,|\,1\rangle\langle 0|\,\sigma^B\,|\,1\rangle + \langle 1|\,\sigma^A\,|\,1\rangle\langle 1|\,\sigma^B\,|\,1\rangle) \\
&= 0.5\,(\langle 0|\,\sigma^A\,|\,0\rangle\langle 0|\,\sigma^B\,|\,0\rangle + \langle 1|\,\sigma^A\,|\,1\rangle\langle 1|\,\sigma^B\,|\,1\rangle) \\
&= 0.5\,(\langle 0|\,\sigma_x^A\,|\,0\rangle\langle 0|\,\sigma_x^B\,|\,0\rangle + \langle 1|\,\sigma_x^A\,|\,1\rangle\langle 1|\,\sigma_x^B\,|\,1\rangle) = \cos\beta\,.
\end{aligned}$$

The above result is exactly the same as (16) with $\theta_0 = 0$, which was obtained from the much simpler statistical approach. A number of statistical features in the QM approach contribute to this same result. First, the calculation of the expected value in QM (i.e. $\langle \sigma^A \sigma^B \rangle = \langle \psi\,|\sigma^A \otimes \sigma^B\,|\,\psi \rangle$) is

based on a probability-weighted average. Second, the rule of tensor product ($\langle 11\,|\,\sigma^A\otimes\sigma^B\,|\,00\rangle = \langle 1\,|\,\sigma^A\,|\,0\rangle\langle 1\,|\,\sigma^B\,|\,0\rangle$) makes an operator (e.g. σ^A or σ^B) work on the wavefunction on its space only. This is exactly the case of measurement (or vector component decomposition) on different axes. Third, the orthogonal condition of basis wavefunctions mimics the measurement of the projection onto the orthogonal axes, e.g. $\langle 0\,|\,\sigma^A\,|\,0\rangle = +1$, $\langle 1\,|\,\sigma^B\,|\,1\rangle = -1$, and $\langle 1\,|\,\sigma^A\,|\,0\rangle = 0$. Fourth, the space (or axis) separation is consistent with the concept of correlation. For example, since Alice measures on the x-axis, only the x-component of the measurement by Bob is relevant to the correlation calculations. This is manifested by $\langle 0\,|\,\sigma^A\,|\,0\rangle\langle 0\,|\,\sigma^B\,|\,0\rangle = \langle 0\,|\,\sigma^A_x\,|\,0\rangle\langle 0\,|\,\sigma^B_x\,|\,0\rangle$. Finally, the normalized wavefunction automatically normalizes the calculated expected value so that it fits the requirement of correlation.

If we use other entangled wavefunctions to perform similar calculations, we would arrive at essentially the same results but with a negative sign for some wavefunctions. For example, with $\phi = (|01\rangle + |10\rangle)/\sqrt{2}$, we find:

$$\langle\sigma^A\sigma^B\rangle = \langle\phi\,|\,\sigma^A\otimes\sigma^B\,|\,\phi\rangle = -\cos\beta\,.$$

The above result is equivalent to (16) with $\theta_0 = \pi$. This is not surprising as this wavefunction indicates a negative correlation. If we use a wavefunction of separable states to calculate the expected joint measurement, we would find a value of zero. This is expected because there is no correlation between separable states.

If the measurement axes change randomly, we cannot put a vector on either the A or B axis. In this case, the QM derivation of the joint detection rate involves a projection process similar to that used in Fig. 2. Using a matrix presentation, we can express the projection of a vector pointing to (x_1, y_1) onto a specified axis of angle θ as follows:

$$\begin{aligned}&\begin{pmatrix}\cos\theta\\ \sin\theta\end{pmatrix}\begin{pmatrix}\cos\theta & \sin\theta\end{pmatrix}\begin{pmatrix}x_1\\ y_1\end{pmatrix} = \\ &= \begin{pmatrix}\cos^2\theta & \cos\theta\sin\theta\\ \cos\theta\sin\theta & \sin^2\theta\end{pmatrix}\begin{pmatrix}x_1\\ y_1\end{pmatrix}.\end{aligned} \tag{22}$$

In the above equation, if we let θ be the angle of the B axis with respect to the x-axis, i.e. $\theta - \theta_b$ in Fig. 2, and let $x_1 = \overrightarrow{a_x}/\sqrt{2}$ and $y_1 = \overrightarrow{a_y}/\sqrt{2}$, we can obtain the same result as in (19) and (20).

The matrix in (22) is called a projection matrix [28], as it projects a vector onto the axis of angle θ and gives the components of the projection:

$$Q(\theta) = \begin{pmatrix}\cos^2\theta & \cos\theta\sin\theta\\ \cos\theta\sin\theta & \sin^2\theta\end{pmatrix}.$$

Using the above projection matrix and an entangled wavefunction (e.g. $\phi = (|01\rangle + |10\rangle)/\sqrt{2}$), we can calculate the probability of joint measurement as:

$$\begin{aligned}p_{AB} &= \langle\psi\,|\,Q^A\otimes Q^B\,|\,\psi\rangle = 0.5\cos^2(\theta_A-\theta_B)\\ &= 0.25\,[\cos 2(\theta_A-\theta_B)+1]\,.\end{aligned}$$

Since $(\theta_A - \theta_B)$ is the angle of the orientations of detectors, the above result is exactly the same as (18) or (21) that we derived in the statistical approach. The identical result is apparently because the same projection process works in both approaches.

5 Statistical explanation of two-particle Bell tests

Many Bell test experiments are based on the coincidence rate of particle pairs, but a handful of researchers (e.g. [9, 16, 20, 32, 39, 40] have conducted experiments on correlations of 3 or more particles. Multi-particle correlation can be achieved by special designs of experimental setup to obtain specific quantum states (e.g. [9, 32]) or by exploiting the coherent states of Bose-Einstein condensate (e.g. [16, 20]). The statistical foundation of multi-particle correlation is the same as that for particle pairs, so this paper focus on two-particle correlation. Even though we confine our scope to two-particle Bell tests, there still are copious experiments. This section selects only some representative experiments and puts them into two groups: the polarization experiments of entangled photon pairs and non-polarization experiments based on light phase correlation.

5.1 Polarization experiments

Among numerous Bell test using polarization of photon pairs, we consider only two influential papers by Aspect *et al* [5,6]. Like most experiments on the Bell tests, Aspect *et al* [5,6] utilized the derivation of Clauser *et al* [4] for an experimentally applicable quantum mechanical prediction for the counting rates of coincidence. The starting point of their derivation is a probability formula:

$$\begin{aligned}P(a,b) = {}& w[A(a)_+, B(b)_+] - w[A(a)_+, B(b)_-]\\ &- w[A(a)_-, B(b)_+] + w[A(a)_-, B(b)_-]\end{aligned}$$

where w means the probability weighting of each outcome in total emission counts R_0, with:

$$\begin{aligned}R_0 = {}& [A(a)_+, B(b)_+] + [A(a)_+, B(b)_-]\\ &+ [A(a)_-, B(b)_+] + [A(a)_-, B(b)_-]\end{aligned}$$

$$w[A(a)_+, B(b)_+] = [A(a)_+, B(b)_+]/R_0,\ etc.$$

The above equation is a manifest that the net correlation (positive correlation $[A(a)_+, B(b)_+] + [A(a)_-, B(b)_-]$ minus negative correlation $[A(a)_+, B(b)_-] + [A(a)_-, B(b)_+]$) in terms of total counts R_0. This equation is consistent with our derivation of joint detection rate presented in Section 3: the net correlation in (17) is calculated by integrating E_{AB} over the angle $0-2\pi$ while the total counts is obtained by integrating the unit

spin vector over the same range. Due to the same foundation for derivation, the resulting (18) is unsurprisingly the same as that obtained by Clauser *et al* [4] and used by Aspect *et al* [5, 6]. Since the joint detection rate derived from both statistical and quantum approaches is identical, the explanation on the results of Aspect *et al* [5, 6] will be very similar, so we omit this explanation but examine the maximum violation angle derived from quantum mechanics and confirmed by experiments.

Using the coplanar vectors (shown in Fig. 4) introduced by Clauser and Shimony [28] and Aspect *et al* [5] to present the settings of the Bell test experiments, we can derive the same results as the quantum prediction of the Bell test, but without invoking any wavefunctions.

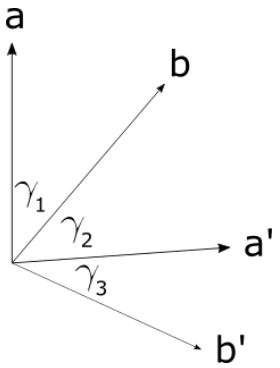

Fig. 4: Coplanar vectors presentation of Bell test settings

In Fig. 4, vectors a, a', b, and b' represent the direction of the spin detectors, and the angles between them are displayed on the graph. For simplicity of presentation, we assume all vectors are of unit modulus and angles γ_1, γ_2, and γ_3 are positive and less than π (for any angle θ greater than π, we can rewrite it as $2\pi - \theta$). Applying the spin correlation results in (16) derived in Section 3 to a case of positively entangled particles (i.e. $\theta_0 = 0$), we can obtain the experimental results as follows:

$$\begin{aligned} E(a,b) &= \cos\gamma_1 \\ E(a,b') &= \cos(\gamma_1+\gamma_2+\gamma_3) \\ E(a',b) &= \cos\gamma_2 \\ E(a',b') &= \cos\gamma_3 . \end{aligned}$$

The theoretical results for the Bell tests should be:

$$\begin{aligned} E_{BT} &= E(a,b) - E(a,b') + E(a',b) + E(a',b') \\ &= \cos\gamma_1 - \cos(\gamma_1+\gamma_2+\gamma_3) + \cos\gamma_2 + \cos\gamma_3 . \end{aligned}$$

Applying the first and second order conditions of maximization (minimization) for the above equation, we know that E_{BT} reaches the maximum or minimum when:

$$\sin\gamma_1 = \sin\gamma_2 = \sin\gamma_3 = \sin(\gamma_1+\gamma_2+\gamma_3) .$$

If γ_1, γ_2 and γ_3 are less than $\pi/2$, the condition of maximum/minimum value necessitates that $\gamma_1 = \gamma_2 = \gamma_3 = \gamma$ and $\sin\gamma$=$\sin 3\gamma$. With some trigonometric manipulations, from $\sin\gamma$=$\sin 3\gamma$ we can have $\sin\gamma\,(4\cos 2\gamma\text{-}1)$=$\sin\gamma$, or γ=π/4.

Similarly, if γ_1, γ_2 and γ_3 are greater than $\pi/2$ (they are less than π as we assumed before for simplicity), we can obtain γ=3π/4.

If some angles are less than $\pi/2$, but some are greater than $\pi/2$, we obtain no satisfying solution. For example, if γ_1 and γ_2 are less than $\pi/2$, but γ_3 is greater than $\pi/2$, from $\sin\gamma_1$=$\sin\gamma_2$=$\sin\gamma_3$, we can infer that $\gamma_1 = \gamma_2$ and $\gamma_3 = \pi - \gamma_2$, so $\sin\gamma_1 = \sin(\gamma_1+\gamma_2+\gamma_3) = \sin(\gamma_1+\pi) = -\sin\gamma_1$, or $\gamma_1 = \gamma_2 = \gamma_3 = 0$. This contradicts our assumption of positive angles and presents a trivial case where all 4 settings coincide.

To sum up, from the first and second order condition we reveal that the maximum and minimum value of E_{BT} occurs at γ=π/4 and γ=3π/4, respectively. If γ=π/4, we have:

$$E_{max} = \cos\pi/4 - \cos 3\pi/4 + \cos\pi/4 + \cos\pi/4 = 2\sqrt{2} .$$

If $\gamma = 3\pi/4$, we have:

$$E_{min} = \cos 3\pi/4 - \cos 9\pi/4 + \cos 3\pi/4 + \cos 3\pi/4 = -2\sqrt{2} .$$

As a result, we obtain the same results as the quantum prediction:

$$\left|E(a,b) - E(a,b') + E(a',b) + E(a',b')\right| \le 2\sqrt{2} .$$

It is worth mentioning that the above derivation shows that the maximum violation of the Bell inequality occurs at the setting $\gamma = \pi/4$ or γ=3π/4, $E = \pm 2\sqrt{2}$. This seems in conflict with the results of Aspect *et al* [5, 6], where the maximum violation of the Bell inequality occurred at θ=π/8, or θ =3π/8.

In fact, this difference highlights the different cases of spin and polarization. Our derivation is based on spin detection. As we discussed in Section 3, the angle must be adjusted when applying (16) and (17) to polarization experiments. In most Bell test experiments using light, including Aspect *et al* [5, 6], a count of photon detection is recorded as +1 and no detection is recorded as -1. As such, if the angle between the polarizer and the polarization of light is $\theta = \pi/2$, the most likely outcome is no detection or -1. We can express the result as $\cos 2\theta = \cos\pi = -1$. It is apparent that one needs to double the angle in the experiment to obtain a result that is consistent with experimental record. On the other hand, our derivation based on spin assumes that a count of photon detection is recorded as +1 and no detection is recorded as 0. If the angle between the polarizer and the polarization of light is $\gamma = \pi/2$, the most likely outcome is no detection or 0. We can express the result as $\cos\gamma = \cos\pi/2 = 0$. This recorded value is equivalent to the case of $\theta = \pi/4$ in Aspect *et al* [5, 6]. From this we can infer that the angle γ used for

spin examples in the present paper is equivalent to twice the angle θ used in Aspect *et al* [5, 6], i.e. $\gamma = 2\theta$. As a result, the angles for maximum violation of the Bell inequality in Aspect *et al* [5, 6] will be half the value as in our derivation.

5.2 Interferometry Bell tests

There are Bell tests that examine the correlations between variables other than polarization. One type of research focuses on the phase correlation (e.g. [19, 34–36]). This type of experiment creates a pair of photons of the same phase and lets them pass through phase shifters and a distance of different lengths, then detects the phase difference at a Michelson interferometer. The experiments are based on the theoretical prediction of Franson [37] which, based on the phase difference of wavefunctions caused by time difference, developed a similar prediction as (18) in the present paper. Using a classical wave theory of light and joint intensity, one can also obtain an equivalent result.

For simplicity, we combine the electrical and magnetic components of a light field, so the normalized light field of a photon pair of the same initial phase at position x and time t can be expressed as:

$$E = \cos(\theta + kx - \omega t)$$

where θ is the initial phase of the photon pair at the source, k is wave vector, ω is angular frequency.

Assume that photon A will be added a phase θ_a by a phase shifter (we use only one phase shifter for simplicity) and, meanwhile, photon B will be added a phase $\theta_b = \omega\Delta t$ due to the different time or distance travelled. The light fields of the pair become:

$$E_A = \cos(\theta + kx - \omega t + \theta_a)$$

$$E_B = \cos(\theta + kx - \omega t + \theta_b)\,.$$

Although this type of experiments use the joint intensity as measurement, as we discussed in Section 3, we cannot calculate the correlation of light intensity by directly multiplying the intensities of light field because the changes in intensity are not independent. Since the light phases and thus the light fields are correlated, the joint intensity needs to be calculated from light field correlation:

$$\begin{aligned} E_{AB} &= E_A E_B \\ &= \cos(\theta + kx - \omega t + \theta_a)\cos(\theta + kx - \omega t + \theta_b) \\ &= 0.5\left[\cos(2\theta + 2kx - 2\omega t + \theta_a + \theta_b) + \cos(\theta_a - \theta_b)\right]. \end{aligned}$$

The initial phase of photon pair θ can change randomly, so the item related to θ in the above equation will net out to zero (by integrating E_{AB} over θ in the range of $0 - 2\pi$). As a result, the above equation becomes:

$$E_{AB} = 0.5\cos(\theta_a - \theta_b)\,.$$

As such, the joint intensity can be calculated as:

$$I_{AB} = E_{AB}^2 = 0.25\cos^2(\theta_a - \theta_b) = 0.125\left[\cos 2(\theta_a - \theta_b) + 1\right].$$

This result is equivalent to the quantum prediction in Franson [37, Eq. (16)] or Brendel *et al* [34, Eq. (4)]. From the above derivation we can conclude that the light intensity difference stems from the phase difference caused by phase shifter and by different travel time. Probability law also works in this case because it ensures that the initial random phase of photon pairs have no impact on the interferometry results.

By examining representative experiments, we can conclude that the violation of the Bell inequality is caused by the correlation in source particles as well as the physical relationship between the spin/polarization angle and its component on detection axes, or between the phase of electromagnetic wave and the light field correlation. With varying detection conditions (i.e. random changes in detection angles or adding arbitrary phases), probability law can still maintain the correlation of source particles. This leads to the violation of the Bell inequality and the correct statistical predictions, which are consistent with experimental outcomes.

6 Conclusions

The paper presents statistical predictions of two-particle Bell tests, which are equivalent to, but more general than, the QM predictions. By comparing the statistical and QM approaches, the paper shows that probability law is at the heart of both approaches. The statistical presentation of two-particle Bell tests in this paper has far-reaching implications.

First, it can improve our understanding of quantum mechanics and help to demystify it. Although the concepts of superposition and entanglement are widely accepted among physicists, the explanation of these concepts is difficult and thus causes significant misunderstanding. The statistical interpretation of the Bell tests shows that the superposition of entangled states in the two-particle Bell test is nothing more than statistical correlation between states. For the correlated particles at the polarizer or spin detector, probability law can maintain the correlation through the expected value, so there is no need for communication (let alone faster-than-light or instantaneous communication) between different locations in the Bell experiments. As quantum entanglement is explained by probability law, the Bell test results and quantum mechanics are no longer mysterious.

Second, it has significant implications for quantum computing, which relies on quantum entanglement. Since the quantum entanglement phenomenon results from probability law, statistical noise is a natural and unavoidable part of quantum computing. Understanding the nature of this noise may shed light on how to improve the signal-to-noise ratio and thus is crucial to the success of quantum computing.

Third, the paper pinpoints the cause for the violation of the Bell inequality and thus explains why the local hidden

variable theory is wrong. Although numerous Bell tests reject the local hidden variable theory and support quantum mechanics, they have not shed any light on why the former is wrong and the latter is right. This paper shows that the key lies in probability law, which underpins the Bell test results. Because probability law is universal, if we regard the statistical mechanism (which causes statistical variation around the mean) as a "hidden variable", it is not a local one but a global one. The local hidden variable theory misrepresents this nature and thus fails. It is also this global law that leads to the correct prediction from quantum mechanics.

Last but not least, the paper may stimulate a reassessment of the role of determinism and realism. Broadly, the experimental results on the Bell inequality are interpreted as being a rejection of determinism or local realism, and an embracing of randomness. While this paper highlights the importance of randomness and probability law, it does not totally reject determinism and realism. In the Bell tests, probability law works only when the particles arrive at and interact with the detector (polarizer or spin analyzer) – it plays no role before and after. When probability law is not in action, it is determinism, realism and logic that describe the behaviour of the particles. In other words, both randomness and realism play important roles in our understanding of physics.

Acknowledgements

The author thanks Sean Hodgman and David Shin for useful discussions and comments.

Received on May 20, 2021

References

1. Einstein E., Podolsky B., Rosen N. Can quantum-mechanical description of physical reality be considered complete? *Physical Review*, 1935, v. 47, 777–780.
2. Bohm D. A Suggested Interpretation of the quantum theory in terms of "hidden" variables. *Physical Review*, 1952, v. 85, 169–193.
3. Bell J. On the Einstein Podolsky Rosen paradox. *Physics*, 1964, v. 1 (3), 195–200.
4. Clauser J. F., Horne M. A., Shimony A., Holt R. A. Proposed experiment to test local hidden-variable theories. *Physical Review Letters*, 1969, v. 23, 880.
5. Aspect A., Grangier P., Roger G. Experimental tests of realistic local theories via Bell's theorem. *Physical Review Letters*, 1981, v. 47 (7), 460–463.
6. Aspect A., Grangier P., Roger G. Experimental realization of Einstein-Podolsky-Rosen-Bohm Gedankenexperiment: A new violation of Bell's Inequalities. *Physical Review Letters*, 1982, v. 49 (2), 91–94.
7. Tittel W., Brendel J., Gisin B., Herzog T., Zbinden H., Gisin N. Experimental demonstration of quantum-correlations over more than 10 kilometers. *Physical Review A*, 1998, v. 57 (5), 3229–3232.
8. Weihs G., Jennewein T., Simon C., Weinfurter H., Zeilinger A. Violation of Bell's inequality under strict Einstein locality conditions. *Physical Review Letters*, 1998, v. 81 (23), 5039–5043.
9. Pan J. W., Bouwmeester D., Daniell M., Weinfurter H., Zeilinger A. Experimental test of quantum nonlocality in three-photon GHZ entanglement. *Nature*, 2000, v. 403 (6769), 515–519.
10. Rowe M. A., Kielpinski D., Meyer V., Sackett C. A., Itano W. M., Monroe C., Wineland D. J. Experimental violation of a Bell's inequality with efficient detection. *Nature*, 2001, v. 409 (6822), 791–794.
11. Gröblacher S., Paterek T., Kaltenbaek R., Brukner S., Zukowski M., Aspelmeyer M., Zeilinger A. An experimental test of non-local realism. *Nature*, 2007, v. 446 (7138), 871–875.
12. Salart D., Baas A., van Houwelingen J., Gisin N., Zbinden H. Spacelike Separation in a Bell Test Assuming Gravitationally Induced Collapses. *Physical Review Letters*, 2008, v. 100 (22), 220404.
13. Ansmann M., Wang H., Bialczak R., Hofheinz M., Lucero E., Neeley M., O'Connell A. D., Sank D., Weides M., Wenner J., Cleland A. N., Martinis J. M. Violation of Bell's inequality in Josephson phase qubits. *Nature*, 2009, v. 461, 504–506.
14. Giustina M., Mech A., Ramelow S., Wittmann B., Kofler J., Beyer J., Lita A., Calkins B., Gerrits T., Nam S. W., Ursin R., Zeilinger A. Bell violation using entangled photons without the fair-sampling assumption. *Nature*, 2013, v. 497 (7448), 227–230.
15. Christensen B. G., McCusker K. T., Altepeter J., Calkins B., Gerrits T., Lita A., Miller A., Shalm L. K., Zhang Y., Nam S. W., Brunner N., Lim C. C. W., Gisin N., Kwiat P. G. Detection-Loophole-Free Test of Quantum Nonlocality, and Applications. *Physical Review Letters*, 2013, v. 111 (7448), 130406.
16. Schmied R., Bancal J.-D., Allard B., Fadel M., Scarani V., Treutlein P., Sangouard N. Bell correlations in a Bose-Einstein condensate. *Science*, 2016, v. 352 (6284), 441–444.
17. Handsteiner J., Friedman A. S., Rauch D., Gallicchio J., Liu B., Hosp H., Kofler J., Bricher D., Fink M., Leung C., Mark A., Nguyen H. T., Sanders I., Steinlechner F., Ursin R., Wengerowsky S., Guth A. H., Kaiser D. I., Scheidl T., Zeilinger A. Cosmic Bell Test: Measurement Settings from Milky Way Stars. *Physical Review Letters*, 2017, v. 118 (6), 060401.
18. BIG Bell Test Collaboration. Challenging local realism with human choices. *Nature*, 2018, v. 557 (7704), 212–216.
19. Hensen B., Bernien H., Dréau A. E., Reiserer A., Kalb N., Blok M. S., Ruitenberg J., Twitchen R. F. L. Vermeulen & Schouten R. N. & Abellán C. & Amaya W. & Pruneri & Mitchell M. W. & Markham D. J., Elkouss D., Wehner S., Taminiau T. H., Hanson R. Loophole-free Bell inequality violation using electron spins separated by 1.3 kilometres. *Nature*, 2015, v. 526, 682–686.
20. Shin D. K., Henson B. M., Hodgman S. S., Wasak T., Chwedenczuk J., Truscott A. G. Bell correlations between spatially separated pairs of atoms. *Nature Communications*, 2019, v. 104447.
21. Thenabadu M., Cheng G.-L., Pham T. L. H., Drummond L. V., Rosales-Zárate L., Reid M. D. Testing macroscopic local realism using local nonlinear dynamics and time settings. *Physical Review A*, 2020, v. 102, 022202.
22. Bell J. Introduction to the hidden variable question. In: d'Espagnat B., ed. Foundations of Quantum Mechanics. 1971, pp. 171–181.
23. Myrvold W., Genovese M., Shimony A. Bell's Theorem. In: Edward N. Zalta, ed. The Stanford Encyclopedia of Philosophy. Metaphysics Research Lab, Stanford University, 2019.
24. Pierce D. T., Celotta R. J., Kelley M. H., Unguris J. Electron spin polarization analyzers for use with synchrotron radiation. *Nuclear Instruments and Methods in Physics Research A*, 1988, v. 266, 550–559.
25. Getzlaff M., Heidemann B., Basmann J., Westphal C., Schonhense G. A variable-angle electron spin polarization detection system. *Review of scientific instruments*, 1998, v. 69 (11), 3913–3923.
26. Yu D., Math C., Meier M., Escher M., Rangelov G., Donath M. Characterisation and application of a SPLEED-based spin polarisation analyser. *Surface Science*, 2007, v. 601, 5803–5808.
27. Winkelmann A., Hartung D., Engelhard H., Chiang C.-T., Kirschner J. High efficiency electron spin polarization analyser based on exchange scattering at Fe/W(001). *Review of Science Instruments*, 2008, v. 79, 083303.

28. Clauser J. F., Shimony A. Bell's theorem: experimental tests and implications. *Reports on Progress in Physics*, 1978, v. 41, 1881.

29. Bell J. Bertlmann's socks and the nature of reality. *Journal De Physique*, 1981, v. C2, 41–62.

30. Fine A. Hidden variables, joint probability, and the Bell inequalities. *Physical Review Letters*, 1982, v. 48 (5), 291–295.

31. Ou Z. Y., Mandel L. Violation of Bell's inequality and classical probability in a two-photon correlation experiment. *Physical Review Letters*, 1988, v. 61 (1), 50–53.

32. Bouwmeester D., Pan J. W., Daniell M., Weinfurter H., Zeilinger A. Observation of three-photon Greenberger-Horne-Zeilinger entanglement. *Physical Review Letters*, 1999, v. 82 (7), 1345–1349.

33. Greenberger D. M., Horne M. A., Zeilinger A. Going beyond Bell's theorem. In: Kafatos M., ed. Bell's Theorem, Quantum Theory and Conceptions of the Universe. Kluwer Academics Dordrecht, The Netherlands, 1989, pp. 69–72.

34. Brendel J., Mohler E., Martienssen W. Time-resolved dual-beam two-photon interferences with high visibility. *Physical Review Letters*, 1991, v. 66 (9), 1142–1145.

35. Rarity J. G., Tapster P. R. Experimental violation of Bell's inequality based on phase and momentum. *Physical Review Letters*, 1990, v. 64 (21), 2495–2498.

36. Tittel W., Brendel J., Zbinden H., Gisin N. Violation of Bell inequalities by photons more than 10km apart. *Physical Review Letters*, 1998, v. 81 (17), 3563–3566.

37. Franson J. D. Bell inequality for position and time. *Physical Review Letters*, 1989, v. 62 (19), 2205–2208.

38. Freedman S. J., Clauser J. F. Experimental test of local hidden-variable theories. *Physical Review Letters*, 1972, v. 28, 938–941.

39. Lanyon B. P., Zwerger M., Jurcevic P., Hempel C., Dür W., Briegel H. J., Blatt R., Roos C. F. Experimental violation of multipartite Bell inequalities with trapped ions. *Physical Review Letters*, 2014, v. 112 (10), 100403.

40. Eibl M., Gaertner S., Bourennane M., Kurtsiefer C., Żukowski M., Weinfurter H. Experimental observation of four-photon entanglement from parametric down-conversion. *Physical Review Letters*, 2003, v. 90, 200403.

A Quantitative Description of Atmospheric Absorption and Radiation at Equilibrium Surface Temperature

Y. C. Zhong

ERICHEN Consulting, Queensland, Australia. E-mail: drzhong88@yahoo.com

An analytical theory is proposed for the earth-atmosphere system at its equilibrium surface temperature, 289.16 K. A non-linear relation is formulated between atmospheric absorption and atmospheric radiation by modifying Kirchhoff's law on thermal radiation. For the first time, the Global Energy Balance can be realized in a wide range of atmospheric absorptivity, transmittance, and surface emissivity. It is revealed that atmospheric radiation becomes negative once the atmospheric absorptivity is below its threshold value. It is proven that the upward cumulative long-wave atmospheric radiation spontaneously increases from 3.8 $\mathrm{W\,m^{-2}}$ to 199.4 $\mathrm{W\,m^{-2}}$ as the long-wave atmospheric absorptivity increases from 0.4 to 1.0 whilst the long-wave atmospheric transmittance decreases from 0.6 to 0.1.

1 Introduction

For over a century, many attempts have been made to balance the global energy budget, both at the top of the atmosphere (TOA) and at the Earth's surface [1]. It is known that the lack of precise knowledge of the surface energy fluxes profoundly affects the ability to study climate change [2]. In fact, the power equation at the surface remains unbalanced as the uncertainty in the net energy flux between the surface and the atmosphere is over 17 $\mathrm{W\,m^{-2}}$ [3]. To date, many static explanations for the global energy balance have been confined to using one set of fixed parameters to describe atmospheric absorption and radiation [2], whereas the taken-for-granted Kirchhoff's law at the core of the radiative transfer description of atmospheric absorption and radiation seems theoretically invalid [4].

In this paper, several thermodynamic variables of theoretical importance are redefined to formulate the basic equations, including those previously treated as constants. By continuously mapping the surface emissivity and longwave (LW) atmospheric absorptivity, several coupled quadratic equations are derived and simultaneously solved, which are in quantitative agreement with the latest experimental observations. In light of these new findings, implications for some fundamental issues in climate studies are briefly discussed.

2 Theory

In general, the thermodynamic variables in the atmosphere-surface system are dependent and should be described in coupled equations.

2.1 Outgoing longwave radiation and surface radiance

It is known that the total power balance at the TOA can be written as

$$\pi R^2 S\,(1-r) = 4\pi R^2 I_{LW}^{\uparrow} \tag{1}$$

where S is the solar constant, R the radius of the Earth, r the effective reflectivity of the Earth at the TOA, including the SW solar radiation reflected at the surface and then transmitted upward to the TOA, and $I_{LW}^{\uparrow}$ denotes the outgoing LW radiation (OLR) into outer space. From (1),

$$I_{LW}^{\uparrow} = \frac{S\,(1-r)}{4}\,. \tag{2}$$

Notice that OLR is merely determined by the albedo and the solar constant.

By treating the Earth as a graybody, the surface radiation can be obtained from the Stefan-Boltzmann law,

$$I_E = \varepsilon_E \sigma T^4\,, \tag{3}$$

where ε_E is defined as the Earth's mean surface emissivity, and T is the equilibrium mean surface temperature. In general, ε_E is to be treated as a thermodynamic variable in this study, although it has been often approximated as unity so far.

2.2 Modification of Kirchhoff's Law

In theory, the upward *cumulative* atmospheric absorption at any altitude can be calculated using the line-by-line method provided all of the relevant lineshape functions are known. At the TOA, the total LW atmospheric absorption can be expressed as

$$A_{LW} = \iint_0^{\infty} \alpha_\lambda\,(T_A)\,\rho\,(z)\,I_E\,(\lambda, z)\,d\lambda\,dz\,, \tag{4}$$

where α_λ is the spectral absorptivity of the atmosphere, predominately determined by water vapor, T_A is the atmospheric temperature at at a given altitude, ρ is the air density, $I_E\,(\lambda, z)$ represents the attenuated surface LW emission spectra at different altitudes. Naturally, α_λ represents both the resonant and continuum absorption by air molecules detected under continuous excitation [5,7]. Note that α_λ is scaled by the Planck function $B\,(\lambda, T)$ with its maximum at the center of the atmospheric window near 10 μm.

To proceed further, an effective LW cumulative atmospheric absorptivity, a_{LW}, at the TOA can be introduced

$$A_{LW} = a_{LW} I_E \,. \tag{5}$$

Obviously, the maximum LW atmospheric absorption is I_E when $a_{LW} = 1$.

Similarly, SW atmospheric absorption can be written as

$$A_{SW} = a_{SW} \left[1 + r_{SE} \left(1 - a_{SW}\right)\right] I^{\downarrow}_{SW} \left(TOA\right) \,. \tag{6}$$

where $I^{\downarrow}_{SW}\left(TOA\right)$ in the actual downward SW solar radiation at the TOA by subtracting the reflected SW solar radiation at the TOA, r_{SE} is defined the SW surface reflectivity. In this study, the SW atmospheric absorption is fixed.

Using Kirchhoff's law, it would appear that $\alpha = \varepsilon$, where α and ε are the spectral absorptivity and the emissivity of a non-scattering medium, respectively. Nevertheless, it seems unrealistic to expect that atmospheric radiation is equal to atmospheric absorption. So far, many attempts have been made at *ab initio* calculation of atmospheric radiation based on Schwarzschild's equation with the Planck function and an effective emissivity, but the results seem over-simplified. Besides, it has been revealed that Kirchhoff's law is problematic and should not be considered as a basic law [4].

In this paper, it is postulated that the fraction, denoted by β, of upward cumulative atmospheric radiation (UCAR), is proportional to the LW atmospheric absorptivity

$$a_{LW} = \gamma \beta \tag{7}$$

where γ denotes the proportionality factor that is used to parameterize the rest of the unclear dependence during radiative transfer in the atmosphere. In effect, (7) can be considered as a modified Kirchhoff's law for atmospheric radiation. In the absence of internal reflection, it would appear the sum of the LW atmospheric absorptivity and the LW atmospheric transmittance, τ_{LW}, is unity.

$$\tau_{LW} = 1 - a_{LW} \,. \tag{8}$$

Substituting (7) into (8) yields

$$\tau_{LW} = 1 - \gamma \beta \,. \tag{9}$$

It is shown in this study, however, that (8) and (9) are invalid in the presence of atmospheric radiation which is empowered by atmospheric absorption and other non-radiative energy fluxes.

2.3 Formulation for power balance conditions

To derive the power balance equation at the surface, that ensures the net energy flux at surface is exactly zero at thermal equilibrium, the net downward energy flux (NDEF) is denoted as N_0. Thus the power balance equation at the surface can be simply written as

$$N_0 = I_E \,. \tag{10}$$

As the downward SW solar radiation into the surface $I^{\downarrow}_{SW}\left(0\right)$ is known, it can be taken away from N_0 and explicitly expressed in the power balance condition,

$$N + I^{\downarrow}_{SW}\left(0\right) = I_E \,, \tag{11}$$

where N represents the NDEF when $I^{\downarrow}_{SW}\left(0\right)$ is excluded from N_0, *viz.*

$$N = N_0 - I^{\downarrow}_{SW}\left(0\right) \,. \tag{12}$$

Note that (11) and (12) are equivalent irrespective of the value of $I^{\downarrow}_{SW}\left(0\right)$.

At the TOA, the power balance equation for OLR can be expressed as,

$$I^{\uparrow}_{LW} = \tau_{LW} I_E + I^{\uparrow}_{A} \tag{13}$$

where τ_{LW} is the LW atmospheric transmittance, $I^{\uparrow}_{A}$ is the UCAR that can escape from the atmosphere into space. It is to be shown that the upward LW radiation at the TOA is a constant.

2.4 Formulation for atmospheric radiation

In the absence of the physical surface underneath the atmosphere while the LW radiation were still available, the upward LW atmospheric radiation at the TOA can be obtained by assuming it is proportional to the total atmospheric absorption without invoking Stefan-Boltzmann law.

$$I^{\uparrow}_{A} = \beta \left(A_{LW} + A_{SW}\right) \,. \tag{14}$$

The two absorption terms in (14) belong to, respectively, the one-way cumulative LW atmospheric absorption from the surface radiation A_{LW}, and the two-way cumulative SW atmospheric absorption from the solar radiation A_{SW}. In this hypothetical case, those non-radiative energy exchange processes are absent.

Similarly, the downward cumulative atmospheric radiation (DCAR) at the bottom of the atmosphere, can be derived

$$I^{\downarrow}_{A} = \left(1 - \beta\right) \left(A_{LW} + A_{SW}\right) \,. \tag{15}$$

Adding (14) and (15) yields,

$$I^{\uparrow}_{A} + I^{\downarrow}_{A} = a_{LW} I_E + A_{SW} \,, \tag{16}$$

which is simply an energy conservation statement.

In reality, however, the bottom of the atmosphere is physically in contact with the Earth's surface, hence the thermal energy exchange, in addition to radiation, is inevitable. As a result, (14)–(16) should be modified accordingly. Specifically, a portion of the total energy absorbed by the atmosphere must be used to achieve and maintain the thermal equilibrium in the atmosphere-surface system, as required by (11), which is exactly equal to N. Thus we have,

$$I^{\uparrow}_{A} = \beta \left(A_{LW} + A_{SW} - N\right) \,, \tag{17}$$

$$I_A^{\downarrow} = (1-\beta)\,(A_{LW} + A_{SW} - N)\,, \tag{18}$$

$$I_A^{\uparrow} + I_A^{\downarrow} = a_{LW} I_E + A_{SW} - N\,. \tag{19}$$

Note that (19) predicts that the total atmospheric radiation can either be zero or negative if the total atmospheric absorption is equal to or less than N, respectively. Here, (19) is to be used as the criterion to quantitatively determine the eventuating total atmospheric radiation, $I_A^{\uparrow} + I_A^{\downarrow}$, which, in turn, allows calculation for other climate variables, such as LW atmospheric transmittance and the net downward energy flux (NDEF).

2.5 Corollary

Substituting (5), (7), and (17) into (13), the power balance condition at the TOA can be rewritten as a quadratic function of the UCAR fraction β,

$$\tau_{LW} = -\gamma\beta^2 - \left(\frac{A_{SW} - I_E + I_{SW}^{\downarrow}(0)}{I_E}\right)\beta + \frac{I_{LW}^{\uparrow}}{I_E}\,, \tag{20}$$

with its y-intercept close to 0.6, which is determined by the ratio of OLR to the surface radiation. Note that (20) indicates that LW atmospheric transmittance is not unity in the absence of UCAR, as derived from (9) and shown in Fig. 1, due to the contribution of SW absorption by the atmosphere.

Substituting (7) into (20), we obtain the dependence of LW atmospheric transmittance on the LW atmospheric absorptivity,

$$\tau_{LW} = -\frac{a_{LW}^2}{\gamma} - \left(\frac{A_{SW} - I_E + I_{SW}^{\downarrow}(0)}{\gamma I_E}\right)a_{LW} + \frac{I_{LW}^{\uparrow}}{I_E}\,, \tag{21}$$

which indicates that the relation between LW transmittance and LW absorptivity is not linear, but quadratic, as shown in Fig. 2. As a result, the well-known linear relation between τ_{LW} and a_{LW}, (9), should be replaced by (21). To obtain the analytical formula for the atmospheric radiation that satisfies energy conservation law, substituting (5) and (7) into (17) yields a quadratic equation for UCAR,

$$I_A^{\uparrow} = \gamma I_E \beta^2 + \left(A_{SW} - I_E + I_{SW}^{\downarrow}(0)\right)\beta\,. \tag{22}$$

Dividing (17) by (18) and then substituting the result into (22) yields,

$$I_A^{\downarrow} = (1-\beta)\left(\gamma I_E \beta + A_{SW} - I_E + I_{SW}^{\downarrow}(0)\right)\,. \tag{23}$$

3 Calculated results

Based on the latest experimental data used in [7] and [8], as shown in Table 1, all of the numerical calculations are based on solving the coupled quadratic equations, (20) to

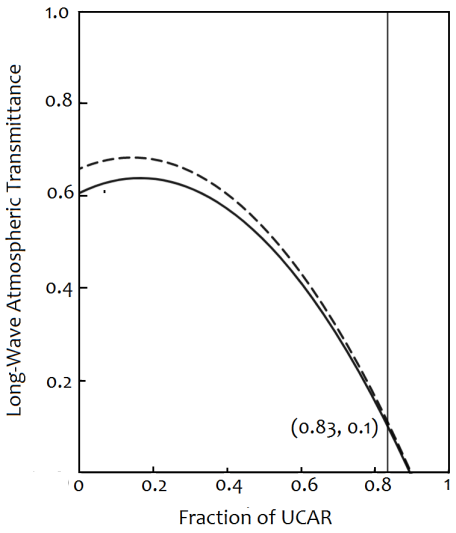

Fig. 1: Dependence of LW atmospheric transmittance τ_{LW} on the fraction of UCAR at the TOA, calculated from (20) assuming the surface emissivity is 1.0 (solid curve) and 0.92 (dashed curve). The coordinate (0.83, 0.1) represents the maximum β at $\tau_{LW} = 0.1$, used in this study.

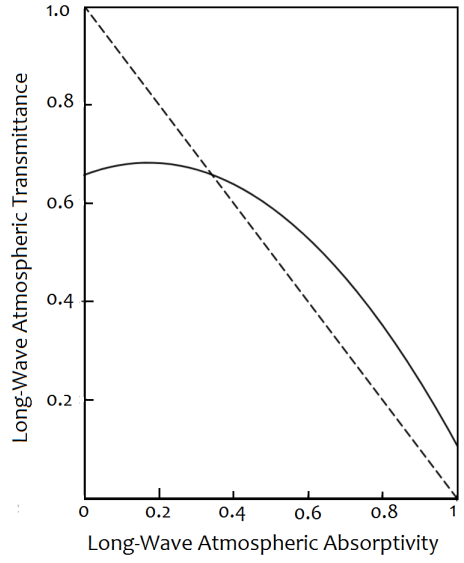

Fig. 2: Dependence of LW atmospheric transmittance on LW atmospheric absorptivity at the TOA, obtained from (21) in this study (solid curve) and from (8) (dashed line).

surface mean temperature	289.16	K
albedo	0.2985	
solar constant	1365.2	$\mathrm{W\,m^{-2}}$
reflected solar radiation at TOA	101.9	$\mathrm{W\,m^{-2}}$
SW atmospheric absorption	78	$\mathrm{W\,m^{-2}}$
surface solar SW radiation	161	$\mathrm{W\,m^{-2}}$

Table 1: The observed data used in [7] and this study.

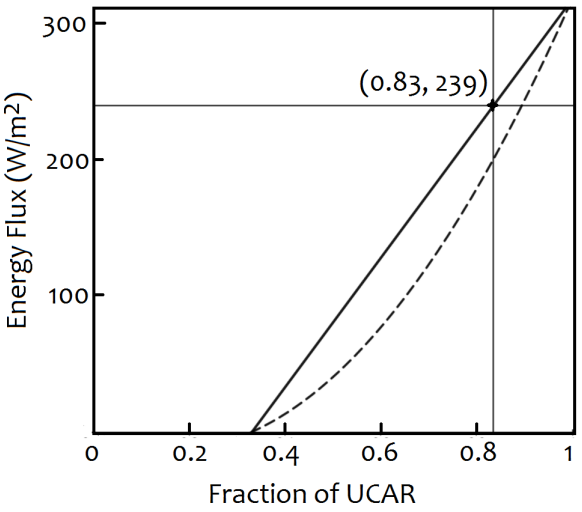

Fig. 3: Dependence of the total LW atmospheric radiation (solid line) and LW UCAR (dashed curve) on the fraction of UCAR the at the TOA, calculated from (19) and (22), respectively.

(24). A wide range of different values for surface emissivity and LW atmospheric absorptivity are considered. Specifically, the proportionality γ-factor in (7) is first determined by using the LW atmospheric transmittance $\tau_{LW} = 0.1009$ at the surface emissivity $\varepsilon_E = 1$ and then by maximizing the LW atmospheric absorptivity to $a_{LW} = 100\%$. This operation is equivalent to first assuming the atmospheric transmittance becomes its minimum whilst the LW atmospheric absorption reaches to its maximum, $A_{LW} \to I_E$.

Based on (16), the proportionality γ-factor in (7) is calculated, $\gamma = 1.196235$. Meanwhile, the β-factor for UCAR, 0.8354, is obtained simultaneously, which is also the maximum value for the β-factor, as shown in Fig. 3. Furthermore, the calculations are made for the surface emissivity ε_E <1. Note that the proportionality γ-factor is kept as a constant once it is determined in the first place, whilst neither additional parameters nor approximation are applied.

4 Discussion

4.1 Connecting radiation to cumulative absorption

In line with Kirchhoff's law, absorptivity and emissivity is often considered as identical in a non-scattering optical medium. In the case of the atmosphere, this implies that the absorbed radiation energy in each thin layer of an atmospheric model is completely emitted in the form of photons without being transformed into internal thermal energy in the atmosphere. Nevertheless, such an radiative transfer description seems invalid for the real atmospheric radiation where photon-particle scattering and radiation heating cannot be described by using Schwarzschild's equation. Hence, Kirchhoff's law is modified in this study with quantitative agreement with the latest observations.

In history, atmospheric radiation detected near the surface was described by using Stefan-Boltzmann law, such as the empirical equation used by Ångström [6],

$$I_A^{\downarrow} = \varepsilon_A \sigma T_A^4 , \tag{24}$$

where ε_A is the atmospheric emissivity, T_A is the air temperature near the surface. As the atmosphere can hardly be treated as a single isothermic layer, ε_A is in fact a random variable. Hence (24) is unfit for formulating atmospheric radiation. It has been recently shown that the atmospheric emissivity ε_A be equal to LW absorptivity a_{LW} only in the absence of clouds, see (78) in [7], but the fundamental link between atmospheric radiation and atmospheric absorption seems obscure. In general, it would appear that the distinction between the spontaneous resonant emission from the water vapor and other LW-radiation absorbers, such as CO_2, and the continuum thermal radiation governed by Planck's law remains to be further explored.

To circumvent such theoretical uncertainties, the fraction of upward *cumulative* atmospheric radiation (UCAR) at TOA, β, is introduced as a new variable in (7). In effect, the proportionality γ-factor is phenomenologically used to link the thermal radiation by the atmosphere to the *cumulative* LW atmospheric absorption based on (7). In this way, LW atmospheric radiation can be formulated. Further, the γ-factor in (7) is theoretically determined as one of the simultaneous solutions, $\gamma = 1.196235$, which appears an intrinsic invariant for the surface-atmosphere system.

4.2 Realization of the global energy balance

Because numerous energy fluxes exist between the Earth's surface and the atmosphere, it seems unlikely to identify and account all of them with absolute uncertainty. In fact, inconsistencies often arise when these different components are brought together to the power balance equation [3]. Specifically, efforts have been made to determine the net LW surface radiation, defined as the difference between the upward and downward radiation intensities,

$$I_N^{(LW)} = I_A^{\downarrow} - I_E . \tag{25}$$

Using the optimal estimates for $I_E = 398\,\mathrm{W\,m^{-2}}$ and $I_A^{\downarrow} = 342\,\mathrm{W\,m^{-2}}$, (25) gives $I_N^{(LW)} = -56\,\mathrm{W\,m^{-2}}$, whereas a wide range for the net LW surface radiation , $-49 > I_N^{(LW)} > -65\,\mathrm{W\,m^{-2}}$, was predicted by individual CMIP5 models [2]. Using the net SW downward radiation, $I_{SW}^{\downarrow}(0) = 161\,\mathrm{W\,m^{-2}}$, the global mean surface net radiation,

$$I_N = I_N^{(LW)} + I_{SW}^{\downarrow}(0) , \tag{26}$$

is used to obtain $I_N = 105\,\mathrm{W\,m^{-2}}$, which happens to be about half way between two uncompromising values, $113\,\mathrm{W\,m^{-2}}$

τ_{LW}	a_{LW}	β	var.(W m^{-2})	Zhong	[7]	[8]
0.1	0.899		OLR	–	239.4	239
0.1	1.0	a_{LW}/γ	OLR	239.4		
0.1	0.899	0.39	$I_{LW}^{(N)}$	–	64.4	
any	any	a_{LW}/γ	$I_{LW}^{(N)}$	0		
0.1	0.899		$A_{LW}+A_{SW}$	–		521
0.1	0.899	0.38	$A_{LW}+A_{SW}$	–	521.8	
0.1	1.0	$1/\gamma$	A_{max}	474.4		
0.1	1.0	0.83	$A_{LW}+A_{SW}$	474.4		
0.24	0.899	0.744	$A_{LW}+A_{SW}$	430.8		
0.33	0.8	0.67	$A_{LW}+A_{SW}$	395.1		
0.51	0.6	0.49	$A_{LW}+A_{SW}$	315.8		
0.6	0.4	0.34	$A_{LW}+A_{SW}$	236.6		
0.63	0.2	0.24	$A_{LW}+A_{SW}$	157		
0.1	0.899	–	UCAR $I_A^{\uparrow}$	–		199
0.1	0.899	0.39	UCAR $I_A^{\uparrow}$	–	199.4	
0.1	1.0	0.38	UCAR $I_A^{\uparrow}$	199.4		
0.33	0.8	0.67	UCAR $I_A^{\uparrow}$	106.8		
0.51	0.6	0.49	UCAR $I_A^{\uparrow}$	40.3		
0.6	0.4	0.34	UCAR $I_A^{\uparrow}$	3.8		
0.63	0.2	0.24	UCAR $I_A^{\uparrow}$	-13		
		$1-\beta$				
0.1	1.0	0.17	DCAR $I_A^{\downarrow}$	39.3		
0.1	0.899	–	DCAR $I_A^{\downarrow}$	–		333
0.1	0.826	0.62	DCAR $I_A^{\downarrow}$	–	332	
0.23	0.899	0.35	DCAR $I_A^{\downarrow}$	49.4		
0.33	0.8	0.33	DCAR $I_A^{\downarrow}$	52.9		
0.51	0.6	0.51	DCAR $I_A^{\downarrow}$	40.1		
0.6	0.4	0.66	DCAR $I_A^{\downarrow}$	0.77		

Table 2: Calculated thermodynamic variables (var.).

and 98 W m^{-2}, estimated by Stephens *et al* [3] and Trenberth *et al* [8], respectively. To explain the remaining imbalance, both the global mean sensible heat flux and the latent heat flux were considered, knowing the lack of adequate information from direct observations. Thus, it was recommended that the surface budget estimates not be used as references [2, 8].

By introducing the net downward energy flux (NDEH) at the surface, nevertheless, such statistical estimates become unnecessary. Moreover, a number of climate scenarios previously unconsidered have been quantitatively predicted, under the same Global Energy Balance condition with zero net surface energy flux, as shown in the fourth row in Table 3. In essence, any actual thermal energy transfer between the surface and the atmosphere that appears either undefined or difficult to be measured can be implicitly treated as part of N. Note that (10) implies the net downward energy flux N_0 should be solely determined by the mean surface temperature and the surface emissivity as $I_E = \varepsilon_E \sigma T_E^4$, rather than by LW DCAR as previously taken for granted in other studies [2,3], although LW DCAR may well be part of N_0. In passing, NDEH at the surface is conceptually different from the net downward heat flux introduced by Gregory *et al* [11] to describe a hypothetical vertical radiative transfer process initiated at the TOA.

4.3 The stable range of atmospheric absorption

It is shown that the total atmospheric absorption be limited by the maximum external radiation, both from the Sun and the Earth's surface. To remain at the current equilibrium surface temperature, 289.16 K, it is theoretically predicted that the minimum of the total atmospheric absorption is close to 236 W m^{-2}, being significantly lower than the value that has been assumed so far. In a recent study [7], for example, the total absorption by the atmosphere 521.8 W m^{-2} was assumed. This seems unlikely because the value is 46.6 W m^{-2} higher than the maximum atmospheric absorption, I_E+A_{SW} = 396.4 + 78 = 474.4 W m^{-2}. In another report [2], it was claimed that LW DCAR $I_A^{\downarrow}$ = 342 W m^{-2} which requires atmospheric absorption even higher than 521 W m^{-2}.

It could be argued that such an unrealistically high atmospheric absorption is merely fabricated for invoking an imaginary greenhouse effect, bearing in mind that the average solar radiation at the TOA is 342 W m^{-2}. Moreover, it is revealed that (8) and (9) are incorrect in studying the earth-atmosphere system due to the limitation associated with Kirchhoff's law in formulating thermal radiation. From those radiation and energy budget diagrams, e.g. [7–9], it is clear that (8) was used to obtain the LW atmospheric absorption, 356 W m^{-2}, based on that the assumed transmitted surface radiation at the TOA is 40 W m^{-2}, which yields the LW atmospheric absorptivity and the LW atmospheric transmittance equal to 89.91% and 10.01%, respectively.

By using (19), by way of contrast, the predicted LW atmospheric transmittance is close to 0.24 given the LW atmospheric absorptivity is 89.91%, as shown in Table 2, in order to satisfy the power balance condition, determined by (11). As a result, the sum of the LW and SW atmospheric absorption is 430.4 W m^{-2}, instead of 521.8 W m^{-2} as previously assumed in [7,8].

Further, it is shown that the proposed theory is self-consistent as the calculated OLR at TOA from (13) is indeed a constant, independent of the LW atmospheric absorption, as indicated in (2). This implies that a previous calculation of radiation forcing by assuming a change in OLR due to CO_2-doubling [7] appears inconsistent with the definition of OLR in (1). In essence, any increase in LW atmospheric absorption will spontaneously increase in UCAR to exactly keep OLR a constant, as shown in Fig. 4, consistent with Le Chatelier's principle of thermodynamics.

4.4 Characterization of atmospheric radiation

It is found that the fraction for UCAR, β, is always larger than the portion for DCAR whenever the LW atmospheric absorptivity $a_{LW} > 60\%$. This can be explained as the fact that UCAR can easily reach outer space whereas DCAR would

be increasingly attenuated towards the Earth's surface. Since DCAR is treated as part of NDEF, the difference $N - I_A^{\downarrow}$ actually represents the contribution to NDEF from other thermal energy transfer processes, both radiative or non-radiative. In fact, it is found that the cumulative downward atmospheric radiation at the surface $I_A^{\downarrow}$ is about one-fourth of NDEF, which implies that DCAR would be more effectively converted into the thermal energy towards the lower-altitude atmospheric layers as it approaches towards the surface where both the air density and the air temperature are the highest, whilst the collisions are the most frequent. Hence, the relatively low range of DCAR found in this study seems consistent with the observed stable surface temperature.

It is noted that whenever LW atmospheric absorptivity decreases to a critical value, ~40%, the total atmospheric radiation, the sum of UCAR and DCAR, becomes zero, as shown in Fig. 4, which implies that no cumulative atmospheric radiation can be detected at the TOA and the surface under this condition. This can be explained in terms of total internal absorption in the atmosphere when its internal thermal energy is insufficient to maintain its equilibrium with the surface. Under this critical condition, the atmospheric radiation is completely absorbed by the atmosphere itself. This explanation is consistent with the definitions of UCAR and DCAR whose sum become negative whenever the total atmospheric absorption is less than the net downward energy flux N in (19), required for preventing the radiation cooling at the surface. Note that once the atmosphere reaches its thermal equilibrium with the surface, the surplus LW atmospheric radiation is primarily utilized by the atmosphere to cool down itself and hence increase its entropy, rather than to warm up the surface.

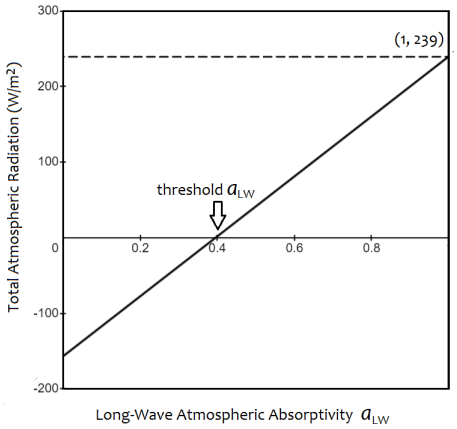

Fig. 4: Dependence of total atmospheric radiation on LW atmospheric absorptivity. Notice that the net atmospheric radiation is negative if LW atmospheric absorptivity a_{LW} is less than 0.4. The coordinate (1, 239) represents the maximum total cumulative atmospheric radiation at the TOA and the surface, 239 W m^{-2}, at the maximum LW atmospheric absorptivity $a_{LW} = 100\%$.

ε_E	1.0	0.99	0.95	0.92	unit
I_E	396.4	392.44	376.58	364.69	W m^{-2}
$I_{LW}^{\uparrow}$	239.41	239.43	239.44	239.43	W m^{-2}
$I_{LW}^{(N)}$	0.0	0.0	0.0	0.0	W m^{-2}
N	235.4	231.44	215.58	203.69	W m^{-2}
a_{LW}^{th}	0.3971	0.391	0.3653	0.3446	
β	0.8357	0.8359	0.8354	0.8354	

Table 3: Calculated dependence on the surface emissivity.

4.5 The role of surface emissivity

The Earth's surface emissivity is explicitly treated as a thermodynamic variable in this study, whilst in the previous studies the surface emissivity was larger than 0.99 [10]. Note that the surface radiation decreases noticeably from 396.4 W m^{-2} to 364.69 W m^{-2} as the surface emissivity changes from 1.0 to 0.92 and the so-called best estimate for the surface radiance [2], 398 W m^{-2}, is 1.6 W m^{-2} higher than the calculated value at $\varepsilon_E = 1$ in this study. It is of interest to find that atmospheric radiation, both UCAR and DCAR, is independent of the surface emissivity at the maximum LW atmospheric absorptivity a_{LW} =1, although atmospheric radiation decreases non-linearly with the decrease of a_{LW}. This implies that the β-factor in (7) belongs to the intrinsic compositional properties of the atmosphere and hence independent of the intensity of the surface radiation. It is also found that LW atmospheric transmittance increases noticeably as surface emissivity changes from 1.0 to 0.92, as shown in Fig. 1, corresponding to the equilibrium NDEF decreases from 235.4 W m^{-2} to 203.69 W m^{-2}, as shown in Table 3. This indicates the atmosphere can spontaneously adjust its LW transmittance in response to the change in the surface radiance. However, such an spontaneous capability seems incapable of fully maintaining the transmitted surface radiation in the range $a_{LW} < 0.4$ unless atmospheric radiation completely ceases below each threshold value of a_{LW} for a given surface emissivity. Such detailed effects seem unexpected because the surface emissivity was often assumed as unity after Houghton [12]. Thus, the LW surface reflectivity, $r_{LW} = 1 - \varepsilon_E$, can be treated as a key variable in climate modeling. Further studies in this direction are certainly worthwhile.

5 Conclusion

In conclusion, it is shown that Kirchhoff's law on thermal radiation is oversimplified and must be modified in connecting atmospheric radiation with atmospheric absorption. Due to complicated thermal mixing processes associated with atmospheric absorption and emission, the equation for atmospheric transmittance and the atmospheric absorptivity is far from linear. Further, it is revealed that the long-wave atmospheric radiation can be completely absorbed by the atmo-

sphere itself before it reaches to a thermal equilibrium between the surface. For the first time, both the upward cumulative atmospheric radiation and the downward cumulative atmospheric radiation can be theoretically calculated without uncertainty. It is also shown that upward cumulative atmospheric radiation at the top of the atmosphere is in general stronger than downward cumulative atmospheric radiation at the Earth's surface. It is explained that the atmospheric absorption only plays a passive role in achieving its thermal equilibrium with the Earth's surface whilst atmospheric radiation plays a proactive role in enabling the atmosphere to adapt to a wide range of variation in the atmospheric absorptivity values. In essence, only a small fraction of the atmospheric radiation, less than 55 $W\,m^{-2}$, can be absorbed by the surface, whereas the larger portion of the atmospheric radiation, up to 199 $W\,m^{-2}$, can spontaneously escape into the outer space, providing a unique mechanism for radiation cooling to maximize the entropy of the atmosphere. It is shown that the Global Energy Balance can be realized in a number of climate scenarios without any estimates. It is expected that the proposed theory can be applied in elucidating commonly concerned climate issues without invoking Kirchhoff's law and the greenhouse effect.

Acknowledgements

The author thanks H. Harde from Helmut-Schmidt University for his detailed comments and W. Happer for his encouragement at the early stage of this study. All of the graphical visualization and numerical calculation are carried out at desmos.com free of charge.

Received June 10, 2021

References

1. Ohmura A. The Development and the Present Status of Energy Balance Climatology. *J. Meteorl Soc. Jpn*, 2014, v. 92 (4), 245–285.
2. Wild M. Progress and challenges in the estimation of the global energy balance. *AIP Conference Proceedings*, 2017, v. 1810, 020004.
3. Stephens G. L., Li J., Wild M., Clayson C. A., Loeb N., Kato S., L'Ecuyer T., Stackhouse Jr. P. W., Lebsock M., and Andrews T. An Update on Earth's energy balance in light of the latest global observations. *Nature Geoscience*, 2012, v. 5 (10), 691–696.
4. Robitaille P. M. and Crothers S. J. The Theory of Heat Radiation Revisited: A Commentary on the Validity of Kirchhoff's Law of Thermal Emission and Max Planck's Claim of Universality. *Progress in Physics*, 2015, v. 11 (2), 120–132.
5. Zhong Y. C., Pilbrow J. R. A Consistent Description of EPR Spectra. *J. Magn. Reson.*, 1991, v. 93, 447–457.
6. Ångström A. Solar and terrestrial radiation. Report to the international commission for solar research on actinometric investigations of solar and atmospheric radiation. *Q. J. R. Meteorol. Soc.*, 1924, v. 50 (210), 121–126.
7. Harde H. Advanced Two−Layer Climate Model for the Assessment of Global Warming by CO^2. *Open J. Atmos. Climate Change*, 2014, 2374–3794. ISSN(Online), 2374–3808.
8. Trenberth J. E., Fasullo J. T., and Kiehl J. Earths Global Energy Budget. *Bulletin of the American Meteorological Society*, 2009, v. 90 (3), 311–323.
9. Kiehl J. T., and Trenberth K. E. Earth's annual global mean energy budget. *Bull. Am. Meteorol. Soc.*, 1997, v. 78 (2), 197–208.
10. Wilber A. C., Kratz D. P., and Gupta S. K. Surface emissivity maps for use in satellite retrievals of longwave radiation. *NASA Tech. Publication*, 1999, NASA/TP-1999-209362, 35 pp.
11. Gregory J. M., Ingram W. J., Palmer M. A., Jones G. S., Stott P. A., Thorpe R. B., Lowe J. A., Johns T. C., and Williams K. D. A new method for diagnosing radiative forcing and climate sensitivity. *Geophys. Res. Lett.*, 2004, v. 31, L03205.
12. Houghton J. T. The Emissivity of the Earth's Surface. *Nature*, 1959, v. 183, 367.

Explicit Values for Gravitational and Hubble Constants from Cosmological Entropy Bound and Alpha-Quantization of Particle Masses

Alexander Kritov

E-mail: alex@kritov.ru, Moscow, Russian Federation.

In this study, we propose a method to derive expressions and numerical values for the gravitational and Hubble constants employing the "reverse engineering" path approach. Using the explicit form of Bekenstein bound for the cosmological horizon, we show that Nambu's mass-formula (the empirical alpha-quantization of elementary particle masses) is related to the proposed 3-D analogy of the holographic principle. The obtained form in the "median case" leads to the expression for the Hubble constant with the value of $H_0 = 71.995$ km/s/Mpc. The accuracy of obtained H_0 allows precise numerical calculation of the cosmological entropy bound, which coincides with the number of $\left(216 \times 2^{128}\right)^3$ bits. Conversely, the number leads to the expression for the gravitational constant resulting in $G = 6.67437305 \times 10^{-11}$, which exactly fits into the CODATA2018 value and the AAFII(2018) measurement [32]. As a coincidence, the proposed approach combined with the previous formulation of the LNNC (Large Numerical Number Coincidences) [10] allows obtaining the numerical value for the proton-to-electron mass ratio μ with an accuracy of 10^{-6}.

Note: SI units are deployed.

1 Introduction

Dimensionless numbers, including the mass ratios of the elementary particles and large numbers introduced by Dirac [45], remain unresolved puzzles in physics. To understand the significance of large number relations, the constant H_0 and G must be precisely measured, and their deviations in time and space must be constrained. However, at present, we know the value of the Hubble constant with a precision of $< 10\%$ [35]. Today, those using Planck and cosmic background data to measure a value for the Hubble constant arrive at a figure of 67.4 ± 0.5. However, the local approach provides a figure of 73.5 ± 2 [41, 43]. In contrast, the gravitational constant G is known to have better precision; however, its value has a relative accuracy of 2×10^{-5} depending on the measurement methods performed.

This paper presents an attempt to connect the Bekenstein cosmological entropy bound with the alpha-quantization of elementary particle masses. As a result, the Dirac large numbers appear as an intrinsic property of the cosmological entropy bound, which allows us to obtain the numerical value and to express G and H_0.

In 1952, Nambu proposed an empirical formula for the mass spectrum of elementary particles, known as "alpha quantization" [1]

$$m_n \approx \frac{n}{2}\,\alpha^{-1}\,m_e \tag{1}$$

where n is a natural number, α is the fine structure constant, and m_e is the electron mass. The mass interval is predicted as a half-integral multiple of approximately 70 MeV. It provides the muon mass with $n = 3$, the pion mass for $n = 4$, and the proton mass for $n = 27$ *etc*. Currently, at least 21 fundamental particles with lifetimes $>10^{-24}$ s are covered by this rule, with deviations of less than 1% [9]. The alpha quantization of elementary particle masses is extensively reviewed in the modern literature [16–28]. In particular, it is valid, for example, for the heaviest known particle, the top quark for which $n = 137 \times 36$ [20]. The Nambu formula was derived empirically and did not have any theoretical background. However, along with the new approaches to elaborate it in the frame of modern models, there were a few almost forgotten attempts to refine the formula, for example, by Nambu in 1966 [2], Hermann [3], and later [36–39] extending the quantum oscillator model, which led to clarifications and more accurate results for the mass ratios of elementary particles.

2 Bekenstein entropy bound for cosmological horizon

The cosmological (Hubble or de Sitter) horizon corresponds to the radius and volume.

$$R_H = \frac{c}{H_0}\,, \quad V_H = \frac{4\pi}{3}\left(\frac{c}{H_0}\right)^3\,, \tag{2}$$

where H_0 denotes the Hubble constant. Because we are looking for the upper limit of entropy, we shall consider the entire mass-energy content of the universe with $\Omega_{Tot} = 1$. Therefore, the critical density $\rho_{cr} = 3H_0^2/8\pi G$ within the Hubble volume provides the mass-energy

$$E = V_H\,\rho_{cr}\,c^2 = \frac{c^5}{2GH_0}\,. \tag{3}$$

It is easy to see that in such a case (i.e. $\Omega_{Tot} = 1$), the cosmological horizon also coincides with the Schwarzschild black

hole radius*. The Bekenstein entropy bound for the black hole is

$$S = \frac{\lambda RE}{\hbar c} = \frac{4\pi RE}{\hbar c}. \quad (4)$$

The original Bekenstein formula [30] was derived based on the general considerations for "an arbitrary system of effective radius R" and contains factor $\lambda = 2\pi$. Recently the factor was clarified [31]; it was explicitly shown that particularly in the application to the Schwarzschild black hole case the factor is $\lambda = 4\pi$, which is strictly derived based on the entropy associated with the Hartle-Hawking state. Since the cosmological horizon coincides with the Schwarzschild black hole radius, as shown, the expression (4) has $\lambda = 4\pi$. The substitution of R and E from (3) leads to the value of the upper bound for the entropy of the universe

$$S = 2\pi \frac{c^5}{\hbar G H_0^2}. \quad (5)$$

The number (measured as the number of bits†) is known by its order and is also referred to as the computational capacity of the universe [44]. Notably, the critical mass of the universe can be written in terms of the obtained expression for the total entropy:

$$M_U = \frac{c^3}{2GH_0} = S \times m_0, \quad m_0 := \frac{\hbar H_0}{4\pi c^2}. \quad (6)$$

Hence, the mass m_0 can be interpreted as the minimal possible quanta of the mass-energy carrying one bit of information.

Note on Oldershaw-Fedosin scaling of the Planck constant

Using (5), one may consider the "scaled" Planck constant $\hbar^*$ such that‡

$$\hbar^* = \frac{S}{2\pi}\hbar, \quad h^* = S\,\hbar. \quad (7)$$

The constant $\hbar^*$ plays the role of the reduced Planck constant in a multiverse, where our universe represents an elementary particle or a quantum oscillation [4,5]. The Heisenberg uncertainty relation, which is hypothetically valid in a multiverse, is then given as

$$\Delta E\,\Delta\left(\frac{1}{H_0}\right) \geq \frac{\hbar^*}{2}. \quad (8)$$

On the other hand, the substitution of (7) into the expression leads to the Bekenstein law, which bounds the entropy by corresponding the total energy and time $1/H_0$ (or radius c/H_0) for the universe. Such notable correspondence to the Heisenberg uncertainty relation for the cosmological case is possible when using the above-mentioned factor $\lambda = 4\pi$ for the cosmological case.

3 3-D analogue of Holographic Principle with the "cell of space volume"

The Bekenstein bound implies the holographic principle [29]. Applying it to the cosmological horizon, the Hubble area can be represented as

$$A_H = 4\pi\left(\frac{c}{H_0}\right)^2 = S \times A_{Pl}, \quad (9)$$

where A_{Pl} is the Planck area§ and S is the Bekenstein cosmological bound (5). As the Plank area plays the role of a 1-bit unit of the area, analogous to that we may also introduce "the cell of space volume" V_0 such that the total Hubble volume is

$$V_H = \frac{4\pi}{3}\left(\frac{c}{H_0}\right)^3 = S \times V_0. \quad (10)$$

Thus, the introduced V_0 shall play a similar role for 3-D being a 1-bit unit for the volume, as the Planck area does for 2-D. The substitution of (5) leads to the explicit form

$$V_0 = \frac{V_H}{S} = \frac{2}{3}\frac{G\hbar}{H_0 c^2}. \quad (11)$$

This parameter V_0 was introduced in the author's previous work [12, 13]. The new parameter of the space volume cell V_0 may imply a different sense than *the grain of space* used in the loop quantum gravity (LQG) approach [46, 47], where the grain of space is considered to be of the order of Planck length l_{Pl}^3. In contrast, the volume cell V_0 is of the order of the cube of the reduced Compton wavelength of an elementary particle. Simultaneously, similar constraints are given for the V_0-dependent uncertainty relation in the LQG approach [47].

4 The Nambu formula for alpha-quantization of particle masses

The V_0-dependent uncertainty relation is:

$$\left(\frac{1}{2}\frac{\hbar}{mc}\right)^3 \geq V_0. \quad (12)$$

Based on that, one may consider the quantization of elementary particle masses (1) as a classic quantum harmonic oscillator [40]. The particles' rest masses correspond to the oscillator eigenstates

$$E_n = m_n c^2 = \frac{n}{2}\hbar\omega, \quad \omega = \frac{c}{L},$$

where $L = V_0^{1/3}$ is the characteristic length of the oscillator, and n is a natural number for both parity cases with non-zero

*Since $R_S = (2G/c^2)(c^3/2GH_0)$.

†The entropy S is the number of states, the exact number of the Plank areas in covering area when using the holographic principle (9). Hence, factor ln(2) in the Bekenstein expression to obtain the number of bits, which appears in many textbooks is highly arguable and shall not be used.

‡Here it would be natural to introduce the "reduced" $\bar{S} = S/2\pi$ such that (7) takes the simpler form $\hbar^* = \bar{S}\hbar$, $h^* = \bar{S}\,h$.

§In such a way, the Plank area acquires a prefactor of two as $A_{Pl} = 2G\hbar/c^3$.

ground state ($n = 1$). Therefore, for elementary particles with mass m_n, the following condition holds:

$$\frac{n}{2}\,\frac{\hbar}{m_n c} = V_0^{1/3}\,. \tag{13}$$

The substitution of (11) for V_0 leads to particle masses that satisfy the above requirement

$$m_n = \frac{n}{2}\left(\frac{3}{2}\,\frac{\hbar^2 H_0}{Gc}\right)^{1/3}\,. \tag{14}$$

By direct calculation, it can be noted that

$$\left(\frac{3}{2}\,\frac{\hbar^2 H_0}{Gc}\right)^{1/3} \approx 137\, m_e\,,$$

where m_e is the mass of an electron. Thus, the obtained expression (14) represents Nambu's original mass formula (1), which is now related to the Bekenstein cosmological bound. The exact match to the factor to α^{-1} is achieved when the Hubble constant is $H_0 = 71.9949$ km/s/Mpc, as reviewed in the next section.

5 The Hubble constant, the Universe entropy number and G in the "median" case

Considering the "median case" or the "ideal" case when the exact equality in (14) holds as

$$\left(\frac{3}{2}\,\frac{\hbar^2 H_0}{Gc}\right)^{1/3} = \alpha^{-1}\, m_e\,, \tag{15}$$

it becomes possible to express the Hubble constant via better known G as

$$H_0 = \frac{2}{3}\,\frac{G\,c\,\alpha^{-3}\,m_e^3}{\hbar^2} = \frac{2}{3\alpha}\,\frac{G m_e}{r_e^2\,c}\,, \quad \text{where } r_e = \frac{ke^2}{m_e c^2}\,, \tag{16}$$

which results in 71.9949 km/s/Mpc or $2.333\times10^{-18}\,\mathrm{s}^{-1}$ when using CODATA2018 for G. Substituting H_0 into (11) yields

$$V_0 = \left(\frac{ke^2}{m_e c^2}\right)^3 = r_e^3\,. \tag{17}$$

Furthermore, the substitution of the obtained H_0 (16) into (5) yields an explicit value for the universe total entropy bound:

$$S = \frac{4\pi}{3}\left(\frac{ke^2}{Gm_e^2}\,\frac{3\alpha}{2}\right)^3\,. \tag{18}$$

The obtained expression allows the accurate calculation of the value as 3.9711×10^{122} till the 5th digit (corresponding to the accuracy of G). Moreover, because we expect the entropy S to be a *natural number* (number of bits of information), and as binary, it most probably should contain powers of 2. The search leads to the number that represents the cosmological entropy bound as a factor of two first primes

$$S = 3^9 \times 2^{393} = \left(216\times 2^{128}\right)^3\,. \tag{19}$$

Remarkably, the found number appears to be the cube of a natural number. The number provides a sufficient relative accuracy of 3×10^{-5} with (18) corresponding to the accuracy of G (see Section 8 for a more detailed discussion on this number). Furthermore, the reverse substitution of the number to (18) allows us to express the gravitational constant:

$$G = \frac{ke^2}{m_e^2}\left(\frac{3\alpha}{2}\right)\left(\frac{4\pi}{3S}\right)^{1/3} = \left(\frac{4\pi}{3}\right)^{1/3}\frac{\alpha}{144}\,\frac{ke^2}{m_e^2}\,2^{-128} \tag{20}$$

resulting in $G = 6.67437305\times10^{-11}$. This value perfectly fits the value of CODATA2018 for G. The obtained value also coincides with the AAFII(2018) measurement of 6.674375(82) performed with very high precision [32]. Moreover, the use of the obtained G in (16) results in the expression for the Hubble constant

$$H_0 = \frac{c}{r_e}\left[\left(\frac{4\pi}{3}\right)^{1/3}\frac{1}{216}\right]2^{-128}\,, \tag{21}$$

where r_e is the classical electron radius (16). Notably, to satisfy the equality to α in (15), the expressions acquire the factor given in square brackets. Denoting this factor as $\alpha_s = 1/133.995..$ (or "alpha-substitute"), both expressions can be written in the simpler form

$$H_0 = \alpha_s\,\frac{c}{r_e}\,2^{-128}\,, \quad G = \alpha_s\,\alpha\,\frac{3}{2}\,\frac{ke^2}{m_e^2}\,2^{-128}\,, \tag{22}$$

where

$$\alpha_s \coloneqq \left(\frac{4\pi}{3}\right)^{1/3}\frac{1}{216}\,.$$

The significance of this parameter is reviewed further.

6 Proton to electron mass ratio from deviated G and H_0

We have considered the "median" or ideal case of exact equality to α in the extended Nambu's mass formula (14). In a real-life scenario, the masses of the elementary particles deviate from the median values by ±1%. There are two alternative ways to refine the Nambu mass formula to obtain more accurate masses for elementary particles. The first approach, as mentioned in Section 1, clarifies the quantum oscillator model. This leads to the appearance of eigenvalues or zeros of some functions instead of the natural number n in (1). The second alternative is to introduce the deviation of G and H_0 in the mass formula (14), which would also lead to nonconstancy of V_0 and deviated states of the entropy from S depending on the nature of the particle. The first method appears to be preferable and requires further studies using QM.

However, in this section, we evaluate the second "heuristic" alternative.

One may recall the previously proposed expressions for G and the Hubble constants (LNNC) [10]. Denoting them with a prime ($'$) to distinguish them from the obtained "median" values, they are

$$H_0' = \frac{m_e c^2}{\hbar}\, 2^{-128}\,, \quad G' = \frac{3}{20}\,\frac{ke^2}{m_e m_p}\, 2^{-128}\,, \qquad (23)$$

where m_p is the proton mass. The value for $H_0' = 70.39882$ km/s/Mpc differs by 2%* from the "median" case of H_0 (16). It is evident that the formula for H_0' can be treated as derived from the expression for H_0 (22), wherein the latter, α_s is simply *substituted* by α.

The value of the gravitational constant is $G' = 6.6746305 \times 10^{-11}$, which deviates from the median G (22) by 3×10^{-5}, and is closer to the AAF-I and AAF-III measurements [32]. It is evident that these values (23) do not provide the equality to "alpha" in mass-formula (15); however remarkably H_0' and G' being substituted into (14) with $n = 27$ provide a good approximation of the proton mass, thus the ratio becomes

$$\mu = \frac{m_p}{m_e} = \left(\frac{5}{4}\, 3^9\, \alpha^{-1}\right)^{1/2}\,. \qquad (24)$$

Moreover, it can be seen that both suggested formulas for the gravitational constant have relative deviations of 3×10^{-5}, equating G from (23) and (22) gives

$$\alpha^{-1} = \left(\frac{4\pi}{3}\right)^{1/3}\,\frac{5\mu}{108}\,, \qquad (25)$$

where we expect the same relative error of 10^{-5}. The substitution of μ from (24) leads to

$$\alpha^{-1} = \left(\frac{4\pi}{3}\right)^{2/3}\left(\frac{15}{4}\right)^3 = \mathbf{137.03}12258\,, \qquad (26)$$

and substituting it again to (24) results in

$$\mu = \left(\frac{4\pi}{3}\right)^{1/3}\left(\frac{135}{4}\right)^2 = \mathbf{1836.15}959\,, \qquad (27)$$

which has a relative accuracy with the experimental value of the proton-to-electron ratio of 3×10^{-6}. The remarkable property of both expressions is their simple forms that involve powers of the first three primes as $15 = 5\times3$ and $135 = 3^3\times5$. The expression for μ can be assumed to be the best in terms of the precision-simplicity ratio (see [11] to see the complication level of formulae with comparable accuracy for μ). The expressions can also be rewritten in the following forms:

$$\mu = \frac{27}{2}\,(135\,\phi)\,, \quad \alpha^{-1} = 135\,\phi^2\,, \qquad (28)$$

*The ratio for the deviation is $(\alpha^{-2}/10\mu) = (4\pi/3)((5/8)^3)$, as can be seen later.

where

$$\phi := \frac{5}{8}\left(\frac{4\pi}{3}\right)^{1/3}\,,$$

and the "alpha-substitute" is explicitly $\alpha_s^{-1} = 135\,\phi^{-1}$. Thus, the formula for μ restores the original form of Nambu's mass formula with $n = 27$. Hence, the factor $\phi \approx 1.0075$ plays the role of a small deviation and exhibits a deviation of α in Nambu's mass formula. Simultaneously, ϕ^2 shows how α deviates from an integer of 135. The deviation $\phi^3 \approx 1.02$ also provides the explicit ratios of the two values for the Hubble constants given by the expressions (21) and (23) as this deviation is given by the ratio of "alpha-substitute" in (21) to the exact "alpha" in (23).

7 Quantum number of the Universe and Eddington's number of particles

The paper would not be complete without reviewing the Eddington number of particles (pairs of protons and electrons), which he assumed to be $N = 2 \times 136 \times 2^{256}$ [6]. In Section 5, we review the number for the Bekenstein entropy S, which is also expressed by the power of 2 (19). Prior to the calculation of the Eddington number of particles, we calculate the n-number using the obtained mass formula (14) applied to the *entire* universe mass with $\Omega = 1$

$$M_u = \frac{c^3}{2GH_0} = \frac{n_u}{2}\left(\frac{3}{2}\,\frac{\hbar^2 H_0}{Gc}\right)^{1/3}\,. \qquad (29)$$

Because we are applying it to "the median" case, it is clear that $M_u = (n_u/2)(\alpha^{-1}m_e)$. Using the obtained values for G and H_0 (22) after a few manipulations, the number becomes

$$n_u = \frac{2}{3}\left(\frac{3}{4\pi}\,S\right)^{2/3} = \frac{2}{3}\,\alpha_s^{-2}\,2^{256}\,. \qquad (30)$$

Using this number, it is evident that the Eddington number of protons can be expressed as

$$N = \frac{M_u \Omega_{M_p}}{m_p} = \Omega_{M_p}\,\frac{n_u}{2}\,\frac{\alpha^{-1}}{\mu}\,, \qquad (31)$$

where Ω_{M_p} is the proton content of the universe. The obtained good approximations for α and μ of (28) provide the ratio

$$\frac{\alpha^{-1}}{\mu} = \frac{2}{27}\phi\,,$$

and substituting n from (30) results in the number of protons in the universe

$$N = \Omega_{M_p}\,\frac{10}{3}\,\alpha_s^{-1}\,2^{256}\,, \qquad (32)$$

where the second power of α_s^{-1} decreases with ϕ. This expression is fairly close to the famous Eddington number. However, the difference is that it contains the prefactor, and "alpha-substitute" (≈ 134) instead of 136 in Eddington's expression.

8 Discussion

In Section 5, we proposed the numerical value for the "median" cosmological entropy bound as the number of bits, which explicitly equals $(216 \times 2^{128})^3$. The number limits the upper bound of the informational capacity of the universe according to the Bekenstein law. When searching for the numbers of order 10^{122} with a relative accuracy of 10^{-5}, one must observe that there exist 10^{117} alternative natural numbers to choose between. Another good fit, for example, can be given by

$$137 \times \frac{81!}{2} \approx 3.971031 \times 10^{122} \text{ bits}.$$

Notably, the number represents the order of the alternating group $A(81)$ with prefactor 137, which can be considered as a coincidence. However, the key advantage of (19) compared to other alternatives is that it is the simplest number composed of the product of only the first two primes. Second, it represents the cube of another natural number, which reveals its significance during the calculations. Moreover, the number (19) can also be represented by the Mersenne prime $M_{127} = 2^{127} - 1$, where M_{127} has the unique property of being the double Mersenne prime and fourth Catalan-Mersenne number* discovered by Catalan [34]. Hence, $S = (432 \times M_{127})^3$, which possibly connects the median entropy to the cyclic group† $\mathbb{Z}_{M_{127}}$.

Despite the presence of a power of two, the proposed number differs from the Eddington E-numbers [7, 8]. However, further study is required for a possible connection of the proposed number to the Clifford algebras and the finite groups of Lie type [48].

9 Conclusions

In 1935, Heisenberg [42] suggested using the number 432 to calculate the fine structure constant as $\alpha^{-1} = 432/\pi$. The paper has demonstrated that number 432 and its derivatives (108, 216) appear in the "median" or symmetric case of universe entropy bound, and further in the calculation for the dimensionless numbers (25), (19). An intriguing numerical expression for the total universe entropy for the Bekenstein cosmological bound is proposed (19), which contains only powers of 2 and 3. This allowed to construct an expression for the gravitational constant that gives a value of $G = 6.67437294 \times 10^{-11}\ \mathrm{m^3\,kg^{-1}\,s^{-2}}$, which fits the range of CODATA2018 to the latest measurements. Along with the previous formulation for the Hubble constant, the approach provides a new alternative form (greater by 2% from the previous) as given by expressions (21), (16), resulting in $H_0 = 71.994$ km/s/Mpc, which corresponds to the "median" case of the universe entropy bound (19). The current accuracy of measurements of the Hubble constant H_0 limits the study. Further improvements in the measurements of the Hubble constant are required, as it will clarify the concordance of the value of the cosmological entropy bound S to the proposed number.

The paper proposes a path, using the explicit value for Bekenstein bound, to connect the maximum of the observable values such as the Hubble volume, the total mass of the universe with minimal measurable values (V_0 and m_0), which supposedly have to play a role in quantum mechanics. The approach can be extended towards a broader range of physical parameters, such as maximal and minimal force, maximal and minimal acceleration. The introduction of such parameters may lead to new approaches in quantum mechanics and cosmology. Further research is required in the frame of quantum mechanics, the LQG, which would utilize the introduced space volume V_0 parameter in connection to Clifford algebra $Cl_{3,0}$ (APS), where it has the correspondence to volume coordinate x_{123} [14]. Such a study may further refine the quantum oscillator model of elementary particle masses using the introduced parameters.

Received on July 9, 2021

*Since $127 = 2^7 - 1$, $7 = 2^3 - 1$, and $3 = 2^2 - 1$.

†Interestingly; this number also nearly coincides with the order of symplectic group Sp(n, q) with $q = 2^{43}$, $n = 1$ with prefactor 108, and the same for the Chevalley group $A_n(q)$ (PSL(n, q)).

References

1. Nambu Y. An Empirical Mass Spectrum of Elementary Particles. *Prog. Theor. Phys.*, 1952, v. 7, 131.
2. Nambu Y. Relativistic Wawe Equations for Particles with Internal Structure and Mass Spectrum. *Progr. Theoret. Phys. (Kyoto)*, 1966, Suppl., Nos. 37–38, 368–382.
3. Hermann R. General Mass Formula for the Nambu Wave Equations. *Physical Review*, 1968, v. 167, 525.
4. Fedosin S. G. Physics and Philosophy of Similarity from Preones to Galaxies. Perm, 1999 [in Russian].
5. Oldershaw R. The Hidden Meaning of Planck's Constant. *Universal Journal of Physics and Application*, 2013, v. 1 (2), 88–92.
6. Eddington A. S. Relativity Theory of Protons and Electrons. Cambridge University Press, Cambridge, 1936.
7. Eddington A. S. On Sets of Anticommuting Matrices. Part II: The Factorization of E-Numbers. *Journal of the London Mathematical Society*, 1933, v. 1-8 (2), 142–152.
8. Salingaros N. Some remarks on the algebra of Eddington's E numbers. *Foundations of Physics*, 1985, v. 15, 683–691.
9. Greulich K. O. Calculation of the Masses of All Fundamental Elementary Particles with an Accuracy of Approx. 1%. *J. Mod. Phys.*, 2010, v. 1, 300–302.
10. Kritov A. A New Large Number Numerical Coincidences. *Progress in Physics*, 2013, v. 9 (2), 25–28.
11. Kritov A. An Essay on Numerology of the Proton to Electron Mass Ratio. *Progress in Physics*, 2015, v. 11 (1), 10–13.
12. Kritov A. On the Fluid Model of the Spherically Symmetric Gravitational Field. *Progress in Physics*, 2019, v. 15 (2), 101–105.
13. Kritov A. Unified Two Dimensional Spacetime for the River Model of Gravity and Cosmology. *Progress in Physics*, 2019, v. 15 (3), 163–170.
14. Kritov A. Gravitation with Cosmological Term, Expansion of the Universe as Uniform Acceleration in Clifford Coordinates. *Symmetry*, 2021, v. 13, 366.
15. PDG, Physical Review D, 2020.

16. Jensen E. Regularities in the masses of some elementary particles. RVAU-IMS-80-2, Veterin. Agricult. Univ. Dept. Math. Stat., Copenhagen, 1980.
17. Giani S. Particle Mass-Formulae. CERN-OPEN-2004-004, 02 March 2004.
18. Mac Gregor M. H. Electron generation of leptons and hadrons with reciprocal α-quantized lifetimes and masses. arXiv: hep-ph/0506033.
19. Mac Gregor M. H. The top quark to electron mass ratio. arXiv: hep-ph/0603201.
20. Mac Gregor Malcolm H. A "Muon Mass Tree" with α-quantized Lepton. Quark and Hadron Masses. arXiv: hep-ph/0607233.
21. Mac Gregor M. H. Models for Particles. *Lett. Nuovo Cim.*, 1970, v. 7, 211–214.
22. Mac Gregor M. H. The Power of Alpha: The Electron Elementary Particle Generation with Alpha-Quantized Lifetimes and Masses. World Scientific Publishing, Singapore, 2007.
23. Palazzi P. Particles and Shells. CERN-OPEN-2003-006, 2003. arXiv: physics.gen-ph/0301074.
24. Palazzi P. The meson mass system. *Int. J. Mod. Phys.* 2007, v. 22, 546–549.
25. Shah G. N., Mir T. A. Pion and muon mass difference: a determining factor in elementary particle mass distribution. *Mod. Phys. Lett. A.*, 2008, v. 23, 53.
26. Mir T. A., Shah G. N. Order in the mass spectrum of elementary particles. arXiv: physics.gen-ph/0806.1130.
27. Greulich K. O. Calculation of the Masses of All Fundamental Elementary Particles with an Accuracy of Approx. 1%. *J. Mod. Phys.*, 2010, v. 1, 300–302.
28. Chiatti L. A Possible Model for the Mass Spectrum of Elementary Particles. *Phys. Essays.*, 2012, v. 25, 374–386.
29. Bekenstein J. D. Information in the Holographic Universe. *Scientific American*, 2003, v. 289 (2), 58–65.
30. Bekenstein J. D. Universal upper bound on the entropy-to-energy ratio for bounded systems. *Physical Review D*, 1981, v. 23 (2), 287–298.
31. Longo R., Xu F. Comment on the Bekenstein bound. arXiv: math-ph/1802.07184v1, Proposition 2.5.
32. Qing Li, Chao Xue, Jian-Ping Liu, Jun-Fei *et al* Measurements of the gravitational constant using two independent methods. *Nature*, 2018, v. 560, 582–588.
33. Merkatas C., Toman B., Possolo A., Schlamminger S. Shades of Dark Uncertainty and Consensus Value for the Newtonian Constant of Gravitation. arXiv: physics.data-an/1905.09551.
34. Catalan E. Sur la théorie des nombres premiers. Turin, 1876, p. 11. Catalan, E. Théorie des nombres. 1891, p. 376. See also the OEIS A007013.
35. Jackson N. The Hubble Constant. *Living Rev. Relativity*, 2015, v. 18.
36. Salomatov V. N. Relativistic particle in the rest frame. arXiv: physics.gen-ph/1401.6253.
37. Salomatov V. N. Helmholtz equation in relativistic quantum mechanics. *Physics Essays*, 2017, v. 30, 2.
38. Sidharth B. G. A QCD Generated Mass Spectrum. arXiv: physics.gen-ph/0309037v1.
39. Ram B., Halasa R. Meson Spectra with a harmonic-oscillator potential in the Klein-Gordon equation. *Physical Review D*, 1971, v. 19, 11.
40. Landau L. D., Lifshitz E. M. Quantum Mechanics: Non-Relativistic Theory. Course of Theoretical Physics, v. 3. Second Edition. Pergamon Press, 1965, 67–72.
41. Nandita K., Luca I., Marica B. *et al*. A new measurement of the Hubble constant using Type Ia supernovae calibrated with surface brightness fluctuations. *Astronomy and Astrophysics*, 2021, v. A72, 647.
42. Kragh H. Magic number: A partial history of the fine-structure constant. Arch. Hist. Exact Sci., 2003, v. 57, 395–431.
43. Taubenberger S., *et al*. The Hubble constant determined through an inverse distance ladder including quasar time delays and Type Ia supernovae. *Astronomy and Astrophysics* 2019, v. 628, L7.
44. Lloyd S. Computational capacity of the universe. arXiv: quant-ph/0110141.
45. Dirac P. A. M. Cosmological models and the large numbers hypothesis. *Proceedings of the Royal Society of London A*, 1974.
46. Rovelli C. Loop Quantum Gravity. arXiv: gr-qc/9710008v1.
47. Bojowald M. Critical evaluation of common claims in loop quantum cosmology. arXiv: gr-qc/2002.05703v1.
48. Solomon R. A Brief History of the Classifications of the Finite Simple Groups. *American Mathematical Society*, 2001, v. 38 (3), 315–352.

Physics of Transcendental Numbers Determines Star Distribution

Hartmut Müller

Rome, Italy.
E-mail: hm@interscalar.com

Transcendental ratios of physical quantities can provide stability in complex dynamic systems because they inhibit the occurrence of destabilizing resonance between the elements of the system. This approach leads to a fractal scalar field that affects any type of physical interaction. In this paper we verify the model claims on the frequency distribution of interstellar distances in the solar neighborhood.

Introduction

Since the beginning of the past century astronomers began to routinely measure stellar parallaxes. In 1957 this effort was formalized with the publication [1] of 915 stars within 20 pc. Various updates and extensions to larger distances produced what became the Catalogue of Nearby Stars (CNS), including 3803 stars within 25 pc [2] released in 1991. Hipparcos [3] increased the quantity and quality of the CNS content. In 1998 the CNS dataset went online and currently has 5835 entries, but it is no longer updated. The most recent update [4] of the CNS was to provide accurate coordinates taken from the Two Micron Sky Survey (2MASS) [5]. Finally, the Gaia Catalogue of Nearby Stars (GCNS) attempts to make a census of all stars in the solar neighborhood using the Gaia results [6]. In the GCNS, the solar neighborhood is defined as a sphere with a radius of 100 pc centered on the Sun.

In this paper, we will analyze the distribution of the number of stars in the solar neighborhood as function of their mutual distances. This approach is not heliocentric and does not deal with fixed reference points at all.

Conventional models expect an exponential increase of the cumulative number of stars with the distance from a fixed reference point, such as the Sun. As shown in [6], this actually appears to be the case.

We will show that the consideration of all possible pairs of stars within a given range of interstellar distances leads to the appearance of a stable scale-invariant pattern in the frequency distribution of the number of stars as function of the distance between them. This means that there are interstellar distances preferred by the majority of stars in the solar neighborhood. Furthermore, we will derive this scale-invariant pattern from a number theoretic approach.

Methods

In [7] we have shown that the difference between rational, irrational algebraic and transcendental numbers is not only a mathematical task, but it is also an essential aspect of stability in complex dynamic systems. For instance, integer frequency ratios provide resonance interaction that can destabilize a system [8]. Actually, it is transcendental numbers that define the preferred ratios of quantities which avoid destabilizing resonance interaction [9]. In this way, transcendental ratios of quantities sustain the lasting stability of periodic processes in complex dynamic systems. With reference to the evolution of a planetary system and its stability, we may therefore expect that the ratio of any two orbital periods should finally approximate a transcendental number.

Among all transcendental numbers, Euler's number $e = 2.71828\ldots$ is unique, because its real power function e^x coincides with its own derivatives. In the consequence, Euler's number allows inhibiting resonance interaction regarding any interacting periodic processes and their derivatives. Because of this unique property of Euler's number, complex dynamic systems tend to establish relations of quantities that coincide with values of the natural exponential function e^x for integer and rational exponents x.

Therefore, we expect that periodic processes in real systems prefer frequency ratios close to Euler's number and its rational powers. Consequently, the logarithms of their frequency ratios should be close to integer $0, \pm1, \pm2, \ldots$ or rational values $\pm1/2, \pm1/3, \pm1/4, \ldots$ In [10] we exemplified our hypothesis in particle physics, astrophysics, cosmology, geophysics, biophysics and engineering.

Based on this hypothesis, we introduced a fractal model of matter [11] as a chain system of harmonic quantum oscillators and could show the evidence of this model for all known hadrons, mesons, leptons and bosons as well. In [12] we have shown that the set of stable eigenstates in such systems is fractal and can be described by finite continued fractions:

$$\mathcal{F}_{jk} = \ln(\omega_{jk}/\omega_{00}) = \langle n_{j0}; n_{j1}, n_{j2}, \ldots, n_{jk} \rangle \qquad (1)$$

where ω_{jk} is the set of angular eigenfrequencies and ω_{00} is the fundamental frequency of the set. The denominators are integer: $n_{j0}, n_{j1}, n_{j2}, \ldots, n_{jk} \in \mathrm{Z}$. The cardinality $j \in \mathrm{N}$ of the set and the number $k \in \mathrm{N}$ of layers are finite. In the canonical form, all numerators equal 1. We use angle brackets for continued fractions.

Any finite continued fraction represents a rational number [13]. Therefore, the ratios ω_{jk}/ω_{00} of eigenfrequencies are always irrational, because for rational exponents the natural exponential function is transcendental [14]. This circumstance provides for lasting stability of those eigenstates of a

chain system of harmonic oscillators because it prevents resonance interaction [15] between the elements of the system.

The distribution density of stable eigenstates reaches local maxima near reciprocal integers $\pm 1/2, \pm 1/3, \pm 1/4, \ldots$ that are attractor points (fig. 1) in the fractal set $\mathcal{F}_{jk}$ of natural logarithms. Integer logarithms $0, \pm 1, \pm 2, \ldots$ represent the most stable eigenstates (main attractors).

In the case of harmonic quantum oscillators, the continued fractions $\mathcal{F}_{jk}$ define not only fractal sets of natural angular frequencies ω_{jk}, angular accelerations $a_{jk} = c \cdot \omega_{jk}$, oscillation periods $\tau_{jk} = 1/\omega_{jk}$ and wavelengths $\lambda_{jk} = c/\omega_{jk}$ of the chain system, but also fractal sets of energies $\mathrm{E}_{jk} = \hbar \cdot \omega_{jk}$ and masses $\mathrm{m}_{jk} = \mathrm{E}_{jk}/c^2$ which correspond with the eigenstates of the system. For this reason, we call the continued fraction $\mathcal{F}_{jk}$ the *Fundamental Fractal* of stable eigenstates in chain systems of harmonic quantum oscillators.

Fig. 1: The distribution of stable eigenvalues of $\mathcal{F}_{jk}$ for $k = 1$ (above) and for $k = 2$ (below) in the range $-1 \leqslant \mathcal{F}_{jk} \leqslant 1$.

The spatio-temporal projection of the Fundamental Fractal $\mathcal{F}_{jk}$ of stable eigenstates is a fractal scalar field of transcendental attractors, the *Fundamental Field* [16].

The connection between the spatial and temporal projections of the Fundamental Fractal is given by the speed of light c = 299792458 m/s. The constancy of c makes both projections isomorphic, so that there is no arithmetic or geometric difference. Only the units of measurement are different.

Figure 2 shows the linear 2D-projection $\exp(\mathcal{F}_{jk})$ of the first layer of the Fundamental Field

$$\mathcal{F}_{\mathrm{j1}} = \langle n_{j0}; n_{j1} \rangle = n_{j0} + \frac{1}{n_{j1}}$$

in the interval $-1 < \mathcal{F}_{\mathrm{j1}} < 1$. The upper part of figure 1 shows the same interval in the logarithmic representation. The Fundamental Field is topologically 3-dimensional, a fractal set of embedded spheric equipotential surfaces. The logarithmic potential difference defines a gradient directed to the center of the field that causes a central force of attraction. Because of the fractal logarithmic hyperbolic metric of the field, every equipotential surface is an attractor.

The Fundamental Field is of pure arithmetical origin, and there is no particular physical mechanism required as field source. It is all about transcendental ratios of frequencies [9] that inhibit destabilizing resonance. Therefore, we postulate the universality of the Fundamental Field that affects any type of physical interaction, regardless of its complexity.

In fact, scale relations in particle physics [11] and astrophysics [17] obey the same Fundamental Fractal (1), without any additional or particular settings. The proton-to-electron rest energy ratio approximates the first layer of the Fundamental Fractal that could explain their exceptional stability.

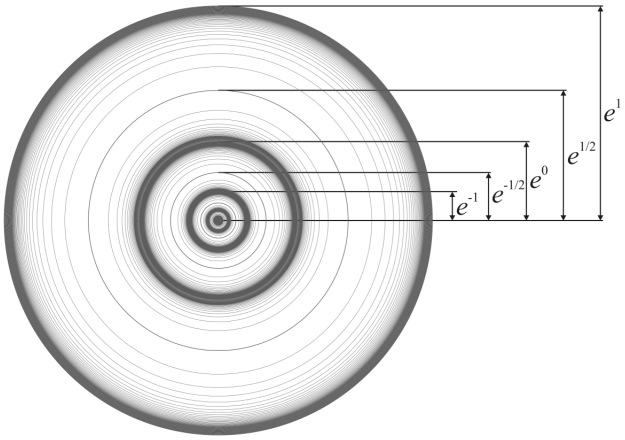

Fig. 2: The equipotential surfaces of the Fundamental Field in the linear 2D-projection for $k = 1$.

In fact, the life-spans of the proton and electron top everything that is measurable, exceeding 10^{29} years [18].

Property	Electron	Proton
$\mathrm{E} = \mathrm{mc}^2$	0.5109989461(31) MeV	938.2720813(58) MeV
$\omega = \mathrm{E}/\hbar$	$7.76344 \cdot 10^{20}$ Hz	$1.42549 \cdot 10^{24}$ Hz
$\tau = 1/\omega$	$1.28809 \cdot 10^{-21}$ s	$7.01515 \cdot 10^{-25}$ s
$\lambda = c/\omega$	$3.86159 \cdot 10^{-13}$ m	$2.10309 \cdot 10^{-16}$ m

Table 1: The basic set of the physical properties of the electron and proton. Data from Particle Data Group [18]. Frequencies, oscillation periods and wavelengths are calculated.

The proton-to-electron ratio (tab. 1) approximates the seventh power of Euler's number and its square root:

$$\ln\left(\frac{\lambda_e}{\lambda_p}\right) = \ln\left(\frac{3.86159 \cdot 10^{-13}\,\mathrm{m}}{2.10309 \cdot 10^{-16}\,\mathrm{m}}\right) \simeq 7 + \frac{1}{2} = \langle 7; 2 \rangle$$

In the consequence of this potential difference of the proton relative to the electron, the scaling factor $\sqrt{e} = 1.64872\ldots$ connects attractors of proton stability with similar attractors of electron stability in alternating sequence. The following Diophantine equation describes the correspondence of proton calibrated attractors n_p with electron calibrated attractors n_e. Non considering the signature, only three pairs (n_p, n_e) of integers are solutions to this equation: (3, 6), (4, 4), (6, 3).

$$\frac{1}{n_p} + \frac{1}{n_e} = \frac{1}{2}$$

Figure 3 demonstrates this situation on the first layer of the Fundamental Fractal (1). Both, the attractors of proton and electron stability are represented at the first layer, so we can see clearly that among the integer or half, only the attractors $\pm 1/3$, $\pm 1/4$ and $\pm 1/6$ are common. In these attractors, proton

stability is supported by electron stability and vice versa, so we expect that they are preferred in real systems.

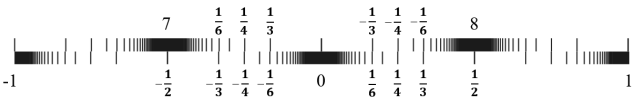

Fig. 3: The distribution of the attractors of proton (bottom) stability in the range $-1 < \mathcal{F} < 1$ of the attractors of electron (top) stability. Natural logarithmic representation.

These unique properties of the electron and proton predestinate their physical characteristics as fundamental units. Table 1 shows the basic set of electron and proton units that can be considered as a fundamental metrology (c is the speed of light in a vacuum, $\hbar$ is the Planck constant). In [12] was shown that the fundamental metrology (tab. 1) is completely compatible with Planck units [19]. Originally proposed in 1899 by Max Planck, these units are also known as natural units, because the origin of their definition comes only from properties of nature and not from any human construct. Max Planck wrote [20] that these units, "regardless of any particular bodies or substances, retain their importance for all times and for all cultures, including alien and non-human, and can therefore be called natural units of measurement". Planck units reflect the characteristics of space-time.

We assume that scale invariance according to the Fundamental Fractal (1), which is calibrated to the physical properties of the proton and the electron, is a universal characteristic of organized matter and criterion of stability. This hypothesis we have called *Global Scaling* [10].

In this paper we will show that the distribution of interstellar distances in the solar neighborhood corresponds with the distribution of attractors in the Fundamental Field.

Results

In [21] we applied the Fundamental Fractal (1) to macroscopic scales interpreting gravity as attractor effect of its stable eigenstates. Indeed, the orbital and rotational periods of planets, planetoids and large moons of the solar system correspond with attractors of electron and proton stability [12]. This is valid also for the planets [10] of the systems Trappist 1 and Kepler 20. Planetary and lunar orbits [17] correspond with equipotential surfaces of the Fundamental Field.

Figure 4 shows the distribution of the number of exoplanets with orbital periods in the range 5 d $< T <$ 24 d that corresponds with logarithms $59.2 < ln\,(T/2\pi\tau_e) < 60.8$ on the horizontal axis. According with table 1, τ_e is the electron angular oscillation period. The histogram contains data of 1430 exoplanets and shows clearly the maximum corresponding with the main attractor $\mathcal{F}\langle 60\rangle$. Other maxima correspond with the attractors $\mathcal{F}\langle 59; 2\rangle$ and $\mathcal{F}\langle 60; 2\rangle$; even the subattractors $\mathcal{F}\langle 60; -4\rangle$ and $\mathcal{F}\langle 60; 4\rangle$ can be distinguished.

The histogram evidences that the majority of the 1430 exoplanets [22] prefer orbital periods close to 10–11 days corresponding with the main attractor $\mathcal{F}\langle 60\rangle$, as well as periods close to 6–7 days or close to 17–18 days corresponding with the attractors $\mathcal{F}\langle 59; 2\rangle$ and $\mathcal{F}\langle 60; 2\rangle$. Because of the logarithm 7+1/2 of the proton-to-electron ratio, the attractors $\mathcal{F}\langle 59; 2\rangle$ and $\mathcal{F}\langle 60; 2\rangle$ of *electron* stability are actually the main attractors $\mathcal{F}\langle 67\rangle$ and $\mathcal{F}\langle 68\rangle$ of *proton* stability.

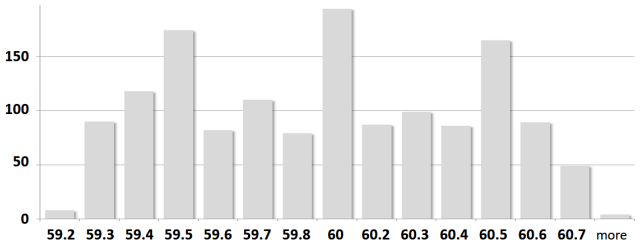

Fig. 4: The histogram shows the distribution of the number of exoplanets with orbital periods in the range 5 d $< T <$ 24 d. The logarithms ln $(T/2\pi\tau_e)$ are on the horizontal axis. Corresponding with table 1, τ_e is the electron angular oscillation period. Data of 1430 exoplanets are taken from [22].

Figure 5a shows the distribution of the number of stars as function of their distances R from the Sun up to 25 light-years that correspond with the logarithms $ln\,(R/\lambda_e) < 68.6$ on the horizontal axis. According with table 1, λ_e is the Compton wavelength of the electron. The histogram contains 192 distances and shows clearly the maxima corresponding with the attractors $\mathcal{F}\langle 67\rangle$, $\mathcal{F}\langle 67; 2\rangle$, $\mathcal{F}\langle 68\rangle$ and $\mathcal{F}\langle 68; 2\rangle$.

Knowing the right ascension, declination and distances of two stars from the Sun, it is not difficult to calculate the distance between them. In preparation of this paper, the mutual distances between the 192 best measured stars including Vega within a radius of 25 light-years around the Sun were calculated. The number of pairs of stars is given by the formula:

$$P = N(N-1)/2$$

where N is the number of stars; P is the number of pairs. For 192 stars, we calculated $P = 18,336$ interstellar distances.

Figure 5b shows the distribution of the number of stars as function of their distances R from Sirius up to 33 light-years. Also this histogram shows clearly the maxima corresponding with the attractors $\mathcal{F}\langle 67\rangle$, $\mathcal{F}\langle 67; 2\rangle$, $\mathcal{F}\langle 68\rangle$ and $\mathcal{F}\langle 68; 2\rangle$. The same $\mathcal{F}$-pattern appears in the histograms of interstellar distances measured from Barnard's star (fig. 5b), Tau Ceti (fig. 5d) and other stars in the 25-light-years solar neighborhood. Only the expression of the $\mathcal{F}$-pattern differs in strength.

Conclusion

Standard models expecting an exponential increase of the cumulative number of stars with the distance from a fixed reference point, perhaps could interpret the local maxima in the histograms as anomalies evidencing that the solar neighborhood is still in transformation. Within our approach, on the contrary, the coincidence of the maxima with attractors of the Fundamental Field evidences that the solar neighborhood has

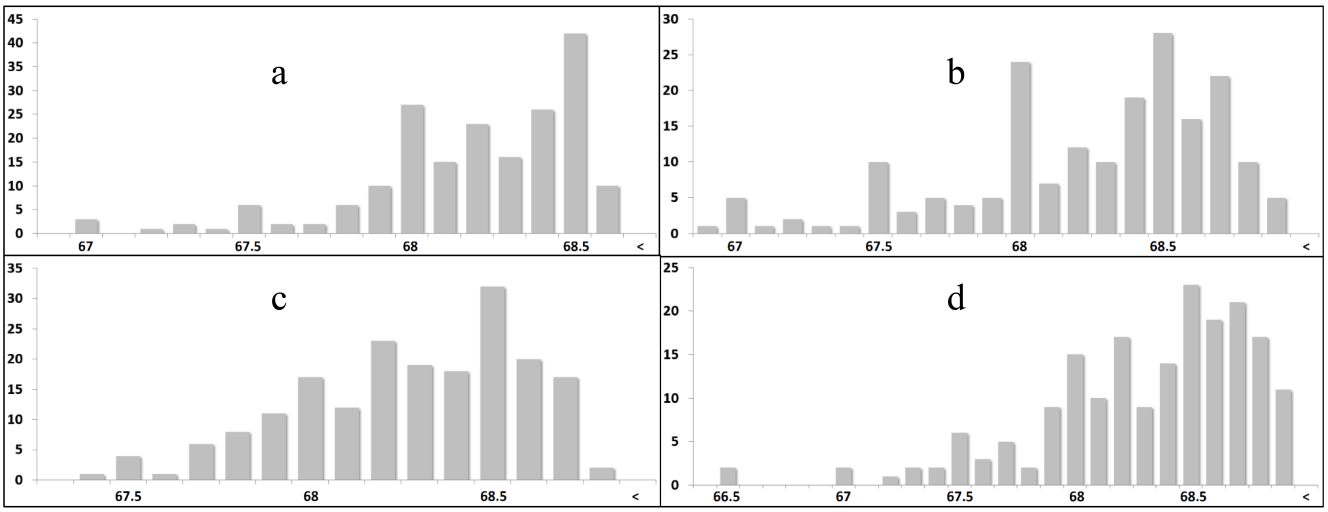

Fig. 5: The histogram shows the distribution of the number of stars in the solar neighborhood as function of their distances R from the Sun (a), Sirius (b), Barnard's star (c) and Tau Ceti (d). The logarithms ln (R/λ_e) are on the horizontal axis. Corresponding with table 1, λ_e is the Compton wavelength of the electron. Data of 192 stars are taken from [23].

already reached a certain level of stability. Moreover, we expect a continuous amplification of $\mathcal{F}$-patterns in histograms as trend of interstellar distances. Most likely, the appearance of patterns corresponding with the Fundamental Fractal (1) is a universal criterion of stability.

Since the Fundamental Fractal is of number theoretic origin, it determines the frequency distributions of interstellar distances as well as the wavelengths of elementary particles. Interscalar cosmology [10] bases on this approach.

Acknowledgements

The author is grateful to Simon Shnoll, Viktor Panchelyuga, Valery Kolombet, Oleg Kalinin, Viktor Bart, Michael Kauderer, Ulrike Granögger and Leili Khosravi for valuable discussions.

Submitted on August 27, 2021

References

1. Gliese W. Astronomisches Rechen-Institut Heidelberg Mitteilungen Serie A, 1957, v. 8, 1.
2. Gliese W., Jahreiß H. Preliminary Version of the Third Catalogue of Nearby Stars: The Astronomical Data Center CD-ROM. Selected Astronomical Catalogs, (1991).
3. Perryman M. A. C. The Hipparcos Catalogue. *Astron. Astrophys.*, 1997, v. 323, L49–L52.
4. Stauffer J. et al. *PASP*, 2010, v. 122, 885.
5. Skrutskie M. F. et al. *AJ*, 2006, v. 131, 1163.
6. Gaia Collaboration, Smart R. L. et al. Gaia Early Data Release 3: The Gaia Catalogue of Nearby Stars. arXiv:2012.02061v1 [astro-ph.SR] 3 Dec 2020.
7. Müller H. On the Cosmological Significance of Euler's Number. *Progress in Physics*, 2019, v. 15, 17–21.
8. Dombrowski K. Rational Numbers Distribution and Resonance. *Progress in Physics*, 2005, v. 1, no. 1, 65–67.
9. Müller H. The Physics of Transcendental Numbers. *Progress in Physics*, 2019, v. 15, 148–155.
10. Müller H. Global Scaling. The Fundamentals of Interscalar Cosmology. *New Heritage Publishers*, Brooklyn, New York, USA, ISBN 978-0-9981894-0-6, (2018).
11. Müller H. Fractal Scaling Models of Natural Oscillations in Chain Systems and the Mass Distribution of Particles. *Progress in Physics*, 2010, v. 6, 61–66.
12. Müller H. Scale-Invariant Models of Natural Oscillations in Chain Systems and their Cosmological Significance. *Progress in Physics*, 2017, v. 13, 187–197.
13. Khintchine A.Ya. Continued fractions. University of Chicago Press, Chicago, (1964).
14. Hilbert D. Über die Transcendenz der Zahlen e und π. *Mathematische Annalen*, 1893, v. 43, 216–219.
15. Panchelyuga V.A., Panchelyuga M. S. Resonance and Fractals on the Real Numbers Set. *Progress in Physics*, 2012, v. 8, no. 4, 48–53.
16. Müller H. Quantum Gravity Aspects of Global Scaling and the Seismic Profile of the Earth. *Progress in Physics*, 2018, vol. 14, 41–45.
17. Müller H. Global Scaling of Planetary Systems. *Progress in Physics*, 2018, v. 14, 99–105.
18. Tanabashi M. et al. (Particle Data Group), Phys. Rev. D 98, 030001 (2018), www.pdg.lbl.gov
19. Astrophysical constants. Particle Data Group, pdg.lbl.gov
20. Planck M. Über Irreversible Strahlungsvorgänge. *Sitzungsbericht der Königlich Preußischen Akademie der Wissenschaften*, 1899, v. 1, 479–480.
21. Müller H. Gravity as Attractor Effect of Stability Nodes in Chain Systems of Harmonic Quantum Oscillators. *Progress in Physics*, 2018, v. 14, 19–23.
22. Catalog of Exoplanets. Observatoire de Paris, http://exoplanet.eu/
23. Gaia EDR3, https://www.cosmos.esa.int/web/gaia/earlydr3

A Solution to the Pioneer Anomalous Annual and Diurnal Residuals

Eduardo D. Greaves[1], Carlos Bracho[2], Stephan Gift[3], and An Michel Rodriguez[4]

[1]Universidad Simón Bolívar. Apartado 89000, Caracas, Venezuela. E-mail: egreaves20002000@yahoo.com
[2]Facultad de Ingeniería, Universidad Central de Venezuela, Caracas, Venezuela. E-mail: bracho_carlos@hotmail.com
[3]Department of Electrical and Computer Engineering, Faculty of Engineering, The University of the West Indies, St Augustine, Trinidad and Tobago, West Indies. E-mail: stephan.gift@sta.uwi.edu
[4]Universidad Simón Bolívar. Apartado 89000, Caracas, Venezuela. E-mail: anmichel.rodriguez@gmail.com

NASA's reported Pioneer 10 and 11 anomalous annual and diurnal Doppler residuals remain largely unexplained. We show they are due to the use of an invariant value of the speed of light c in the Doppler formula. The addition of the orbital speed of the Earth ($\sim 30\,\mathrm{km/s}$) and the Earth's tangential rotational speed ($\sim 0.4\,\mathrm{km/s}$) to the speed of light in the Doppler formula, as [18] has shown to be the velocity addition to be used, adequately fit the measured annual and diurnal Pioneer residuals. This experimentally confirms that the galilean addition of relative velocities to the speed of light satisfactorily explains the measured residuals. The newly reported values from independent analyses of the data, of the reputably constant anomalous Pioneer acceleration as a function of time, or distance from the Sun, are calculated. The values obtained, without any adjustable parameters, coincide within a percent with the experimentally measured values and are consistent with the change of the speed of light due to a decrease in the gravitational energy density with distance from the Sun as postulated by the Céspedes-Curé hypothesis. This result implies reassessment of all astronomical velocity measurements based on the Doppler Effect that have led to current cosmological theories: the Hubble constant, the expansion of the universe, the flat rotation curve of galaxies and the extreme values of the redshifts of very far away galaxies.

1 Introduction

Most of the physics related to astronomy and cosmology had been in the past based on passive astronomical observation of the measurements used to derive the theories. This is the case for Isaac Newton who derived his universal theory of gravitation from Johannes Kepler, who in turn used his own and the detailed observations of Tycho Brahe to develop his laws of planetary motion. Likewise, observations of the total Sun eclipse of 1919 by the team led by Arthur Stanley Eddington provided the first evidence in support of Einstein's General Theory of Relativity

In recent times, observational instruments have become increasingly powerful expanding visual telescopes to other ranges of the electromagnetic spectrum such as to the lower region, and to the higher regions with the radio telescopes and the x-ray and gamma ray observational satellites. These instruments have expanded our vision to ever further regions of the past history of the Universe. Moreover, with the advent of space exploration with Earth satellites and the launch of deep space probes, astronomy and cosmology now routinely utilize experimental probes to examine, refine, support or create physical theories of the cosmos. With the introduction of digital processing, computing power, extremely precise timing and the development of very high frequency electronics, accurate observations have increased to previously unforeseen ranges.

One such case is the measurement by the space agencies of extremely small phenomena that have shown minute but significant deviations from the values predicted by accepted physical theories and that have defied for lengths of time satisfactory explanation. Two examples are deviations from the predicted hyperbolic movement of space probes: the Flyby Anomaly [1, 2] and the Pioneer Anomaly [3–5]. In the Flyby Anomaly, the energy assist maneuver about the planets has been shown in several probes to deviate from the expected energy conservation prediction. In this case, speed deviations of mm/s reported are detected with errors of 10^{-2} mm/s on probes moving at speeds of several km/s.

The Pioneer Anomaly measurements of the hyperbolic movement of Pioneer 10 and 11 as well as Ulysses and Galileo have shown a minute acceleration in excess of the expected slowing towards the Sun due to its gravitational attraction. The deviations are of the order of 10^{-8}. The realization of these measurements is an extraordinary accomplishment considering that the probes are located far away in the solar system, moving at velocities in the range of several km/s. The anomalous measurements are reported with an accuracy of $\sigma_{at} = 0.32 \times 10^{-10}\,\mathrm{m/s^2}$ [5].

In addition to the assumed constant anomalous acceleration, Pioneer's Doppler residual measurements have shown annual and diurnal oscillations about the average acceleration with amplitude of about $0.8 \times 10^{-9}\,\mathrm{m/s^2}$ (see Fig. 4). The magnitudes of the diurnal terms are reported to be comparable to those of the annual term. These results have been the subject of considerable discussion in the published literature: Anderson *et al* in 2002 [3, p. 40–43] concluded that they are

not spacecraft-related phenomena nor artifacts of the measuring system but that they are Earth-related phenomena. In particular, the diurnal Doppler residuals exhibit a period that is close to the Earth's sidereal period.

Nieto and Anderson in 2005 [6] reported, in a very clear review, sinusoidal fits to the annual residuals showing similar values for Pioneer 10 and 11 and a phase difference of 173.2 degrees, similar to the angular separation of the two spacecrafts in ecliptic longitude.

There have been other attempts to explain the periodic anomalies. O. Olsen in 2007 [7] stated that unmodeled short-term effects are claimed to be consistent with expected values of radio plasma delay and the electron content of the Sun's Coronal Mass Ejections. Small annual and diurnal terms are considered to be artifacts of the maneuver estimation algorithm and unmodeled effects.

A. Ghosh in 2007 [8] attempted to explain these fluctuating components as due to the motions of the Earth and excess redshifts of the signal caused by velocity dependent inertial induction. He appears to be able to explain the annual and diurnal fluctuations in the anomalous acceleration of Pioneer 10.

Levi *et al* in 2009 [9] performed a data analysis independent of that of Anderson *et al* (2002), using the same data and confirming the existence of a secular anomaly. This anomaly has amplitude of about 0.8×10^{-9} m/s^2 that is compatible with that reported by Anderson *et al*. Their fit to the diurnal residuals showed the presence of significant periodic terms with the periods measured with respect to a day of 86 400 s. They reported, very accurately, periodic terms consistent with variations of one sidereal day, half a sidereal day, and half a year.

A later report on the Pioneer Anomaly by Turyshev and Toth in 2010 [5, Sec. 5.5.4, p. 86] acknowledged the presence of these oscillatory Doppler residuals ascribing them to "a mismodeling of the orbital inclination of the spacecraft to the ecliptic plane". However, in Section "7.2 Unresolved questions", it is mentioned that "Even after a best fit analysis is completed, the resulting residual is not completely random: both annual and diurnal variations are clearly visible. Is it possible to pinpoint the source of these variations?".

The current opinion (2021) that the Pioneer Anomaly was resolved as a thermal effect rests on a paper by S. G. Turyshev *et al* (2012) [10] which does a complex parametrized model for the thermal recoil force of the Pioneer spacecraft with several adjustable parameters. In particular the two adjustable parameters of Eq. (1) on page 2 predict the anomaly. However, any other parameters would negate the thermal origin of the anomaly.

Other reports that also support the thermal origin are: Rievers and Lammerzahl (2011) [12] and Francisco *et al* (2012) [13]. However, the detailed paper about the Pioneer Anomaly (55 pages of Phys. Rev. by J. D. Anderson *et al* (2002) [3]) clearly argues (see Sections VIII.B, C and D, pp. 32–35) that thermal recoil cannot account for the anomaly. Additionally, an anomaly similar to the Pioneer spacecraft was detected in Galileo spacecraft (see Section V C, p. 21) [3] and in the Ulysses spacecraft (see Section V D, p. 21) [3]. Both spacecrafts have completely different geometries and the thermal recoil theory is not applicable to them. Furthermore, the anomalous acceleration is reported to change value, decreasing rapidly and then increasing, (see discussions below, Sections 2.2 and 5.3 and references therein) during the spacecrafts' Jupiter and Saturn encounters. These reported changes of the anomaly as well as the harmonic annual and diurnal variations clearly cannot be explained by a thermal recoil theory.

More recently, L. Bilbao in 2016 [11], making use of the Vibrating Rays Theory [14], claims that relating the velocity of light and the corresponding Doppler effect with the velocity of the source at the time of detection, instead of the time of emission, it is possible to explain quantitatively and qualitatively the spacecraft anomalies. Values calculated for the annual residual approximately coincide with reported measurements for Pioneer 10 at 40 AU, $\Delta f \approx 14$ mHz and for Pioneer 11 at 69 AU, $\Delta f \approx 4.8$ mHz [11, p 310]. However, on the same arguments, the theory would predict values 5 or 6 orders of magnitude smaller than reported for the diurnal Doppler residuals measurements.

In this paper, an explanation of the constant term of the Pioneer Anomaly by Greaves in 2008 [4, 15] is reviewed with updated results and a new explanation of the oscillatory nature of the annual and diurnal Doppler residuals is presented. Both explanations are in agreement with the galilean velocity addition. The harmonic fluctuations make use of the results of analysis by Gift in 2010 of the Doppler Effect [16], in 2014 [17] and in 2017 of the Global Positioning System (GPS) [18].

2 Pioneer anomaly reported values

In order to compare the theoretical predictions with the reported values, in this section we review the literature with special emphasis on the particular phenomena pertinent to the theory presented about the anomalous acceleration values. In the light of the results below that imply different values depending on distances from the Sun and hence at the various measurement times, we do not find it surprising that a variety of values are reported.

The Pioneer Anomaly is the result of a complicated modeling procedure involving the gravitational physics predicting the probe trajectory, newtonian and relativistic, as well as a cornucopia of other phenomena such as solar radiation pressure and electromagnetic line of sight effects. The result of the modeling is compared to the measured Doppler signals received and processed by the Deep Space Network (DSN) by means of mathematical least squares fitting procedures. While there may be several possible onboard causes of anomalous results such as gas leaks or the now popular

effect of asymmetric thermal radiation pressure, the different programs that have been developed generally agree on the existence of an anomaly.

We start by citing the anomalous measurements of the Galileo and Ulysses spacecrafts given by Anderson *et al* (2002) [3, p. 22, Eq. (18)]. Unfortunately, not many details are given for these anomalous measurements.

2.1 Galileo

The reported JPL values of Aerospace's analysis for the dates 2 December 1992 to 24 March 1993 give an anomalous acceleration of $a_{P(G)} = (8 \pm 3) \times 10^{-8}\,\mathrm{cm/s^2}$.

Galileo performed a second flyby of Earth at 303.1 km height at 15:09:25 UTC on 8 December 1992, adding 13,320 km/h to its cumulative speed on the way to Jupiter. Hence the reported Galileo $a_{P(G)}$ is just on or after the Earth flyby at approx. 1 AU distance from the Sun, and under full Earth and Sun gravitational acceleration field [19].

2.2 Ulysses

The JPL analysis gives $a_{P(U)} = (12 \pm 3) \times 10^{-8}\,\mathrm{cm/s^2}$. The data is from 30 March 1992 to 11 August 1994. Ulysses arrived at Jupiter on 8 February 1992 for a flyby maneuver that increased its inclination to the ecliptic by 80.2 degrees southward, away from the ecliptic plane entering an orbit around the Sun. The orbital period is approximately six years. The Sun's gravitational acceleration at the Jupiter orbit is $g_S = 2.1 \times 10^{-4}\,\mathrm{m/s^2}$, four orders of magnitude smaller than Jupiter's $g_j = 0.227\,\mathrm{m/s^2}$ gravitational acceleration at the nearest point in the flyby (4.09×10^8 m). The flyby was engineered to bring Ulysses into a Sun elliptical orbit, so that after the flyby Ulysses began movement towards the Sun with the resulting gravitational acceleration $\vec{g}_U = \vec{g}_S + \vec{g}_j$ pointing generally towards Jupiter for some time until the distance to the Sun was ≈ 5 AU. Thereafter Ulysses acceleration $\vec{g}_U$ points generally towards the Sun. Aerospace's analysis using CHASMP reports no numerical value due to measurement difficulties. However, it is stated: "The measured anomalies randomly changes sign and magnitude. The values go up to about an order of magnitude larger than a_P" [3, p 22]. This measurement and remark of Ulysses' anomalous acceleration is when the spacecraft was under Jupiter gravitational attraction just after the flyby and hence with net gravitational acceleration towards Jupiter and sometime later towards the Sun.

2.3 Pioneer 10 and 11

Table 1 of Anderson *et al* (2002) [3, p 23] reproduced below, with its original caption, gives an indication of the variability of reported values. The original data analyzed is for the following periods:

Pioneer 10: 11 years time interval (3 January 1987 to 22 July 1998), covers a heliocentric distance interval from 40 AU to 70.5 AU.

Program/Estimation method	Pio 10 (I)	Pio 10 (II)	Pio 10 (III)	Pio 11
Sigma, WLS, no solar corona model	8.02 ± 0.01	8.65 ± 0.01	7.83 ± 0.01	8.46 ± 0.04
Sigma, WLS, with solar corona model	8.00 ± 0.01	8.66 ± 0.01	7.84 ± 0.01	8.44 ± 0.04
Sigma, BSF, 1-day batch, with solar corona model	7.82 ± 0.29	8.16 ± 0.40	7.59 ± 0.22	8.49 ± 0.33
CHASMP, WLS, no solar corona model	8.25 ± 0.02	8.86 ± 0.02	7.85 ± 0.01	8.71 ± 0.03
CHASMP, WLS, with solar corona model	8.22 ± 0.02	8.89 ± 0.02	7.92 ± 0.01	8.69 ± 0.03
CHASMP, WLS, with corona, weighting, and F10.7	8.25 ± 0.03	8.90 ± 0.03	7.91 ± 0.01	8.91 ± 0.04

Table 1: Determinations of a_P in units of $10^{-8}\mathrm{cm/s^2}$ from the three time intervals of Pioneer 10 data and from Pioneer 11. As described in the text, [our Ref. 3] results from various ODP-Sigma and CHASMP calculations are listed. For ODP-Sigma, "WLS" signifies a weighted least-squares calculation, which was used with i) no solar corona model and ii) the 'Cassini' solar corona model. Also for ODP/Sigma, "BSF" signifies a batch-sequential filter calculation, which was done with iii) the 'Cassini' solar corona model. Further (see Section IX C), a 1-day batch-sequential estimation for the entire data interval of 11.5 years for Pioneer 10 yielded a result $a_P = (7.77 \pm 0.16) \times 10^{-8}\,\mathrm{cm/s^2}$. The CHASMP calculations were all WLS. These calculations were done with i) no solar corona model, ii) the 'Cassini' solar corona model, iii) the 'Cassini' solar corona model with corona data weighting and F10.7 time variation calibration. Note that the errors given are only formal calculational errors. The much larger deviations of the results from each other indicate the sizes of the systematics that are involved. (Acronyms are: ODP - JPL's Orbit Determination Program; CHASMP - Aerospace Corporation's Compact High Accuracy Satellite Motion Program.)

Pioneer 11: data of 3 years (5 January 1987 to 1 October 1990), covers a heliocentric distance interval much closer to the Sun, from 22.42 to 31.7 AU.

Additionally, Anderson *et al* (2002) [3, on p. 27] quote: "For Pioneer 10, two different analysis programs: Sigma and CHASMP (*measurements*) are similar, $7.82 \times 10^{-8}\,\mathrm{cm/s^2}$ and $7.89 \times 10^{-8}\,\mathrm{cm/s^2}$, the weighted average of these two to yield $a_{Pio10} = (7.84 \pm 0.01) \times 10^{-8}\,\mathrm{cm/s^2}$ (experimental).

"For Pioneer 11, we only have the one 3 3/4 year data arc. The weighted average of the two programs' no corona results is $(8.62 \pm 0.02) \times 10^{-8}\,\mathrm{cm/s^2}$."

2.3.1 Information of planetary encounters

The Pioneer 10 original data spans heliocentric distance interval from 40 AU to 70.5 AU, as mentioned above. Hence it does not include the Jupiter flyby at 5.2027 AU on 1974.

Pioneer 11's original data covers a heliocentric distance interval from 5.80 to 29.50 AU. It includes just after the Jupiter flyby at 5.2027 AU and the Saturn encounter at 9.546 AU on 1979. Also near encounter with Uranus at 19.2 AU on approx. 1986 and with Neptune at 30.09 AU on approx. 1990. Moreover, a report in 2005 of Nieto and Anderson [6] pro-

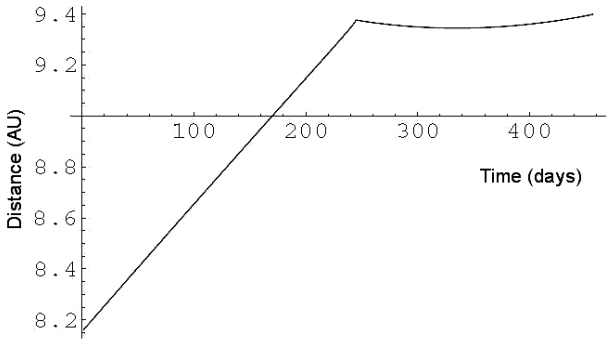

Fig. 1: "A plot of Pioneer 11's distance from the Sun (in AU) vs time (in days starting with 1 Jan. 1979) near Saturn encounter (on Sept. 1, 1979)" [6, p 14]. *Captions of axes added.*

vides additional insight to the planetary encounters and the harmonic residuals. They report that the initial two points in the Pioneer 11 anomalous acceleration shown in their Figures 4 and 5 (our Fig. 2) were near the distances of Jupiter and Saturn encounters. They provide a figure showing the distance (AU) as a function of time (in days) around the Saturn flyby of Pioneer 11. See Fig. 1 with its original caption.

We find this figure very illuminating as at these times the spacecraft was under the gravitational attraction of Saturn and perhaps also under the influence of its higher space energy density as discussed below.

Regarding the annual residuals, Nieto *et al* [6] mention on p. 14:

> Plots of the anomaly versus time were also made from these data points. These showed, as might be suspected from Figures 4 and 5, [our Fig. 2] a possible annual variation. This observation would be a forerunner of the discussion in Section IX-C of [12], [our Ref. [3]]. Doing fits to the data points, the best estimate of the amplitude of the Pioneer 10 sine wave is $(0.525 \pm 0.155) \times 10^{-8}$ cm/s^2 and that of the Pioneer 11 wave is $(0.498 \pm 0.176) \times 10^{-8}$ cm/s^2 (here with the first three points omitted). The sine waves seem real, with, e.g. a 95 percent probability that the Pioneer 10 amplitude lies between 0.199 and 0.834×10^{-8} cm/s^2. The difference in phase between the Pioneer 10 and Pioneer 11 waves is 173.2 degrees, similar to the angular separation of the two spacecrafts in ecliptic longitude. [This is 204.28 degrees at the present time.]

Useful information is provided in Table II which contains the numerical data for each spacecraft containing the distance, dates, reported anomalous acceleration a_P and the error ΔP. Using this information, we find it helpful to plot the reported dates and distances (see Fig. 3) as this information allows the determination of the distance or dates of reported a_P when the information is not given.

Craft	Distance	Dates	a_P	σ_P
Pioneer 11	5.80	77/270-1	0.69	1.48
(Saturn Encounter)	9.38	79/244		
	9.39	80/66-78	1.56	6.85
	12.16	82/190-1	6.28	1.77
	14.00	83/159	8.05	2.16
	16.83	84/254	8.15	0.75
	18.90	85/207	9.03	0.41
	22.25	86/344-5	8.13	0.69
	23.30	87/135-6	8.98	0.30
	26.60	88/256-7	8.56	0.15
	29.50	89/316-7	8.33	0.30
Pioneer 10	26.36	82/19	8.68	0.50
	28.88	82/347-8	8.88	0.27
	31.64	83/346	8.59	0.32
	34.34	84/338-9	8.43	0.55
	35.58	85/138	7.67	0.23
	37.33	86/6-7	8.43	0.37
	40.59	87/80	7.45	0.46
	43.20	88/68	8.09	0.20
	45.70	89/42-3	8.24	0.20

Table 2: Pioneer 11 and 10 early data points (Distance in AU, Date year/days-of-year, anomaly a_P and error σ_P in units of 10^{-8} cm/s^2 from [6].

Toth and Turyshev in 2007 [20, p. 15] comment results found during the Jupiter–Saturn cruise phase: "Right at the time of the Saturn encounter, however, when the spacecraft passed into an hyperbolic escape orbit, *there was a rapid increase in the anomaly, whereafter it settled into the canonical value*" [our emphasis].

2.3.2 Independent analysis of Pioneer data

There have been several further independent analyses of the original data which were made available since 2002 and are reviewed below.

C. Markwardt (2002) [21] performed an independent analysis of radio Doppler tracking data from the Pioneer 10 spacecraft for the time period 1987–1994. His best-fit value for the acceleration, including corrections for systematic biases and uncertainties, is $(8.60 \pm 1.34) \times 10^{-8}$ cm/s^2, directed towards the Sun.

O. Olsen (2007) [7] does an independent analysis of the Pioneer 10 and 11 data using the HELIOSAT program developed by one of the authors at the University of Oslo. The data used spans the three periods defined by Anderson *et al* (2002) for Pioneer 10: Interval I spans 1 January 1987 to 17 July 17 1990, Interval II spans 17 July 1990 to 12 July 12 1992 and Interval III continues up to 21 July 1998. The anomalous accelerations ($\times 10^{-8}$ cm/s^2) obtained are given in his Table I from which we extract: Pioneer 10: Interval I = 7.85 ± 0.02;

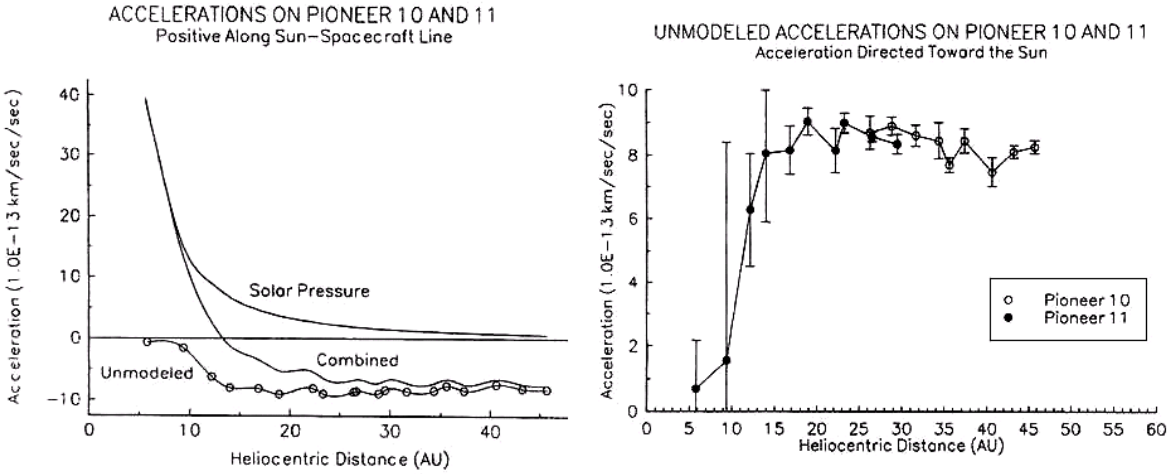

Fig. 2: Left: Accelerations on the Pioneer spacecraft. Right: Anomalous acceleration as a function of distance [3, p. 19].

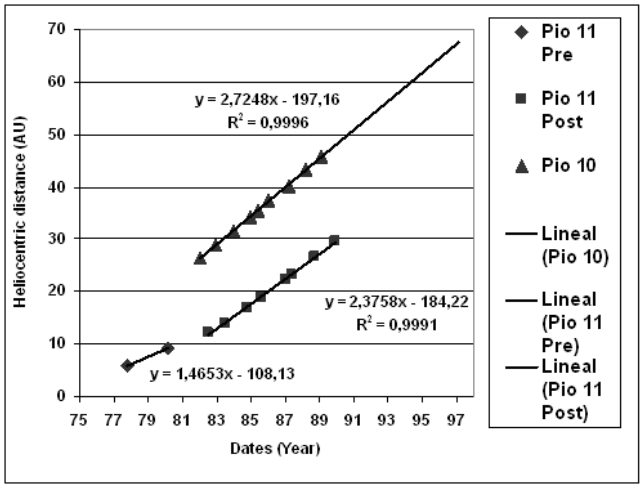

Fig. 3: Heliocentric distance (AU) as a function of dates (year) for Pioneer 10 and 11 positions. Lines are linear fits. For Pioneer 11 pre and post Jupiter flyby. (Data from Table II.)

Interval II = 8.78 ± 0.01; Interval III = 7.75 ± 0.01; Pioneer 11 = 8.10 ± 0.01. From the paper's conclusions: "The unmodeled short term effects are claimed to be consistent with expected values of radio plasma delay and the electron content of Coronal Mass Ejections. Small annual and diurnal terms are ascribed as artifacts of the maneuver estimation algorithm and unmodeled effects acting on the spacecraft or on the radio transmissions."

V. T. Toth does an independent analysis of the orbit of the Pioneer spacecrafts reporting in 2009 [22, p. 18] for Pioneer 10* $a_{P10} = (9.03 \pm 0.86) \times 10^{-8}\,\mathrm{cm/s^2}$ (period 1987 to 1998) and for Pioneer 11 $a_{P11} = (8.21 \pm 1.07) \times 10^{-8}\,\mathrm{cm/s^2}$ (period 1986 to August 1990). Toth also attempted in his analysis to test the extent to which the anomalous acceleration is constant in time. To this end, he implemented the ability to estimate a secondary acceleration, i.e. "jerk" term in the orbital solution.

The results obtained were: for Pioneer 10, $a_{P10} = (10.96 \pm 0.89) \times 10^{-8}\,\mathrm{cm/s^2}$ [3, p. 20], with a variation rate of $da_{P10}/dt = -(0.21 \pm 0.04) \times 10^{-6}\,\mathrm{cm/s^2/year}$ and for Pioneer 11, the result was $a_{P11} = (9.40 \pm 1.12) \times 10^{-8}\,\mathrm{cm/s^2}$, with a variation rate of $da_{P11}/dt = -(0.34 \pm 0.12) \times 10^{-8}\,\mathrm{cm/s^2/year}$. Toth goes on to state: "an anomalous acceleration that is a slowly changing function of time (*decreasing*) cannot be excluded at present" [our italics].

Levi *et al* in 2009 [23] performed a data analysis independent from that of Anderson *et al* (2002) using the same Pioneer 10 data confirming the existence of a secular anomaly with an amplitude of about $8 \times 10^{-8}\,\mathrm{cm/s^2}$ compatible with that reported by Anderson *et al* (2002) and providing additional insight into the phenomenon.

2.4 Annual and diurnal Doppler residuals

The first indication of the oscillatory nature of the Pioneer Anomaly came from an examination of the data in Fig. 2. The observations are addressed in detail in Anderson *et al* (2002) [3, pp. 40-41]. From that report, we show Figs. 4, 5 and 6.

Levi *et al* in 2009 [9], performed an important and illuminating independent analysis of the diurnal periodic terms during a short time span of (we quote): "23 November 1996 to

*Toth and Levi *et al* express all values in SI units. We have converted accelerations to $\mathrm{cm/s^2}$ as used in most Pioneer reports.

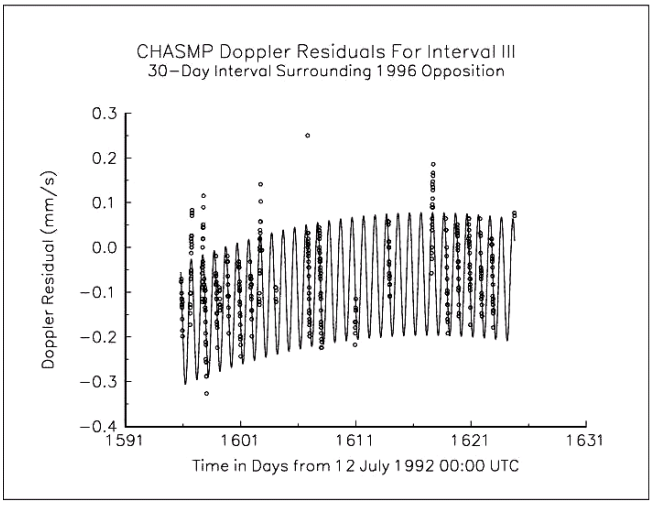

Fig. 4: Diurnal residuals. "CHASMP acceleration residuals from 23 November 1996 to 23 December 1996" [3, Fig. 18, p. 41].

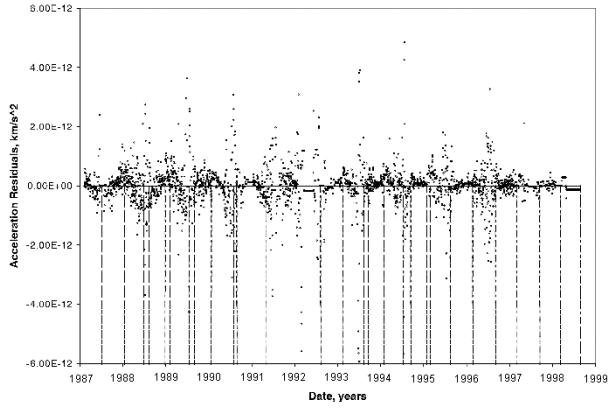

Fig. 5: Annual residuals. "ODP 1-day batch-sequential acceleration residuals using the entire Pioneer 10 data set. Maneuver times are indicated by the vertical dashed lines". [3, Fig. 17, p. 40].

23 December 1996 when Pioneer 10 was on opposition (Sun, Earth and Pioneer 10 aligned in this order). This data set is thus less affected by solar plasma and it shows daily variations of the residuals". The analysis of residuals shows the presence of significant diurnal periodic terms with the periods measured with respect to a day = 86 400 s. Their spectral analysis of the periodic terms yields the following measured periods: T1 = 0.9974 ± 0.0004 day, T2 = (1/2)(0.9972 ± 0.0004) day and T3 = 189 ± 32 days. "As T = 0.997 day = 1.0 sidereal day, these periods are consistent, (*within 0.02 percent*), with variations of one sidereal day, half a sidereal day, and half a year." (Year/2 = 182.5 days) [Our italics]. These results clearly indicate that the periodic terms in the Doppler residuals are not produced by on-board phenomena or due to solar corona affecting transmission signals, but rather that

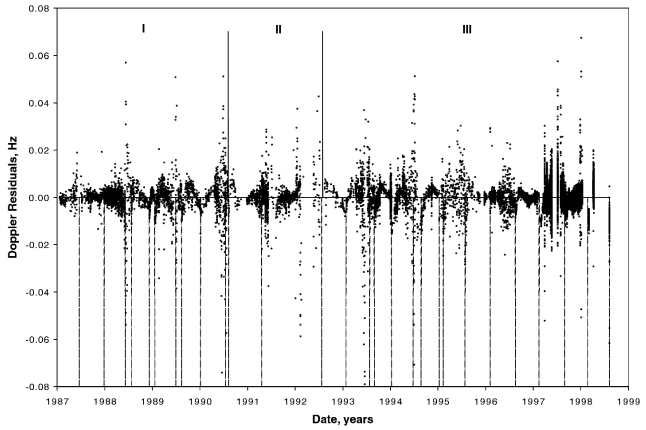

Fig. 6: "ODP Doppler residuals in Hz for the entire Pioneer 10 data span. The two solid vertical lines in the upper part of the plot indicate the boundaries between data Intervals I/II and II/III, respectively. Maneuver times are indicated by the vertical dashed lines in the lower part of the plot." [3, Fig. 13, p. 25].

they are intimately related to Earth movement relative to the Pioneer position in the sky. To illustrate their results we reproduce below (Fig. 7) a section of Figure 3 in that report.

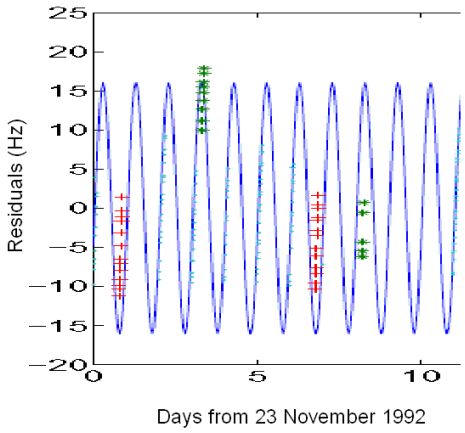

Fig. 7: Fitted residuals of the Doppler tracking data of Pioneer 10, for a 10-day period near opposition. Different symbols or colors refer to different couples of receiving stations [6, expanded section of Figure 3, p. 6]

All of the reports shown above use the original data and do not include the early stage of the Pioneer missions. It has been stated in several reports [6, 20, 24] the convenience to recover and analyze the data from the beginning of the missions. A very commendable effort has been made to recover the earlier data, which after considerable effort, has been secured in modern digital media. A detailed report of this contribution is found in [22, p. 4]. However, to our knowledge, the required detailed analysis of the earlier stages has not been

reported.

At the present times, Pioneer 10 is in the constellation of Taurus. The current Right Ascension of Pioneer 10 is 05h 16m 17s and the Declination is $+26^{\circ}02'40''$. Pioneer 11 is currently in the constellation of Scutum. The current Right Ascension of Pioneer 11 is 18h 53m 32s and the Declination is $-08^{\circ}42'43''$ [25].

3 Pioneer anomaly "constant" term

In this section, we review the theory of the calculation of the Pioneer 10 and 11 anomalous "constant" term. We start with the statement of the Céspedes-Curé Hypothesis [26, p. 279], [4, 27–29] Eq. (1): The speed of light on Earth's surface at 1 AU (S Sun, E Earth) is given by

$$c = \frac{k}{\sqrt{\rho}} = \frac{k}{\sqrt{\rho^* + \rho_S + \rho_E}} \tag{1}$$

where k is a proportionality constant and ρ the energy density in $\mathrm{J/m^3}$ on the surface of the Earth which is a sum of the contribution of the constant energy density due to far away stars and galaxies ρ^* and the constant values due to the Sun ρ_S and Earth ρ_E given by (2) below. Calculation shows that the contribution of the Moon and other planets are negligible.

The energy density of a mass [26, p. 163], [2, Eq. (2), p. 50], [4] is given by

$$\rho = \frac{GM^2}{8\pi r^4} \tag{2}$$

where G is Newton's gravitational constant, M is the mass and r is the distance from the mass center. Eq. (2) shows the energy density of a mass decreases very rapidly due to the r exponent of 4 in the denominator.

The speed of light far away from Earth and the Sun, at Pioneer's position, is given by

$$c' = \frac{k}{\sqrt{\rho'_{far}}}\,. \tag{3}$$

Here ρ'_{far} is the energy density at the site of Pioneer. In (3), ρ'_{far} contains a sum of the gravitational energy density of the far away stars and galaxies ρ^*, the Sun's and the energy density of other planets, which are relatively near in the spacecraft's trajectory towards outer space. These include the Earth in the very early stage of the mission and any planets during flyby or relative close approach, which includes the Jupiter flyby, the Saturn flyby and possibly near encounters to other planets. Hence

$$\rho'_{far} = \rho^* + \frac{G}{8\pi}\sum_{i=1}^{n}\frac{M_i^2}{r_i^4}\,. \tag{4}$$

Figs. 8 and 9 shown below give an indication of these encounters. A close look at these figures clearly shows that the gravitational energy density and gravitational acceleration along the trajectory of Pioneer 10 and 11 are different predicting different values of the anomalous acceleration as is reported.

The index of refraction of space, relative to the vacuum index on Earth, at Pioneer's position is obtained using (1) and (3):

$$n' = \frac{c}{c'} = \frac{\sqrt{\rho'_{far}}}{\sqrt{\rho}}\,, \tag{5}$$

so that the speed of light far away is:

$$c' = c\,\frac{\sqrt{\rho}}{\sqrt{\rho'_{far}}}\,. \tag{6}$$

Eq. (6) implies that c' is *greater* than c and increases with distance as ρ'_{far} decreases with distance. However, c' becomes almost constant when Pioneer goes past the planets and their energy density becomes negligible. The Sun's contribution continues to decrease leaving ρ^*, the constant energy density of far away stars and galaxies

Spacecraft velocity and accelerations are measured basically with the Doppler formula $\Delta f = f\,(v/c)$ where f would be a spacecraft-generated signal. However, Pioneer spacecraft did not have an accurate oscillator onboard. Communication uplink from Earth is at $\sim$ 2.11GHz. The spacecraft's coherently received signal is accurately multiplied by the (240/221) ratio and signals beamed at approximate downlink frequency 2.295 GHz. The signals are sent and received by the Deep Space Network (DSN) and processed in the manner described in detail by Anderson *et al* [3, pp. 7–12]. In this manner, the observable is a very precise Doppler shifted frequency $\Delta f = (f/c)(dl/dt)$ [3, p. 9, Eq. (1)], where l is the overall optical distance. In our notation $v = (dl/dt)$ so that the spacecraft speed is obtained with:

$$\vec{v} = \frac{c\Delta f}{f}\,\frac{\vec{r}}{|r|}\,. \tag{7a}$$

Differentiating (7a) with respect to time, the measured spacecraft acceleration is

$$\vec{a}_{JPL} = \frac{d\Delta f}{dt}\,\frac{c}{f}\,\frac{\vec{r}}{|r|}\,. \tag{7b}$$

Here Δf is the shift of the frequency f and $\dfrac{d\Delta f}{dt}$ the measured drift of the frequency due to the Pioneer acceleration produced by gravitation at the spacecraft site, mainly due to the Sun. $\vec{a}_{JPL}$ is a derived acceleration vector in the direction of the gravitational force causing it. Examination of (7a) and (7b) shows that, if the velocity of light c is not invariant but rather given by (6) as proposed in this work, measurement of velocity and acceleration in locations of space with lower

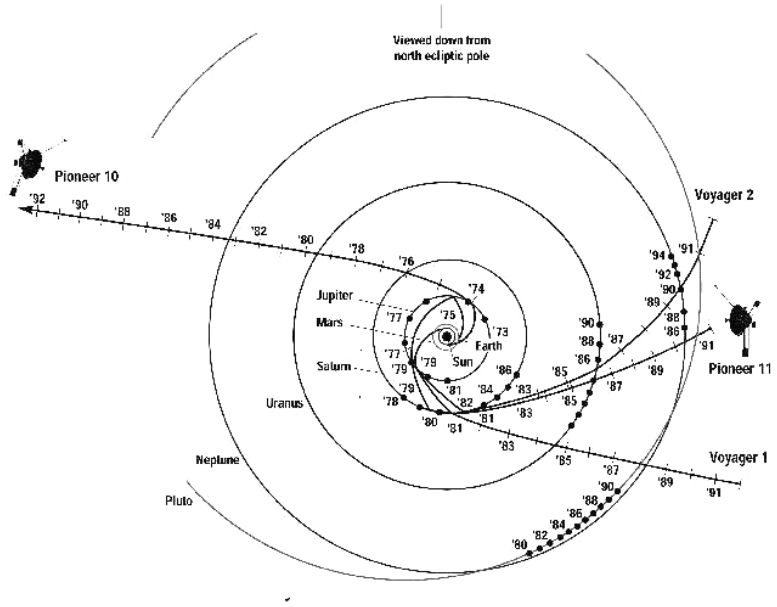

Fig. 8: "Ecliptic pole view of Pioneer 10, Pioneer 11, and Voyager trajectories. Pioneer 11 is traveling approximately in the direction of the Sun's orbital motion about the galactic center. The galactic center is approximately in the direction of the top of the figure." [3, p. 5].

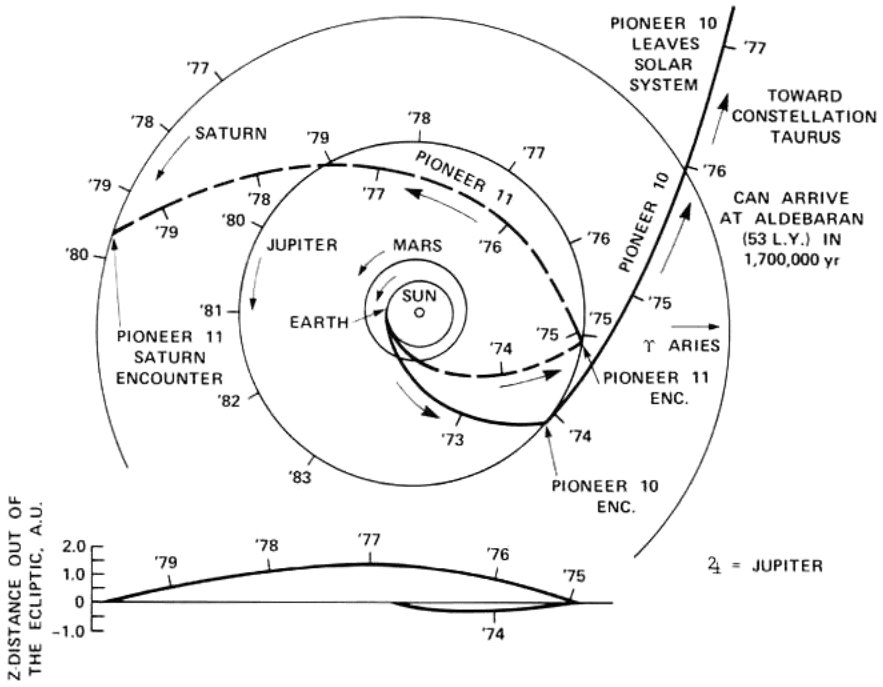

Fig. 9: Detail of early trajectories [6, p. 3].

gravitational energy density than on Earth's surface, both result in overestimation of these quantities. This leads to the belief that an anomalous acceleration towards the sun is acting.

At this point it is instructive to mention that c' differs very little from c and the magnitudes of n', the index of refraction of space, that are predicted with (5) are very nearly equal to 1. The values of n' on the surface of planets differ from Earth's

Planet	n'	Planet	n'
Mercury	0.99997382	Saturn	100.000.349
Venus	0.99999527	Uranus	0.99999524
Earth	100.000.000	Neptune	100.000.737
Mars	0.99997758	Pluto	0.99997385
Jupiter	100.014.145	Moon	0.99997454

Table 3: Values of the vacuum index of refraction n' on the surface of the planets and the Moon. The value of $\rho^* = 1.09429 \times 10^{15}\,\mathrm{J/m^3}$ calculated by Céspedes-Curé [26, p. 279] was used in evaluating n' with (5).

by very little. Table III from [4] shows the results of calculating n' with the use of (5). The values of the planets are close to 1.0 being caused by the local gravitational energy density being not too different from the surface of the Earth.

The correct value of Pioneer's acceleration is obtained with Newton's gravitational force:

$$\vec{a}_N = G \sum_{i=1}^{n} \frac{M_i}{r_i^2} \frac{\vec{r}}{|r|} . \tag{8}$$

Here the acceleration of gravity (i = Sun and planets) is mainly from the Sun, but in the early stages of the mission it will be affected by other planets which are relatively near during energy assist maneuvers (flyby) or near encounter in its trajectory towards outer space.

The Pioneer acceleration is measured with the Doppler formula (7b) with the accepted value c of the speed of light and the uplink $f = 2.113\,\mathrm{GHz}$ frequency. If instead of c we use the speed of light c' given by (6), we get a corrected Doppler-derived acceleration:

$$\vec{a}' = \frac{d\Delta f}{dt} \frac{c}{f} \frac{\sqrt{\rho}}{\sqrt{\rho'_{far}}} \frac{\vec{r}}{|r|} . \tag{9}$$

The difference between the acceleration $\vec{a}'$ as proposed here in (9) and $\vec{a}_{JPL}$ calculated with (7b) gives the predicted anomalous acceleration:

$$\vec{a}_P = \frac{d\Delta f}{dt} \frac{c}{f} \left(\frac{\sqrt{\rho}}{\sqrt{\rho'_{far}}} - 1 \right) \frac{\vec{r}}{|r|} . \tag{10}$$

4 Pioneer annual and diurnal residuals

Here, we present the theory to calculate the harmonic Doppler residuals of the Pioneer 10 and 11 spacecraft. Due to Earth's rotation and translation, the measured acceleration a_{JPL}, has superimposed Doppler shifts due to the components of these movements in the direction of the spacecraft. They are incorporated in the models used to predict the spacecraft movement by the standard galilean addition of velocities, to the predictions of gravitational theory.

We treat first the effect of Earth's rotation. Let V_{ER} be the equatorial tangential velocity (≃0.4 km/s). At the latitude λ of the DSN antennas, the tangential velocity in the direction of Pioneer changes by $\cos\lambda$. As the day progresses, the component decreases by the factor $\cos(\omega_R t + \phi_R)$, where ω_R is the Earth's *sidereal* angular rotation velocity and ϕ_R an Earth rotational phase angle. Hence the rotational Earth's velocity in the direction of Pioneer is

$$v_E = v_{ER} \cos\lambda \cos(\omega_R t + \phi_R) . \tag{11}$$

For argument's sake, we take $(\omega_R t + \phi_R)$ to be equal to 0 degrees when Pioneer is just in the East of the DSN station. Then $\cos(\omega_R t + \phi_R) = 1$ and the velocity predicted is maximum when Pioneer is in the East horizon of the DSN antenna. The component reaches a null value when Pioneer is in the zenith of the DSN station $(\omega_R t + \phi_R) = 90^{\mathrm{o}}$, and becomes negative, reaching a maximum negative value when it is exactly in the West sky of the DSN station. This component has to be added to the speed of light in (10).

In regards to Earth's translation about the Sun, let v_{ET} be Earth's translation velocity (approx. 30 km/s). The component of the translation velocity in the direction of Pioneer is

$$v_E = v_{ET} \cos\lambda \cos(\omega_T t + \phi_T) \tag{12}$$

with ω_T the Earth's sidereal angular translational velocity about the Sun and ϕ_T an Earth translational phase angle.

This component is a maximum when Pioneer is in quadrature and becomes null when it is in opposition (Sun, Earth, Pioneer alignment) or in conjunction with the Sun (Earth, Sun, Pioneer alignment). See Fig. 10.

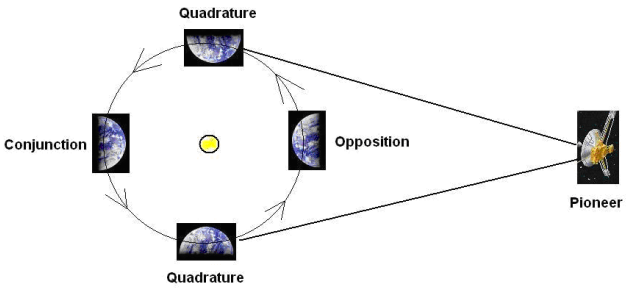

Fig. 10: The Earth translation under the position of Pioneer.

To calculate the annual and diurnal Doppler residuals, we use the galilean velocity addition as demonstrated by Gift [18] adding *to the speed of light* in (10) the Earth's orbital translation and rotational velocity

$$\vec{a}_P = \frac{d\Delta f}{dt} \frac{1}{f} \Big(c + v_{ET} \cos\lambda \cos(\omega_T t + \phi_T) + \\ + v_{ER} \cos\lambda \cos(\omega_R t + \phi_R) \Big) \left(\frac{\sqrt{\rho}}{\sqrt{\rho'_{far}}} - 1 \right) \frac{\vec{r}}{|r|} . \tag{13}$$

In order to calculate $\vec{d}'_P$ with (13) as a function of distance, it is necessary to know the frequency drift $d\Delta f/dt$. The value of the frequency drift for different distances is not available. It has been measured and considered to be constant for the later part of the trajectories. Nevertheless, its value is important for calculating the earlier part of the trajectories. We see that it is possible to calculate values by equating the correct newtonian acceleration given by (8) to the measured acceleration given by (7b). Solving for the frequency drift we obtain:

$$\frac{d\Delta f}{dt} = \frac{f}{c} G \sum_{i=1}^{n} \frac{M_i}{r_i^2} . \tag{14}$$

Here we have to use an invariant c as used by JPL.

On page 16 of Anderson *et al* (2002), it is stated that the measured frequency in Hz is converted to Doppler velocity by the use of their Eq. (13), namely $v = c\,\Delta f/2f$ in our notation. This indicates that the values reported are obtained using a *double* Doppler (uplink–downlink) velocity. Hence our formulation for the frequency shift has to be multiplied by a factor of 2:

$$\frac{d\Delta f}{dt} = \frac{2f}{c} G \sum_{i=1}^{n} \frac{M_i}{r_i^2} . \tag{15}$$

With (15) in (13) we get:

$$\begin{aligned} \vec{d}'_P = 2 \Bigg[1 + \frac{v_{ET}}{c} \cos\lambda \cos(\omega_T t + \phi_T) + \\ + \frac{v_{ER}}{c} \cos\lambda \cos(\omega_R t + \phi_R) \Bigg] + \\ + G \sum_{i=1}^{n} \frac{M_i}{r_i^2} \left(\frac{\sqrt{\rho}}{\sqrt{\rho'_{far}}} - 1 \right) . \end{aligned} \tag{16}$$

Eq. (16) predicts both the constant term of the Pioneer anomalous acceleration towards the Sun and the smaller harmonic Doppler residuals in units of acceleration ($\mathrm{m/s^2}$). It predicts different values for Pioneer 10 and 11 with the differences notably contained in the gravitational acceleration acting on the spacecraft (particularly during planetary encounters in the early phase of the missions). This difference is also due to the distances contained in the ρ'_{far} factor, and the different phase angles ϕ_T for the two spacecrafts.

Since they are going in different directions in the ecliptic plane, the difference $\Delta\phi = \phi_{TPio10}$ - ϕ_{TPio11} should be equal to the difference of their Right Ascensions. This is a variable quantity during the early phase of the mission. However, at the present time, it is nearly constant and equal to (Pioneer 10: 05h 16m 17s) – (Pioneer 11: 18h 53m 32s) = 204.3 degrees.

The much higher translational velocity v_{ET} of Earth with an annual period dominates over the smaller diurnal variations of $\vec{a}'_P$. However the annual variations are slow and the Earth–Pioneer component of v_{ET} is very small during conjunction and opposition.

Figure 4 from Anderson *et al* (2002) [3] clearly shows the harmonic Doppler residuals after subtracting the constant term. These figures are made up of very many different measurements without any established periodicity. Measurements were made when the probe was in the sky of one of the DSN station antennas at arbitrary times of the rotational and translational positions of Earth, which means for (16), different values of the rotational and translational phase angles ϕ_R and ϕ_T.

There are 3 DSN Stations located approximately 120 degrees apart (Madrid, Spain, Goldstone, California and Camberra, Australia). This means that measurements from each station differ in phase angle ϕ_R by about 120 degrees so that in general, it is not expected that Doppler residuals exhibit an oscillatory continuity for any length of time. Nevertheless, as mentioned and reviewed in Section 2 above, previous workers have made detailed analyses of these harmonic Doppler residuals taking into account the phase differences.

We may also derive the Pioneer annual and diurnal Doppler residuals in units of velocity or alternatively in units of frequency as has been reported [3, 9, 22].

The Doppler formula is

$$\Delta f = \frac{v_P}{c} f \tag{17}$$

with v_p the speed of the Pioneer spacecraft, f the transmitting frequency, Δf the frequency change and c the speed of light considered a constant. In the case of the Pioneer spacecraft, it is a "Double" Doppler effect as mentioned above, hence:

$$\Delta f = 2\,\frac{v_P}{c} f . \tag{18}$$

If, instead of c, we use c plus the Earth speed following the results of Gift (2017) [18], then we write

$$\Delta f'' = 2\,\frac{v_P}{c + v_E} f . \tag{19}$$

NASA expects (18) and gets Δf plus or minus a "residual" which we think is due to not using (19). Hence the residual must be (18) minus (19):

$$\Delta f'' = \Delta f - \Delta f' = 2 v_P f \left(\frac{1}{c} - \frac{1}{c + v_E} \right) . \tag{20}$$

Or

$$\Delta f'' = 2 v_P f \left(\frac{v_E}{(c^2 + c v_E)} \right) .$$

This approximates to

$$\Delta f'' \approx 2 v_P f \left(\frac{v_E}{c^2} \right) . \tag{21}$$

This relation gives the maximum values. To calculate the diurnal Doppler residuals as a function of time, we substitute (11) in (21):

$$\Delta f''_D \approx 2f\,\frac{v_P\, v_{ER}}{c^2} \cos\lambda \cos(\omega_R t + \phi_R) . \tag{22a}$$

The equivalent relation for annual residuals is obtained by substituting (12) in (21)

$$\Delta f_A'' \approx 2f \frac{v_P v_{ET}}{c^2} \cos\lambda \cos(\omega_T t + \phi_T) . \qquad (22b)$$

The result (22) gives the annual and diurnal residuals $\Delta f''$ in units of frequency (Hz). We want to compare with results in velocity units such as (mm/s) as shown in Fig. 4. To convert from Hz to m/s Anderson *et al* (2002) [3, p. 16] uses

$$\Delta v'' = \frac{\Delta f'' c}{2f} . \qquad (23)$$

Then substituting (22) in (23) we get for the diurnal Doppler residuals in [m/s]:

$$\Delta v_D'' = \frac{v_P v_{ER}}{c} \cos\lambda \cos(\omega_R t + \phi_R) . \qquad (24a)$$

The equivalent relation for annual residuals is

$$\Delta v_D'' = \frac{v_P v_{ET}}{c} \cos\lambda \cos(\omega_T t + \phi_T) . \qquad (24b)$$

5 Results

In this section we use the theory developed above to predict qualitatively and quantitatively the reported Pioneer Anomaly "constant" and harmonic Doppler residuals.

5.1 Pioneer 10 anomaly at 20 AU

At 20 AU we calculate the anomalous acceleration with (16). For this "constant" term, we omit the terms dealing with the harmonic Doppler residuals and consider only the gravitational acceleration and energy density (in ρ'_{far}) due to the Sun and Earth:

$$\vec{a}_P = 2G\left(\frac{M_S}{r_S^2} + \frac{M_E}{r_E^2}\right)\left(\frac{\sqrt{\rho}}{\sqrt{\rho'_{far}}} - 1\right)\frac{\vec{r}}{|r|} . \qquad (25)$$

This expression predicts:

$$a_P = 7.754 \times 10^{-8}\,\mathrm{cm/s^2} . \qquad (26)$$

This calculated value differs by just 1.2 percent from the value $a_P = 7.85 \pm 0.02 \times 10^{-8}\,\mathrm{cm/s^2}$ reported by O. Olsen (2007) [7] in an independent analysis of the Pioneer 10 data for Interval I. The value calculated in (26) also coincides, within the error estimation, with the result quoted by Anderson *et al* (2002) [3, p. 24]: "1-day batch-sequential estimation for the entire data interval of 11.5 years for Pioneer 10 (*which*) yielded a result $a_P = (7.77 \pm 0.16) \times 10^{-8}\,\mathrm{cm/s^2}$." In this case our calculation differs by just −0.2 percent.

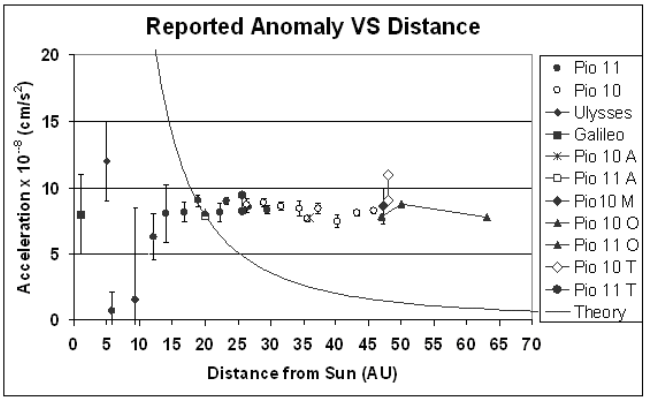

Fig. 11: Anomalous acceleration $\times 10^{-8}$ in units of (cm/s^2) as a function of distance from the Sun. Values of anomalous acceleration reported and reviewed above are plotted with the theoretical line according to (25) (A Anderson, M Markwardt, O Olsen, T Toth).

5.2 Pioneer anomaly as a function of distance from the Sun

To present the anomalous acceleration predicted as a function of distance, we show below results of a simple model with the influence of the Sun and Earth ignoring the other planets.

The theoretical curve in Fig. 11 shows a variable slope decreasing with distance. V. Toth (2009) reports in his independent analysis, as quoted above, values for a_P variation rates for Pioneer 10 and 11. However, it is not stated for what distances or dates are these quantities deduced. The value reported for Pioneer 10 [22, p 20] is $da_{P10}/dt = -(0.21 \pm 0.04) \times 10^{-6}\,\mathrm{cm/s^2/year}$. We find that the theoretical curve in Fig. 11 exhibits that slope exactly, within the uncertainty shown, at a distance between 42 and 48 AU.

For Pioneer 11, the Toth reported variation rate is $da_{P11}/dt = -(0.34 \pm 0.12) \times 10^{-8}\,\mathrm{cm/s^2/year}$. We find that the theoretical curve in Fig. 11 exhibits that slope exactly, within the uncertainty shown, at distances between 29 and 38 AU. Hence, we fully agree with Toth's comment: "an anomalous acceleration that is a slowly changing function of time (*decreasing*) cannot be excluded at present" [our italics].

5.3 Pioneer anomaly during Jupiter flyby

Ulysses, Pioneer 10 and 11 had close encounters with Jupiter as part of mission exploration objectives and for orbit modifications or energy assistance maneuvers. We show now how the theory developed here can explain some of the observations reported during Jupiter flyby by these spacecrafts. The effects of the gravitational energy density due to the planets are very short range according to (2) and even for the Sun [4]. Likewise the gravitational acceleration produced by the planets is relatively short range compared to the large distances traversed by these spacecrafts. To put the values in perspective, we show in Fig. 12 the gravitational acceleration of the

Sun and the planets each centered about their orbital distance to the Sun.

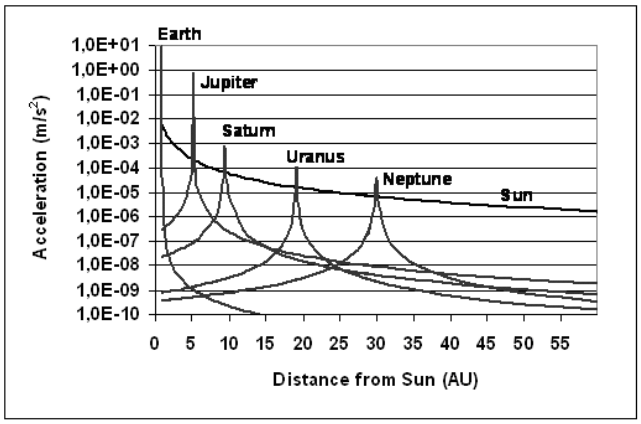

Fig. 12: Gravitational acceleration of the Sun, Earth and planets centered about the position of their orbits about the Sun. (Values are calculated to within 0.2 AU of each planet, and centered at nominal orbital distance).

Fig. 12, top line, shows that compared to the gravitational acceleration of the Sun the planet's acceleration affects only their immediate vicinity. If we rewrite (16) considering just the Sun and Jupiter and emphasizing the vectorial character of $\vec{a}_P$, we get

$$\vec{a}_P = 2G\left(\frac{\sqrt{\rho}}{\sqrt{\rho'_{far}}} - 1\right)\left(\frac{M_S}{r_S^2}\,\frac{\vec{r}}{|r_S|} + \frac{M_J}{r_J^2}\,\frac{\vec{r}}{|r_J|}\right). \qquad (27)$$

Figs. 13 and 14 show the Jupiter flybys of the Pioneer spacecraft. Judging from the incoming and outgoing trajectories towards Jupiter in the polar view of the Pioneer 11 flyby, we deduce that the resulting vectorial gravitational acceleration due to Jupiter and the Sun was mainly in the direction of the Sun, but with the gravitational attraction of Jupiter in the opposite direction. Hence the initial two points in the Pioneer 11 anomalous acceleration (see Fig. 2) which, as reported by Nieto and Anderson (2005) [6], correspond to a time when the spacecraft was under the gravitational attraction of Jupiter and Saturn, are expected to be of a smaller magnitude and additionally, exhibit a large error due to the measurement of a fast changing quantity as they cross the gravitational field of the planets.

In regards to the Pioneer 11 Saturn flyby, we can rewrite (27) in terms of the planet's gravitational field:

$$\vec{a}_P = 2G\left(\frac{\sqrt{\rho}}{\sqrt{\rho'_{far}}} - 1\right)\left(\frac{M_S}{r_S^2}\,\frac{\vec{r}}{|r_S|} + \frac{M_{Sat}}{r_{Sat}^2}\,\frac{\vec{r}}{|r_{Sat}|}\right). \qquad (28)$$

Toth and Turyshev (2007) [20, p. 15] comment about the Pioneer 11's Saturn encounter:

> ...for Pioneer 11, a small value for the anomaly was found during the Jupiter–Saturn cruise phase. Right at the time of the Saturn encounter, however, when the spacecraft passed into a hyperbolic escape orbit, there was a rapid increase in the anomaly, whereafter it settled into the canonical value.

Unfortunately, no numerical values are quoted. However, in the light of Fig. 15 and (28) this text can be explained: When the spacecraft was in the incoming Saturn flyby, it went from an area of gravitational acceleration towards the Sun to an area of stronger gravitational acceleration towards Saturn. This has the effect of decreasing a_P until closest encounter.

Furthermore, as the spacecraft nears the planet it goes from the interstellar gravitational energy density (relatively low) and enters the area of Saturn's energy density with the highest value just at nearest encounter. In this area, $n' = \sqrt{\rho}\,/\,\sqrt{\rho'_{far}}$ increases towards a value similar to Earth's (see the value of n' for Saturn in Table I). Hence, the first term in brackets in (28) decreases rapidly until the nearest point to Jupiter and then increases rapidly settling in the interstellar n' value. This is precisely as reported by Toth and Turyshev.

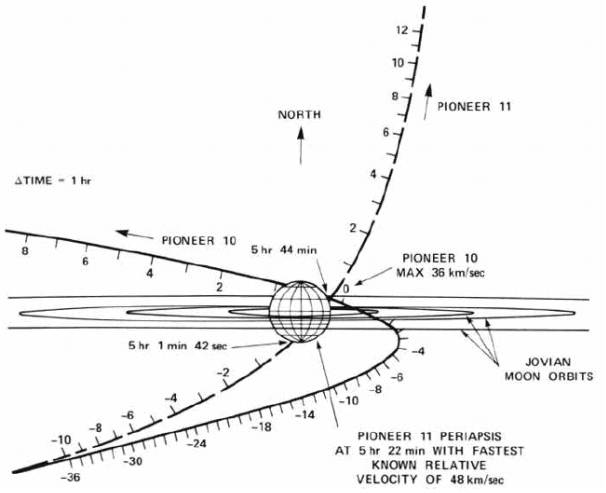

Fig. 13: The Jupiter Flyby of the Pioneer spacecraft, equatorial view [6, Fig. 2, p. 3].

5.4 Pioneer diurnal and annual Doppler residuals

In (16), the diurnal and annual residuals are essentially contained in the first bracket, namely

$$\left(1 + \frac{v_{ER}}{c}\,\cos\lambda\cos(\omega_R\,t + \phi_R) + \frac{v_{ET}}{c}\,\cos\lambda\cos(\omega_T\,t + \phi_T)\right)$$

which multiplies the "constant" term.

The term $\cos\lambda$ is the cosine of the DSN latitude. The latitude of the three stations are Goldstone = 35.4267° N, Madrid

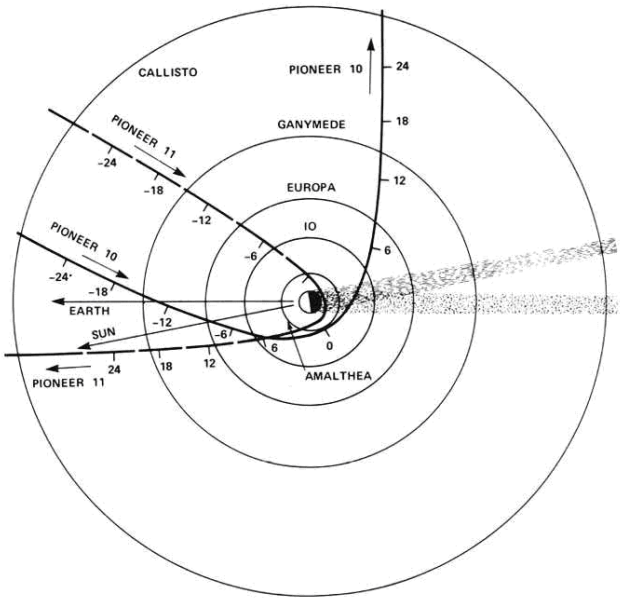

Fig. 14: The Jupiter Flyby of the Pioneer spacecraft. Polar view. From [6, Fig. 2, p. 3].

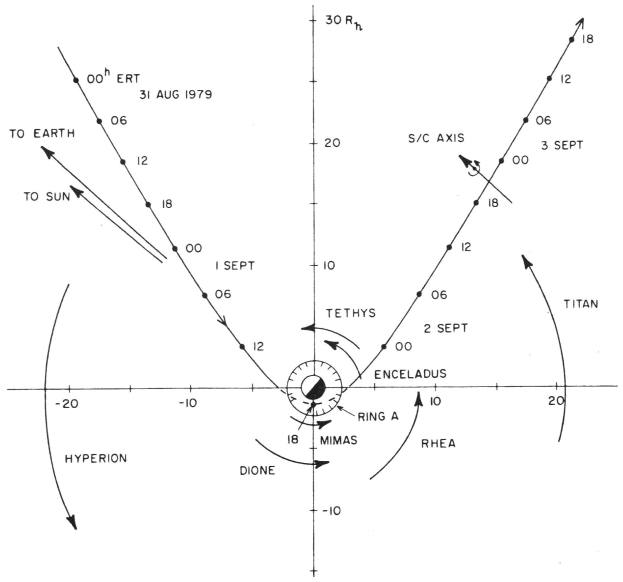

Fig. 15: Pioneer 11 Saturn flyby on the 1st of September 1979. From [6, Fig.3, p. 6].

= 40.4314° N, and Canberra = 35.4013° S. We take the average 37.0864 so that the term $\cos\lambda = 0.79772$. If we substitute the Earth's equatorial rotational velocity $v_{ER} = 465.1$ m/s [30] and Earth's translational velocity $v_{ET} = 2.978 \times 10^4$ m/s and multiply by $\cos\lambda$, we get the following expression:

$$\Big(1 + 1.22402 \times 10^{-6} \cos(\omega_R t + \phi_R) + \\ + 7.92424386 \times 10^{-5} \cos(\omega_T t + \phi_T)\Big). \quad (29)$$

The "cos" term on the left describes the diurnal Doppler residuals with $\omega_R = 7.292 \times 10^{-5}$ rad/s, the Earth's sidereal angular rotation, and the "cos" term on the right describes the annual Doppler residuals with $\omega_T = 2.020$ x 10^{-7} rad/s, the Earth's sidereal angular rotation around the Sun. The sum of the three terms in (29) is very nearly equal to unity. For example, for the maximum amplitude of both oscillatory terms we get (29) to be: 1.00008046. On the other hand at opposition (Sun, Earth and Pioneer in that order) the third translational term is null and the maximum oscillatory term is due to Earth rotation and equal to 1.000001224.

The actual amplitude of the oscillations is obtained by multiplying (29) by the "constant" term in (16). As we have shown above, this is a variable value that depends on the distance to the Sun and also to the planets during encounters or flyby maneuvers. Hence to compare accurately with reported values, it is required to know at what distance or on what date were the measurements made.

5.4.1 Annual residuals

To compare with the Pioneer 10 sine wave reported, Fig. 4, we consider that for Pioneer 10 the data spans a distance from approximately 25 to 45 AU (as reported in Fig. 3). The result of multiplying the maximum amplitude of the oscillatory terms due to Earth's translation velocity, 1.00007924, by the calculated anomaly in this distance range, results in 5.1 to 1.6×10^{-8} cm/s^2. These values compare favorably to the amplitude of the annual oscillatory term reported by Anderson *et al* (2002) [3, p. 40] of "about 1.6×10^{-8} cm/s^2". However, they are larger than the estimate given by the same authors on [3, p. 14]: "the best estimate of the amplitude of the Pioneer 10 sine wave is $(0.525 \pm 0.155) \times 10^{-8}$ cm/s^2 and that of the Pioneer 11 wave is $(0.498 \pm 0.176) \times 10^{-8}$ cm/s^2. These values have a systematic error of $\sigma_{at} = 0.32 \times 10^{-8}$ cm/s^2" as reported for the entire Pioneer data span by Turyshev and Toth (2009) [24, p. 86].

The reported angular velocity of the annual Doppler residuals is approximately 2×10^{-7} rad/s. This value coincides with the Earth's sidereal translational rotation velocity which is 2.0200×10^{-7} rad/s as proposed in this work.

Figs. 5 and 6 show clearly the measured annual residuals. We wish to compare the results of the theory above to the undulating information contained in Fig. 5. To that end, we write the last term in (29) that deals with the annual Doppler residuals as a function of time for Pioneer 10 as:

$$(1 + 7.92424 \times 10^{-5} \cos(2.020 \times 10^{-7} t + \phi_R)) \quad (30)$$

where $\omega_T = 2.020 \times 10^{-7}$ rad/s is the Earth's angular rotation around the Sun.

Eq. (30) has to be multiplied by the calculated anomalous acceleration a_P. This value changes with distance as shown in Fig. 11. From 42 to 63 AU, the predicted anomaly calcu-

lated with (25) ranges from (1.84 to 0.837) $\times 10^{-8}$ cm/s^2 respectively. Hence we chose to select the middle of the three distance intervals as shown in Table IV (distance values derived using data in Fig. 3).

Interval	Dates	Mid date	Mid distance (AU)	Predicted a_P (10^{-8} cm/s^2)
I	1887-1990	1988.5	43	1.758
II	1990-1992	91	52	1.214
III	1993-1998	95.5	63	0.837

Table 4: Predicted a_P for the mid-distance of Pioneer 10 intervals. Values that were chosen to calculate the annual residuals.

Fig. 16 shows the agreement between the calculated annual Doppler residuals and the published results. The amplitude of the predicted oscillations are larger in interval I and decrease in intervals II and III as is reported by Anderson *et al* (2002): "At early times the annual term is largest. During Interval II, the interval of the large spinrate change anomaly, coherent oscillation is lost. During Interval III the oscillation is smaller and begins to die out." [3, p 40].

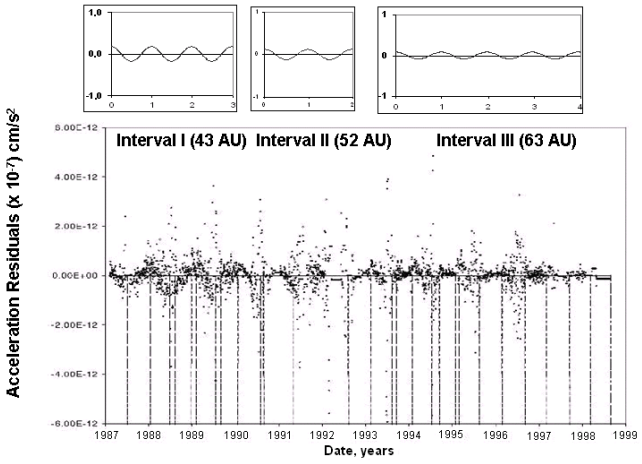

Fig. 16: Comparison of reported annual residual undulations with the predicted Doppler residuals. For uniformity, the original scale in units of [km/s^2] [3, Fig. 17, p. 40], is shown in units of [cm/s^2 $\times$ 10^{-7}]. Inlays plots were drawn to approximately the same X–Y scale as the original data and show the predicted decreased calculated amplitudes corresponding to the center of each of the three intervals.

5.4.2 Diurnal residuals

Levi *et al* (2009), in their spectral analysis of the periodic terms yields the following measured periods: T1 = 0.9974 ± 0.0004 day, T2 = (1/2)(0.9972 ± 0.0004) day and T3 = 189 ± 32 days. As T = 0.9972 day = 1.0 sidereal day, these periods are consistent, within 0.02 percent, with variations of one sidereal day, half a sidereal day, and half a year.

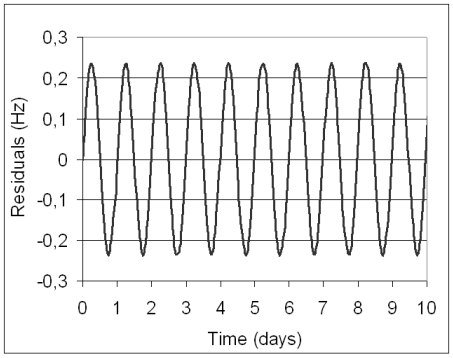

Fig. 17: Diurnal Doppler residuals calculated with (22).

The diurnal oscillations reported by Levi *et al* (2009) [9] between 23 November 1996 to 23 December 1996, reviewed above in Fig. 7 were at an estimated distance of 66.73 to 66.96 AU from the Sun (determined by the use of Fig. 3). Also, they were done at opposition, so that the annual rotational term is almost null and solar coronal influence is minimized.

The diurnal Doppler residuals in frequency units (Hz) may be calculated with (22a) namely:

$$\Delta f_D'' \approx 2f \frac{v_P\, v_{ER}}{c^2} \cos\lambda \cos\left(\omega_R t + \phi_R\right).$$

In this relation the speed of Pioneer v_P at a distance of 66.8 AU was estimated at 12 500 m/s and with the Earth's equatorial rotation velocity of 465.1 m/s, (22) leads to the oscillations shown in Fig. 17 next to the oscillations reported by Levi *et al* [9] in Fig. 18.

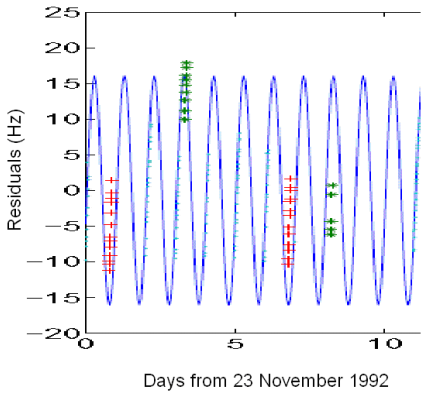

Fig. 18: Diurnal Doppler residuals reported by Levi *et al* [9].

We see that the frequency of diurnal oscillations reported by Levi *et al* (2009) [9] coincides with our predicted frequency $\omega_R = 2\pi f_E$, of Earth rotation, to within 0.02 percent.

A further conclusion of Levi *et al* (2009) [9, p. 10] is: "The main new result of the paper is that a large part of these diurnal and seasonal anomalies may be explained by a simple

geometrical model where the light line on the tracking path is modified in a manner depending on the azimuthal angle ϕ between the Sun-Earth and Sun-probe lines."

We reflect about this conclusion that the azimuthal angle ϕ between the Sun-Earth and Sun-probe lines will show diurnal variations superimposed on annual variations which are wholly compatible with the first bracket of (16) and expression (29) above. With the use of (24a), namely:

$$\Delta v_D'' = \frac{v_P v_{ER}}{c} \cos\lambda \cos(\omega_R t + \phi_R),$$

we can calculate the diurnal Doppler residuals in velocity units as reported by Anderson *et al* (2002) [3] and shown in Fig. 4, using the rotational velocity of Earth 465,1 m/s, and the estimated speed of Pioneer 10 in 1995 of 12 500 m/s. A comparison of the results is shown in Fig. 19 and Fig. 20.

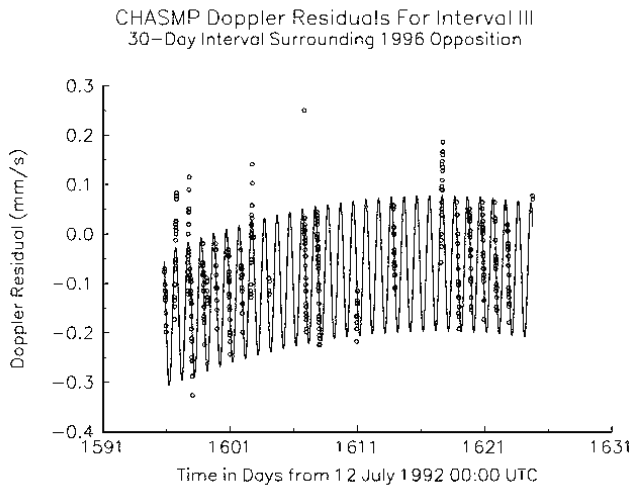

Fig. 19: Diurnal Doppler residuals in velocity units from [3, Fig. 18, p. 41].

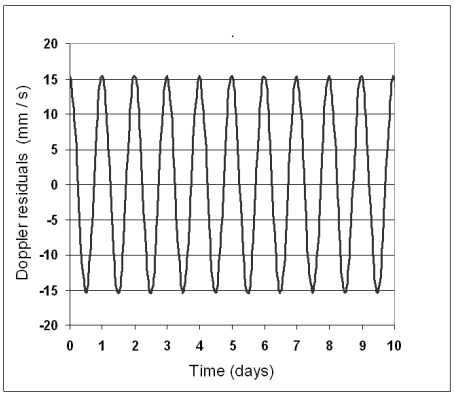

Fig. 20: Diurnal Doppler residuals in velocity units calculated with the use of (24a).

5.5 On the energy density due to far away stars and galaxies

In this work, we have used the value of $\rho^* = 1.094291 \times 10^{15}$ J/m^3, the energy density of space due to far away stars and galaxies, a value calculated by J. Céspedes-Curé [26, p 279], obtained using starlight deflection measurements during total sun eclipses. With this value in the equations, in this work, it has been possible to calculate numerically the anomalous Pioneer acceleration.

It is possible to work in the inverse order and use the empirically determined values of the anomaly to calculate in an independent way the value of this physical magnitude. When this is done, using the accurately reported Pioneer Anomaly at 20 AU, the result gives for the energy density of space due to far away stars and galaxies the value $\rho^* = 1.0838 \times 10^{15}$ J/m^3. This value differs by less than 1 percent from the value determined by J. Céspedes-Curé on the basis of a completely different phenomenon, the bending of light rays during solar eclipses.

We would like to briefly review the procedure that was published to make this determination. For details please consult [4]. The calculation uses the following formulas: Eq. (19) in [4]:

$$n' = 1 - \frac{E_D\, c}{2 f_e\, G \left(\frac{M_S}{r_S^2} + \frac{M_E}{r_E^2} \right)}, \tag{31}$$

and Eq. (8) in [4]:

$$\rho^* = \frac{\rho_{\mathrm{Sfar}} + \rho_{\mathrm{Efar}} - n'^2(\rho_{S\,1AU} + \rho_E)}{n'^2 - 1} \tag{32}$$

where (numerical values in SI units)

- n' = index of refraction of space at 20 AU (comes out to 0.999973567943846).
- ρ^* = energy density of space due to far away stars and galaxies.
- E_D = a steady frequency drift of 5.99×10^{-9} Hz/s from the Pioneer 10 spacecraft [3, p. 20].
- f_e = 2 295 MHz, the frequency used in the transmission to the pioneer spacecraft [3, p. 15].
- c = 299792458.0 m/s. Speed of light on Earth at the surface.
- $G = 6.67300 \times 10^{-11}$ m^3 kg^{-1} s^{-2}, Newton's universal constant of gravitation.
- $M_S = 1.98892 \times 10^{30}$ kg, mass of the Sun.
- $M_E = 5.976 \times 10^{24}$ kg, mass of the Earth.
- The distances r_S and r_E are the distances from the spacecraft at 20 AU (20 AU from the Sun, 19 AU from the Earth) to the center of the Sun and Earth respectively. To calculate them use was made of:

- 1 Astronomical Unit (AU) = 149 598 000 000 meters.

To calculate Eq. (8) in [4], use is made of the energy density given by our Eq. (2), namely

$$\rho = \frac{GM^2}{8\pi r^4}$$

where r is the distance from the centre of the Sun or Earth to the point where the energy density is being calculated as follows:

- for the Earth surface: $r_E = 6\,378\,140$ m, radius of the Earth.
- for the Sun at 1 AU: $r_S = 149\,598\,000\,000$ meters.
- for the Sun at 20 AU: twenty times the previous value used to calculate $\rho_{S\,far}$.
- for the Earth at 20 AU: radius of the Earth + 19 times 149 598 000 000 meters used to calculate $\rho_{E far}$.

Values were calculated with Microsoft Office Excel 2003 which uses 15 significant digits.

6 Discussion

The theoretically calculated Pioneer Anomalous acceleration shown in Fig. 11 has a decreasing value as a function of distance contrary to the generally accepted opinion that it is a "constant" value. However, the numerical evidence supplied by V. Toth (2009) [22] in his independent analysis, gives confirmation that the anomaly is a decreasing function which coincides exactly with the theoretical slope for Pioneer 11 at a distance between 29 and 38 AU and also with the theoretical slope for Pioneer 10 at a distance from the Sun between 42 and 48 AU.

At a distance from the Sun of 20 AU, the theoretical curve predicts $a_P = 7.754{\times}10^{-8}$ cm/s^2 which differs by just 1.2 percent from the value $a_P = 7.85 \pm 0.02 \times 10^{-8}$ cm/s^2 reported by O. Olsen (2007) [7] in his independent analysis of the Pioneer 10 data for Interval I. Furthermore, the theoretical value differs by just −0.2 percent from the 1-day batch-sequential estimation for the entire data interval of 11.5 years for Pioneer 10 reported by Anderson *et al* (2002) [3, p. 24] .

The theory predicts that the anomalous acceleration has a vectorial character $\vec{a}_P$ in the direction of the resultant gravitational acceleration field at the position of the spacecraft. This fact allows satisfactory explanation of the reported anomalous behavior of Ulysses, Pioneer 10 and 11 during Jupiter flyby. The observations of the peculiar values reported for the first 3 values of Pioneer 11 (see Fig. 11) are adequately explained with consideration that they correspond to the spacecraft being affected by the Jupiter gravitational acceleration which at close distances exceeds the Sun's gravitational acceleration (see Fig. 12). The prediction that the anomalous acceleration is in the direction of the resultant gravitational acceleration field at the position of the spacecraft gives an answer to this question, which is posed by several publications on the Pioneer Anomaly.

With regard to the harmonic behavior of the Doppler residuals, relaxing the assumption that the value of the speed of light c in the Doppler formula is invariant and adopting the galilean addition of the Earth rotational and translational velocity to the speed of light, results in an almost exact agreement with the measured *frequencies* for the annual (within 1 percent) and diurnal (within 0.02 percent) residuals as shown in Sections 5.4.1 and 5.4.2 above. However, the values for the magnitudes of the oscillations do not all agree as well.

In the case of the annual residuals, we do a visual comparison in Fig. 16 which agrees quite well. Particularly if we take into account that the reported values have significant errors: A systematic error of $\sigma_{at} = 0.32 \times 10^{-8}$ cm/s^2 ($\sigma_{at} = 3.2 \times 10^{-7}$ cm/s^2 in the scale of Fig. 16) is reported for the entire Pioneer data span by Turyshev and Toth (2009) [24, p. 86]. Considering the scatter of the measured values, the predicted magnitude adequately fits the data in this case.

In the case of the diurnal residuals, expressed in frequency units (Hz) as shown in Fig. 13, there is a discrepancy in the *amplitude* of the order of a factor of about 70 smaller in the calculated value of the oscillations in comparison with the amplitude of the oscillations reported by Levi *et al* [9]. With the calculated oscillations in velocity units (mm/s) the reverse is obtained. As shown in Fig. 19 the calculated amplitude is a factor of about 50 larger than the values in Fig. 4 by Anderson *et al* [3]. In view of these differences it is instructive to compare the amplitudes of the different reported values which also show significant differences.

The amplitude of the diurnal residuals in *frequency* units (Hz) reported by Levi *et al* [9, p. 6], shown in Fig. 7 are a factor of about 250 times greater than the amplitude of diurnal residuals in frequency units (Hz) reported by Anderson *et al* (2002), our Fig. 4 [3, Fig. 18, p. 41]. Both reports are for the same interval of time (23 November to 23 December 1996).

Regarding the annual residuals there is also a discrepancy in the amplitudes expressed in *acceleration* units (cm/s^2) reported by Anderson *et al* in the 2002 paper. The amplitude of the annual oscillations shown in Fig. 4 are about 10 times greater than those reported in the same paper in Fig. 12 [3, p. 26]. In view of the good agreement in the prediction of the frequencies of the harmonic Doppler residuals, it is not clear what are the sources of the discrepancies between reported amplitudes, or the differences between reported and the calculated amplitudes.

7 Conclusions

As summarized in the Discussion above, the theory presented in this work is capable of explaining qualitatively and quantitatively the phenomena associated with the Pioneer Anomaly, both, the secular and the harmonic terms that up to now had no plausible explanation. These precise calculations of the

Pioneer Anomaly, without any adjustable parameters, provide additional confirmation of the Céspedes-Curé hypothesis, that c the speed of light depends on the gravitational energy density of space as defined by (1) namely: $c = k / \sqrt{\rho}$. The highly accurate calculation of the observed frequencies of the annual and diurnal Doppler residuals and some of the amplitudes of the annual oscillations supply additional evidence that the speed of Earth adds to c, the speed of light, according to the galilean addition of velocity, thereby confirming this conclusion put forth by the analysis of S. Gift using the Global Positioning System [16–18].

The extremely accurate measurements provided by NASA as empirical data and the theoretical explanation, agreeing within 1 percent, presented in this work for the Céspedes-Curé hypothesis, have profound consequences in the current cosmology theories. The dependence of the speed of light on the gravitational energy density of space implies a revision of all astronomical measurements of velocity based on the Doppler, blue and red shifts, of stars and galaxies. These have importance in the determination of matters such as the Hubble constant, the expansion of the universe, the flat rotation curve of galaxies (which gave birth to the theory of dark matter) and the extreme values of the redshifts of very far away galaxies (so called inflation) which gave birth to the theory of dark energy.

Acknowledgements

We would like to acknowledge the independent verification of numerical calculations provided by Simon E. Greaves.

Received on June 3, 2021

References

1. Anderson J. D., Campbell J. K., Ekelund J. E., Jordan E. and Jordan J. F. Anomalous Orbital-Energy Changes Observed during Spacecraft Flybys of Earth. *Phys. Rev. Letters*, 2008, v. 100 (091102), 1–4.
2. Greaves E. D., Bracho C. and Mikoss I. A Solution to the Flyby Anomaly Riddle. *Progress in Physics*, 2020, v. 16 (1), 49–57.
3. Anderson J. D., Laing Ph. A., Lau E. L., Liu A. S., Nieto M. M. and Turyshev S. G. Study of the anomalous acceleration of Pioneer 10 and 11. *Phys. Rev. D*, 2002, v. 65 (082004).
4. Greaves E. D. NASAs astonishing evidence that c is not constant: The pioneer anomaly. arXiv: physics.gen-ph/0701130v1.
5. Turyshev S. G. and Toth V. T. The Pioneer Anomaly. arXiv: gr-qc/1001.3686v2.
6. Nieto M. M. and Anderson J. D. Using early data to illuminate the Pioneer anomaly. *Classical and Quantum Gravity*, 2005, v. 22, 5343–5354. arXiv: gr-qc/0507052v2.
7. Olsen O. The constancy of the Pioneer anomalous acceleration. *Astronomy and Astrophysics*, 2007, v. 463, 393–397.
8. Ghosh A. On the Annual and Diurnal Variations of the Anomalous Acceleration of Pioneer 10. *Apeiron*, 2007, v. 14 (3).
9. Levy A., Christophe B., Berio P., Metris G., Courty J. M. and Reynaud S. Pioneer Doppler data analysis: study of periodic anomalies. *Adv. Space Res.*, 2009, v. 43, 1538–1544. arXiv gr-qc/0809.2682.
10. Turyshev S. G., Toth V. T., Kinsella G., Lee S.-C., Lok S. M., Ellis, J. Support for the Thermal Origin of the Pioneer Anomaly. *Physical Review Letters*, 2012, v. 108 (24), 241101. arXiv: /1204.2507.
11. Bilbao L. Does the velocity of light depend on the source movement? *Prog. in Phys.*, 2016, v, 12 (4), 307–312.
12. Rievers B. and Lämmerzahl C. High precision thermal modeling of complex systems with application to the Flyby and Pioneer Anomaly. *Annalen der Physik*, 2011, v, 523 (6), 439–449.
13. Francisco F., Bertolami O., Gil P. J. S. and Páramos J. Modelling the reflective thermal contribution to the acceleration of the Pioneer spacecraft. arXiv: physics.space-ph/1103.5222v2.
14. Bilbao L., Bernal L. and Minotti F. Vibrating Rays Theory. arxiv: abs/1407.5001.
15. Greaves E. D. A Neo-Newtonian Explanation of the Pioneer Anomaly. *Revista Mexicana de Astronomia y Astrofisica*, 2009, v. 35, 23–24. ISSN 0185-1101, www.redalyc.org/articulo.oa?id=57115758008, accessed August 2021.
16. Gift S. J. G. Doppler Shift Reveals Light Speed Variation. *Apeiron*, 2010, v. 17 (1), 13–21.
17. Gift S. J. G. Time Transfer and the Sagnac Correction in the GPS. *Applied Physics Research*, 2014, v. 6 (6), 1–9.
18. Gift S, J. G. One-way Speed of Light Using the Global Positioning System. In: Torres, G., ed. Global Positioning Systems (GPS): Performance, Challenges and Emerging Technologies, Nova Publishers, NY, 2017, pp. 45–66.
19. NASA Solar System Exploration – Galileo. solarsystem.nasa.gov/missions/galileo/in-depth/, retrieved August 2020.
20. Toth V. T. and Turyshev S. G. The Pioneer Anomaly: Seeking an explanation in newly recovered data. *Can. J. Phys.*, 2007, v. 84, 1063–1087.
21. Markwardt C. Independent Confirmation of the Pioneer 10 Anomalous Acceleration. arXiv: gr-qc/0208046v1.
22. Toth V. T. Independent Analysis of the Orbits of Pioneer 10 and 11. *Int. J. Mod. Phys.*, 2009, v. D18, 717–741. arXiv: /0901.3466.
23. Levy A., Christophe B., Bério P., Métris G., Courty J.-M. and Reynaud S. Pioneer 10 Doppler data analysis: disentangling periodic and secular anomalies. *Advances in Space Research*, 2009, v. 43, 1538–1544. arXiv: gr-qc/0809.2682v2,
24. Turyshev S. G. and Toth V. T. The Pioneer Anomaly in the Light of New Data. arXiv: gr-qc/0906.0399v1.
25. Pioneer 10 coordinates: theskylive.com/pioneer10-info. Pioneer 11 coordinates: theskylive.com/pioneer11-info. Topocentric coordinates computed for the selected location of Greenwich, United Kingdom, accessed July 2021.
26. Céspedes-Curé J. Einstein on Trial or Metaphysical Principles of Natural Philosophy. et al. Organization, Caracas, Venezuela, 2002. www.nuclear.fis.usb.ve/Cespedes-Cure-2002-Einstein-on-Trial-J.pdf, retrieved 10 January 2019.
27. Greaves E. D. (2015) La hipótesis de Céspedes-Curé y el índice de refracción del espacio en un campo magnético. (The Céspedes-Curé hypothesis and the index of refraction in a magnetic field). *Acta Científica Venezolana*, 2015, v. 66 (4), 226–229.
28. Greaves E. D. The index of refraction of quasi-empty space. Unpublished, Universidad Simón Bolívar, Caracas, Venezuela, 2015. www.nuclear.fis.usb.ve/fn/wp-content/uploads/2015/07/GREAVES-ED-Index-of-refraction-of-quasi-empty-space-V11.pdf, retrieved 19 April 2019.
29. Greaves E. D. Propiedades del espacio vacío. (Properties of empty space). Memorias del II Congreso de ABAE, September 18–22, 2017.
30. Cox, A. N. ed. Allen's Astrophysical Quantities. Springer, 2015, p. 244.

Gamow Theory for Transmission and Decay of Unbound Diprotons

Tianxi Zhang

Department of Physics, Chemistry, and Mathematics, Alabama A & M University, Normal, Alabama 35762, USA.
E-mail: tianxi.zhang@aamu.edu

Transmission and decay of unbound diprotons have been investigated in accordance with the Gamow theory for the quantum tunneling and radioactive decays. It is shown that a diproton, once formed, will be quickly decayed with two typical decay modes: (1) the proton decay, which causes the diproton to be separated into two separate protons and (2) the β^+ decay, which causes the diproton to be changed and fused into a deuteron after emitting a positron and a neutrino. For both of the decay modes, the transmission probabilities rapidly increase with the energy of the emitted particle. The β^+ decay from a diproton is much rarer ($< 10^{-4}$ times less) in general than the proton decay. The lifetimes for both of the two decay modes slowly decrease with the energy of the emitted particle and are extremely short to about 10^{-21} s. In addition, we have also modeled the diproton decay of a typical proton-rich radioactive heavy nucleus such as ^{15}Ne and obtained result of lifetimes consistent with measurements

1 Introduction

Helium-2 or ^{2}He is an isotope of helium. Its nucleus consists of only two protons and is usually called a diproton. It is extremely unstable and believed to be in an unbound state with a negative binding energy due to the spins of the two protons to be anti-aligned according to the Pauli Exclusion Principle [1, 2]. A diproton can be formed in two ways: (1) by combination of two separate protons or (2) by decay from radioactive heavy nuclei. Two separate protons, when they collide with enough energy to tunnel through the Coulomb barrier between them, form a diproton, ^{1}H+^{1}H+Energy $\longrightarrow$ ^{2}He. On the other hand, some proton-rich (or neutron-rare) heavy nuclei have been experimentally found to emit diprotons. For instances, the radioactive nuclei ^{15}Ne and ^{11}O can decay, respectively, to ^{13}O and ^{9}C after emitting a diproton [3,4]. This type of event for a diproton to be emitted from a radioactive nucleus is usually called the diproton decay.

A diproton, once formed via either one of the two ways as described above, will quickly decay through either one of the two different modes [5]. It most likely undergoes a proton decay to change immediately back to two separated protons, $^2\mathrm{He} \longrightarrow {}^1\mathrm{H} + {}^1\mathrm{H}$, with a probability greater than 99.99%. In this case, both of the emitted particle and the leftover nucleus are protons. The formed diproton can also very rarely undergo a positron (or β^+) decay and get fused to form a deuteron, $^2\mathrm{He} \longrightarrow {}^2\mathrm{H} + \mathrm{e}^+ + \nu_\mathrm{e}$, with a probability less than 0.01%. In this case, one of the two protons in the formed diproton decays to a neutron after emitting a positron and a neutrino. Meanwhile, the neutron immediately fuses with the other proton to form a deuteron and release nuclear energy. It can be seen that the β^+ decay of diprotons is much rarer (about ten thousand or more times rarer) than the proton decay of diprotons. The lifetime of a diproton is extremely short and believed to be much much less than 10^{-9} s. Up to now, scientists have only provided these upper bound values for both of the rareness of β^+ decay and the lifetime of diprotons. The actual rareness of the β^+ decay and the lifetime of diprotons are still uncertain.

The Sun is a giant natural fusion reactor with an emission power of 3.85×10^{26} W from the nuclear fusion of its core's 1.2×10^{56} protons at a rate of about 3.6×10^{38} protons per second to produce helium nuclei or α-particles [6]. A diproton is an intermediate in the first step of the proton-proton chain nuclear reaction that is occurring in the cores of stars including our Sun. Therefore, the instability of diprotons critically affects the rate of nuclear fusion reactions in the core of the Sun. From classical physics, no proton should be able to overcome the 820 keV Coulomb barrier between protons to form a diproton and then get fused in the Sun's core, where the temperature is about 1.5 keV. According to Gamow's theory or model for the quantum tunneling probability [7], however, one part per million of the core's protons can penetrate or tunnel through the Coulomb barrier to form diprotons. Considering the high ion-collision frequency (over about 20 terahertz), one can find approximately 10^{63} sufficient collisions for diprotons to be formed in one second in the core of the Sun. Even though as mentioned above less than 0.01% of diprotons are fused to deuterons via the β^+ decay, the fusion reaction rate in the core of the Sun is still around 10^{21} times higher in magnitude than the actually observed fusion reaction (or power emission) rate. This extremely high fusion rate would lead the Sun to have an intensive explosion, if there does not exist any other fusion inhibitors.

Recently, the author proposed that the plasma waves, globally destabilized in the core of the Sun, can significantly reduce the nuclear fusion reaction rate to the observed power emission rate or luminosity and thus effectively prevent the Sun from an instantaneous explosion [8]. Through significantly reducing the electric permittivity of the core plasma, plasma waves can extremely raise the Coulomb barrier and

shift the Gamow peak to a higher energy of particles to extremely inhibit the fusion reaction. It has been shown that, if the frequency of plasma waves that are globally generated in the core plasma of turbulences is about 1.28 times the plasma frequency, the Sun can have the actual fusion rate or shine on at the currently observed luminosity. This implies that, in addition to the quantum tunneling effect and rareness of β^+ decay, plasma waves are also playing the essential role in solar nuclear fusion and power emission.

In this paper, we study the transmission and lifetime for the proton and β^+ decays of unbound diprotons according to the Gamow theory for the quantum tunneling. We obtain that the transmission probability and lifetime of unbound diprotons depend on the energy of the emitted or decayed particles. When the energy of emitted protons is about 800 keV or higher, more than 99.99% of diprotons will decay into separate protons. When the energy of emitted positrons is about 10 eV or lower, less than 0.01% of diprotons will decay and fuse to deuterons. The lifetimes of a diproton via both of the two decay modes decrease with the energy of emitted particles and are about 10^{-21} s or shorter. The speeds of a proton with hundreds of keV and an electrons with several eV are typically valued at about 10^6 m/s.

2 Gamow theory for transmission and decay of diprotons

In 1928, George Gamow proposed a theory for α-decay of radioactive heavy nuclei [7]. Since the α particle, i.e. the helium nucleus, is a positively charged particle (with charge Z_1e, where $Z_1 = 2$ for the α particle), it will be electrically repelled by and further escape from the leftover nucleus (with charge Z_2e). Here Z_1 and Z_2 are the atomic numbers of the nuclear elements or the proton number in the nucleus of the emitted particle and the leftover nucleus, $\epsilon_0 = 8.85 \times 10^{-12}$ $C^2/(J\,m)$ is the permittivity of free space, and $e = 1.6 \times 10^{-19}$ C is the charge of the proton. Gamow's theory approximately modeled the potential energy by a finite potential square well to represent the attractive nuclear force and joined with a Coulomb repulsive potential tail [9],

$$V(r) = \begin{cases} -V_0 & \text{for } 0 < r < r_1 \\ \frac{1}{4\pi\epsilon_0}\frac{Z_1Z_2e^2}{r} & \text{for } r_1 < r < \infty \end{cases} . \qquad (1)$$

Fig. 1 sketches the potential energy $V(r)$ given by (1) as a function of radial distance r in all the classical and quantum regions. The width of the potential square well is noted by r_1, which is determined by the radius of the nucleus or by the sum of the radii of both the emitted particle and the leftover nucleus. The depth of the potential square well is noted by V_0, which is much greater than the maximum height of the Coulomb barrier, U_c. The outer turning point (i.e. r_2) can be determined, in terms of the energy E of the emitted α particle to be equal to the potential energy at r_2, by

$$r_2 = \frac{4\pi\epsilon_0 E}{Z_1Z_2e^2} . \qquad (2)$$

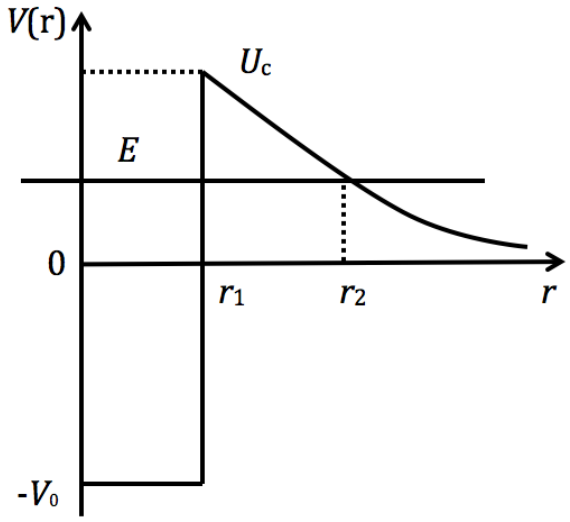

Fig. 1: Gamow's modeling of the potential energy for an electrically charged particle to decay or be emitted from a radioactive nucleus. It consists of the potential energy square well for the attractive nuclear force and the Coulomb potential energy tail for the repulsive electric force between the emitted particle and the leftover nucleus of the decay.

In the central potential $V(r)$, the radial Schrödinger equation is,

$$\frac{d^2u(r)}{dr^2} = \frac{2\mu}{\hbar^2}[V(r) - E]u(r) + \frac{l(l+1)}{r^2}u(r) , \qquad (3)$$

where $u(r)$ is the radial wave function, μ is the reduced mass, $\mu = m_1m_2/(m_1 + m_2)$ with m_1 the mass of the emitted particle and m_2 the mass of the leftover nucleus. The integer l is the quantum number for the magnitude of angular momentum and $\hbar$ is defined by $\hbar = h/2\pi$ with $h = 6.62 \times 10^{-34}$ J s, the Planck constant. A two-body system with a central force or potential can be treated as a system of one body with the reduced mass.

Applying the WKB approximation and considering the case of $l = 0$, one can approximately solve the radial Schrödinger equation and find the radial wave functions to be

$$u(r) = \frac{C}{\sqrt{|p(r)|}} \exp\left[\pm\frac{1}{\hbar}\int |p(r)|dr\right] , \qquad (4)$$

where $p(r)$ is defined by

$$p(r) = \sqrt{E - V(r)} . \qquad (5)$$

Here it should be pointed out that the general solution of the radial Schrödinger equation should be the combination of these two.

Then, from the solved wave function, the transmission (or tunneling) probability is obtained as

$$T = e^{-2\gamma} , \qquad (6)$$

where γ is determined by

$$\gamma = \frac{1}{\hbar}\int_{r_1}^{r_2} dr\sqrt{E - V(r)} = \frac{\sqrt{2\mu E}}{\hbar}\left[r_2\left(\frac{\pi}{2} - \arcsin\sqrt{\frac{r_1}{r_2}}\right) - \sqrt{r_1(r_2 - r_1)}\right]. \quad (7)$$

And the lifetime of the parent nucleus is given by

$$\tau = \frac{2r_1}{v}e^{2\gamma} \quad (8)$$

where $v = \sqrt{2E/m_1}$ is the speed of the emitted (or α) particle. It should be noted that, although being proposed for explaining the α decay of radioactive nuclei, the Gamow model is applicable in general for the decay or emission of any type of charged particles from a radioactive nucleus such as the proton decay from a diproton, β^+ decay from a diproton, and emission of a diproton from a radioactive heavy nucleus (e.g. diproton decays of ^{15}Ne and ^{11}O), and so on.

For the proton decay mode of a diproton, the emitted particle is a proton and the leftover nucleus is also a proton. In this case, we have $Z_1 = Z_2 = 1$, $m_1 = m_2 = m_p$, and $\mu = m_p/2$, where $m_p = 1.67 \times 10^{-27}$ kg is the proton mass. The width of the potential square well or the radius of the diproton can be chosen as $r_1 = 1.75 \times 10^{-15}$ m. With the values of these parameters and (6)–(8), we can plot, in Fig. 2, the transmission probability for the proton decay of the diproton (solid line) and the lifetime of the diproton via the proton decay mode (dashed line) as a function of the energy of the proton. It is seen that the transmission probability increases with the energy. Most diprotons undergo this decay mode when the energy of the emitted particle is greater than about some hundred keV. In other words, diprotons rarely decay into protons with energy much below about the Coulomb barrier such as one hundred keV or less. The lifetime of unbound diprotons via this decay mode is very short and slowly decreases with the energy of the emitted particle. When the energy of the emitted particle is greater than about some hundred keV, the lifetime of diprotons is as short as about 10^{-21} s.

For the β^+ decay mode of a diproton, the emitted particle is a positron and the leftover nucleus is a deuteron. In this case, we have $Z_1 = Z_2 = 1$, $m_1 = m_e$, $m_2 = 2m_p$, $\mu = m_e$, where $m_e = 9.1 \times 10^{-31}$ kg is the electron mass. The width of the potential square well or the radius of the diproton can be chosen again as $r_1 = 1.75 \times 10^{-15}$ m. With the values of these parameters and (6)–(8), we can plot, in Fig. 3, the transmission probability for the β^+ decay of a diproton (solid line) and the lifetime of diproton via this decay mode (dashed line) as a function of the energy of the positron. It is seen that the transmission probability increases with the energy. Diprotons rarely undergo this decay mode when the energy of the positron is less than about some hundred eV. The reason for the β^+ decay of the diproton to be extremely rare is because the energy of the emitted positron is far below the 820 keV Coulomb barrier. For the transmission probability to be about 10^{-21}, the energy of the emitted positron must be less than an eV, which may not be reasonable. Therefore, the result obtained here supports the existence of other physics effects such as plasma oscillations or waves that the author recently proposed to significantly inhibit the nuclear fusion reaction in the core of the Sun [8]. The lifetime of unbound diprotons via this β^+ decay mode is also very short and slowly decreases with the energy of the emitted positron. When the energy of the emitted positron is as high as about some hundred eV, the lifetime of diprotons is also as short as about 10^{-21} s.

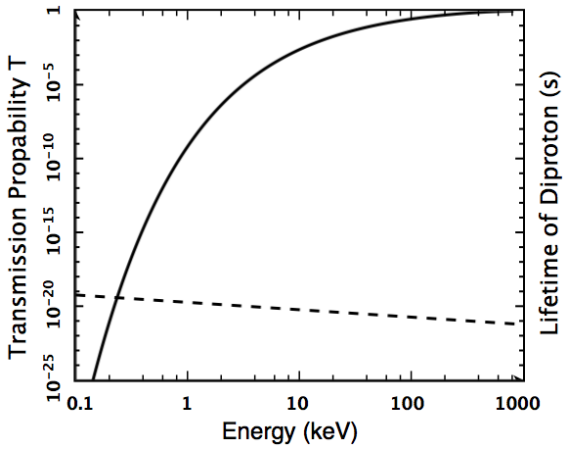

Fig. 2: Proton decay and lifetime of an unbound diproton. The solid line plots the transmission probability of a proton from the unbound diproton in the potential energy well to tunnel through the Coulomb barrier as a function of the energy of the proton. The dashed line plots the lifetime of the diproton.

For the diproton decay of radioactive heavy nuclei such as ^{15}Ne, the emitted particle is a diproton and the leftover nucleus is ^{13}O. In this case, we have $Z_1 = 2$, $Z_2 = 8$, $m_1 = 2m_p$, $m_2 = 13m_p$, $\mu = 1.73\,m_p$, Here we have considered approximately both proton and neutron having about the same mass. The width of the potential square well or the radius of ^{15}Ne nucleus can be chosen as $r_1 = 4 \times 10^{-15}$ m. With the values of these parameters and (6–8), we can plot, in Fig. 4, the transmission probability for the diproton decay from a radioactive nucleus ^{15}Ne (solid line) and the lifetime of the nucleus ^{15}Ne via this diproton decay mode (dashed line) as a function of the energy of the diproton. It is seen that the transmission probability increases with the energy. Most ^{15}Ne nuclei undergo the diproton decay when the energy of the emitted particle is greater than about some MeV. The lifetime of the radioactive nucleus ^{15}Ne via the diproton decay mode is very short and slowly decreases with the energy of the emitted diproton. When the energy of the emitted diproton is as high as about some MeV, the lifetime of the radioactive nucleus ^{15}Ne is

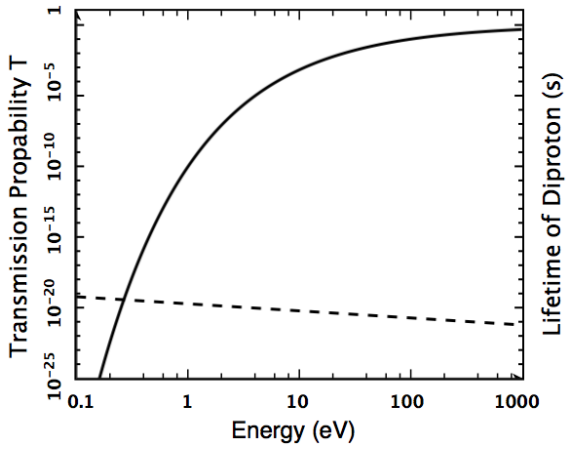

Fig. 3: Positron (or β^+) decay and lifetime of an unbound diproton. The solid line plots the transmission probability of a positron from the unbound diproton in the potential energy well to tunnel through the Coulomb barrier as a function of the energy of the positron. The dashed line plots the lifetime of the diproton.

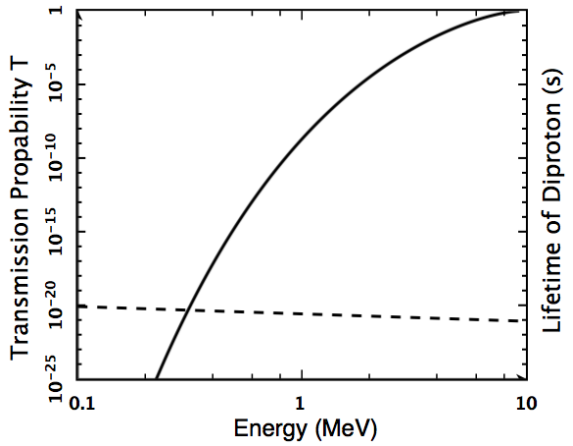

Fig. 4: Diproton decay and lifetime of ^{15}Ne nucleus. The solid line plots the transmission probability of a diproton from the radioactive ^{15}Ne nucleus in the potential energy well to tunnel through the Coulomb barrier as a function of the energy of the diproton. The dashed line plots the lifetime of ^{15}Ne nucleus.

as short as about 10^{-21} s, consistent with measurements [10]. The diproton decay was also detected from other nuclei such as ^{18}Ne nucleus [11, 12].

3 Discussions and Conclusions

If diprotons are bound, stars would burn about a billion billion times brighter in luminosity or faster in nuclear reaction, resulting in a universe to fail the life support [13, 14]. This diproton disaster can be overcome by plasma oscillations or waves, which have been shown recently to be able to be extremely efficient in inhibiting the nuclear reaction [8], to have the observed luminosity without need to adjust the stars' central temperature, density, and initial number of deuterons. In future study, we will study in more detail the transmission probability of bound diprotons for the fusion reaction.

As a consequence of this study, we have investigated the transmission and decay of unbound diprotons according to the Gamow theory. An unbound diproton is extremely unstable and quickly decays through two types of decay modes with lifetime to be extremely short down to about 10^{-21} s and transmission probability to be significantly energy dependent. A diproton mostly undergoes a proton decay to be two separate protons with a transmission probability higher than 99.99%, and rarely undergoes a β^+ decay to form a deuteron with a transmission probability lower than 0.01%. In the reasonable energy range, the β^+ decay of diproton is not rare enough for the Sun to have the observed reaction rate, which supports the author's recently proposed other inhibition effect such as plasma oscillation in solar nuclear fusion. The result obtained for the diproton decay from a radioactive nucleus can also be consistent with measurements.

Acknowledgements

The author acknowledges the reviewer and the editor for improving the manuscript quality.

Received on June 9, 2021

References

1. Pauli W. Exclusion Principle and Quantum Mechanics. Writings on Physics and Philosophy, 1946, 165–1981.
2. Bertulani C. A. Nuclear Physics in a Nutshell. Princeton University Press, 2007, ISBN 978-0-691-12505-3.
3. Wamers F. *et al*. First Observation of the Unbound Nucleus ^{15}Ne. *Physical Review letters*, 2014, v. 112, 132502.
4. Web T. B. *et al*. First Observation of Unbound ^{11}O, the Minor of the Halo Nucleus ^{11}Li. *Physical Review Letters*, 2019, v. 122, 122501.
5. https://en.wikipedia.org/wiki/Isotopes of helium.
6. Zirin H. Astrophysics of the Sun. Cambridge and New York, Cambridge Univ. Press, 1988.
7. Gamow G. Zur Quantentheorie des Atomkernes. *Z. Physik*, 1928, v. 51, 204–212.
8. Zhang T. X. The Role of Plasma Oscillation Played in Solar Nuclear Fusion. *Progress in Physics*, 2021, v. 17, 67–71.
9. Grffiths D. J. Introduction to Quantum Mechanics, 2nd Edition. Person Prentice Hall, 2005.
10. Blank B., Ploszajczak M. Tow-Proton Radioactivity. *Reports on Progress in Physics*, 2008, v. 71, 046301.
11. del Campo G. J. *et al*. Decay of a Resonance in ^{18}Ne by the Simultaneous Emission of Two Protons. *Physical Review Letters*, 2001, v. 66, 43–46.
12. Raciti G. *et al*. Experimental Evidence of ^{2}He Decay from ^{18}Ne Excited States. *Physical Review Letters*, 2008, v. 100, 192503–192505.
13. Bradford R. A. W. The Effect of Hypothetical Diproton Stability on the Universe. *J. of Astrophys. Astron.*, 2009, v. 30, 119–131.
14. Barnes L. A. Binding the Diproton in Stars: Anthropic Limits on the Strength of Gravity. *JCAP*, 2015, No. 12, 050.

Entropy Analysis of the Bioelectrical Activity of Plants

Hartmut Müller, Roberta Baccara, Rose Line Hofmann, Giuseppe Lonero,
Simona Muratori, Giuliana Papa, Francesca Santoni, Loretta Todesco,
Francesco Zanellati, Leili Khosravi

Rome, Italy.
E-mail: hm@interscalar.com

The paper introduces entropy analysis of bioelectrical activity based on harmonic signal distortion. Over a period of one year, the ultradian dynamics of the electrical activity of higher plants and the response on low frequency electromagnetic fields and modulated light were recorded. Biological active frequencies increasing or decreasing the entropy of bioelectrical activity were identified.

Introduction

Bioelectricity are electric potentials and currents produced by or occurring within living organisms. The experiments of Luigi Galvani and Alessandro Volta in the 18^{th} century proved the connection between electricity and muscle contraction in frogs and other animals. Today, electrical effects originating in active cells of the heart and the brain are commonly monitored and analyzed for diagnostic purposes.

In 1873, John Burdon-Sanderson [1] discovered bioelectrical activity in the leaf of the Venus flytrap due to stimulation. Recent studies evidence that intracellular electrical signals serve for information transmission in plant cells [2]. Electrical signals have been shown to accompany many processes in plant life, including respiration [3], water uptake and transport [4], leaf movement [5] and stress response [6]. Electrical signals also play an important role in physiological activities e.g. gas exchange, pollination, fertilization and gene expression [7].

Plant tissue is a good conductor of electricity, so that electrical resistivity is used for quantification of root structures and functioning. Studies of the spatiotemporal characteristics of the electrical network activity of the root apex evidence the existence of excitable traveling waves in plants [8], similar to those observed in non-nerve electrogenic tissues of animals. Electrical activity is mostly observed in the transition zone of the root apex, and points to a possible physiological role of synchronized electrical activity in this region.

Stefano Mancuso [9] has found rising evidence that the root apex is the key to the intelligence of higher plants. He argues that plants use the root system as a complex network instead of a single powerful brain. The plant-neurobiological paradigm of Mancuso assumes that plants have electrical activity similar to neurological ones. Recent research evidences that plants are endowed with feeling [10], complex social relations and can communicate with themselves and with animals, show behaviors similar to sleeping and playing.

Obviously, not only higher plants show intelligent behavior, but also unicellular organisms. For example, the plasmodium of the slime mould physarum polycephalum has the ability to find the minimum-length solution between two points in a labyrinth – a kind of tasks we used to think only animals could perform. Physarum polycephalum shows cognition without a brain, but also without neurons at all [11].

It is well known that the boundary frequencies of the electrical activity of the human brain are common to other mammals [12]. Furthermore, the frequencies of electrical brain activity and the natural frequencies of the electromagnetic activity of the Earth's atmosphere [13] are of the same range. This coincidence suggests that the frequencies of electrical brain activity could be of more fundamental concern and not limited to mammalian neurophysiology and, perhaps, higher plants, being embedded in the electromagnetic environment of the Earth, operate with the same frequencies of electrical activity.

Mammals including human have electrical brain activity [14] of the Theta type in the frequency range between 3 and 7 Hz, of Alpha type between 8 and 13 Hz and Beta type between 14 and 37 Hz. Below 3 Hz the brain activity is of the Delta type, and above 37 Hz the brain activity changes to Gamma. It is the physical separation of different states of brain activity that is essential for its stability. The violation of this separation can cause neurological disorders. In the case of human neurophysiology, Theta-Alpha or Alpha-Beta violation can cause speech and comprehension difficulties [15], depression and anxiety disorders [16].

Hence, the stability of the frequency boundaries separating Theta activity from Delta, and Beta activity from Alpha and Gamma is essential for neurophysiological health. The frequencies 3.0 Hz, 8.2 Hz, 13.5 Hz and 36.7 Hz define the boundaries. What is so special about these frequencies?

In [17] we have shown that the ratios of the boundary frequencies of the brain waves approximate Euler's number and its square root. Being attractors of transcendental numbers, they allow avoiding any resonance between the brain wave boundaries and thus stabilize the central nervous system. Indeed, the natural logarithms of the ratios of the boundary frequencies are close to integer and half values:

$$\ln\left(\frac{8.2}{3.0}\right) = 1.00 \qquad \ln\left(\frac{13.5}{8.2}\right) = 0.50 \qquad \ln\left(\frac{36.7}{13.5}\right) = 1.00$$

Furthermore, in [18] we have shown that these boundary frequencies approximate integer powers of Euler's number relative to the natural frequencies of the proton and the electron:

$$\ln\left(\frac{8.2\,\mathrm{Hz}}{\omega_e}\right) = -46 \qquad \ln\left(\frac{13.5\,\mathrm{Hz}}{\omega_p}\right) = -53$$

where $\omega_e = 7.76344 \cdot 10^{20}$ Hz and $\omega_p = 1.42549 \cdot 10^{24}$ Hz are the angular frequencies of the electron and the proton:

$$\omega_p = \frac{\mathrm{E}_p}{\hbar} \qquad \omega_e = \frac{\mathrm{E}_e}{\hbar}$$

where $\mathrm{E}_p = 938.272$ MeV and $\mathrm{E}_e = 0.511$ MeV are the rest energies of the proton and the electron [19], and $\hbar$ is the reduced Planck constant.

The fact that the brain wave boundary frequencies fit with integer powers of Euler's number relative to the natural frequencies of the proton and the electron indicates that *quantum* physical stability of the frequency boundaries is essential for brain activity.

Similar frequencies we find also in the Earth's electromagnetic spectrum, for example the Schumann resonances. Solar X-ray bursts can cause their variations [20]. In this case, the fundamental 7.8 Hz increases up to 8.2 Hz reaching exactly the stable Theta-Alpha boundary. The second Schumann mode 13.5 Hz coincides precisely with the Alpha-Beta boundary. It is remarkable that solar activity affects this mode much less or does not affect it at all because of its Euler stability. The third Schumann mode currently has a frequency of 20.3 Hz and must increase to 22.2 Hz in order to reach the next island of electron stability. By the way, such an increase is observed recently.

The coincidence of the boundary frequencies of brain activity with Schumann resonances demonstrates how precisely the electrical activity of biological systems is embedded in the electromagnetic activity of the Earth. Important to know that Euler's number and its roots make possible this embedding, because they are attractors of transcendental numbers and form islands of stability. They allow for exchanging information between systems of very different scales – the biophysical and the geophysical. Considering the universality of this embedding, it is very likely that it includes also the bioelectrical activity of plants.

In 1892, Otto Haake [21] showed that light can trigger the bioelectrical activity of plants. Changes in the light conditions may trigger variation in the potential of the guard cell membrane. In 1923, Alexander Gurwich discovered the phenomenon of mitogenetic radiation of biophotons – ultraweak biophysical photon emissions – detected in the UV-range of the spectrum [22]. He observed that these emissions can accelerate cell proliferation. In 1979, Vlail Kaznacheev [23] demonstrated experimentally that IR-A and UV-A biophotons are carriers of intercellular communication. In 1994, Fritz Popp [24, 25] discovered the regulatory significance of coherent biophotonic emissions and of non-random lognormal distributions of physiological parameters. Therefore, we recorded not only the ultradian dynamics of the electrical activity of the plants, but also their bioelectrical response on modulated red and infrared light.

Due to the potential use of bioelectrical phenomena for indicating the physiological condition of plants in agricultural fields, there have been several attempts to analyze these signals and extract their features using statistical and signal processing methods [26].

In his book 'What is Life?', Erwin Schrödinger stated that life feeds on negative entropy, or negentropy [27]. Biosystems are indeed fare from thermodynamic equilibrium, and the second law of classic thermodynamics does not apply to them. Within the thermodynamics of open systems developed by Ilya Prigogine [28], entropy can only be exchanged and, like energy, can neither be generated nor eliminated. From this point of view, Schrödinger's negentropy is a local decrease of entropy that appears as a consequence of entropy exchange of the biosystem with the environment. The ability of lower the own entropy through entropy exchange with the environment seems to be a universal criterion of vitality.

Therefore, for bioelectric signal processing, we applied entropy analysis based on harmonic signal distortion. Over a period of one year, we recorded the ultradian dynamics of the electrical activity in leafs of Orchidaceae phalaenopsis, Aloe vera, Ocimum basilicum and Panax ginseng, including the response on low frequency electromagnetic fields and modulated light.

Methods

Approaches to the study of electrical activities in plants include intracellular and extracellular measurements. The latter can detect the electrical signals produced by the tissue, and is applicable to the monitoring of an individual plant. The bioelectric resting potential across a cell membrane is typically about 50 millivolts. As electrical signals in plants are weak, they usually must be amplified and the recording device must have a high input impedance [29]. Therefore, for recording the bioelectrical signals in plant tissues we used a digital oscilloscope and attached the measuring electrode to a leaf.

For the purpose of shielding against uncontrolled external electromagnetic sources during the measurement, we placed the plant or the leaf in a container made of 1/16 aluminum sheet, similar to the described in [30] polyhedrons. Inside the container we placed also a coil generating a low frequency electromagnetic field. Figure 1 illustrates the experimental setup. Modulated red LED-light we applied as well. For light and field modulation, we chose the brain activity boundary frequencies and further frequencies of electron and proton stability in the range from 3 Hz to 15 kHz.

In [31] we have shown that destabilizing parametric resonance in oscillating systems of any complexity can be avoided

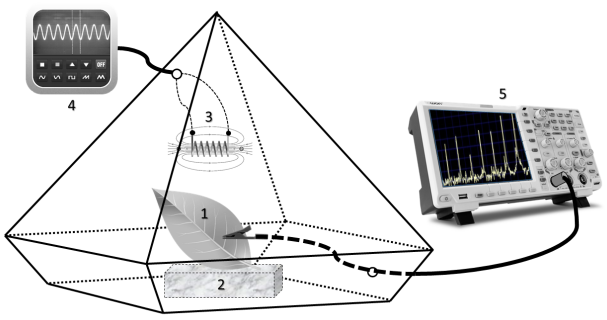

Fig. 1: The experimental setup: The plant or the leaf (1) was placed on a wooden platform (2) in a polyhedral container made of 1/16 aluminum sheet. Inside the container we placed also a coil (3) alimented by a frequency generator device (4). The bioelectrical signals were recorded by a digital oscilloscope (5).

if all frequency ratios correspond to integer powers of Euler's number. Essential for lasting stability in *real* systems is the prevention of proton and electron resonance. Therefore, also biosystems prefer frequencies corresponding to the electron or proton natural frequency divided by integer powers of Euler's number:

$$f_p = \frac{\omega_p}{e^n} \qquad f_e = \frac{\omega_e}{e^m}$$

where f_p and f_e are frequencies of proton respectively electron stability. The exponents n, m are integer.

As we already mentioned, the brain wave boundary frequencies are of electron and proton stability. However, it may be that some frequencies of bioelectrical processes in plants surpass the range of brain waves. Therefore, we applied also higher frequencies of electron and proton stability for field and light modulation (table 1).

n	$f_p = \omega_p/e^n$	m	$f_e = \omega_e/e^m$
46	15,011	39	8,965
47	5,522	40	3,298
48	2,032	41	1,213
49	747	42	446
50	275	43	164
51	101	44	60
52	37	45	22
53	14	46	8
54	5	47	3

Table 1: Frequencies (rounded) of proton f_p and electron f_e stability, which we applied for field and light modulation, and the corresponding integer exponents n, m of Euler's number.

For the purpose of control, we recorded the bioelectrical activity of the same plant or leaf alternately inside and outside the container. In a dark room, we applied also red and infrared light emitted by LEDs having 660 nm and 850 nm peak wavelengths, which was modulated by the same frequencies of electron and proton stability (table 1).

The measuring electrode of the oscilloscope picked up the bioelectrical signal directly from the leaf (fig. 1). The internal FFT-processor of the oscilloscope automatically stored the frequencies and amplitudes (voltages) of the harmonics to built-in memory. Based on the frequencies and amplitudes of the first 8 – 16 harmonics (depending on the field and light modulation frequency), the harmonic distortion HD of the bioelectrical signal was calculated:

$$\mathrm{HD} = \frac{\sqrt{(V_2^2 + V_3^2 + \cdots + V_n^2)/n}}{V_1}$$

where V_n is the n^{th} harmonic voltage and V_1 is the fundamental component. For example, a pure symmetrical triangle wave has HD of 12%, a square wave has 48%, and a sawtooth signal possesses 80%.

In this way, the distortion of a waveform relative to a pure sinewave can be measured by splitting the output wave into its constituent harmonics and noting the amplitude of each relative to the fundamental. The HD indicates the degree of order – disorder associated with the frequency spectrum of a signal. Therefore, we interpret the HD in terms of Shannon's information entropy [32].

Shannon's idea of information is that the value of a communicated message depends on the degree to which the content of the message is surprising. If an event is very probable, it is no surprise; hence the transmission of such a message carries very little information. From this point of view, HD is surprising, because it violates the expected $1/n^2$ decrease of the amplitudes of higher harmonics.

In order to process the HD-calculation automatically, we wrote a software that reads the FFT-datafile directly from the oscilloscope and stores the calculated HD values on SSD.

Results

We started recording the ultradian dynamics of the HD of bioelectrical signals in leafs of Orchidaceae phalaenopsis, Aloe vera, Ocimum basilicum and Panax ginseng in May 2020. To date we made a total of 1014 measurements of the bioelectrical response on low frequency electromagnetic fields and modulated light of these plants alternately inside and outside the shielding container (fig. 1).

The HD of the bioelectrical signals we measured varied between 67 and 88%. Figure 2 shows the ultradian dynamics of the HD measured on leafs in laboratory outside the container under conditions of natural illumination. The ultradian dynamics of HD measured on a leaf of the Orchidaceae phalaenopsis shows the typical increase in HD around noon and

the decrease at sunset (fig. 2a) under otherwise constant environmental conditions. Fig. 2b shows clearly the continuous decrease of HD immediately after the weekly watering of Panax ginseng at 10 am. Even if it rained, but the plant in the laboratory did not get any water, the HD declined slightly. The increase of HD after 10 am in fig. 2c coincides with a powerful thunderstorm. All investigated plants showed similar reactions of HD on thunderstorm.

EXPONENT	FREQUENCY, Hz	HD Basil, %	HD Aloe, %
E46	15,011	83	77
P39	8,965	75	81
E47	5,522	81	76
P40	3,298	74	83
E48	2,032	79	69
P41	1,213	77	80
E49	747	76	71
P42	446	68	74
E50	275	85	81
P43	164	76	84
E51	101	79	67
P44	60	78	83
E52	37	83	81
P45	22	77	82
E53	14	84	75
P46	8	68	82
E54	5	78	69
P47	3	72	81

Table 2: Frequencies applied for field modulation inside the container (fig. 1) and the corresponding daily HD minima for Ocimum basilicum and Aloe vera. In accordance with tab. 1, P-exponents indicate frequencies of *proton* stability while E-exponents indicate frequencies of *electron* stability.

Fig. 2d illustrates how the HD dynamics of Orchidaceae phalaenopsis follows the weather conditions. The decrease in HD during the first 2 hours coincides with increasing cloudiness and the minimum HD with 1 hour of rain. As the cloudiness decreases after the rain, the HD will increase until the plant has been watered. Immediately afterwards the HD falls to the daily minimum. This reaction of the HD to weather conditions confirms that Orchidaceae phalaenopsis as well as Panax ginseng like a humid atmosphere but do not like intense sunlight. Fig. 2e shows the HD dynamics of Ocimum basilicum at the same day. In contrast to Orchidaceae phalaenopsis, increasing cloudiness provokes a significant increase of the HD in the electrical activity of O. basilicum. As the cloudiness decreases after the rain, the HD decreases as well, and the watering causes only a 1% fluctuation of HD. During and after the sunset the HD continuously increases. Obviously, Ocimum basilicum and Aloe vera are light-loving plants and show a significant decrease in HD with moderate sunlight and an increase in HD with a lack of light. All these conformities evidence the suitability of HD measurements for estimating trends in bioelectrical activity of plants.

In addition to these measurements, we studied the ultradian dynamics of HD on the same plants inside the shielding container (fig. 1), where we installed a coil for generating weak electromagnetic fields modulated by brain wave boundary frequencies and other frequencies of electron and proton stability (tab. 1). Inside the container, the plants did show very simple ultradian dynamics of HD with only one minimum and no usual reaction on weather conditions. Fig. 2f shows the HD minimum of Ocimum basilicum at noon. The frequency 453 Hz was applied for field modulation. The signal was sinus.

It is remarkable that the plants showed stable changes in the daily HD minimum as a function of the modulation frequency. Table 2 shows the frequencies of proton (P) and electron (E) stability applied for field modulation inside the container and the corresponding daily HD minima for Ocimum basilicum and Aloe vera. Apparently, O. basilicum prefers P-frequencies, and A. vera E-frequencies. The application of modulated light lead to similar results.

Conclusion

In this paper we introduced HD analysis of bioelectric signals as method of entropy variation measurement that could be applied as an efficient alternative agronomic tool at the service of producers for decision support and as tool of food quality control. Our study evidences that HD analysis of bioelectrical signals is a reliable method for evaluating the vitality of higher plants.

It is very likely that the HD of a bioelectrical signal is not just a measure of its entropy, but a way of bioelectrical intercellular communication. In this case, the relatively high HD values we measured could turn out to be an indicator of information density. Perhaps, the relative amplitude of each harmonic encodes some biologically significant information. This possibility and the ability of plants to communicate with other organisms could be the subject of further research.

Acknowledgements

The authors are grateful to the Community of Living Ethics for permanent support on all stages of the study.

Submitted on September 3, 2021

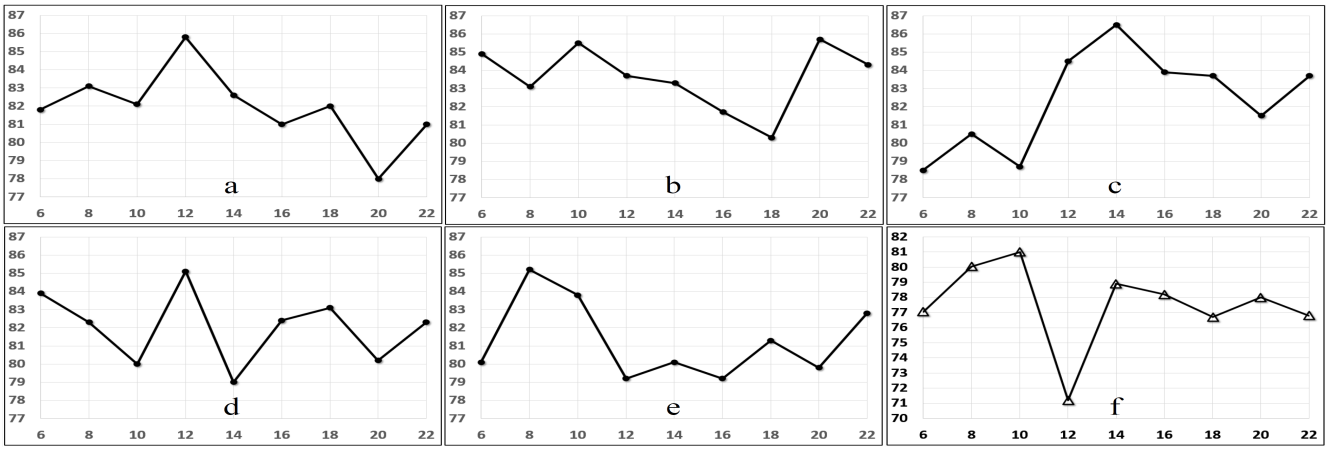

Fig. 2: Some examples of the ultradian dynamics of HD (vertical axes in %) measured on leafs in laboratory under conditions of natural illumination (a - e) and inside the aluminum container (f) in intervals of 2 hours starting at 6 am until 10 pm (horizontal axes). For detailed description, please read the main text.

References

1. Burdon-Sanderson J. Note on the electrical phenomena which accompany irritation of the leaf of Dionaea muscipula. *Proceedings of The Royal Society of London*, 1873, v. 21, 495.
2. Fromm J., Lautner S. Electrical signals and their physiological significance in plants. *Plant, Cell, Environment*, 2007, v. 30, 249–257.
3. Dziubinska H., Trebacz K., Zawadski T. The effect of excitation on the rate of respiration in the liverwort Conocephalum conicum. *Physiologia Plantarum*, 1989, v. 75, 417–423.
4. Davies E., Zawadski T., Witters D. Electrical activity and signal transmission in plants: how do plants know? In: Penel C., Greppin H. Plant signaling, plasma membrane and change of state. *University of Geneva*, 119–137, (1991).
5. Pickard B. G. Action potentials in higher plants. *The Botanical Review*, 1973, v. 39(2), 172–201.
6. Maffei M., Bossi S. Electrophysiology and plant responses to biotic stress. In: Volkov A. G. Plant electrophysiology – theory and methods. Springer-Verlag, 461–481, (2006).
7. Trebacz K., Dziubinska H., Krol E. Electrical signals in long-distance communication in plants. In: Baluska F., Mancuso S., Volkmann D. Communication in plants – neuronal aspects of plant life. Berlin, Heidelberg, *Springer-Verlag* p. 277–290, (2006).
8. Masi E. et al. Spatiotemporal dynamics of the electrical network activity in the root apex. *PNAS*, 2009, v. 106, no. 10, 4053.
9. Baluska F., Mancuso S., Volkmann D. Communication in Plants: Neuronal Aspects of Plant Life. ISBN 978-3-540-28516-8, (2006).
10. Calvo P., Sahi V. P., Trewavas A. Are plants sentient? *Plant, Cell, Environment*, 2017, v. 40, 2858–2869.
11. Nakagaki T. et al. Maze-solving by an amoeboid organism. *Nature*, 2000, v. 407, 470.
12. Stewart M., Fox S. E. Hippocampal theta activity in monkeys. *Brain Research*, 1991, v. 538(1), 59–63.
13. Constable C. Earth's Electromagnetic Environment. *Surveys in Geophysics*, 2016, v. 37, 27–45.
14. Tesche C. D., Karhu J. Theta oscillations index human hippocampal activation during a working memory task. *PNAS*, 2000, v. 97, no. 2, 919–924.
15. Kandana Arachchige Kendra G. et al. The Role of Iconic Gestures in Speech Comprehension: An Overview of Various Methodologies. *Frontiers in psychology*, 2021, v. 12, 634074.
16. Al-Ezzi A., Kamel N., Faye I., Gunaseli E. Review of EEG, ERP, and Brain Connectivity Estimators as Predictive Biomarkers of Social Anxiety Disorder. *Frontiers in Psychology*, 2020, v. 11, 730.
17. Müller H. Chain Systems of Harmonic Quantum Oscillators as a Fractal Model of Matter and Global Scaling in Biophysics. *Progress in Physics*, 2017, v. 13, 231–233.
18. Müller H. Global Scaling. The Fundamentals of Interscalar Cosmology. *New Heritage Publishers*, Brooklyn, New York, USA, ISBN 978-0-9981894-0-6, (2018).
19. Tanabashi M. et al. (Particle Data Group), Phys. Rev. D 98, 030001 (2018), www.pdg.lbl.gov
20. Roldugin V. C. et al. Schumann resonance frequency increase during solar X-ray bursts. *Journal of Geophysical Research*, 2014, v. 109, A01216.
21. Haake O. Über die Ursachen elektrischer Ströme in Pflanzen. *Flora*, 1892, v. 75, 455–487.
22. Gurvich A. G. Mitogenetic radiation. *Gosmedizdat*, Moscow, (1945).
23. Kaznacheev, V. P., Mikhailova, L. P., Radaeva, I. F. et al. Conditions for distant intercellular interaction during ultraviolet radiation. *Bulletin of Experimental Biology and Medicine*, 1979, v. 87, 492–495.
24. Popp F. A., Li K. H., Gu Q. Recent Advances in Biophoton Research and Its Applications. Singapore, (1992).
25. Chang J. J., Fisch J., Popp F. A. Biophotons. *Springer*, (1998).
26. Yan X. et al. Research progress on electrical signals in higher plants. *Progress in Natural Science*, 2009, v. 19, 531–541.
27. Schrödinger E. What is Life? *Cambridge University Press*, (1944).
28. Prigogine I., Nicolis G. Biological order, structure and instabilities. *Quarterly Reviews of Biophysics*, 1971, v. 4, 107–148.
29. Davies E. Electrical signals in plants. In: Volkov A. G. Plant electrophysiology. Berlin, *Springer-Verlag*, p. 407–422, (2006).
30. Müller H. et al. On the Acceleration of Free Fall inside Polyhedral Structures. *Progress in Physics*, 2018, v. 14, 220–225.
31. Müller H. On the Cosmological Significance of Euler's Number. *Progress in Physics*, 2019, v. 15, 17–21.
32. Shannon C. E. A Mathematical Theory of Communication. *Bell System Technical Journal*, 1948, v. 27(3), 379–423.

Ocean Currents and Tidal Movements: The Real Causes

Vladimir I. Danilov

Krasnoselsky, Kostroma, Russia. E-mail: danvlad@bk.ru

This article lists a pretty simple, radically different from other hypotheses, proved by measurement data, universal to any place at planet mechanism of causing currents and tides.

1 Introduction

Currents are classified on the basis of:

1. The causing forces (genetic classifications);
2. Stability;
3. Depth of location in the water column;
4. The nature of movement;
5. Physical and chemical properties.

There are three groups of currents:

- Gradient currents caused by horizontal gradients of hydrostatic pressure, arising when the isobaric surfaces are tilted relative to isopotential (level) surfaces
  - Density caused by horizontal density gradient
  - Compensatory caused by wind-induced sea level tilt
  - Barogradient caused by uneven atmospheric pressure over the sea surface
  - Seiche, resulting from seiche fluctuations in sea level
  - Stock, or wastewater, resulting from the emergence of excess water in any area of the sea (as a result of the influx of continental waters, precipitation, melting ice)
- Currents caused by wind
  - Drift caused only by the enticing action of the wind
  - Wind induced by both the pulling action of the wind and the inclination of sea level and changes in the density of the water caused by the wind
- Tidal currents caused by tides
  - Rebound current

All these types of currents do not explain the main permanent global current near the equator, directed from East to West, which, in the absence of continents, would be closed in round-like dust rings as in the atmosphere of Jupiter. (The nature of the equatorial countercurrent is not considered here. You can learn about it in the book *Equatorial countercurrents in the oceans* by V. B. Shtokman Leningrad 1948 [2].) .

2 A modern view of the causes of currents and tides

Sometimes the formation of currents is attributed to the Coriolis forces, while not taking into account that these forces are not real but conditional, used to describe different linear velocities of motion for points at different distances from the center on the radius, when the body rotates. In the case of the Earth's rotation, there is no movement of water along the radius, which can cause the appearance of such forces and such a constant movement of water around the circle.

Oceanic tides in modern scientific literature are considered as the rise of water due to the attraction from the Sun and the Moon, and at the same time they constantly try, using correction factors and various models, to lead to some kind of mathematics [1], considering that the Earth is, as it were, a body with its own vibration frequency. At the same time, forgetting that any oscillations have a decay time, and the processes under consideration last for many years. In fact, without identifying the main causes of the tides, this method is no better, and even worse, due to its complexity, a simple statistical table, that is, a method that has long been successfully used in the practice of navigation.

And the difference in the forces of gravity on an interval even of several kilometers (let's say that this is the depth of the ocean) at a distance of 380 000 km from the Moon, and 150 000 000 km from the Sun, cannot be so great as to cause the rise and movement of water. And this despite the fact that the entire mass of the Earth is nearby, which is much larger than the Moon.

The emphasis on tidal forces caused by the influence of the Sun and the Moon during the rotation of the Earth is made, for example, in the article [3], where a moving "hump" of the mantle allegedly causes the movement of water (discrete-wave motion). But it is not taken into account that the hump moves at a depth, and the main flows of the current do not fall below 200 meters [2], thus such a mechanism cannot work.

The action of tidal forces directly on the body of the ocean also cannot cause such a flow, for the reason that these forces act on masses of water, first from the East, and then in the same way from the West. Even if, which is not possible, they will first shift the mass of water in one direction, then they will return it back by the same amount.

Fig. 1 shows the current map and a conventional drawing [3] showing the similarity of the structures of large-scale currents of the Pacific, Atlantic and Indian oceans.

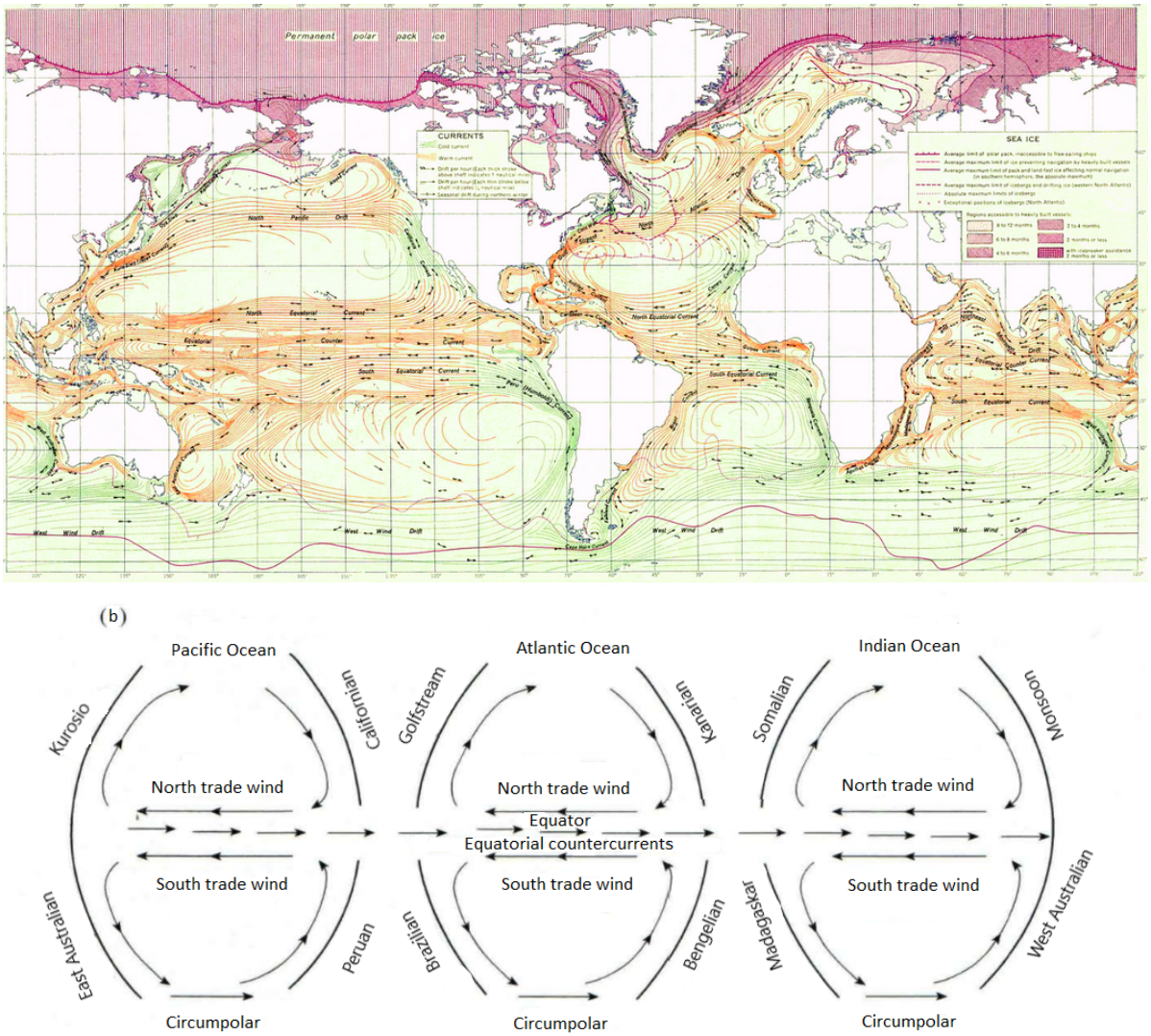

Fig. 1: Current map (1a) and a conventional drawing (1b) [3] showing the similarity of the structures of large-scale currents of the Pacific, Atlantic and Indian oceans.

3 The real reasons causing currents and tides

But there are currents and quite significant – the speed of movement is measured from 30 to 150 cm/s [2], which means there is a force that causes it. Moreover, this force is centuries old, constant direction. There are no external, observable forces. So there are internal ones.

Let's imagine the Earth as a kind of ball with a rather thin, relative to the total volume, shell, which can deform from the movement of the internal mass, if it is attracted to the external mass (Sun, Moon). Roughly it can be compared with an inflated air ball into which water has also been poured. Water, due to the force of gravity, will cause deformation of the shell, and when the ball rotates, this deformation will move in a circle. This is an analogue of the tide of a solid part of the Earth. But this is not an ocean tide! The high tide near the coast on the water will be caused by the ebb from the point of maximum rise of the mainland to the shores. If, for example, you pour water into a plastic plate and press from below, then the water will overflow to the edges. This fact is clearly visible when overlaying the graphs of the measured behavior of gravitational forces, the graph of the water level and the positions of the Sun and Moon at one measurement point.

In Fig. 2 (and also in Fig. 3), the maximum rise of water at high tides is clearly visible near the shores of the oceans. Fig. 2 shows measurement data at station "Posiet" of the Pacific coast, where

- On the horizontal axis Universal Time.
- Black is the measured force of gravity in μgal.
- Red is the Sun position.

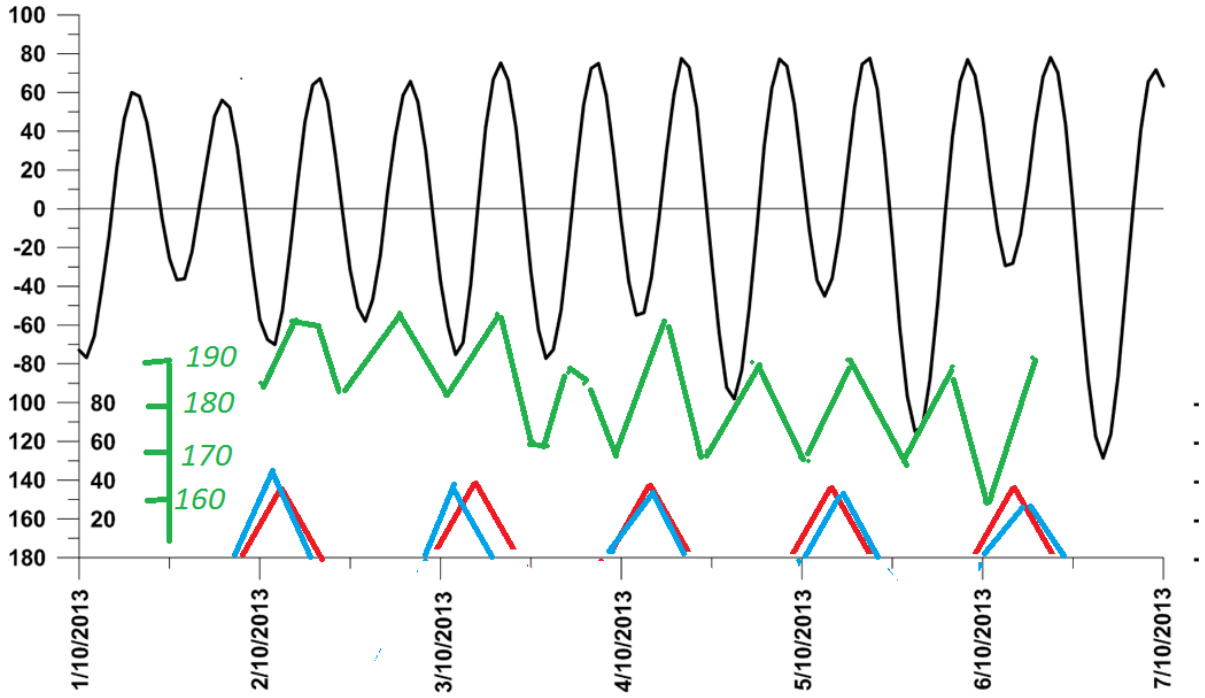

Fig. 2: Measurement data. Station "Posiet" of the Pacific coast.

- Blue is the position of the Moon in degrees above the horizon (time of sunrise, maximum position, sunset).
- Green is the ocean water level in cm.

The time interval is specially selected when the Sun and the Moon are close to the sky and at the same time affect the core of the Earth.

Measurement data of grav: the forces were provided by the staff of the laboratory of gravimetry of the POI FEB RAS. Station coordinates:

- ELLIPSOIDAL LATITUDE (DEGREE) 42.583
- ELLIPSOIDAL LONGITUDE (DEG. EAST) 131.158

Ocean level data: measurements taken at Posiet station, courtesy of the staff.

The data of the times of rise, maximum position, set and angle of ascent of the Sun and Moon were taken from the StarCalc program with reference to the station location.

It can be seen that a couple of hours before the passage of the Sun and the Moon to the zenith point, there is an ebb and flow of water and at the same time a decrease in the force of gravity, i.e. tide of the solid part of the planet. The ebb of water is also visible at night, when the tide of the mantle occurs from the departure of the planet's core to the opposite part of the Earth.

The time interval was specially selected when the Sun and the Moon are close and simultaneously affect the core of the Earth.

It is this fact that explains not the coincidence of the tides, but the coincidence of the ebb on the water with the positions of the Sun and the Moon at the zenith.

The "hump" on the mantle will change its position and size depending on:

- season (tilt of the axis of rotation);
- remoteness of the Moon and the Sun from the Earth;
- "dephasing", i.e. different positions between the Moon and the Sun;

then the tide near the coast will not be constant, but depend on these factors.

Now about the rise (tide) of the mantle on the opposite side of the globe. Unfortunately, it is difficult to demonstrate clearly, as in the first case, but even here everything is quite simple. The mass of the planet's core displaced towards the Sun and Moon will weaken the force of attraction on the opposite side of the ball in proportion to the square of the displacement distance. In the above graph, these will be the dips of the gravitational forces (black) during periods when there is neither the Sun nor the Moon above the measurement point. There is no other way to explain such a decrease in the forces of attraction, since the gravimeter reacts only to the force of attraction (mass).

In this way, multidirectional forces act on the gravimeter sensor:

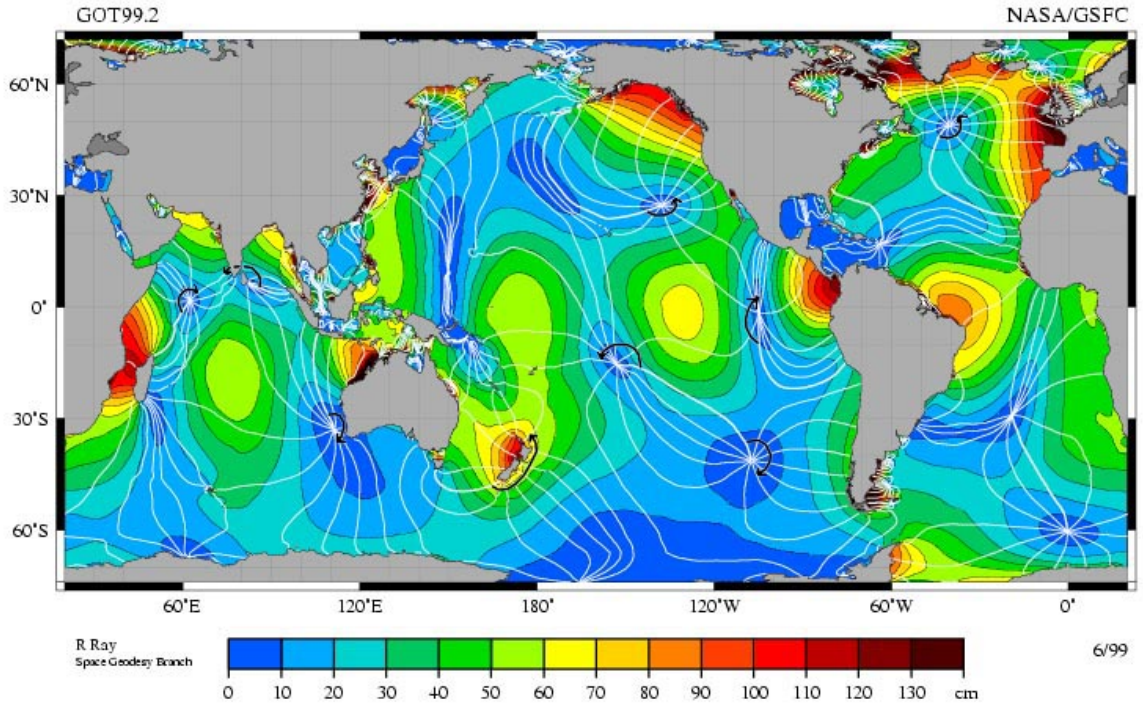

Fig. 3: Codial lines.

- attraction from the bulk of the Earth – constant force;
- attraction from the sun – variable force;
- attraction from the moon – variable force;
- attraction from the moving mass of the Earth's core – variable force, depending on the position of the Sun, Moon, season.

Based on the fact that there are many variables, mutually related quantities, calculating the mass of the moving part of the Earth's core is difficult (at least for me). When the Earth rotates, the "hump" will describe cyclic circular trajectories – this is the only observed movement in one direction, coinciding with the direction of movement of the main oceanic current [3]. The force of attraction of the mass of the moving inner core of the planet close to the water will force the mass of water to move in the same direction, but with a different force depending on the season. This is the reason for the main ocean current.

Since the bulk of the core moves in the equatorial region, the waters near the equator are also set in motion. Meeting the continents on its way, this current diverges to the sides of the equator and, since the basins of the oceans are practically closed, the water for the most part moves in a closed loop (see Fig. 1).

The change in the water level of the seas and oceans is only a demonstration of the change in the level of the solid surface of the planet. Water, due to the properties of fluidity, changes its level depending on the topography of the bottom and the coast. At the same time, the values of changes in the solid shell of the Earth depend on its structure and thickness. Mountain and continental massifs with large deep parts will naturally be less affected than lower, thinner, underwater areas. That is why the waters of the lakes practically do not change their level, since they are located on the body of massive continents and at the same time the level of the bottom of the entire reservoir changes slightly. On the plain of the oceans, amphidermal points (where there are no tides) and codial lines (lines connecting all points on the map where the crest of a tidal wave appears simultaneously, that is, points in which full water occurs simultaneously). If the tide would arise only from exposure to water, this could not be.

4 Conclusion

In addition to the processes under consideration, the movement of the planet's core leads to such consequences as the formation of the Earth's magnetic field, mountain building, continental drift, earthquakes, an astronomical shift relative to the reference time, *etc* [4].

Received on August 13, 2021

References

1. Melchior P. Earth Tides. MIR Publishing House, Moscow, 1968.
2. Shtokman V. B. Equatorial countercurrents in the oceans. Gidrometeoizdat, Leningrad, 1948.
3. Garetsky R. G., Dobrolyubov A. I. Tidal discrete-wave motions and continental drift. *Geotectonics*, 2016, v. 1, 3–13.
4. Danilov V,I. Consequences of the mutual influence of the planets. *Geophysical Bulletin*, 2017, v. 3, 11.

Searching for the Feynman Diagram IIc

Oliver Consa
Department of Physics and Nuclear Engineering, Universitat Politècnica de Catalunya
Campus Nord, C. Jordi Girona, 1-3, 08034 Barcelona, Spain.
E-mail: oliver.consa@gmail.com

The calculation of the electron g-factor was carried out in 1950 by Karplus and Kroll. Seven years later, Petermann detected and corrected a serious error in the calculation of a Feynman diagram. Although it's hard to believe, neither the original calculation nor the subsequent correction was ever published. Therefore, the entire prestige of QED and the Standard Model depend on the calculation of a single Feynman diagram (IIc) that has never been published and cannot be independently verified. In this article, we begin the search for any published recalculation of this Feynman diagram IIc that allows us to independently validate the theoretical calculation.

1 The big problem

1.1 Renormalization

The Standard Model of Particle Physics brings together two different physical theories: Electroweak Theory (EWT) and Quantum Chromodynamics (QCD). For decades, a "Grand Unification Theory (GUT)" has been unsuccessfully sought to integrate both theories into one unified theory.

Both QCD and EWT are mainly mathematical theories. The aim is to identify a set of gauge symmetries for each theory that allows a concrete mathematical formulation to be obtained. EWT forms a $SU(2)\times U(1)$ symmetry gauge group while QCD forms a SU(3) symmetry gauge group. The theory is considered correct if the theoretical values obtained with these mathematical formulas coincide with the experimental values obtained with particle colliders.

Both QCD and EWT are based on and completely dependent on the validity of quantum electrodynamics (QED), developed by Feynman, Schwinger, and Dyson. QED in turn is a quantum field theory (QFT). QFT emerged in the 1930s in an attempt to quantify the electromagnetic field itself. But QFT has a serious problem. All calculations give the same result: Infinity.

In the 1940s, QED developers managed to solve the infinities problem using a technique called "Renormalization". Many methods can be used to eliminate these infinities, but the main ones are:

- Substitution: replacing a divergent series with a specific finite value that has been arbitrarily chosen (for example, the energy of an electron).
- Separation: separating an infinite series into two components, one that diverges to infinity and another that converges to a finite value. Eventually, the infinite component is ignored and only the finite part remains.
- Cut-off: focusing on an arbitrary term in the evolution of a series that diverges to infinity and ignoring the rest of the terms of the series.

As an example of the use of these Renormalization techniques we can look at the calculation of the Casimir effect [4]. The equation of the Casimir effect depends on the Riemann function. However, the Riemann function is defined only for positive values, since for negative values the Riemann function diverges to infinity.

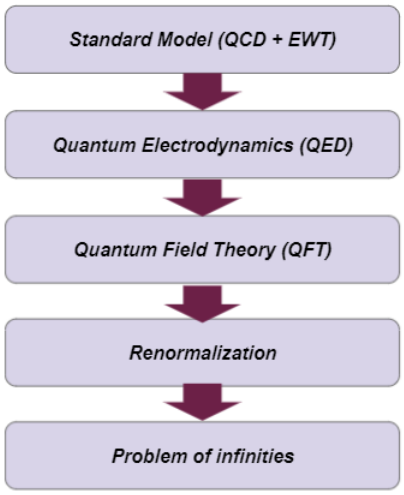

Fig. 1: Layers of logical dependencies.

$$\frac{F_c}{A} = \frac{d}{da}\frac{< E >}{A} = -\frac{\hbar c\pi^2}{2a^4}\,\zeta(-3) = \frac{\hbar c\pi^2}{20a^4}\,\zeta(-1) \qquad (1)$$

In particular the Riemann function of -1, $\zeta(-1)$, corresponds to the value of the sum of all positive integers. Applying a Renormalization technique, the Indian mathematician Ramanujan came to the conclusion that the sum of all positive integers is not infinity but $-1/12$ [3]. And this is precisely the value that is used in the equation of the Casimir effect.

$$\zeta(-1) = \sum_{n=1}^{\infty} n = 1 + 2 + 3 + 4 + 5 + ... = \frac{-1}{12} \qquad (2)$$

$$\frac{F_c}{A} = \frac{\hbar c\pi^2}{20a^4}\left(\frac{-1}{12}\right) = -\frac{\hbar c\pi^2}{240a^4} \qquad (3)$$

Despite being one of the main creators of QED, Feynman was not very convinced about Renormalization:

> The shell game that we play is technically called 'renormalization'. But no matter how clever the word, it is still what I would call a dippy process! Having to resort to such hocus-pocus has prevented us from proving that the theory of quantum electrodynamics is mathematically self-consistent. It's surprising that the theory still hasn't been proved self-consistent one way or the other by now; I suspect that renormalization is not mathematically legitimate. [1]

For his part, Dirac was always clearly against these techniques:

> I must say that I am very dissatisfied with the situation because this so-called 'good theory' does involve neglecting infinities which appear in its equations, ignoring them in an arbitrary way. This is just not sensible mathematics. Sensible mathematics involves disregarding a quantity when it is small – not neglecting it just because it is infinitely great and you do not want it! [2]

Today, the scientific community accepts these renormalization techniques as fully legitimate. But if Dirac was right and renormalization is not a legitimate mathematical technique, then the Standard Model, EWT, QCD, QED and all theories based on QFT would be incorrect and worthless.

1.2 QED precision

The entire credibility of the renormalization techniques is based on its level of precision of the theoretical value with respect to the experimental value. As an example, the electron g-factor offers an impressive level of precision of 12 decimal places:

- Experimental value [12]: 1.001 159 652 180 73 (28),
- Theoretical value [13]: 1.001 159 652 182 032 (720).

In 1970, Brodsky and Drell summarised the situation in their paper *The present status of the Quantum Electrodynamics* as follows:

> The renormalization constants are infinite so that each calculation of a physical quantity has an infinity buried in it. Whether this infinity is a disease of the mathematical techniques of perturbation expansions, or whether it is symptomatic of the ills accompanying the idealization of a continuum theory, we don't know. Perhaps there is a "fundamental length" at small distances that regularizes these divergences (...). Quantum electrodynamics has never been more successful in its confrontation with experiment than it is now. There is really no outstanding discrepancy despite our pursuing the limits of the theory to higher accuracy and smaller (...) however, and despite its phenomenal success, the fundamental problems of renormalization in local field theory and the nature of the exact solutions of quantum electrodynamics are still to be resolved. [14]

It seems inconceivable that using an incorrect theory, we can obtain the correct results with an unprecedented level of precision. And it is extremely unlikely that this finite theoretical value coincides with the experimental value by pure chance. Therefore, the only reasonable explanation is that renormalization techniques must be mathematically legitimate even though we cannot prove it at the moment.

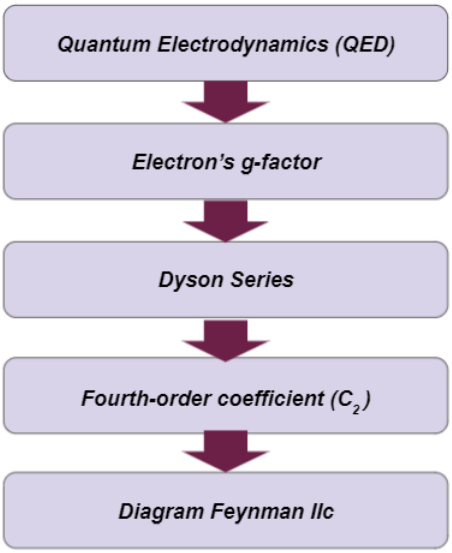

Fig. 2: Layers of logical dependencies.

1.3 Dyson series

Quantum Electrodynamics (QED) is considered the most accurate theory in the history of science. However, this impressive precision is limited to a single experimental value: the anomalous magnetic moment of the electron (g-factor).

According to Quantum Electrodynamics (QED), the theoretical value of the electron g-factor is obtained by calculating the coefficients of a number series called the Dyson series [4]. Each coefficient in the series requires the calculation of an increasing number of Feynman diagrams.

$$g = C_1\left(\frac{\alpha}{\pi}\right) + C_2\left(\frac{\alpha}{\pi}\right)^2 + C_3\left(\frac{\alpha}{\pi}\right)^3 + C_4\left(\frac{\alpha}{\pi}\right)^4 + C_5\left(\frac{\alpha}{\pi}\right)^5 \ldots \quad (4)$$

The first coefficient in the Dyson series is the Schwinger factor and has an exact value of 0.5. The second coefficient was initially calculated in 1950 by Karplus and Kroll [5], and it was corrected in 1957 by Petermann [6], who obtained a result of -0.328. The rest of the coefficients in the Dyson series were calculated many decades later with the help of supercomputers.

$$g = 1 + \frac{1}{2}\left(\frac{\alpha}{\pi}\right) - 0,328\left(\frac{\alpha}{\pi}\right)^2 = 1,0011596 \quad (5)$$

This result of the C_2 coefficient (fourth-order coefficient) of the Dyson series was decisive for the acceptance of the

renormalization techniques proposed by Feynman, Schwinger, and Tomonaga, who received the Nobel Prize in 1965 for the development of QED. It can therefore be considered the most relevant theoretical calculation in modern physics.

1.4 Feynman diagram IIc

The error in the calculation of C_2 discovered by Petermann was found in the calculation of the Feynman diagram IIc.

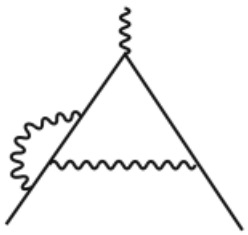

Fig. 3: Feynman diagram IIc.

According to the Karplus and Kroll original calculation, the value of diagram IIc was -3.178 while in the Petermann correction the value of diagram IIc was -0.564.

[Karplus & Kroll]

$$II_c = -\frac{323}{24} + \frac{31}{9}\pi^2 - \frac{49}{6}\pi^2 \ln(2) + \frac{107}{4}\zeta(3) = -3.178 \quad (6)$$

[Petermann]

$$II_c = -\frac{67}{24} + \frac{1}{18}\pi^2 + \frac{1}{3}\pi^2 \ln(2) - \frac{1}{2}\zeta(3) = -0.564 \quad (7)$$

However, hard to believe, neither the original calculation carried out in 1950 by Karplus and Kroll nor the subsequent correction of Petermann were ever published. Therefore, the entire legitimacy of the Standard Model and QED depends on the calculation of a single Feynman diagram (IIc) that has never been published and cannot be independently verified [11].

2 Searching for the missing calculation

2.1 Barbieri & Remiddi

At this point, we set out on a mission to find the missing calculation of the Feynman diagram IIc. We assume that given the seriousness of the situation, someone must have recalculated previously this Feynman diagram and published it years ago.

After a long search, we believe we found the paper we were looking for. It is a paper published in 1972 and written by Remiddi among other authors [8]. Remiddi is one of the most prestigious researchers in the calculation of the electron g-factor because in 1996 he published the definitive analytical value of the C_3 coefficient (sixth-order coefficient).

The paper is a long 93-page document entitled *Electron form factors up to fourth order*. It was published in 1972 by Barbieri and Remiddi. According to the authors:

> This paper is devoted to the analytic evaluation of the two form factors of the electromagnetic vertex of the electron in quantum electrodynamics, up to fourth order of the perturbative expansion (...) [Calculation] of the fourth-order form factors can also be found in the literature. They are the famous fourth-order anomalous magnetic moment evaluated by Petermann and Sommerfield (...). Such values are obviously reproduced in this paper. (...) Calculations are done in the framework of the usual Feynman-graph expansion of the S-matrix in the interaction representation, using the Feynman gauge for the photon propagator. The relevant graphs for second-order and fourth-order radiative corrections are shown (..). The approach is dispersive, and the discontinuities of the various Feynman graphs are obtained by means of the Cutkosky rules. [8]

From this introduction we understand that Barbieri and Remiddi performed a recalculation of the Feynman diagrams corresponding to the fourth-order coefficient (C_2) and they confirmed the results obtained by Petermann.

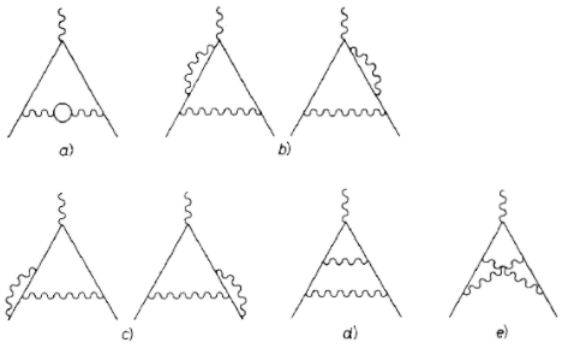

Fig. 4: C_2 Feynman diagrams.

The authors identify the Feynman IIc diagram as the "c" diagram in Fig. 4, divide it into two symmetrical diagrams and give it the descriptive name of "Corner Graphs". The result shown in the paper is identical to that published by Petermann in 1957.

In the 93 pages of the paper, the authors describe several of the techniques they have used to renormalize the divergences that appear in the calculations and how they have overcome the problems they have encountered. On the specific calculations, the authors state the following:

> Once these problems are mastered, a very long and complicated algebra is also needed to do in practice the calculation. Fortunately, the major part of it, like traces, straightforward algebraic manipulations, bookkeeping of analytic formulae, integrations by parts, differentiations and so on, was done by computer, us-

> ing the program SCHOONSCHIP of VELTMAN, without whose continuous and determinant help the present work could hardly have been accomplished. [8]

That is, they used a computer program to perform the mathematical calculations, but they did not publish the code of the programs used, so again, it is not possible to replicate the calculations.

Considering the date of the paper (1972) it is quite plausible to assume that there are no more calculations, since it was considered unnecessary to carry out more checks of the C_2 coefficient. Fortunately, in the paper itself, the authors identify two other independent calculations of the C_2 coefficient. One published in 1960 by Smrz and Uleha and the other published in 1962 by Terentiev.

2.2 Smrz & Uleha

We obtained the paper published in 1960 by these two Czech researchers [9]. It is a short paper of two pages where the situation generated in 1957 by Petermann's correction is explained. The paper indicates that the difference between the original Feynman IIc diagram calculation of Karplus and Kroll with respect to the one performed by Petermann is excessive. The authors state that they performed an independent calculation of the Feynman IIc diagram and obtained exactly the same result as Petermann.

> Since the considerable difference between the original value of the magnetic moment (Karplus & Kroll [5]) and the values calculated later (Petermann [6]) originates in the calculation of the contribution from the third diagram, only the value of this contribution was determined by the standard technique and the above regularization in the infra-red region. The contribution from the third diagram (-0.564) is in complete agreement with Petermann's value. [9]

Unfortunately, when searching for the reference of the work we note that it has not been published either: *Smrz P., Diploma thesis, Faculty of Tech. and Nucl. Physics, Prague 1960, unpublished*.

Just another unpublished paper claiming to have calculated the Feynman IIc diagram but with no one to review it.

2.3 Terentiev

We obtained a copy of the paper published by Terentiev in 1962. The paper contains about 50 pages [10]. The paper is only in Russian and there is no English translation. We identify the equation "60" of the paper as the C_2 coefficient of the Dyson series, with the same expression and value obtained by Petermann and Sommerfield.

$$g = 1 + \frac{1}{2}\left(\frac{\alpha}{\pi}\right) - 0,328\left(\frac{\alpha}{\pi}\right)^2 = 1,0011596 \qquad (8)$$

Analyzing the document, we interpret that this equation is the result of the sum of nine other equations identified as equations 22, 24, 27, 31, 33, 47, 51, 58 and 59. There are nine equations instead of the five Feynman diagrams of Karplus and Kroll and none of the these equations correspond to the Feynman Diagram IIc.

However, it is not necessary to carry out a more in-depth analysis of the paper. On the first page of the Barbieri-Remiddi paper we can read a reference to Terentiev's paper:

> Actually, dispersion relations are used in the Terentiev work only to write down suitable multiple integral representations, which are in general manipulated to get the final result, without explicitly evaluating the discontinuities. The problem of infra-red divergences has been further overlooked, and many of the intermediate results are wrong, even if somewhat ad hoc compensations make the final result correct.

Year	Author	Status
1950	Karplus & Kroll	Wrong and unpublished
1957	Petermann	Right but unpublished
1957	Sommerfield	Right but using Green Functions instead of Feynman diagrams
1960	Smrz & Uleha	Right but unpublished
1962	Terentiev	Wrong intermediate results with ad hoc compensations to make the final result correct
1972	Remiddi	Right but unpublished computer calculation

Table 1: Fourth-order coefficient calculations.

3 Summary

Incredible as it may seem to believe, the most important calculation in the history of modern physics was published in 1950 by Karplus and Kroll and turned out to be completely incorrect. The error was not detected until seven years later by Petermann and Sommerfield. Neither the original calculation nor the subsequent correction was ever published. Therefore, the entire legitimacy of the Standard Model and QED depends on the calculation of a single Feynman diagram (IIc) that has never been published and cannot be independently verified.

In this paper we have detected three other published recalculations of the fourth-order coefficient of the g-factor. The detailed calculations of two of them were also not published (Barbieri-Remiddi and Smrz-Uleha). In the third calculation performed by Terentiev, serious errors were detected ten years after the original publication. Erroneous intermediate results manipulated with ad hoc compensations to obtain the correct final result.

Our search has been extensive, so we believe that there are no other published calculations of the Feynman IIc dia-

gram. The only line of investigation that remains open would be to find the source code of the computer programs that are currently used to carry out this type of calculation.

Submitted on August 27, 2021

References

1. Feynman R. P. QED: The Strange Theory of Light and Matter. Princeton University Press, Pinceton, 1985. ISBN 0691024170.
2. Kragh H. Dirac: A scientific biography. Cambridge University Press, Cambridge, 1990. ISBN 0521017564.
3. Baez J. Euler's Proof That 1 + 2 + 3 + ⋯ = - 1/12. http://math.ucr.edu/home/baez/qg-winter2004/zeta.pdf, 2003.
4. Casimir H. B. G., Polder D. The Influence of Retardation on the London-van der Waals Forces. *Phys. Rev.*, 1948. v. 73 (4), 360–372.
5. Karplus R., Kroll N. Fourth-order corrections in quantum electrodynamics and the magnetic moment of the electron. *Phys. Rev.*, 1950. v. 77 (4), 536–549.
6. Petermann A. Fourth order magnetic moment of the electron. *Helvetica Physica Acta*, 1957, v. 30, 407–408.
7. Sommerfield C. M. Magnetic Dipole Moment of the Electron. *Phys. Rev.*, 1957, v. 107 (1), 328–329.
8. Barbieri, Mignaco, Remiddi. Electron Form Factors up to Fourth Order. I & II. *Il Nuovo Cimento*, 1972, v. 1 (4), 824–916.
9. Smrz P., Ulehla I. Electrodynamic corrections to magnetic moment of electron. *Czech. Journ. Phys.*, 1960, v. 10, 966–968.
10. Terentiev M. V. *Zh. Eksp. Theor. Fiz.*, 1962, v. 43, 619.
11. Consa O. The unpublished Feyman Diagram IIc. *Progress in Physics*, 2020, v. 16 (2), 128–132.
12. Hanneke D., Fogwell S., Gabrielse G. New Measurement of the Electron Magnetic Moment and the Fine Structure Constant. *Phys. Rev. Lett.*, 2008, v. 100 (12), 120801–120805.
13. Aoyama T., Kinoshita T., Nio M. Revised and improved value of the QED tenth-order electron anomalous magnetic moment. *Phys. Rev. D.*, 2018, v. 97 (3), 036001.
14. Brodsky S. J., Drell S. D. The present status of the Quantum Electrodynamics. *Ann. Rev. Nucl. Part. Sci.*, 1970, v. 20, 147–194.

The Curse of Dimensionality in Physics

P. Reshma[1], P. Prasanth[2], and K. M. Udayanandan[3]

[1]Department of Physics, S N Polytechnic College, Kanhangad 671315, India. E-mail: reshmaperayil@gmail.com
[2]Department of Physics, Govt. Engineering College, Thrissur 680009, India. E-mail: prasanthpnairg@gmail.com
[3]Department of Physics, Associate Professor (Rtd), NAS College, Kanhangad 671314, India.
Corresponding author E-mail: udayanandan@gmail.com

The curse of dimensionality is a well-discussed issue in mathematics. Physicists also require n-dimensional space but because of the phase space choice, there is no need to worry about its consequences. This issue connected with dimensionality and related problems are discussed in this paper.

1 Introduction

We live in a 3-dimensional world and any dimension beyond this is called hyper-dimension. In the early decades of the 19th century, many articles were published listing works on "hyper-volume and surface" n-dimensional geometry. Swiss mathematician Ludwig Schlafli wrote a treatise on the subject in the early 1850's [1]. In 1858, a short description of this was translated into English by Arthur Cayley which gives the volume formula for an n-ball, commenting that it was determined long ago. In this paper, there were footnotes citing papers published in 1839 and 1841 [2] by the mathematician Eugene Catalan regarding descriptive geometry, number theory, *etc*. Though the earliest works encountered problems in computations, it was William Kingdon Clifford who published a solution in 1866 [3]. In the 1897 thesis, Heyl derived formulas for both volume and surface area and gives a clear idea of multidimensional geometry [4]. In 1911, Duncan Sommerville published a bibliography of non-Euclidean and n-dimensional geometry [5] giving the details on the works on hyper-sphere volumes. A book *An Introduction to the Geometry of N Dimensions* [6], by Duncan Sommerville, was published in 1929 which explains the n-ball formula and has a table of values for dimensions 1 to 7. In this paper, in the first section, we will give the formula for hyper-volume whose derivation is available in many statistical mechanics textbooks [7, 8]. In the other sections, we will discuss the so called "curse of dimensionality" and its consequences.

2 Hyper-volume

The n-dimensional volume of an Euclidean ball of radius R in n-dimensional Euclidean space [9] is

$$V_n(R) = \frac{\pi^{\frac{n}{2}}}{\Gamma\left(\frac{n}{2}+1\right)} R^n \,, \tag{1}$$

where Γ is Euler's gamma function. The gamma function extends the factorial function to non-integer arguments. The volume of an n-dimensional sphere depends on the radius of the sphere (if we are considering the momentum space, the radius will be momentum) and the number of degrees of freedom. Now we want to know how the variation in n and R affects volume. For that, in the next section, we will numerically evaluate the variation of hyper-volume with increasing n for different radius.

3 The curse of dimensionality

We are all accustomed to live in low dimension spaces, mostly up to three dimensions. But relativity says we live in four dimensions [10] where the fourth dimension is time. String theory uses about ten dimensions [11, 12]. Our intuition about space can be misleading in high dimensions, rather more surprises awaits us there. Consider the case of an n dimensional sphere, and let us evaluate the volume for different dimensions for radius $R = 1$ and $R = 1.5$ which are given in Table 1. Initially an increase in volume is observed but later, volume decreases dramatically and almost approaches to zero at higher and higher dimensions. This effect is called the "curse of dimensionality" [13], often described as a phenomenon that arises when studying and using high-dimensional spaces. For $R = 1$, we can see that after reaching 5.26 the volume decreases, whereas for $R = 1.5$, after reaching 177.22, the volume decreases. These numbers depend on how the ratio $\pi^{\frac{n}{2}}/\Gamma(\frac{n}{2}+1)$ changes with n. Richard Bellman was the one who coined the term in 1957 [14, 15] when considering problems in dynamic programming.

In Fig. 1, we plot a graph with n along the x-axis and volume along the y-axis for ($R = 1$, 1.05, 1.10, 1.15, 1.20). In the graph, we can see that the volume first increases with n, reaches a maximum value for a particular value of n, called n_{max}. If we increase n further, the volume decreases. We can see that n_{max} shifts towards the right when R increases. All plots show that the volume of the n-ball vanishes to nothing as n approaches infinity.

4 What is really happening to the volume for large n?

First, we will check how the dimension will be influenced by the radius R. Taking the logarithm of the expression for the n-dimensional volume and applying Stirling's approximation in (1), we get

$$\ln V_n(R) \simeq \frac{n}{2} \ln \pi + n \ln R - \frac{n}{2} \ln \frac{n}{2} + \frac{n}{2} \,. \tag{2}$$

Dimension n	V_n for $R = 1$	V_n for $R = 1.5$
0	1	1
1	2	3
2	3.14	7.06
3	4.19	14.13
4	4.94	24.98
5	5.26	39.97
6	5.17	58.86
7	4.73	80.72
8	4.06	104.02
9	3.30	126.80
10	2.55	147.05
11	1.88	162, 97
12	1.33	173.24
13	0.91	177.22
14	0.59	174.94
15	0.38	167.03

Table 1: Values of hyper-volumes for $R = 1$ and $R = 1.5$.

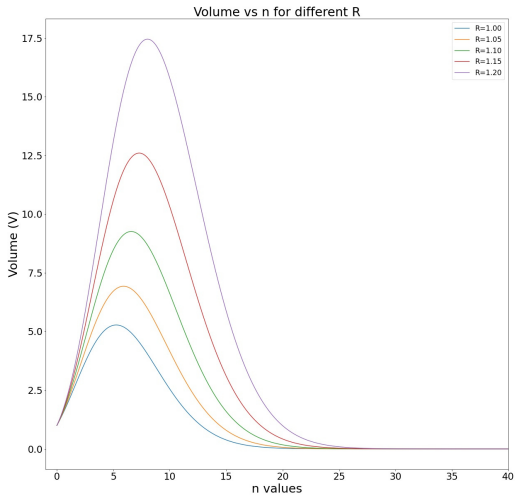

Fig. 1: A graph between n and volume for $R = 1$, 1.05, 1.10, 1.15, 1.20.

To find when the volume will decrease for different R, we take the derivative with respect to n of the above equation which gives

$$\frac{1}{V_n(R)}\frac{dV_n(R)}{dn} \simeq \frac{1}{2}\ln\pi + \ln R - \frac{1}{2}\ln\frac{n}{2}\,. \tag{3}$$

In order for the volume to be a maximum, $\frac{dV_n(R)}{dn}$ must be zero for a particular n. Hence we obtain

$$n_{max} \simeq 2\pi R^2\,. \tag{4}$$

This relation of n_{max} for various R has a parabolic-type dependence which means the radius has no role in the decrease of volume. Next, we will find out what is happening to the volume for large n. There are arguments to show that data confined in the volume will be spreading to an outer shell for large n [16, 17]. Let us check whether this is true or not. For a sphere with radius ΔR less than R, the volume will be

$$V_n(R) = \frac{\pi^{\frac{n}{2}}}{\Gamma\left(\frac{n}{2}+1\right)}(R-\Delta R)^n\,. \tag{5}$$

The volume of the shell will be given by subtracting (1)−(5). We calculated the volumes of n-dimensional spheres and shells for different n which is given in Table 2. A graph is also plotted with n along the x-axis and volumes of n-dimensional sphere and shell along the y-axis as in Fig. 2.

Dimension n	$V_n(R)$	$V_n(\Delta R)$
4	4.93	1.69
5	5.26	2.15
10	2.55	1.66
15	0.38	0.30
20	0.02	0.02
99	9.47×10^{-40}	9.47×10^{-40}
100	2.36×10^{-40}	2.36×10^{-40}

Table 2: Values of volumes of n-dimensional sphere and shell for different n.

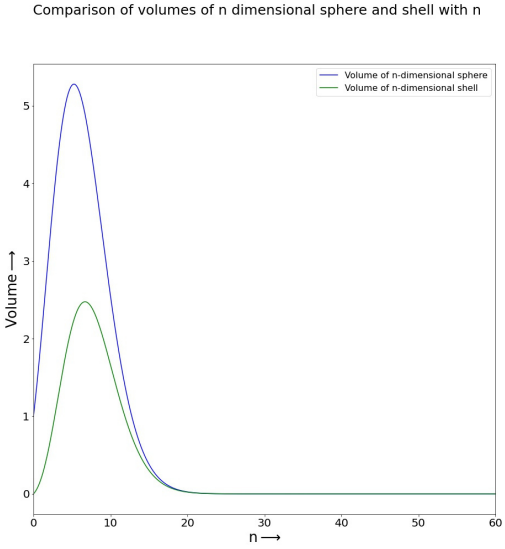

Fig. 2: A graph between n and volumes of n-dimensional sphere and shell.

Initially the volume of the shell is much less than the volume of the sphere. As n increases, both volumes decrease and become equal. We also found the percentage change in volume of the sphere to shell. The fraction of volume contained

in the shell with thickness ΔR will be equal to

$$\text{Fractional volume} = \frac{\frac{\pi^{\frac{n}{2}}}{\Gamma\left(\frac{n}{2}+1\right)}R^n - \frac{\pi^{\frac{n}{2}}}{\Gamma\left(\frac{n}{2}+1\right)}(R-\Delta R)^n}{\frac{\pi^{\frac{n}{2}}}{\Gamma\left(\frac{n}{2}+1\right)}R^n}\,.$$

On simplification,

$$\text{Fractional volume} = 1 - \left(1 - \frac{\Delta R}{R}\right)^n\,. \tag{6}$$

For $R = 1, \Delta R = 0.1$ and $R = 2, \Delta R = 0.1$, the fractional volumes in percentage are given in Table 3. All these show that the popular concept that the volume content is spreading into the surface area is not correct. Hence the curse of dimensionality remains unchanged.

Dimension	$R = 1$	$R = 2$
1	10	5
5	40.95	22.62
10	65.13	40.12
15	79.41	53.67
20	87.84	64.15
299	100	99.99
300	100	99.99

Table 3: Values of percentage of fractional volume for different n.

5 How Physicists overcome the curse using Statistical Mechanics

Statistical Mechanics (SM) provides the basis for many important branches of physics, including atomic and molecular physics, solid state physics, biophysics, astrophysics, environmental and socioeconomic physics. In statistical mechanics, we are interested in finding the thermodynamic properties of a system using n-dimensional space [18, 19]. It involves number of particles of the order of 10^{23} which are in continuous movement and hence have a continuous transformation in their position and momenta. So in order to predict the properties, we need to have information about all the possible values of position and momentum. For this, we construct a new space called a "phase space" which is a fusion of momentum and position spaces which is a six-dimensional space for N particles. In this space, the bridging equation to find the properties was given by Boltzmann [20, 21] as

$$S = k \ln \Omega \tag{7}$$

where S is the entropy, k is the Boltzmann constant and Ω is the number of available states in phase space which is given by [7, 22]

$$\Omega = \frac{V^{\frac{n}{3}}\pi^{\frac{n}{2}}}{h^n\,\Gamma\left(\frac{n}{2}+1\right)}R^n, \tag{8}$$

where V is the spatial volume and h is Planck's constant. Momentum volume of $3N$-dimension is [7, 22]

$$V_n = V_{3N} = \frac{\pi^{\frac{3N}{2}}R^{3N}}{\Gamma\left(\frac{3N}{2}+1\right)} = \frac{\pi^{\frac{n}{2}}R^n}{\Gamma\left(\frac{n}{2}+1\right)}\,. \tag{9}$$

In SM, we never have V_{3N} alone. We have both spatial volume V and momentum volume V_{3N} such that the total volume

$$V_{Total} = V^N V_{3N}\,. \tag{10}$$

But SM requires only Ω, the number of micro-states. Substituting for V_{Total}, we find the number of micro-states as

$$\Omega = \frac{V_{Total}}{h^{3N}N!} = \frac{V^N V_{3N}}{h^{3N}N!} = \frac{V^N\pi^{\frac{3N}{2}}R^{3N}}{h^{3N}N!\Gamma\left(\frac{3N}{2}+1\right)} \tag{11}$$

where $N!$ is used to avoid Gibbs paradox [7]. Simple calculations show that the number of micro-states (Ω) goes to infinity even for N just above 3 (Ω is of the order of 10^{1000} for $N = 100$). But because of the bridging equation, we require only $\ln\Omega$ and for that we carry out the following steps. Let us consider non-relativistic classical particles with energy $E = p^2/2m$. Then we have the radius of the momentum sphere $R = p = \sqrt{2mE}$ and we get

$$\Omega = \frac{\left(\frac{V}{h^3}\right)^N (2\pi mE)^{\frac{3N}{2}}}{N!\,\Gamma\left(\frac{3N}{2}+1\right)}\,. \tag{12}$$

Applying Stirling's approximation and carrying out suitable simplifications we arrive at

$$\ln\Omega \simeq N\ln\frac{V}{\lambda^3} - N\ln N + \frac{5}{2}N \tag{13}$$

where λ is the de Broglie wavelength. So we plot a graph between $\ln\Omega$ and N as in Fig. 3. The first graph shows a nonlinear variation because our choice of V/λ^3 is not realistic. In practice V/λ^3 will be always greater than 10^{25} and hence $\ln\Omega$ will be always proportional to N. This shows that in SM there is no need to worry about the decrease in volume of the n-dimensional space and we are not affected by the curse of dimensionality.

6 Conclusion

In statistical mechanics, in micro-canonical ensembles, we use the hyper-dimensional space to find the thermodynamic properties of a system. There are much literature [16, 17, 23, 24] showing that hyper-dimensional volume vanishes at large dimension or for large N. But this does not affect the properties of a system, which remains a paradox for physicists. This paradox is resolved in this paper. In SM, the classical particles are always in motion and hence to specify them we require both position and momentum simultaneously, which results in the phase space. We showed that because of the choice of the phase space, the curse of hyper-dimension is not affecting the properties and calculations in SM.

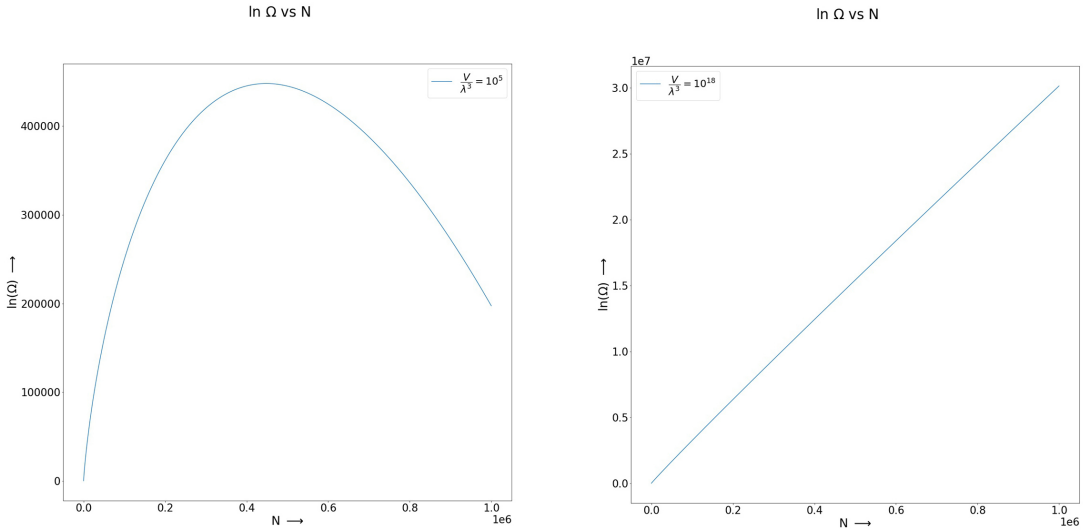

Fig. 3: A graph between $\ln\Omega$ and N for different V/λ^3.

Acknowledgements

During the preparation of the paper, the authors have been in constant discussions with Prof. K. P. N. Murthy, a great teacher of Physics from India, who died recently. As a token of respect to his inspiring comments, we wish to dedicate this paper to him. The authors also wish to thank Gautham Dathatreyan, Department of Science, Amrita Vishwa Vidyapeetham, Coimbatore for the computations using Python.

Received on August 18, 2021

References

1. Schläfli L. On a multiple integral. *The Quarterly Journal of Pure and Applied Mathematics*, 1858, v. 2, 269–301.
2. Catalan E. *Journal de Mathématiques Pures et Appliquées*, 1841, v. 6, 81–84.
3. Clifford W. K. *Mathematical Questions, with Their Solutions, from the "Educational Times"*, 1866, v. 6, 83–87.
4. Heyl P. R. Properties of the locus r = constant in space of n dimensions. *Mathematics*, 1897, v. 1, 33–39.
5. Sommerville D. M. Y. Bibliography of Non-Euclidean Geometry, Including the Theory of Parallels, the Foundation of Geometry, and Space of N Dimensions. Harrison and Sons, London, 1911.
6. Sommerville D. M. Y. An Introduction to the Geometry of N Dimensions. Dover Publications, New York, 1929.
7. Pathria R. K. and Beale P. D. Statistical Mechanics. Third Edition. Academic Press, Elsevier, 2011.
8. Kerson H. Introduction to Statistical Physics. Second edition. Chapman and Hall/CRC, 2009.
9. Callen H. B. Thermodynamics and An Introduction to Thermostatistics. 2nd ed. John Wiley and Sons, New York, 1985.
10. Florian C. Origins of Fourth Dimension Concepts. *The American Mathematical Monthly*, 1926, v. 33 (8), 397–406.
11. Jia B. Topological String Theory Revisited I: The Stage. *Int. J. Mod. Phys. A*, 2016, v. 31, 1650135.
12. Pincak R., Pigazzini A., Jafari S. and Ozel C. The "Emerging" Reality from "Hidden" Spaces. *Universe*, 2021, v. 7 (3), 75.
13. Donoho D. L. High-dimensional data analysis: The curses and blessings of dimensionality. In: Proceedings of the American Mathematical Society Conference on Math Challenges of the 21st Century. Los Angeles, CA, 2000.
14. Bellman R. Dynamic programming. Princeton University Press, Princeton, 1957.
15. Bellman R. E. Adaptive control processes: a guided tour. Princeton University Press, Princeton, 1961.
16. Ball K. An elementary introduction to modern convex geometry. In: Levy S., ed. Flavors of Geometry. Cambridge University Press, Cambridge, 1997.
17. Hayes B. An adventure in the Nth dimension. *American Scientist*, 2011, v. 99(6), 442.
18. Greiner I. W., Neise L., Stocker H. and Rischke D. Thermodynamics and Statistical Mechanics. Springer, 2001.
19. Bagchi B. Statistical Mechanics for Chemistry and Materials Science. Francis-Taylor, CRC Press, 2018.
20. Laird B. B. Entropy, Disorder, and Freezing. *J. Chem. Educ.*, 1999, v. 76, 1388–1390.
21. Schoepf D. C. A statistical development of entropy for the introductory physics course. *American Journal of Physics*, 2002, v. 70, 128.
22. Reif F. Fundamentals of Statistical and Thermal Physics. 1st ed. McGraw-Hill, Singapore, 1984.
23. Arfken G. B. Mathematical Methods for Physicists. Academic Press, Orlando, 1985.
24. Collins G. P. The Shapes of Space. *Sci. Amer.*, 2004, v. 291, 94–103.

Anomalous Magnetic Moment in Discrete Time

Young Joo Noh

E-mail: yjnoh777@gmail.com, Seongnam, Korea

The concept of causal delay in discrete time provides a correction for minimal coupling in electromagnetic interactions. This correction gives energy scale-dependent changes to the charge and mass of the elementary particles. As an application example of these results, this paper attempts to explain the anomaly of the g-factor. In particular, for the muon, $a = 0.001166$ is obtained from the approximation of its energy.

1 Introduction

In my last paper [1], I analyzed the effect of causal delay on the description of a dynamic system from a discrete time perspective. As a result, the dynamics system was divided into two worlds to which fundamentally different dynamical principles were applied, namely, type 1 and type 2. In the case of free particles, type 1 corresponds to ordinary matter that satisfies the existing relativistic quantum mechanics, and type 2 has properties similar to dark matter.

In this paper, I will discuss the interactions of type 1 particles, especially electromagnetic interactions. To do this, first, it is necessary to know the meaning of the result of type 1 in the case of free particles. In the case of free particles, the spinor state of type 1 satisfies the following equation

$$(x^\mu + \Delta x^\mu)\,\Psi(x) - x^\mu \Psi(x + \Delta x) = \Delta x^\mu e^{-i\Delta x^\alpha P_\alpha}\Psi(x)\ . \quad (1)$$

The left side of (1) means the sum of contributions from $x - \Delta x$ and $x + \Delta x$ at x if the second term is translated by $-\Delta x$. The right-hand side means that the spinor change is only in phase, that is, the spinor forms a plane wave. Therefore, the above equation means that the sum of contributions from $x - \Delta x$ and $x + \Delta x$ forms a plane wave, that is, harmonic oscillation.

These facts require a new perspective on the matter field. In the existing field theory, especially quantum field theory, the field is based on the ontological basis of the statistical-mechanical analogy of the gathering of harmonic oscillators. From this point of view, harmonic oscillation is a property inherently immanent in the field. On the other hand, the matter field implied by (1) does not assume the property of harmonic oscillation inherent in nature. That is, harmonic oscillations are simply "formed" by the sum of contributions from the past and future of Δt_d. If we look at harmonic oscillations from this point of view, it can be said that interactions "deform" harmonic oscillations.

In the next section, I will discuss interactions in relativistic quantum mechanics with this new perspective on the matter field.

2 Modified Dirac equation

First, I will try to find the evolution operator equation for interacting particles corresponding to the evolution operator (1) for free particles. If the momentum at x and $x + \Delta x$ is p and $p+\Delta p$, and the spinor state is $\Psi(x, p)$ and $\Psi(x + \Delta x, p + \Delta p)$, respectively, the difference of cause-effect vector is as follows

$$\begin{aligned}
&(x^\mu + \Delta x^\mu)\,\Psi(x, p) - x^\mu \Psi(x + \Delta x, p + \Delta p)\\
&= (x^\mu + \Delta x^\mu)\,\Psi(x, p) -\\
&-x^\mu \sum_{m,n=0}^{\infty} \frac{1}{m!}\left(\Delta P^\alpha \frac{\partial}{\partial P^\alpha}\right)^m \frac{1}{n!}\left(\Delta x^\alpha \frac{\partial}{\partial x^\alpha}\right)^n \Psi(x, p)\\
&= (x^\mu + \Delta x^\mu)\,\Psi(x, p) -\\
&-e^{\Delta P \frac{\partial}{\partial P}}\ x^\mu \left(1 + \Delta x^\alpha \frac{\partial}{\partial x^\alpha} + \sum_{n=2}^{\infty} \frac{1}{n!}\left(\Delta x^\alpha \frac{\partial}{\partial x^\alpha}\right)^n\right)\Psi(x, p)\\
&= \left(\Delta x^\mu - x^\mu \Delta x \frac{\partial}{\partial x}\right)\Psi - \left(e^{\Delta P \frac{\partial}{\partial P}} - 1\right)\left(x^\mu + x^\mu \Delta x \frac{\partial}{\partial x}\right)\Psi -\\
&-e^{\Delta P \frac{\partial}{\partial P}} x^\mu \sum_{n=2}^{\infty} \frac{1}{n!}\left(\Delta x \frac{\partial}{\partial x}\right)^n \Psi\\
&= \left\{\Delta x^\mu - e^{\Delta P \frac{\partial}{\partial P}}\left(x^\mu + x^\mu \Delta x \frac{\partial}{\partial x}\right) + x^\mu\right\}\Psi -\\
&-e^{\Delta P \frac{\partial}{\partial P}} x^\mu \sum_{n=2}^{\infty} \frac{1}{n!}\left(\Delta x \frac{\partial}{\partial x}\right)^n \Psi\\
&= \left\{x^\mu + \Delta x^\mu - e^{\Delta P \frac{\partial}{\partial P}}(x^\mu + \Delta x^\mu) - e^{\Delta P \frac{\partial}{\partial P}}\left[x^\mu, \Delta x \frac{\partial}{\partial x}\right]\right\}\Psi -\\
&-e^{\Delta P \frac{\partial}{\partial P}}\left[x^\mu, \sum_{n=2}^{\infty} \frac{1}{n!}\left(\Delta x \frac{\partial}{\partial x}\right)^n\right]\Psi\\
&= \left\{(x^\mu + \Delta x^\mu)\left(1 - e^{\Delta P \frac{\partial}{\partial P}}\right) - e^{\Delta P \frac{\partial}{\partial P}}\left[x^\mu, e^{\Delta x \frac{\partial}{\partial x}}\right]\right\}\Psi(x, p)\\
&= \left\{(x^\mu + \Delta x^\mu)\left(1 - e^{\Delta P \frac{\partial}{\partial P}}\right) + e^{\Delta P \frac{\partial}{\partial P}} \Delta x^\mu e^{-i\Delta x \cdot P}\right\}\Psi(x, p)\ . \quad (2)
\end{aligned}$$

The right-hand side of (2) is the evolution operator of interacting particles. If we apply operator $e^{-\Delta P \frac{\partial}{\partial P}}$ to both sides of (2) to get a simpler expression, it is as follows

$$\begin{aligned}
&(x^\mu + \Delta x^\mu)\,\Psi(x, p - \Delta p) - x^\mu \Psi(x + \Delta x, p)\\
&= \left\{\Delta x^\mu e^{-i\Delta x \cdot P} + (x^\mu + \Delta x^\mu)\left(e^{-\Delta P \frac{\partial}{\partial P}} - 1\right)\right\}\Psi(x, p)\ .
\end{aligned} \quad (3)$$

In (3), the first term on the right side is the evolution operator of a free particle and the second term is the interaction

term. Since interaction is a local phenomenon, x in the interaction term can be set to Δx. And if

$$\mathrm{e}^{-\Delta \mathrm{P}\frac{\partial}{\partial \mathrm{P}}}\mathrm{e}^{\mathrm{i}\Delta \mathrm{x}\cdot \mathrm{P}} = \mathrm{e}^{-\mathrm{i}\Delta \mathrm{p}\cdot \Delta \mathrm{x}}\mathrm{e}^{\mathrm{i}\Delta \mathrm{x}\cdot \mathrm{P}} \tag{4}$$

is used, the final evolution operator O becomes

$$\mathrm{O}\Psi(x,p) = \left\{\mathrm{e}^{-i\Delta x\cdot P} + 2\left(\mathrm{e}^{-\mathrm{i}\Delta \mathrm{x}\cdot \Delta \mathrm{p}} - 1\right)\right\}\Psi(x,p)\,. \tag{5}$$

A little trick is needed here. Although not in practice, it is assumed that Ψ is analytic in order to maintain the conventional dynamics view. Then evolution operator O also needs to be defined as a locally continuous variable. What we need here is $\Delta x = x$. Therefore, the evolution operator O is equal to

$$\mathrm{O} = \mathrm{e}^{-ix\cdot P} + 2\left(\mathrm{e}^{-ix\cdot \Delta p} - 1\right)\,. \tag{6}$$

The evolution operator of free particles satisfies the Dirac equation. Therefore, the modified Dirac equation that the interaction evolution operator (6) must satisfy can be put as

$$\left(i\gamma^{\mu}\partial_{\mu} - m + A\right)\left\{\mathrm{e}^{-ix\cdot P} + 2\left(\mathrm{e}^{-ix\cdot \Delta p} - 1\right)\right\}\Psi(x,p) = 0\,. \tag{7}$$

By finding A in (7), the following modified Dirac equation can be obtained

$$\mathrm{D_m}\Psi = \left(i\gamma^{\mu}\partial_{\mu} - f_{1r}\gamma^{\mu}p_{\mu} - f_{2r}\gamma^{\mu}\Delta p_{\mu}\right)\Psi = 0 \tag{8}$$

where

$$\begin{aligned} f_{1r} &= \mathrm{Re}f_1 = \frac{1}{3}\mathrm{Re}\frac{\mathrm{e}^{-ix\cdot p}}{\mathrm{e}^{-ix\cdot p} + 2\left(\mathrm{e}^{-ix\cdot \Delta p} - 1\right)} \\ f_{2r} &= \mathrm{Re}f_2 = \frac{1}{3}\mathrm{Re}\frac{2\mathrm{e}^{-ix\cdot \Delta p}}{\mathrm{e}^{-ix\cdot p} + 2\left(\mathrm{e}^{-ix\cdot \Delta p} - 1\right)}\,. \end{aligned} \tag{9}$$

In (9), the 1/3 factor is introduced under the condition that the sum of the coefficients in (8) is 0, that is $f_{1r} + f_{2r} = 1$. Now let's find the Hamiltonian using $\gamma^{\mu}p_{\mu} = m$. From (8),

$$\begin{aligned} &\mathrm{H}\Psi = i\partial_0\Psi \\ &= \left(-i\vec{\alpha}\cdot\vec{\nabla} + f_{1r}\beta m + f_{2r}\beta\gamma^{\mu}\Delta p_{\mu}\right)\Psi \\ &= \left\{\vec{\alpha}\cdot\vec{p} + f_{1r}\beta m + f_{2r}\left(\Delta p_0 - \vec{\alpha}\cdot\Delta\vec{p}\right)\right\}\Psi \\ &= \left\{\vec{\alpha}\cdot\left(\vec{p} - f_{2r}\Delta\vec{p}\right) + f_{1r}\beta m + f_{2r}\Delta p_0\right\}\Psi\,. \end{aligned} \tag{10}$$

Comparing the meaning of (10) with Hamiltonian $\mathrm{H}_0 = \vec{\alpha}\cdot\vec{p} + \beta m$ of free particles, it means that when there is a change in momentum and energy due to interactions, correction by $-f_{2r}\Delta\vec{p}$ and $-f_{2r}\Delta E$ is required, respectively. According to the existing minimal coupling theory, when a charge q interacts with an electromagnetic field, the momentum and energy become $\vec{p} - q\vec{A}$ and $E - q\phi$. Here, it can be inferred that the momentum change $\Delta\vec{p}$ and the energy change ΔE are $-q\vec{A}$ and $-q\phi$. Therefore, the combined momentum and energy of minimal coupling and causal delay are $\vec{p} - q\vec{A} + f_{2r}q\vec{A}$ and $E - q\phi + f_{2r}q\phi$. Rewriting, the resulting Hamiltonian is

$$\mathrm{H} - (1 - f_{2r})\,q\phi = \vec{\alpha}\cdot\left\{\vec{p} - (1 - f_{2r})\,q\vec{A}\right\} + \beta f_{1r}m\,. \tag{11}$$

Comparing (11) with the existing minimal coupling Hamiltonian, mass and charge can be newly defined as shown in (12) below. That is, the causal delay gives a modified mass and charge concept dependent on the energy scale:

$$\begin{aligned} m' &= f_{1r}m \\ q' &= (1 - f_{2r})\,q\,. \end{aligned} \tag{12}$$

3 Anomalous magnetic moment

The discovery of the Dirac equation made it possible to understand the property of spin of elementary particles, and predicted that the g-factor was 2. But, as a result of the measurement, anomaly exists, which was explained by a completely different paradigm of quantum field theory. However, according to the discussion in the previous section, considering the change in charge and mass due to the effect of causal delay, there is a possibility that the anomaly can be explained from the perspective of modified relativistic quantum mechanics.

When a particle with mass m' and charge q' is placed in an external field $A^{\mu} = \left(\phi, \vec{A}\right)$, the equation for calculating the magnetic moment is as follows

$$(\mathrm{H} - q'\phi)^2 = \left(\vec{p} - q'\vec{A}\right)^2 + m'^2 - q'\vec{\Sigma}\cdot\vec{B}. \tag{13}$$

where

$$\Sigma_j = \begin{pmatrix}\sigma_j & 0\\ 0 & \sigma_j\end{pmatrix}.$$

If $q' = -e' = -(1 - f_{2r})\,e$, the nonrelativistic limit of (13) is obtained as follows

$$\mathrm{H} \cong m' + \frac{\left(\vec{p} + e'\vec{A}\right)^2}{2m'} - e'\phi + \frac{e'}{2m'}\vec{\Sigma}\cdot\vec{B} \tag{14}$$

where

$$\frac{e'}{2m'}\vec{\Sigma}\cdot\vec{B} = \frac{e}{2m}\frac{(1 - f_{2r})}{f_{1r}}2\vec{S}\cdot\vec{B} \equiv g\frac{e}{2m}\vec{S}\cdot\vec{B}\,. \tag{15}$$

Then, under the condition of $p \gg \Delta p$, the g-factor and the anomalous magnetic moment are as follows

$$\begin{aligned} \frac{g}{2} &= \frac{1 - f_{2r}}{f_{1r}} = 3 - 2\cos(x\cdot p) \\ a &= \frac{g}{2} - 1 = 2 - 2\cos(x\cdot p)\,. \end{aligned} \tag{16}$$

Previously local variable $x = \Delta x$. Then the phase value is

$$\Delta x\cdot p = E\,\Delta t - \vec{p}\cdot\Delta\vec{x} = \Delta t\left(E - \frac{\vec{p}^2}{m}\right). \tag{17}$$

In (17), Δt is the causal delay time. If $\Delta t = 0$, i.e. continuous time, there is no anomaly. Now let's define the physical meaning of Δt as follows.

Assumption: For a particle, the causal delay is the time it takes for light to pass through the particle's reduced Compton wavelength

$$\Delta t \equiv \frac{\lambda\!\!\!^{-}_c}{c} = \frac{\hbar}{mc^2}\,. \tag{18}$$

The Compton wavelength of a particle is a certain "region" of that particle. Therefore, the time it takes for light to pass through the region is the difference in time between cause and effect in the interaction between the particle and light.

Equation (18) is related to the "Penrose clock" [5]. According to him, *any individual stable massive particle plays a role as a virtually perfect clock.* And since $E = mc^2 = h\nu$, the frequency becomes $\nu = m\left(c^2/h\right)$. This can be said to be the same as (18). Since $\Delta t = 1/\nu$, the frequency becomes $\nu/2\pi = m\left(c^2/h\right)$. Therefore, it can be said that the causal delay time of massive particles plays the role of a fundamental clock that exists in nature.*

By the definition of Δt, the phase value of (17) can be calculated, and consequently the anomalous magnetic moment can be determined. An easy way to do this is the anomalous magnetic moment of the muon. In the case of the muon, at the so-called "magic momentum" $p_0 = 3.094$ GeV/c, the effect of the applied electric field for confinement of the muon is negligible. This means that the potential term in the energy value of (17) can be neglected. Therefore, the phase value of (17) is as follows

$$\begin{aligned} &\frac{\vec{p}^2}{m} = \frac{E^2 - m_\mu^2}{m} = \frac{m_\mu^2\left(\gamma^2 - 1\right)}{m_\mu \gamma} = \beta^2 E \\ &\text{thus} \quad E - \frac{\vec{p}^2}{m} = \frac{E}{\gamma^2} = \frac{m_\mu}{\gamma} \\ &\text{and} \quad \therefore \Delta t\left(E - \frac{\vec{p}^2}{m}\right) = \frac{1}{\gamma}\,. \end{aligned} \tag{19}$$

Therefore, the anomalous magnetic moment of the muon is

$$a_\mu = 2 - 2\cos\frac{1}{\gamma}\,. \tag{20}$$

Using (20) to find a_μ, γ corresponding to $E = 3.094$ GeV is 29.28, so

$$a_\mu = 0.001166\,. \tag{21}$$

Meanwhile, the value of a_μ recently announced by Fermilab is as follows.

$$a_\mu\,(\text{FNAL}) = 0.00116592040\,(54)\,. \tag{22}$$

The value of (21) is only calculated as an approximation of the muon energy. Thus, how accurately (20) predicts a_μ depends on the determination of γ, which is possible as an independent measurement of the cyclotron frequency $\omega_c = eB/m\gamma$.

*Except for (18) and this paragraph, the rest use natural units.

4 Conclusions

Type 1 has a different view from the existing ones on the concept of field. It is that the harmonic oscillation of the field is formed by the sum of contributions from the past and future by Δt, not inherent in nature. And the interactions deform these harmonic oscillations. The result of analyzing the interaction from this point of view shows that it is more than the description of the interaction of the existing relativistic quantum mechanics.

The causal delay effect in discrete time corrects the existing minimal coupling theory, which leads to the result that the charge and mass of elementary particles change depending on the energy scale. As an example of such a result, it is partially shown that the anomalous magnetic moment of the muon can also be explained from this new perspective.

Received on September 8, 2021

References

1. Noh Y. J. Propagation of a Particle in Discrete Time. *Progress in Physics*, 2020, v. 16, 116–122.
2. Albahri T. *et al*. Measurement of the anomalous precession frequency of the muon in the Fermilab Muon *g*-2 Experiment. *Physical Review D*, 2021, v. 103, 072002.
3. Albahri T. *et al*. Magnetic-field measurement and analysis for the Muon *g*-2 Experiment at Fermilab. *Physical Review A*, 2021, v. 103, 042208.
4. Jegerlehner F. The Anomalous Magnetic Moment of the Muon. Springer, Heidelberg, 2007.
5. Penrose R. Cycles of Time. The Bodley Head, 2010.

Representation of the Anomalous Magnetic Moment of the Muons via the Einstein-Podolsky-Rosen Completion of Quantum into Hadronic Mechanics

Ruggero Maria Santilli

The Institute for Basic Research, 35246 U. S. 19N, Suite 215, Palm Harbor, FL 34684, USA.
E-mail: research@i-b-r.org

In this paper, we briefly review half a century of research by various authors in the axiom-preserving completion of quantum mechanics into hadronic mechanics according to the 1935 Einstein-Podolsky-Rosen argument that "quantum mechanics is not a complete theory" (EPR argument). Said completion is intended to represent extended-particles in conditions of deep EPR entanglement with ensuing potential as well as contact non-Hamiltonian interactions represented by the new operator $\hat{T}$ in the associativity-preserving products $A \star B = A\hat{T}B$ of hadronic mechanics. We recall that muons are unstable and decay spontaneously with a mean live $\tau = 2.19703\times10^{-6}$ s, thus suggesting that they are composite, and therefore extended particles with constituents capable of triggering their decay. We then assume that the physical constituents of the muons are the ordinary electrons released in the spontaneous decay with low mode $\mu^- \to e^-, e^+, e^-$, resulting in the structure model according to hadronic mechanics (hm) $\mu^- = (\hat{e}^-_\downarrow, \hat{e}^+_\uparrow, \hat{e}^-_\downarrow)_{hm}$ where the "hat" characterizes iso-renormalizations due to non-Hamiltonian interactions. We show that the indicated hadronic structure model achieves an exact representation of *all* characteristics of muons, including rest energy, charge radius, mean life, spin, charge, spontaneous decays and anomalous magnetic moment.

1 Introduction

Recent, very accurate measurements [1] have established the following difference between the experimental value *muon* g-factor g_μ^{EXP} and its prediction via quantum electrodynamics g_μ^{QED}

$$\begin{aligned} & g_\mu^{EXP} - g_\mu^{QED} = \\ & = 2.00233184122 - 2.00233183620 \\ & = 0.00000000502 > 0\,. \end{aligned} \tag{1}$$

Additional accurate measurements [2] have shown deviations from quantum mechanical predictions for *atoms* in condensed matter, and measurements [3] have indicated bigger deviations from the predictions of quantum mechanics for *heavy ion.*

The above experiments support:

1) The validity of the historical 1935 argument by A. Einstein, B. Podolsky and N. Rosen that "quantum mechanics is not a complete theory" (EPR argument) [4];

2) The significance of historical completions of quantum mechanics, such as the non-linear completion by W. Heisenberg [5], the non-local completion by L. de Broglie and D. Bohm [6], and the completion via *hidden variables* by D. Bohm [7];

3) The validity of the recent verifications of the EPR argument by R. M. Santilli [8, 9] based on the completion of quantum mechanics (qm) into hadronic mechanics (hm) according to the EPR argument for the time-invariant representation of extended particles/wavepackets under potential as well as non-linear, non-local and non-potential interactions (see [10–12] for an outline of the basic methods, [13, 14] for recent overviews and [15–17] for detailed presentations).

2 Isotopic branch of hadronic mechanics

As it is well known, 20th century applied mathematics is characterized by a universal enveloping associative algebra ξ with conventional associative product $AB = A \times B$ between arbitrary quantities A, B, such as numbers, functions, operators, *etc*.

Lie algebras L with bracket between Hermitean operators $[A, B] = AB - BA$, then follow as the antisymmetric algebra attached to $L \approx \xi^-$, resulting in a unique characterization of Heisenberg's time evolution $idA/dt = [A, H]$ for point-particles under action-at-a-distance, potential interactions.

The EPR completion of quantum mechanics into hadronic mechanics has been studied to represent *extended* particles in conditions of mutual penetration, as occurring in the nuclear structure, with expected, additional, contact interactions of non-linear, non-local and non-potential type, hereon referred to as *non-Hamiltonian interactions.*

The axiom-preserving, thus isotopic branch of hadronic mechanics, known as *iso-mechanics,* and its underlying mathematics, known as *iso-mathematics,* represent the extended character of particles and their non-Hamiltonian interactions via the completion of the enveloping associative algebra ξ into the *universal enveloping iso-associative iso-algebra* $\hat{\xi}$ characterized by the *iso-product* (first introduced in Eq. (5), page 71 of [16] and treated in detail in [17])

$$A \star B = A\hat{T}B,\ \hat{T} > 0\,, \tag{2}$$

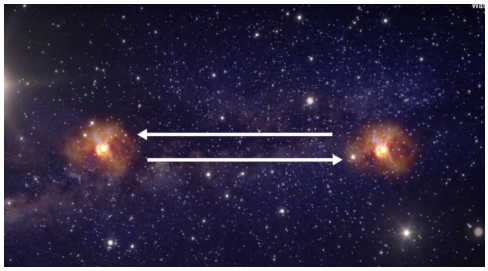

Fig. 1: In this figure, we illustrate the quantum entanglement of particles with instantaneous mutual actions at a distance, and recall the argument by A. Einstein, B. Podolsky and N. Rosen on the need for superluminal communications to represent said entanglement due to the local character of differentials, potentials and wavefunctions of the Schrödinger equation of quantum mechanics which solely allows a point-like characterization of particles [4].

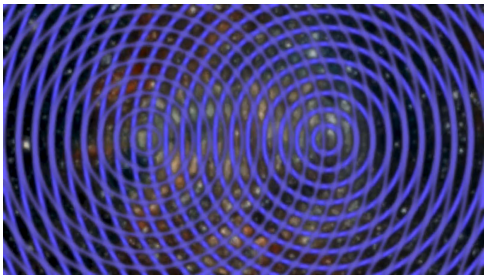

Fig. 2: In this figure, we illustrate the new Einstein-Podolsky-Rosen entanglement of particles introduced in [13], which is characterized by contact, therefore instantaneous and non-Hamiltonian interactions originating in the overlapping of the wavepackets of particles represented via isotopic elements of type (3). As such, the EPR entanglement prevents the applicability of Bell's inequality [18], allows an explicit and concrete realization of Bohm's hidden variables [7], and permits a progressive recovering of Einstein's determinism in the interior of hyperdense particles, with its full recovering at the limit of gravitational collapse [8, 9].

where the quantity $\hat{T}$, called the *isotopic element,* is positive-definite but possesses otherwise an unrestricted dependence on all needed local variables (herein tacitly assumed).

The isotopic element has realizations of the type [12]

$$\hat{T} = \Pi_{\alpha=1,2}\, \text{Diag}\left(\frac{1}{n_{1,\alpha}^2}, \frac{1}{n_{2,\alpha}^2}, \frac{1}{n_{3,\alpha}^2}, \frac{1}{n_{4,\alpha}^2}\right) e^{-\Gamma}, \quad n_{\mu,\alpha} > 0, \quad \Gamma > 0, \quad \mu = 1,2,3,4, \quad \alpha = 1,2,...,N, \tag{3}$$

by charaterizing:

1) The dimension and shape of particles via semi-axes $n_{k,\alpha}^2, k = 1,2,3$ (with n_3 parallel to the spin) and the density $n_{4,\alpha}^2$, all n-characteristic quantities being normalized to the value $n_{\mu,\alpha}^2 = 1$ for the vacuum.

2) Non-Hamiltonian interactions via the term e^{Γ}, where Γ is a positive-definite quantity with an unrestricted functional dependence on the wavefunctions as well as the characteristics of the medium in which the particles are immersed.

Iso-product (2) with realization (3) provides an explicit and concrete realization of Bohm's *hidden variables* [7], by therefore supporting the view that quantum mechanics does indeed admit hidden degrees of freedom, provided that quantum axions are realized in a way more general than that of the Copenhagen school.

It should also be noted that iso-product (2) and realizations (3) provide a quantitative representation of the completion of the conventional *quantum entanglement* of *point-like* particles under Hamiltonian interactions, into the covering *Einstein-Podolsky-Rosen entanglement* [13] which is applicable to *extended* particles with non-Hamiltonian interactions due to the deep overlapping of their wavepackets (see Figs. 1 and 2 and references quoted therein).

Despite its simplicity, iso-product (2) requires, for consistency, a compatible isotopy of the entire 20th century applied mathematics, with no exception known to the author [10]. In fact, iso-product (2) requires the following completions of 20th century applied mathematics (see Vol. I of [17] for a general treatment):

A) The compatible, completion of the basic unit $\hbar = 1$ of quantum mechanics into the integro-differential *iso-unit*

$$\hat{I} = 1/\hat{T} > 0, \quad \hat{I} \star A = A \star \hat{I} = A, \tag{4}$$

with ensuing completion of the conventional numeric field $F(n, \times, 1)$ of real $\mathcal{R}$, complex C and quaternionic Q numbers n into the *iso-fields* $\hat{F}(\hat{n}, \star, \hat{I})$ of *iso-real* $\hat{\mathcal{R}}$, *iso-complex* $\hat{C}$ and *iso-quaternionic* $\hat{Q}$ *iso-numbers* $\hat{n} = n\hat{I}$ and related isotopic operations [19] (see [20] for an independent study).

B) The completion of conventional functions $f(r)$ of a local variable r into *iso-functions* that, to have value on an iso-field, must have the structure [21] (see [22] for an independent study)

$$\hat{f}(\hat{r}) = [f(r\hat{I})]\,\hat{I}, \tag{5}$$

and related iso-differential iso-calculus [21] (see [23] for independent studies).

C) The completion of conventional spaces S over F into *iso-spaces* $\hat{S}$ over iso-fields $\hat{F}$ [21]. In particular, the conventional Minkowski space $M(x, \eta, I)$ over $\mathcal{R}$ with spacetime coordinates $x \in \mathcal{R}$, $x^4 = ct$, metric $\eta = \text{Diag}(1,1,1,-1)$ and unit $I = \text{Diag}(1,1,1,1)$, is mapped into the *iso-Minkowski iso-space* $\hat{M}(\hat{x}, \hat{\Omega}, \hat{I})$ over the iso-real iso-numbers $\hat{\mathcal{R}}$ [24] (see [25] for an independent study) with iso-coordinates $\hat{x} = x\hat{I} \in \hat{\mathcal{R}}$, iso-metric $\hat{\Omega} = (\hat{\eta})\hat{I} = (\hat{T}\eta)\hat{I}$, and iso-interval

$$(\hat{x}^\rho - \hat{y}^\rho)^{\hat{2}} = (\hat{x}^\rho - \hat{y}^\rho) \star \hat{\Omega}_{\rho\nu} \star (\hat{x}^\nu - \hat{y}^\nu) = \left[\frac{(x_1 - y_1)^2}{n_1^2} + \frac{(x_2 - y_2)^2}{n_2^2} + \frac{(x_3 - y_3)^2}{n_3^2} - \frac{(t_x - t_y)^2 c^2}{n_4^2}\right] \hat{I}, \tag{6}$$

where the exponential term $exp\{-\Gamma\}$ is imbedded into the n-characteristic quantities.

D) The compatible completion of all branches of Lie's theory first studied in [16] (see Vol. II of [17] for a general treatment and [26] for an independent study). For instance, an N-dimensional Lie algebra L with Hermitean generators $X_k,\ k = 1, 2, ...\, N$ is completed into the infinite family of Lie-Santilli iso-algebras $\hat{L}$ with iso-commutation rules

$$[X_i\hat{,}X_j] = X_i \star X_j - X_j \star X_i = C_{ij}^k X_k\,, \tag{7}$$

which iso-algebras are called *regular* or *irregular* depending on whether the structure quantities C_{ij}^k are constant or functions of local variables, respectively.

E) The completion of well-known space-time symmetries into the *iso-symmetries* of iso-space-time (6), including the completion of Lorentz's symmetry SO(3.1) into the *Lorentz-Santilli iso-symmetry* $\widehat{\mathrm{SO}}(3.1)$ [24] with iso-transformations

$$\begin{gathered} x^{1'} = x^1, \quad x^{2'} = x^2, \\ x^{3'} = \hat{\gamma}(x^3 - \hat{\beta}\tfrac{n_3}{n_4}x^4), \quad x^{4'} = \hat{\gamma}(x^4 - \hat{\beta}\tfrac{n_4}{n_3}x^3)\,, \end{gathered} \tag{8}$$

where

$$\hat{\beta}_k = \frac{v_k/n_k}{c_o/n_4}, \quad \hat{\gamma}_k = \frac{1}{\sqrt{1-\hat{\beta}_k^2}}\,, \tag{9}$$

which provide the invariance of the local speed of light

$$C = \frac{c}{n_4}\,, \tag{10}$$

with consequential *iso-renormalization* of the energy (that is, renormalization caused by non-Hamiltonian interactions)

$$E = mc^2 \ \to\ \bar{E} = mC^2 = \frac{E}{n_4^2}\,. \tag{11}$$

Additionally, the isotopic representation of the anomalous magnetic moment of the muons requires the completion of the Lorentz-Poincaré symmetry P(3.1) into the *Lorentz-Poincaré-Santilli iso-symmetry* $\hat{\mathrm{P}}(3.1)$ [27], and the completion of the spinorial covering of the Lorentz-Poincaré symmetry $\mathcal{P}(3.1)$ into the *iso-spinorial covering of the Lorentz-Poincaré-Santilli iso-symmetry* $\hat{\mathcal{P}}(3.1)$ (in view of the spin 1/2 of the muons) [28] (see [11] for a recent review and [25] for independent studies).

We should also recall that all aspects of regular iso-mathematics and iso-mechanics can be constructed via the simple *non-unitary transform*

$$UU^\dagger = \hat{I} \neq I\,, \tag{12}$$

of *all* conventional mathematical or physical aspects, under which the unit of quantum mechanics is mapped into the iso-unit of iso-mechanics

$$\hbar = 1 \to U1U^\dagger = \hat{I}\,, \tag{13}$$

the conventional associative product AB is mapped into the iso-product

$$AB \to U(AB)U^\dagger = (UAU^\dagger)(UU^\dagger)^{-1}(UBU^\dagger) = \hat{A}\hat{T}\hat{B}\,, \tag{14}$$

and the same holds for the construction of all remaining regular iso-theories.

Finally, we recall that the isotopic element $\hat{T}$ represents physical characteristics of particles. Hence, the invariance of its numeric value is important for the consistency and experimental verification of any iso-theory. Such an invariance does indeed occur under the *infinite class of iso-equivalence* of isotopic methods which is given by the isotopic reformulation of non-unitary transforms called *iso-unitary iso-transforms*

$$UU^\dagger = \hat{I} \neq I, \quad U = \hat{U}\hat{T}^{1/2}, \quad \hat{U} \star \hat{U}^\dagger = \hat{U}^\dagger \star \hat{U} = \hat{I}\,, \tag{15}$$

under which we have the numeric invariance of the iso-unit [29]

$$\hat{I} \to \hat{U} \star \hat{I} \star \hat{U}^\dagger = \hat{I}' \equiv \hat{I}\,, \tag{16}$$

and of the isotopic element

$$\hat{A} \star \hat{B} \to \hat{U} \star (\hat{A} \star \hat{B}) \star \hat{U}^\dagger = \hat{A}'\hat{T}'\hat{B}', \quad \hat{T}' \equiv \hat{T}\,. \tag{17}$$

3 The structure of muons

As it is well known, the standard model assumes that muons $\mu^\pm$ are *elementary particles,* under which assumption, the sole known possibility of representing deviation (1) is the search for new particles and/or new interactions.

In this paper, we study the view presented on page 849 of the 1978 paper [30] (see also Section 2.5.5, page 163 of [12] for a recent update) according to which *muons are naturally unstable, and therefore they are composite, with a structure suitable to trigger their decay.*

Muons were then represented in [12] as a hadronic bound state of particles produced free in the spontaneous decays with the lowest mode $\mu^- \to e^-, e^\pm, e^-$ (tunnel effect of physical constituents), resulting in the three-body hadronic structure model with ordinary electrons

$$\mu^- = (\hat{e}_\downarrow^-, \hat{e}_\uparrow^+, \hat{e}_\downarrow^-)_{hm}, \tag{18}$$

in which the presence of positrons was instrumental for the representation of the muon spontaneous decays and its mean life.

Note that the constituents of model (18) are iso-electrons $\hat{e}^\pm$, rather than ordinary electrons $e^\pm$, due to their contact, non-Hamiltonian interactions due to their deep EPR entanglement (Fig. 3), which requires their characterization via an iso-irreducible iso-unitary iso-representation of $\hat{\mathcal{P}}(3.1)$ [28].

Note also that, since all constituents have point-like charges, the charge radius of the model is given by the radius of the orbit of the peripheral iso-electrons.

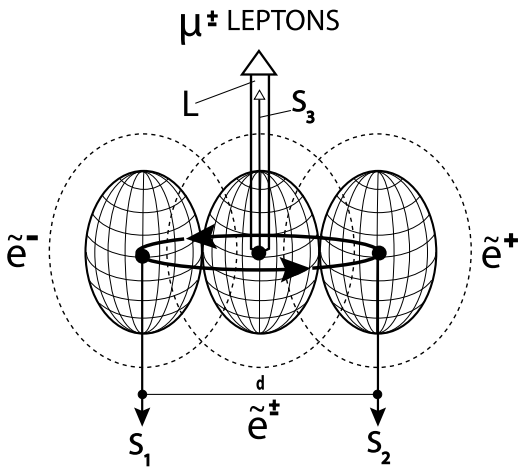

Fig. 3: In this figure, we illustrate structure model (18) of muons in its ground state with $L-0$, first derived in the 1978 paper [30] (see page 849 on and Section 2.5.5, page 163 of the recent update [12]) as a three-body hadronic bound state of ordinary electrons produced free in the spontaneous decay with the lowest mode. The dashed lines represent the 1 fm wavepackets of the electrons and their overlap represents their deep EPR entanglement. Note the stability of model (18) due to the singlet couplings of the pairs of constituents, and the presence of a positron representing the muon spontaneous decay and its mean life via electron-positron annihilation.

The iso-Schrödinger equation of iso-mechanics, Eq. (5.2.4) of [30] (see also Eqs. (54), page 165, [12]) allowed the non-relativistic representation (here omitted for brevity) of the mass $E = 105.658\,\text{MeV}$, charge radius of about $R = d/2 = 10^{-13}$ cm, mean life $\tau = 2.19703\times10^{-6}$ s, spin $S = 1/2$, charge $Q = \pm e$, and parity.

The 1978 paper [30] provided a representation of the magnetic moment of the muons known at that time, namely, that equal to the magnetic moment of the central electrons. This is due to the lack of contribution to the total magnetic moment from the electron-positron pair in the model which has a null charge and magnetic moment.

4 Anomalous magnetic moment of the muons

By keeping in mind that electrons have a point-like *charge* structure (but they have an extended wavepacket with radius of about 1 fm), it appears that the EPR entanglement of the constituents of model (18) (Fig. 3) causes a very small deformation (called *mutation* [30]) of the electrons such as to produce deviation (1). Its quantitative representation can be preliminarily achieved via the following isotopic procedure.

The relationship under isotopies between the magnetic moment and the spin of charged particles has been identified in Eq. (6.5), page 190 of [28], with ensuing relation for the g-factors (here reproduced for brevity without its derivation)

$$\hat{g}_\mu^{EXP} = \frac{n_4}{n_3} g_\mu^{QED} . \tag{19}$$

From value (1), we can then write

$$\frac{n_4}{n_3} = 1.00000000502 . \tag{20}$$

Model (18) for the structure of the muons has been indicated because it is necessary to identify the individual values of the characteristic quantities n_k^2, $k = 1,2,3$, representing the dimension and shape of the muons, and n_4^2, representing its density, with normalization $n_\mu^2 = 1$, $\mu = 1,2,3,4$ for conventional electrons and positrons.

Under the assumption of model (18), the total rest energy of the constituents is $E_{cons} = 3E_e = 1.533\,\text{MeV}$, while the muon rest energy is given by the familiar value $E_\mu = 105.7\,\text{MeV}$. This implies the excess energy

$$\Delta E = 105.7\,\text{MeV} - 1.533\,\text{MeV} = 104.167\,\text{MeV} , \tag{21}$$

under which the Schrödinger equation no longer admits physically meaningful solutions [12, 30].

Isotopic methods provide a *mathematical* representation of excess energy (21) via iso-renormalization (11) with numeric value of the density

$$n_4^2 = \frac{3E_e}{E_\mu} = \frac{1.533}{105.7} = 0.0149 , \tag{22}$$

under which the consistency of the Schrödinger equation is restored at the isotopic level [12].

Excess energy (21) can be *physically* represented e.g. via the kinetic energy of the peripheral constituents. It should be indicated that missing energy (21) also occurs in the synthesis of the neutron from the hydrogen in the core of stars [31], as well as, more generally, in the synthesis of hadrons from lighter particles [12].

The use of normalization

$$n_1^2 + n_2^2 + n_3^2 = 1 , \tag{23}$$

then provides the desired first approximation of the charge distribution and shape of muons

$$n_1^2 = n_2^2 \approx 0.4926, \quad n_3^2 \approx 0.0149 . \tag{24}$$

The above data confirm the expected very prolate character of structure model (18) due to the point-like character of the constituents.

5 Concluding remarks

In the author's view, the most important notion emerging from the preceding study is that of the Einstein-Podolsky-Rosen entanglement representing the instantaneous and continuous

communications between extended particles due to the overlapping of their wavepackets, with ensuing non-Hamiltonian interactions represented by (2) and (3), whose consistent treatment required the construction of iso-mathematics and iso-mechanics [17].

In fact, the EPR entanglement has the following important implications:

1. It prevents the applicability of Bell's inequality [18] due to the presence of non-Hamiltonian interactions first studied in [8];
2. It provides an explicit and concrete realization of Bohm's hidden variables [7] in terms of the isotopic element first achieved in [9]; and
3. It permits a preliminary, yet numerically exact and time invariant representation of all characteristics of muons, including their anomalous magnetic moment [1].

In closing, there seems to be grounds for a new physics, with expected corresponding advances in chemistry and biology, via the axiom-preserving completion of the Copenhagen simplest possible realization of quantum axioms into their broadest possible realization suggested by hadronic mechanics [13].

Received on September 14, 2021

References

1. Miller J. P., de Rafael E. and Roberts B. L. Muon (g-2): experiment and theory. *Rep. Prog. Phys.*, 2007, v. 70, 795–881.
2. Fadel M., Zibold T., Decamps B., Treutlein Ph. Spatial entanglement patterns and Einstein-Podolsky-Rosen steering in Bose-Einstein condensates. *Science*, 2018, v. 360, 409. www.santilli-foundation.org/Basel-paper.pdf.
3. Schukraft J. Heavy-ion physics with the ALICE experiment at the CERN Large Hadron Collider. *Trans. R. Soc.*, 2012, v. A370, 917–932. royalsocietypublishing.org/doi/10.1098/rsta.2011.0469.
4. Einstein A., Podolsky B., and Rosen N., Can quantum-mechanical description of physical reality be considered complete? *Phys. Rev.*, 1935, v. 47, 777. www.eprdebates.org/docs/epr-argument.pdf.
5. Heisenberg W. *Nachr. Akad. Wiss. Gottingen*, 1953, v. IIa, 111. link.springer.com/chapter/10.1007/978-3-642-70079-8_23.
6. Stanford Encyclopedia of Philosophy. Bohmian (de Broglie-Bohm) Mechanics. 2021. plato.stanford.edu/entries/qm-bohm/.
7. Bohm D. A Suggested Interpretation of the Quantum Theory in Terms of "Hidden Variables". *Physical Review*, 1952, v. 85, 166. journals.aps.org/pr/abstract/10.1103/PhysRev.85.166.
8. Santilli R. M. Isorepresentation of the Lie-isotopic SU(2) Algebra with Application to Nuclear Physics and Local Realism. *Acta Applicandae Mathematicae*, 1998, v. 50, 177–190. www.santilli-foundation.org/docs/Santilli-27.pdf.
9. Santilli R. M. Studies on the classical determinism predicted by A. Einstein, B. Podolsky and N. Rosen. *Ratio Mathematica*, 2019, v. 37, 5–23. www.eprdebates.org/docs/epr-paper-ii.pdf.
10. Santilli R. M. Studies on A. Einstein, B. Podolsky, and N. Rosen prediction that quantum mechanics is not a complete theory. I: Basic methods. *Ratio Mathematica*, 2020, v. 38, 5–69. eprdebates.org/docs/epr-review-i.pdf.
11. Santilli R. M. Studies on A. Einstein, B. Podolsky, and N. Rosen prediction that quantum mechanics is not a complete theory. II: Apparent proof of the EPR argument. *Ratio Mathematica*, 2020, v. 38, 71–138. eprdebates.org/docs/epr-review-ii.pdf.
12. Santilli R. M. Studies on A. Einstein, B. Podolsky, and N. Rosen prediction that quantum mechanics is not a complete theory. III: Illustrative examples and applications. *Ratio Mathematica*, 2020, v. 38, 139–222. eprdebates.org/docs/epr-review-iii.pdf.
13. Santilli R. M. Overview of historical and recent verifications of the Einstein- Podolsky-Rosen argument and their applications to physics, chemistry and biology. APAV - Accademia Piceno Aprutina dei Velati, Pescara, Italy, in press, 2021. www.santilli-foundation.org/epr-overview-2021.pdf.
14. Dunning-Davies J. A Present Day Perspective on Einstein-Podolsky-Rosen and its Consequences. *Journal of Modern Physics*, 2021, v. 12, 887–936. www.scirp.org/journal/paperinformation.aspx?paperid=109219.
15. Santilli R. M. Foundation of Theoretical Mechanics. Vol. I, The Inverse Problem in Newtonian Mechanics. Springer-Verlag, Heidelberg, Germany, 1978. www.santilli-foundation.org/docs/Santilli-209.pdf.
16. Santilli R. M. Foundation of Theoretical Mechanics. Vol. II, Birkhoffian Generalization of Hamiltonian Mechanics. Springer-Verlag, Heidelberg, Germany, 1982. www.santilli-foundation.org/docs/santilli-69.pdf.
17. Santilli R. M. Elements of Hadronic Mechanics. Volumes I, II, III. Ukraine Academy of Sciences, Kiev, 1995 (I), 1995 (II), 2016 (III). www.i-b-r.org/Elements-Hadronic-Mechanics.htm.
18. Bell J. S. On the Einstein Podolsky Rosen paradox. *Physics*, 1964, v. 1, 195–200. cds.cern.ch/record/111654/files/vol1p195-200_001.pdf.
19. Santilli R. M. Isonumbers and Genonumbers of Dimensions 1, 2, 4, 8, their Isoduals and Pseudoduals, and "Hidden Numbers" of Dimension 3, 5, 6, 7. *Algebras, Groups and Geometries*, 1993, v. 10, 273–322. www.santilli-foundation.org/docs/Santilli-34.pdf.
20. Jiang C.-X. Foundations of Santilli Isonumber Theory. International Academic Press, Palm Harbor, FL, 2001. www.i-b-r.org/docs/jiang.pdf.
21. Santilli R. M. Nonlocal-Integral Isotopies of Differential Calculus, Mechanics and Geometries. In: Isotopies of Contemporary Mathematical Structures. *Rendiconti Circolo Matematico Palermo, Suppl.*, 1996, v. 42, 7–82. www.santilli-foundation.org/docs/Santilli-37.pdf.
22. Falcon Ganfornina R. M. and Valdes J. Fundamentos de la Isoteoria de Lie-Santilli. International Academic Press, Palm Harbor, FL, 2001. www.i-b-r.org/docs/spanish.pdf.
23. Georgiev S. Foundation of the IsoDifferential Calculus. Volumes I to V. Nova Academic Publishers, New York, NY, 2014 (I), 2014 (II), 2015 (III), 2015 (IV), (2016 (V).
24. Santilli R. M. Lie-isotopic Lifting of Special Relativity for Extended Deformable Particles. *Lettere Nuovo Cimento*, 1983, v. 37, 545–551. www.santilli-foundation.org/docs/Santilli-50.pdf.
25. Aringazin A. K., Jannussis A., Lopez F., Nishioka M. and Vel-janosky B. Santilli's Lie-Isotopic Generalization of Galilei and Einstein Relativities. Kostakaris Publishers, Athens, Greece, 1991. www.santilli-foundation.org/docs/Santilli-108.pdf.
26. Sourlas D. S. and Tsagas G. T. Mathematical Foundation of the Lie-Santilli Theory. Ukraine Academy of Sciences, Kiev, Ukraine, 1993. www.santilli-foundation.org/docs/santilli-70.pdf.
27. Santilli R. M. Nonlinear, Nonlocal and Noncanonical Isotopies of the Poincaré Symmetry. *Moscow Phys. Soc.*, 1993, v. 3, 255. www.santilli-foundation.org/docs/Santilli-40.pdf.
28. Santilli R. M. Recent theoretical and experimental evidence on the synthesis of the neutron. *Chinese J. System Eng. and Electr.*, 1995, v. 6, 177–186. www.santilli-foundation.org/docs/Santilli-18.pdf.

29. Santilli R. M. Invariant Lie-isotopic and Lie-admissible formulation of quantum deformations. *Found. Phys.*, 1997, v. 27, 1159–1177. www.santilli-foundation.org/docs/Santilli-06.pdf.

30. Santilli R. M. Need of subjecting to an experimental verification the validity within a hadron of Einstein special relativity and Pauli exclusion principle. *Hadronic J.*, 1978, v. 1, 574–901. www.santilli-foundation.org/docs/santilli-73.pdf.

31. Norman R., Beghella Bartoli S., Buckley B., Dunning-Davies J., J. Rak J., Santilli R. M. Experimental Confirmation of the Synthesis of Neutrons and Neutroids from a Hydrogen Gas. *American Journal of Modern Physics*, 2017, v. 6, 85–104. www.santilli-foundation.org/docs/confirmation-neutron-synthesis-2017.pdf.

LETTERS TO PROGRESS IN PHYSICS

On Eddington's Temperature of Interstellar Space and the Cosmic Microwave Background Radiation

Pierre A. Millette

E-mail: pierre.millette@uottawa.ca, Ottawa, Canada

We point out that there were several non-cosmological estimates of the blackbody temperature of interstellar space that predated and that were more accurate than the Cosmic Microwave Background (CMB) Big Bang estimates. They are disregarded and considered coincidental as they are not based on the cosmological Big Bang model. We note the importance of this question, as the energy requirements of the two different explanations (galactic vs cosmological) are substantially different. We also point out that the actual correct explanation can't be determined from the measurements done in our local neighbourhood inside the Milky Way.

The great tragedy of Science – the slaying of a beautiful hypothesis by an ugly fact. Thomas Henry Huxley (1825–1895)*.

1 Introduction

Penzias and Wilson [1], while working at Bell Labs, measured an isotropic Microwave Background Radiation (MBR) of approximately 3 K, while using a sensitive antenna/receiver system under development. Initially, they thought the radio noise resulted from their equipment, but eventually they concluded that the background radiation was real.

Physicist Robert Dicke suggested that the background radiation was the Cosmic Microwave Background (CMB) radiation, believed to result from the Big Bang cosmological model. This interpretation was published in side-by-side letters by Penzias and Dicke in Astrophysical Journal Letters [2]. Penzias and Wilson measured an isotropic Microwave Background Radiation which became the Cosmic Microwave Background (CMB) radiation in the serendipitous communication with Dicke, nowadays the only accepted explanation for the measurement.

However, there were other earlier blackbody† temperature predictions, that were much closer to the initial measurement of Penzias and Wilson, than those from the Big Bang, but they were simply ignored as they did not originate from the Big Bang cosmological model. Interestingly enough, the very fact that the remarkably close blackbody temperature predictions do not originate in the Big Bang model is used against the validity of the other models in predicting a blackbody temperature in agreement with the Penzias and Wilson measurement!

At stake is whether the Microwave Background Radiation is universal and cosmic (i.e. CMB) or galactic in nature (i.e. MBR), with possibly every galaxy having slightly different local blackbody temperatures. The energy requirements of the two different explanations are substantially different. The reality is that this can't be determined from the measurements done in our local neighbourhood (at about 27 000 light-years from the galactic centre) within our Milky Way which is about 100 000 light-years across and about 2 000 light-years thick at the thin stellar disk that we are located in.

2 Eddington's "Temperature of interstellar space"

Assis and Neves in their 1995 paper *History of the 2.7 K Temperature Prior to Penzias and Wilson* [3] provide a review of earlier blackbody temperature determinations, prior to the Big Bang cosmological model temperature estimates of the late 1940s, 1950s and early 1960s which varied between 5 K and 50 K. Their conclusion that "the models based on a Universe in dynamical equilibrium without expansion predicted the 2.7 K temperature prior to and better than models based on the Big Bang" is, understandably so, not very popular.

The best-known earlier blackbody temperature prediction is that of $T = 3.2$ K proposed by Arthur Stanley Eddington in 1926 [5], known as the *temperature of interstellar space* to clearly communicate that it is not related to the CMB, especially since Eddington's estimate was derived before the development of the Big Bang cosmological model. Modern commentators constantly remind us that it is coincidental and that it does not derive from the Big Bang model. We don't want people to see it as an explanation of the MBR that would be an alternative to the CMB Big Bang explanation!

Eddington, in his 1926 book *The Internal Constitution of the Stars* [6], further covered the topic in Chapter XIII, *Diffuse Matter in Space*. He computes an effective blackbody temperature of 3.18 K, but again, this has nothing to do with the 2.725 K blackbody spectrum of the Microwave Background Radiation (MBR), which we know is the Cosmic Microwave Background (CMB). Eddington states:

> The total light received by us from the stars is estimated to be equivalent to about 1000 stars of the

*Wikiquote. Thomas Henry Huxley. In his Presidential Address at the British Association in 1870, last modified 07:40 4 May 2019.

†The estimates are described as blackbody temperatures as the Stefan-Boltzmann blackbody radiation law was used to determine the temperature.

> first magnitude. ... We shall first calculate the energy density of this radiation. ... Accordingly the total radiation of the stars has an energy-density ... $E = 7.67 \cdot 10^{-13}$ erg/cm^3. By the formula $E = aT^4$ the effective temperature corresponding to this density is 3.18° absolute. [6, p. 371]

Eddington thus uses the Stefan-Boltzmann blackbody radiation law to determine the temperature of the blackbody equivalent to the estimated energy density of stellar radiation.

Eddington then attempts to specify a model for the spectrum of his estimated interstellar radiation field, based on his hypothesis of the statistical properties of stellar radiation:

> Radiation in interstellar space is about as far from thermodynamical equilibrium as it is possible to imagine, and although its density corresponds to 3.18° it is much richer in high-frequency constituents than equilibrium radiation of that temperature. [6, p. 371]

On this count, Eddington strayed from the data and that part of his analysis missed the mark.

The near-equality of Eddington's blackbody temperature of space and the CMB is considered a coincidence as "[t]he starlight radiation field is concentrated in galaxies like the Milky Way, which only occupy one part per million of the volume of the Universe, while the CMB fills the entire Universe" [7]. This comment demonstrates exactly the point raised in this Letter, and as we have been pointing out, it is hard for cosmologists to think outside of the CMB paradigm.

We also note several other non-cosmological estimates of the temperature of interstellar space that predate and that were more accurate than the Cosmic Microwave Background (CMB) Big Bang estimates [4]. Regener [8] predicted a value of 2.8 K in 1933 based on an analysis of the energy of cosmic rays arriving on Earth. This is remarkably close to the current best estimate of the value of a thermal blackbody spectrum at a temperature of 2.72548±0.00057 K [9]. Mackellar, following his identification of interstellar molecules [10], obtained the value 2.3 K in 1941, using the levels of excitation of the cyanogen molecule (CN) in intergalactic space [11].

3 Cosmic Microwave Background anisotropy

The CMB (or MBR) is highly isotropic, to roughly one part in 100 000. The spectral radiance contains small anisotropies which vary with the size of the region under examination. This anisotropy requires its own analysis separate from this Letter [12–14].

Suffice to say that advanced digital signal processing is performed on the data (e.g. [15]). A dipole anisotropy caused by the velocity of the Sun of about 370 km/s towards the constellation Leo, as determined from the MBR, is first subtracted from the Doppler shift of the background radiation. The root mean square (RMS) variations of the remainder are only 18 μK [7]. This anisotropy is a characteristic of the Microwave Background Radiation, whether it is of galactic or cosmological origin. Occam's razor favours a galactic origin.

4 Discussion and conclusion

In this Letter, we have pointed out that there were several non-cosmological estimates of the blackbody temperature of interstellar space that predated and that were more accurate than the Cosmic Microwave Background (CMB) Big Bang estimates. They are disregarded and considered coincidental as they are not based on the cosmological Big Bang model. We note the importance of this question, as the energy requirements of the two different explanations (galactic vs cosmological) are substantially different. We also point out that the actual correct explanation can't be determined from the measurements done in our local neighbourhood inside the Milky Way.

Received on September 25, 2021

References

1. Penzias A. A. and Wilson R. W. A Measurement of Excess Antenna Temperature at 4080 Mc/s. *Astrophysical Journal Letters*, 1965, v. 142, 419–421.
2. Dicke R. H., Peebles P. J. E., Roll P. J. and Wilkinson D. T. Cosmic Black-Body Radiation. *Astrophysical Journal Letters*, 1965, v. 142, 414–419.
3. Assis A. K. T., Neves M. C. D. History of the 2.7 K Temperature Prior to Penzias and Wilson. *Apeiron*, 1995, v. 2 (3), 79–84.
4. Assis A. K. T., Neves M. C. D. The Redshift Revisited. *Astrophysics and Space Science*, 1995, v. 227, 13–24.
5. Eddington, A. S. Diffuse Matter in Interstellar Space. *Roy. Soc. Proc.*, 1926, v. 111, 424–456.
6. Eddington, A. S. The Internal Constitution of the Stars. Cambridge University Press, Cambridge, 1926/1988 reprint, Chapter 13, p. 371.
7. Wright E. L. Eddington's Temperature of Space. www.astro.ucla.edu/~wright/Eddington-T0.html, last modified 23 October 2006.
8. Regener E. Der energiestrom der ultrastrahlung. *Zeit. Phys.*, 1933, v. 80, 666–669.
9. Fixsen, D. J. The Temperature of the Cosmic Microwave Background. *The Astrophysical Journal*, 2009, v. 707 (2), 916–920. arXiv: astro-ph/0911.1955.
10. Mackellar A. Evidence for the Molecular Origin of Some Hitherto Unidentified Interstellar Lines. *Publications of the Astronomical Society of the Pacific*, 1940, v. 52 (307), 187.
11. Mackellar A. *Pub. Dom. Astrophys. Observatory, Victoria, BC*, 1941, v. 7, 251.
12. Wright E. L. Theoretical Overview of Cosmic Microwave Background Anisotropy. In: Freedman W. L., ed. Measuring and Modeling the Universe. Cambridge University Press, Cambridge, 2004, p. 291. arXiv: astro-ph/0305591.
13. Challinor A. CMB anisotropy science: a review. arXiv: astro-ph.CO/1210.6008.
14. Hoyle F., Burbidge G. and Narlikar J. V. A Different Approach to Cosmology, From a Static Universe through the Big Bang towards Reality. Cambridge University Press, Cambridge, 2000.
15. Hivon E., Górski K. M., Barth Netterfield C., Crill, B. P., Prunet S., Hansen F. MASTER of the CMB Anisotropy Power Spectrum: A Fast Method for Statistical Analysis of Large and Complex CMB Data Sets. arXiv: astro-ph/0105302.

LETTERS TO PROGRESS IN PHYSICS

In Memoriam of Simon Shnoll (1930–2021)

Dmitri Rabounski
Puschino, Moscow Region, Russia. E-mail: rabounski@yahoo.com

Simon Shnoll passed away on September 11, 2021 being 91 years old. He was born on the vernal equinox, March 21, 1930, and was one of the few greatest biophysicists of the 20th century, as well as a very good open hearth person. I have known him closely for many years. Here I want to pay tribute to his memory and his outstanding achievements in science.

Simon Shnoll was born on March 21, 1930, the day of vernal equinox, in Moscow, the USSR. His father Eli Shnoll was a religious philosopher belonging to the Russian Orthodox Church (as well as a polyglot who was fluent in more than twenty languages). In 1933 his father was imprisoned for his faith, together with many hierarchs of the Orthodox Church, to the prisoner camp on the Solovki Islands, but after three years of jail, in 1936, he was released as hopeless ill then died shortly before World War II. His mother Faina was a school teacher. His parents were religious; they had four sons. On the contrary, Simon Shnoll grew up an atheist; he told me many times: "My father was a religious philosopher and was fluent in twenty languages, while I know only one language and do not believe in God, but I believe in the Saints who lived in the past and those who live among us."

Simon Shnoll. Puschino, about 2005.

Simon Shnoll spent his childhood in Kaluga, a city on the Oka River, 160 km south-west of Moscow, where his family lived in exile. Due to job restrictions, his mother was largely unemployed: his family survived on odd jobs. Simon started to work commencing his 6 years as a herdsman in the summer season. His family experienced hunger; his youngest brother died in baby age of hunger in Autumn, 1941, because his mother lost milk due to hunger. Simon Shnoll always told me that only a person who has survived many years of hunger and watched how people have no power to bury the bodies of their relatives can understand the divine aroma of a freshly cooked loaf of bread.

Simon Shnoll first visited the Puschino area being an 11-year-old boy, in the summer of 1941 in search of casual work in the fields on the northern (low) bank of the Oka River opposite Puschino (located on the southern bank, at an altitude of 190 meters). There was a rest house for the officers' school cadets and a beach. Simon decided to freshen up in the river with the cadets who were sunbathing on the beach, but got into a whirlpool that sucked him weakened by hunger, and he began to drown, screaming for help. The cadets, these athletic young men, pulled him out of the river by the hair and, looking at his very skinny body, fed him as best they could. All these cadets were killed in action three months later, in October, 1941, on the fields near Moscow, when, armed only with rifles and grenades, they tried to stop the German tank columns moving towards Moscow (but they did it). The bridge near Puschino across the Oka River connecting Moscow and Tula is named after them.

The battleline very quickly approached Moscow, and at the end of August 1941, when 11-year-old Simon was grazing cattle in the fields on the northern (low) bank of the Oka River, he suddenly saw a chain of small fountains of dust rising from the ground and quickly approaching him, and then he heard pops shots from above: it was a German fighter pilot who decided to "hunt" a boy among a herd of cows... Simon first ran in a zigzag among the cows, then stumbled, fell and waited for death, but the German pilot used up all his ammunition and flew away.

When Simon returned back to Kaluga, there was chaos due to approaching the battleline. In the early morning of October 12, 1941, a military commissar knocked the door of Shnoll's room. The commissar went around all the civilian residents in their borough and told them: "Go away, today the Germans will come and kill you all." He was kind enough to help Shnoll's mom and all her four children get to the train station and then put them on the last train heading towards Moscow. His prediction was prophetic: within 2.5 months from October 12 to December 30, 1941, when Kaluga (50,000 inhabitants) was under occupation, the Germans killed more than 20,000 people in the ghetto and POW

camp, including the captured soldiers and officers of the Kaluga garrison. A few years later, Shnoll's former neighbour, who moved to Moscow after the liberation, told him and his mother that, on their street, German soldiers often shot pedestrians just for fun, using them as targets for shooting training. Those were grey-dressed soldiers of Wehrmacht, and not SS. It was a bloody bacchanalia of war...

The refugees, including Shnoll's family were dropped off a train in a rural area far from Moscow, then Shnoll's mother and four her sons wandered around the villages of the Moscow region for a month in the cold autumn, begging for alms from the peasants. His younger brother, a baby, starved to death during this time. When Shnoll's mother with her three surviving children reached Moscow, they were allowed to stay there, because her husband, an "enemy of the people", had already died, so the restrictions on his family were lifted. Only 2.5 years later, in 1944, she found a permanent job as a teacher in an orphanage, where she and her sons could live and dine with orphans — "children of war".

The wartime in Moscow was accompanied by a surf of street crime. Even the immediate executions at the crime scene by police patrols could not stop the street robberies and murder. Once criminal teenagers who were older than Simon beat him to a pulp; they knocked out all of his front teeth. After this incident, Simon decided to take his fate into his own hands: he took a basic self-defence course from one of sports teachers. This saved his life many years later, in 1956, when the security officer who controlled Shnoll's work at that time, being completely drunk, tried to shoot him due to personal animosity. This happened in the forest on a river bank, during one of the trips of the laboratory employees to wild nature, near the campfire, where they all drank medical alcohol diluted half-to-half with water (they had much medical alcohol in the laboratory for biological purposes, while the laboratory rabbits were a good addition to the dinner table in the conditions of a total deficit of food products in the stores of the USSR). When the others were legless from the alcohol they drank, Simon Shnoll refused to continue drinking with the security officer, which sparked an outburst of his aggression. He told Shnoll: "I will kill you, and then all the Jews". Then he pulled his pistol out of the holster, sent a bullet into the pistol chamber and tried to shoot Simon. However, Simon turned him over with a judo technique, turned his hand with the pistol under his chin and... did not fire. Simon explained to me that this self-defence technique against an armed person necessarily ends with a shot to head: the fighter does not think, but automatically performs all these sequential movements, including the final headshot, which is achieved by long term training. But — said Simon — something stopped him at the last moment and he did not take the mortal sin of murder upon his soul. Simon stunned the security officer with a blow and then, having unloaded his pistol, threw all the bullets into the river. The security officer had a lot of respect for Simon after this incident.

Prior 1944, Simon Shnoll had never visited school. In Moscow, in 1942–1944 he worked as an electrician's assistant boy. In the meantime, he was educated at home by his mother, who was a very educated person. As a result, in 1944, being a 14-year-old boy, Simon Shnoll passed the 9th grade exam and graduated from school in 2 seasons in 1946.

In the summer of 1946, being 16 years old, Simon Shnoll entered the Department of Biology of Moscow University. It was the first peaceful summer after World War II, when hundreds of thousands of demobilized young soldiers tried to enter in universities. The number of applications per one student seat reached several hundreds. To enter, you had to pass all the entrance exams fine. At one of the entrance exams, 16-year-old Simon Shnoll met the love of his life, Maria Kondrashova, who was then 18 years old. She told me how this happened. She and Simon got up from their desks in the exam room at the same time and gave their exam papers to the examiner. The examiner began to check their papers at the same time, while they stood next to his desk. She watched at Simon. He looked like a small, skinny chick. She told me that she immediately felt a strong desire to warm and feed Simon like a child... After checking their exam papers, the examiner looked at them and said: "Both of your exam papers are good enough, but his paper is much better!" She immediately said a reply, looking towards Simon: "What a buster!" Very soon after that day, they realized that they could not live without each other and remained together for 74 years until she passed away on June 11, 2020. They had a son and daughter, as well as many grandchildren.

Maria Kondrashova was a biochemist. She and Simon were graduated from the same Department of Biology, where they had the same teacher, Prof. Sergey Severin, who introduced them into science. Maria and Simon lived in a small room in a shared apartment with neighbours in Moscow until 1963, when they were invited to live and work in Puschino, to a new research institute called the Institute of Theoretical and Experimental Biophysics (a.k.a. the Institute of Biophysics), where each of them headed his own research laboratory. Like Simon Shnoll, she first got a degree of Candidate of Sciences (which is analogous to the PhD degree), then — a degree of Doctor of Sciences. She was also a Professor of Moscow University. In addition to many of her other scientific works, her last major work, which she conducted since the 1990s, was a method of total diagnosis of the whole body using the analysis of just one drop of blood. Her outstanding scientific discoveries and ideas are scattered across many of her scientific articles in Russian, often in a very succinct concise form and, therefore, little known to the scientific community. These results and the technologies she developed are still awaiting rediscovery.

As for her personality, I would call her a "commander" in spite of the fact that she was a very nice and intelligent woman in everyday communication, in particular with me. She quickly recognized the identity of people and then be-

haved with them according to their personality. I discussed this issue with her. She explained to me that in science there is always only one leader who created an idea and developed it, and all the others are only assistants. Otherwise, without a "strong hand" any business, even a very good scientific development, would quickly collapse. Therefore, she always considered those who helped her in her laboratory to be mercenaries. In particular, therefore, she did not have followers in science. Science is moving forward by the forces of bright individuals, of whom there are very few, and not by scientific teams, as many mistakenly think, — she explained. Any scientific team shines with the reflected light emitted by its leader, and as soon as this leader ceases to exist, his or her team "goes out", ceasing to do something new, because only an individual, due to the strength of his of her will, is able to generate ideas and do scientific developments.

As for Simon, her husband, she told me that he is not really the "nice grey-haired old man" I have known for the past three decades. In fact, he is a very determined and risk-taking person, capable of, for example, surviving alone in a wild forest or repelling a gang of armed robbers. His psychology — she said — is rather similar to the psychology of a 14-year-old teenager, since only teenagers are not afraid of death and do everything without thinking about the consequences. The advantage of such a psychology is that Simon Shnoll had his own, completely independent point of view on many familiar things both in everyday life and in science.

Let us go back to Simon Shnoll and his story. After graduating from the Department of Biology in 1951, Simon Shnoll was under risk to be sent as a private for 5 years of military service (like his elder brother, a mathematician, who served 5 years in Red Army after the graduation). It was possible to be free from military service if he was hired by an institution where positions were equated to military service. After two months of nervous searches, Simon Shnoll took a job in a research laboratory of the Department of Radiology of the Institute for the Professional Development of Physicians. The laboratory was directly subordinated to the Soviet atomic project and included both military and civilian doctors; they studied how high doses of radiation exposure affect animals.

Despite the high level of secrecy in the laboratory, there was a complete mess and irresponsibility with safety measures for the staff during the radiation exposure of test animals. As a result, one day Simon Shnoll got a lethal dose of radiation. The female doctor who examined him said he would definitely die from radiation sickness within one month and all she could do for him is to give him as much pain reliever as needed. It was a very sad month in his life. He was ready to die, but his body had overcame the sickness in some incredible way. Moreover, he told me that his body had fully recovered without any repercussions, including the reproductive function. He explained that radiation exposure may not always be fatal, while radiation poisoning is always fatal due to the small radioactive particles penetrated into the body and permanently exposing it with their radiation.

Following this incident, Simon Shnoll became unfit for military service, but he continued to work in the Department of Radiology of the Institute for the Professional Development of Physicians. Then, since 1959, he began to lecture on biochemistry at the Physics Department of Moscow University, where he began as an associate professor, and then a professor until his death.

In 1963, Prof. Gleb Frank, a biophysicist, a member of the USSR Academy of Sciences, as well as a very influential organizer of science in the USSR, invited Simon and Maria to continue their scientific research in Puschino, a new "academic" town just erected 100 km south of Moscow on the southern (high) bank of the Oka River near the radio astronomical observatory of the Academy of Sciences. There were no "outsiders" in the new "academic" town: the peasants of the small village, Puschino, which had been located on the site for the past 600 or 800 years, were deported (except only a few persons who escaped the deportation) just before the construction of the town began in 1959. The absence of "outsiders" in the town created a unique social environment consisting only of scientists (and a small number of builders). Gleb Frank provided Simon and Maria with personal laboratories at a new research institute called the Institute of Biophysics, where he was Director. He also conversated with the town administration about providing them with a 4-bedroom apartment on the 9th (upper) floor of a just erected residential tower, which was luxurious living conditions compared to the small room in the shared apartment, where they huddled in Moscow. These were the first two "settlers" that Frank invited to live and work in Puschino. Simon always told me that Maria was the "settler number 1", and he was "number 2". On the contrary, Maria told me that he was the "settler number 1", and she was only "number 2".

For Simon Shnoll, it was a return to the areas of his childhood on the Oka riverbanks. Simon and Maria moved to Puschino with Maria's mother, who volunteered to took care of their son and daughter, while Simon and Maria spent all their time in their laboratories at the Institute. These were the times of the USSR, when workers received salary regardless of the results of their labour. Therefore, the quality of building work was low. The very first rain revealed many cracks in the waterproofing layer of the roof above the apartment, where Simon and Maria lived. Since there was nowhere to wait for help, Simon made a fire in front of the house, on which he melted down more than a dozen buckets of bitumen, and then going upstairs to the roof with the buckets of molten bitumen (the elevator in their house had not yet worked), filled all the cracks in the waterproofing layer. Also, the common heating system in the town sometimes malfunctioned during the winter seasons so that their slippers and tights of their little children froze to the floor. Nevertheless, life improved year after year. Fresh air (as opposed to the air in Moscow), a view of the endless Russian expanses and of a

natural reserve on the opposite northern (low) bank of the Oka River (the bison natural reserve), as well as weekly picnics in the near forest neutralized all troubles of their first years in Puschino. A few years later, Simon and Maria hired workers who built a house for them in a cottage village of biophysicists near Puschino. Simon got carried away with the cultivation of an orchard and growing potatoes, but soon abandoned this "agricultural hobby", when realized that it takes away almost all of his time and is incompatible with his scientific research.

Simon travelled to Moscow twice a week, where he lectured at the Physics Department of Moscow University. Then there was no rapid express bus connecting Moscow and Puschino and private cab services (as now), and, therefore, such a trip took many hours. Also, in Puschino, as almost elsewhere in the USSR, there was a shortage of food products in stores; even with enough money, people could not freely buy what they wanted. In Puschino, this situation was solved by the fact that each Institute had its own restaurant, where employees had breakfasts and dinners with all their family members. However, the supply in the Moscow stores was good. Therefore, Simon usually travelled to Moscow on the eve of his lecture day. Arriving in Moscow in the evening, he usually purchased two full carry bags and a full backpack of food, then spent the night at the Facility of Biophysics of the Physics Department. Then, in the morning and in the daytime, he gave lectures, after which, already in the evening, he returned by bus to Puschino.

The life and all scientific achievements of Simon Shnoll and Maria Kondrashova after 1963 and until the last years of their lives were associated with Puschino and the Institute of Biophysics, which they considered their home. Shnoll's laboratory was one of the largest at the Institute: he told me that at the years of rise, he had 67 employees who did what he said. Since 1963, the staff of his laboratory were bestowed 26 Doctor of Sciences degrees and more than 120 Candidate of Sciences (PhD) degrees. In addition, many other laboratories of the Institute were founded by his employees, who decided to start their own research in another field of biophysics.

However, the years often change people or, most likely, as Jack London noticed, we often do not see the hidden character traits of some persons, which then become apparent over the years. In the beginning, Shnoll's laboratory staff and their families usually went out on a joint picnic at a weekend in the nearby forest. Then this picnic "decayed" into several smaller picnics, the participants of which tried to ignore others. Then, 10 years after the founding of the Institute, some of his former employees stopped greeting him, meeting him in the town or in the Institute... Maria told him that these were not true scientists, but those who simply wanted to "get well" in life; they got everything they wanted from him — scientific degrees and individual laboratories — and now they no longer need him. Simon Shnoll told me that this poor fact deeply hurt his heart, as he considered all his former employees to be his friends. During the mass "exodus" of scientists from Puschino in 1989–1991, just after the Iron Curtain that separated the USSR from the rest of the world has rushed down, many scientists left Puschino for the USA and Germany. According to Maria, after those two years some Institutes had become 75% empty. Their daughter had already lived in Moscow. Their son left for the USA with his wife and their children (they lived with Simon and Maria in the same 4-bedroom apartment): Simon and Maria were left alone in their apartment... Their circle of close friends narrowed even more; among them were remaining Eugeny Maevski and Heindrich Ivanitski, who held heading positions at their Institute and always supported Simon and Maria.

Simon Shnoll at the dinner table in his laboratory. Puschino, 2005.

However, it was in the early 1990s that Simon Shnoll's research got the most rise (from the use of personal computers). To understand this, it is necessary to go back to 1951, when he first drew attention to a phenomenon that much later, in 2005, I called the *Shnoll effect*.

In 1951, Simon Shnoll, who had just graduated from university, began working in a research radiological laboratory subordinated to the Soviet atomic project (see above). Among other things, he conducted experiments to study the interaction of radioactive amino acids with muscle proteins (this was the topic of his PhD thesis). He discovered that the rate of this (very stable) chemical reaction, measured in hundreds of consecutive very accurate measurements taken during one working day through the same short time intervals, has systematic deviations from the average numerical value, which are not dependent of the experimental conditions, but only on the local time of measurement. It looked as if some very fine noise, with its repeated minima and maxima, was superimposed on the measurements of the very stable rate of this chemical reaction. The study of this systematic noise, its fine structure and origin became the main scientific task of Simon Shnoll throughout his life.

Continuing these studies in the 1950s in Moscow and then in the 1960–1970s in Puschino, Shnoll found that this specific noise is present not only in measurements of the rate of chemical reactions in muscle proteins, but also in any proteins in general. Moreover, in the 1970s, he found this noise in any biochemical reactions that he tested. Even more, in 1970–1980s, he found this noise, with its specific minima and maxima, in any consecutive physical measurement that he tested or analysed, unnecessary biochemical reactions. For example, he found it by measuring the rate of alpha-decay and beta-decay of atomic nuclei. In general, he found the following: the more stable the signal was, the better this noise manifested itself.

When I first met Simon Shnoll in 1991, I asked him: "What should be measured to detect this noise and its fine structure?" He adjusted his glasses with his hand and answered me: "It does not matter what!"

It should be noted that registering the systematic noise in an experiment is only a small percentage of the whole problem. The main trouble is the processing of the measurement results, which allows you to "see" this noise and its fine structure. In the pre-computer era, when performing these experiments based on a sequence of measurements of a signal for one day, month, or year, you had to do the following. First, you had to manually create on paper a histogram of the measured numerical values of the signal for each measurement interval, say, for each interval of 15 or 30 seconds. This would result in about 2,880 hand-drawn histograms per day, about 86,400 hand-drawn histograms per month, and over 1 million hand-drawn histograms per year for 30-second measurement intervals (double the number of histograms for 15-second intervals). Then you had to visually compare all these histograms with each other to find the ones that match each other in their shape. And finally, you had to create a graph that shows when the found similar histograms appear according on the local time. In the pre-computer era, Shnoll was forced to limit himself to only analysing the results of measurements obtained within one or two days. Even so, he had to create over 3,000 hand-drawn histograms for each experiment and then visually compare all those hand-drawn histograms to each other. This is clearly an overwhelming task for one person. Dozens of his employees, mostly young women who graduated from Moscow University, drew these thousands of histograms by hand every day and then compared them with each other. It was a titanic work!

Things got much easier in 1997, when Edwin Pozharski, a young man from Poland, who, just graduated from Physical Technical Institute that is to north of Moscow (he was engaged in X-ray analysis of proteins), created a computer program allowing to create and analyse dozens and hundreds of thousands of histograms. In particular, the use of his program allowed to create and analyse histograms for measurements performed over a week, month and even a year. He created this program not for fame or money (he did it on a volunteer basis), but simply out of great respect for Shnoll and his research. His program has gone through many updates and is still the main working tool in the study of the Shnoll effect. Thanks to him!

The next 10 years of Shnoll's research after 1997 were the most fruitful. Using the computer program to create histograms and analyse them, he found that the discovered fine structure is manifested in any random noise, and not only in the random noises registered in biological and physical processes. In particular, he found the same fine structure in the random noise generated by a random number generator on a computer.

To summarize briefly the Schnoll effect, it is best to give a quote from my 2014 article*, where I already did it:

> "The principal error in understanding the Shnoll effect is that some people think it is a periodical fluctuation of the magnitude of the signal that is measured. This is incorrect, since the magnitude of the signal and the average noise remain the same during the long-term measurements done by Shnoll and his workgroup. Further, such processes are specifically chosen for the study that are very stable in time. Simply put, nothing allegedly changes in the experiments which continue during days, months, and even years. The subject of the measurement is the *fine structure of the noise* registered in stable processes.
>
> Every process contains noise. The noise originates due to the influence of random factors and satisfies the Gaussian distribution (i.e., the Gauss continuous distribution function of the probability of the measured value between any two moments of time). Gaussian distribution is attributed to any random process, such as noise, and is based on the averaging and smoothing of the noise fluctuation measured during a long enough interval of time. Nevertheless, if considering very small intervals of time, the real noise has a bizarre structure of the probability distribution function, which differs for each interval of time. Each of these real functions being considered "per se" cannot be averaged to a Gaussian curve. This is what Shnoll called the fine structure of noise and is the object of research studies originally conducted by Simon Shnoll, commencing in 1951–1954 to this day.
>
> So, the magnitude of noise is measured in a very stable process during a long enough duration of time (days, months, and even years). Then the full row of the measured data is taken under study. The full duration of time is split into small intervals. A histogram of the probability distribution function is then created for each of the small intervals. Each interval of time has

*Rabounski D. and Borissova L. General relativity theory explains the Shnoll effect and makes possible forecasting earthquakes and weather cataclysms. *Progress in Physics*, 2014, v. 10, issue 2, p. 63–70.

its own bizarre distribution function (form of the histogram) that differs from Gaussian function. Nevertheless, Shnoll found that "paired histograms," which have a very similar (almost identical) form, exist along the row of the measured data. That is, the histogram created for each interval of time has its own "twin" which has a similar form. The similar form was found in the histograms which were registered with the following periods of repetition connected with stars, the Sun, and the Moon:

- 24 hours = 1440 min (solar day);
- 23 hours, 56 min = 1436 min (stellar day);
- 24 hours, 50 min = 1490 min (lunar day);
- 27 days, 7 hours, 43 min = 39 343 min (lunar month);
- 31 days, 19 hours, 29 min = 45 809 min (period of the lunar evection);
- 365 days = 525 600 min (calendar year);
- 365 days, 6 hours, 9 min = 525 969 min (stellar year).

Also, aside as the similar forms of histograms, appearance the mirrored forms of histograms was registered by Shnoll with periods of:

- 720 min (half of the calendar/solar day);
- 182 days, 12 hours = 262 800 min (half of the calendar/solar year).

Shnoll called this phenomenon the "palindrome effect". It is one of Shnoll's newest findings: despite his having started the research studies in 1951, the possibility of the appearance of the mirrored forms of histograms only came to his attention in 2004. The "palindrome effect" was first registered in December 2007. Aside from these two periods of the "palindromes", a number of other palindrome cycles were found. However, certain circumstances have not allowed a continuation of these studies in full force yet.

As was shown by Shnoll after many experiments done synchronously at different locations from South Pole to North Pole, an appearance of the similar form (or the mirrored form) of the histograms does not depend on the geographical latitude, but depends only on the geographical longitude, i.e., the same *local time* at the point of observation. In other words, the Shnoll effect is manifested equally at any location on the Earth's surface, according to the local time, meaning the same locations of the celestial objects in the sky with respect to the visible horizon.

It is significant that the process producing the noise that we measure can be absolutely anything. Initially, in 1951, Shnoll started his research studies from measurements of the speed of chemical reactions in the aqueous solutions of proteins. Then many other biochemical processes attracted his attention. After decades of successful findings, he focused on such purely physical processes as alpha-decay and beta-decay of the atomic nuclei. It was shown that not only all the random natural processes of different origins, but even artificial processes as random-number generation by computer software manifest the Shnoll effect. In other words, this is a fundamental effect."

Shnoll told me that neither signal level nor noise level is actually measured in his experiments: their numerical values remain very stable during measurement. Only standard time intervals between adjacent measurements change with the periods that he registered. That is, signal level and noise level remain unchanged, while the "unit time interval" between adjacent measurements is not "unit" but changes according to the fine inhomogeneous structure of space-time, through which the observer, together with his laboratory and the Earth itself, travels in the cosmos. The observer's laboratory is located somewhere on the surface of the Earth, while the Earth's body revolves around its axis, the Earth revolves around the Sun, the planets revolve around the Sun, and the entire Solar System travels along its specific trajectory in the Galaxy... As a result, the observer together with his laboratory travels in the cosmos through the fine structured grid of the standard "unit time intervals", which is caused by the fields of the aforementioned rotating cosmic bodies. This motion of the observer leads to the fact that his measurements of everything are affected by the corresponding periodic changes in the duration of the standard "unit time interval" between consecutive measurements. The more stable the quantity that he measures, the more obvious the fine structure of the grid of time intervals through which he moves in the cosmos.

In other words, Shnoll believed that the fine structure of random noise discovered by him (a.k.a. the Shnoll effect) manifests the fine inhomogeneous structure of time itself*.

In 2007–2008, I was honoured to be the editor of Shnoll's book, in which he explained the entire story of his discovery, starting in 1951, as well as all the details of his experiments and experimental results obtained up to those years. Prior that time, his experimental results were scattered over many dozens of his fragmentary papers. He asked me to help him with the structure of the book: he drafted many chapters on different topics that needed to be somehow connected with each other and combined into a whole book. We spent many hours together discussing every detail of the book. The book was published in Russian in 2009, and its English translation in 2012.† To be honest, I was should translate his book myself, because I knew the subject of the book like no one else. But then I was so physically exhausted that Maria Kondrashova took pity on me and invited two women for translation. Now, I have a great regret about this missed opportunity.

*Shnoll S.E. Changes in the fine structure of stochastic distributions as a consequence of space-time fluctuations. *Progress in Physics*, 2006, v. 2, issue 2, p. 39–45.

†Shnoll S. E. Cosmophysical Factors in Stochastic Processes. American Research Press, Rehoboth (NM), 2012, 388 pages.

This obituary turned out to be very personal, far from officialdom...

I, like most residents of Puschino, often walk along the Green Zone, the main street of the town, which is a 1,700-meter forested boulevard that runs through the town and separates the Institutes from the residential area. This boulevard is framed by the Avenue of Science from the side of the residential buildings and by the Institute Avenue from the side of the Institutes. At the entrance of each of the Institutes, I see memorial plaques on the wall dedicated to the influential scientists of the Soviet period, members of the USSR Academy of Sciences, who worked in Puschino. In addition, several streets of the town are named after some of them. These influential people of the Soviet period were successful organizers of science, rather than outstanding researchers. Their scientific achievements were particular and had not changed biophysics or biochemistry as a whole, while the technologies they have developed (like any technologies in general) are rather the subject of industrial corporations than science: the task of scientists is to discover fundamental laws, which industrial corporations, if they deem necessary, can then use then to develop some technologies.

On the contrary, the Shnoll effect is a fundamental discovery. Understanding this fine structure of the pattern of time through which we, together with the planet Earth, travel in the cosmos, will undoubtedly change not only biophysics as a science and physics in general, but our entire understanding of the world. In this sense, Simon Shnoll is similar to Copernicus, who also once changed the entire understanding of the world. I therefore have no doubt that once the scientific community has evolved enough to understand the significance of the Shnoll effect, then the Green Zone, the main boulevard that runs through the entire town, will be renamed Shnoll Boulevard. This will be not only fair, because Simon Shnol will forever remain the most outstanding research scientist who lived and worked in Puschino, but also symbolic — Shnoll Boulevard, running as a narrow through the entire town of scientists.

Let his memory live for ever!

Received on September 28, 2021

Physics of Transcendental Numbers on the Origin of Astrogeophysical Cycles

Hartmut Müller

Rome, Italy.
E-mail: hm@interscalar.com

Transcendental ratios of physical quantities can provide stability in complex dynamic systems because they inhibit the occurrence of destabilizing resonance between the elements of the system. In this paper we analyze recently discovered astrophysical and geophysical cycles in order to verify this numeric-physical paradigm.

Introduction

The Solar system behaves like a precise chronometer. Indeed, the orbital and rotational periods of the planets, planetoids and large moons are exceptionally stable. In view of the huge number (more than 800.000) of orbiting and rotating celestial bodies, perturbation models based on conventional theories of gravitation predict long-term highly unstable states [1, 2] and have a problem with the real stability of the Solar system. Moreover, they do not explain basic facts, for instance, why the Solar system has established the orbital periods 90560 days (Pluto), 60182 (Neptune), 30689 (Uranus), 10759 (Saturn), 4333 (Jupiter), 1682 (Ceres), 687 (Mars), 365 (Earth), 225 (Venus) and 88 days (Mercury). The current distribution of the planetary and lunar orbital and rotational periods appears to them to be completely coincidental.

Recently discovered astrophysical and geophysical cycles of galactic origin suggest that despite the huge number of stars (more than 200 billion), our Galaxy behaves like a precise chronometer as well. Disappointingly, there is no theory of gravitation that derives the correct movement of stars in galaxies or explains at least the existence of galaxies without introducing a huge amount (corrently 68%) of dark energy [3]. In spiral galaxies, the orbiting of stars seems to strongly disobey both Newton's law of universal gravitation and general relativity. Recently, an 85% dark matter [4] universe is required for saving the conventional paradigm.

Perhaps the concept of gravitation itself requires a revision. Obviously, it is not about details, but an important part of the hole is missing.

In this paper we introduce a basic numeric-physical approach that could be the missing link as it allows resolving stability tasks in dynamic systems of any level of complexity.

Methods

In [5] we have shown that the difference between rational, irrational algebraic and transcendental numbers is not only a mathematical task, but it is also an essential aspect of stability in complex dynamic systems. For instance, integer frequency ratios provide resonance interaction that can destabilize a system [6]. Actually, it is transcendental numbers that define the preferred ratios of quantities which avoid destabilizing resonance interaction [7]. In this way, transcendental ratios of quantities sustain the lasting stability of periodic processes in complex dynamic systems. With reference to the evolution of a planetary system and its stability, we may therefore expect that the ratio of any two orbital periods should finally approximate a transcendental number [8].

Among all transcendental numbers, Euler's number $e = 2.71828\ldots$ is unique, because its real power function e^x coincides with its own derivatives. In the consequence, Euler's number allows inhibiting resonance interaction regarding any interacting periodic processes and their derivatives. Because of this unique property of Euler's number, complex dynamic systems tend to establish relations of quantities that coincide with values of the natural exponential function e^x for integer and rational exponents x.

Therefore, we expect that periodic processes in real systems prefer frequency ratios close to Euler's number and its rational powers. Consequently, the logarithms of their frequency ratios should be close to integer $0, \pm1, \pm2, \ldots$ or rational values $\pm1/2, \pm1/3, \pm1/4, \ldots$ In [9] we exemplified our hypothesis in particle physics, astrophysics, cosmology, geophysics, biophysics and engineering.

Based on this hypothesis, we introduced a fractal model of matter [10] as a chain system of harmonic quantum oscillators and could show the evidence of this model for all known hadrons, mesons, leptons and bosons as well. In [11] we have shown that the set of stable eigenstates in such systems is fractal and can be described by finite continued fractions:

$$\mathcal{F}_{jk} = \ln(\omega_{jk}/\omega_{00}) = \langle n_{j0}; n_{j1}, n_{j2}, \ldots, n_{jk} \rangle \qquad (1)$$

where ω_{jk} is the set of angular eigenfrequencies and ω_{00} is the fundamental frequency of the set. The denominators are integer: $n_{j0}, n_{j1}, n_{j2}, \ldots, n_{jk} \in \mathrm{Z}$. The cardinality $j \in \mathrm{N}$ of the set and the number $k \in \mathrm{N}$ of layers are finite. The numeric occupancy of one layer does not influence the numeric occupancy of other layers, so that each layer can be considered as an independent dimension of a k-dimensional manifold. In the canonical form, all numerators equal 1. We use angle brackets for continued fractions.

Any finite continued fraction represents a rational number [12]. Therefore, the ratios ω_{jk}/ω_{00} of eigenfrequencies are always irrational, because for rational exponents the natural exponential function is transcendental [13]. This circumstance provides for lasting stability of those eigenstates of a

chain system of harmonic oscillators because it prevents resonance interaction [14] between the elements of the system. The distribution density of stable eigenstates reaches local maxima near reciprocal integers $\pm 1/2, \pm 1/3, \pm 1/4, \ldots$ that are attractor points (fig. 1) in the fractal set $\mathcal{F}_{jk}$ of natural logarithms. Integer logarithms $0, \pm 1, \pm 2, \ldots$ represent the most stable eigenstates (main attractors).

In the case of harmonic quantum oscillators, the continued fractions $\mathcal{F}_{jk}$ define not only fractal sets of natural angular frequencies ω_{jk}, angular accelerations $a_{jk} = c \cdot \omega_{jk}$, oscillation periods $\tau_{jk} = 1/\omega_{jk}$ and wavelengths $\lambda_{jk} = c/\omega_{jk}$ of the chain system, but also fractal sets of energies $\mathrm{E}_{jk} = \hbar \cdot \omega_{jk}$ and masses $\mathrm{m}_{jk} = \mathrm{E}_{jk}/c^2$ which correspond with the eigenstates of the system. For this reason, we call the continued fraction $\mathcal{F}_{jk}$ the *Fundamental Fractal* of stable eigenstates in chain systems of harmonic quantum oscillators.

Fig. 1: The distribution of stable eigenvalues of $\mathcal{F}_{jk}$ for $k = 1$ (above) and for $k = 2$ (below) in the range $-1 \leqslant \mathcal{F}_{jk} \leqslant 1$.

In fact, scale relations in particle- [10] and astrophysics [15] obey the same Fundamental Fractal (1), without any additional or particular settings. The proton-to-electron rest energy ratio approximates the first layer of the Fundamental Fractal that could explain their exceptional stability. In fact, the life-spans of the proton and electron top everything that is measurable, exceeding 10^{29} years [16].

Property	Electron	Proton
$\mathrm{E} = \mathrm{mc}^2$	0.5109989461(31) MeV	938.2720813(58) MeV
$\omega = \mathrm{E}/\hbar$	$7.76344 \cdot 10^{20}$ Hz	$1.42549 \cdot 10^{24}$ Hz
$\tau = 1/\omega$	$1.28809 \cdot 10^{-21}$ s	$7.01515 \cdot 10^{-25}$ s
$\lambda = c/\omega$	$3.86159 \cdot 10^{-13}$ m	$2.10309 \cdot 10^{-16}$ m

Table 1: The basic set of the physical properties of the electron and proton. Data from Particle Data Group [16]. Frequencies, oscillation periods and wavelengths are calculated.

The proton-to-electron ratio (tab. 1) approximates the seventh power of Euler's number and its square root:

$$\ln\left(\frac{\omega_p}{\omega_e}\right) = \ln\left(\frac{1.42549 \cdot 10^{24}\,\mathrm{Hz}}{7.76344 \cdot 10^{20}\,\mathrm{Hz}}\right) \simeq 7 + \frac{1}{2} = \langle 7; 2 \rangle$$

In the consequence of this potential difference of the proton relative to the electron, the scaling factor $\sqrt{e} = 1.64872\ldots$ connects attractors of proton stability with similar attractors of electron stability in alternating sequence.

These unique properties of the electron and proton predestinate their physical characteristics as fundamental units. Table 1 shows the basic set of electron and proton units that can be considered as a fundamental metrology (c is the speed of light in a vacuum, $\hbar$ is the Planck constant). In [11] was shown that the fundamental metrology (tab. 1) is completely compatible with Planck units [17]. Originally proposed in 1899 by Max Planck, these units are also known as natural units, because the origin of their definition comes only from properties of nature and not from any human construct. Max Planck wrote [18] that these units, "regardless of any particular bodies or substances, retain their importance for all times and for all cultures, including alien and non-human, and can therefore be called natural units of measurement". Planck units reflect the characteristics of space-time.

We assume that scale invariance according to the Fundamental Fractal (1), which is calibrated to the physical properties of the proton and the electron, is a universal characteristic of organized matter and criterion of stability. This hypothesis we have called *Global Scaling* [9].

In [19] we applied the Fundamental Fractal (1) to macroscopic scales interpreting gravity as quantum attractor effect of its stable eigenstates. We have shown that the orbital and rotational periods of planets, planetoids and large moons of the solar system correspond with attractors of electron and proton stability [11]. This is valid also for exoplanets [15] of the systems Trappist 1 and Kepler 20. In [8] we have shown that the maxima in the frequency distribution of the orbital periods of 1430 exoplanets listed in [20] correspond with attractors of the Fundamental Fractal. In [21] we have shown that the maxima in the frequency distribution of the number of stars in the solar neighborhood as function of the distance between them correspond well with attractors of the Fundamental Fractal.

In this paper we will show that the Fundamental Fractal (1) determines also the Earth axial precession cycle, the obliquity variation cycle as well as the apsidal precession cycle and the orbital eccentricity cycle. In addition, we will show that recently discovered geological cycles, as well as the periodic variations in the movement of the Solar system through the Galaxy, substantiate their determination by the Fundamental Fractal.

Results

Since its birth the Sun has made about 20 cycles around the Galaxy, and during this time the Solar system has made many passages through the spiral arms of the disk. The Sun's orbit in the Galaxy is not circular. There are temporal variations in the distance from the Galactic center with a period of $T_S = 170$ million years [22] that corresponds precisely with the main attractor $\langle 90 \rangle$ of proton stability of the Fundamental Fractal (1):

$$\ln\left(\frac{T_S}{2\pi \cdot \tau_p}\right) = 90$$

$2\pi \cdot \tau_p$ is the oscillation period of the proton (tab. 1). The recently [23] discovered geological cycle with a period of $T_G = 27$ million years corresponds well with the same attractor $\langle 90 \rangle$, but relative to the angular oscillation period of the proton:

$$\ln\left(\frac{T_G}{\tau_p}\right) = 90$$

The connection $T_S = 2\pi \cdot T_G$ suggests that the 27 million years' geological cycle could be caused by angular components of the periodical variations of the distance of the Solar system (and the Earth) from the Galactic center. In addition, [23] reports a geological cycle of 8.9 Ma that approximates the main attractor $\langle 87 \rangle$ of proton stability:

$$\ln\left(\frac{8.9\ Ma}{2\pi \cdot \tau_p}\right) = 87$$

The Sun's path oscillates above and below the Galactic plane with a period of approximately 63 million years [22] that coincides with the main attractor $\langle 89 \rangle$ of proton stability:

$$\ln\left(\frac{63\ Ma}{2\pi \cdot \tau_p}\right) = 89$$

Earth's axial precession cycle (25,770 years) fits the attractor $\langle 83 \rangle$ of proton stability:

$$\ln\left(\frac{25,770\ a}{\tau_p}\right) = 83$$

By the way, 25,770 years is also the time it takes for a signal to travel from the Galactic center to Earth at the speed of light.

The Fundamental Fractal (1) is of pure numeric origin, and there is no particular physical mechanism that creates it. It is all about transcendental ratios of frequencies [8] that inhibit destabilizing resonance interaction. In this way, the Fundamental Fractal concerns all repetitive processes, independently on their temporal or spatial scales.

For instance, Earth's apsidal precession cycle and orbital eccentricity cycle (both of 112,000 years) correspond with the attractor $\langle 77 \rangle$ of electron stability:

$$\ln\left(\frac{112,000\ a}{\tau_e}\right) = 77$$

τ_e is the angular oscillation period of the electron (tab. 1). Earth's obliquity variation cycle (41,000 years) corresponds with the attractor $\langle 76 \rangle$ of electron stability:

$$\ln\left(\frac{41,000\ a}{\tau_e}\right) = 76$$

Naturally, we expect the existence of further galactic cycles that correspond with other main attractors of the Fundamental Fractal. Table 2 gives an overview of expected main attractor cycles in the scale of millions of years.

n	$T_p(n)$, Ma	$t_p(n)$, Ma	n	$T_e(n)$, Ma	$t_e(n)$, Ma
91	463.35	73.75	83	285.41	45.42
90	170.46	27.13	82	105.00	16.71
89	62.71	9.98	81	38.62	6.15
88	23.07	3.67	80	14.21	2.26
87	8.49	1.35	79	5.23	0.83
86	3.12	0.50	78	1.92	0.31

Table 2: Cycles corresponding with main attractors of proton and electron stability in the range of millions of years (Ma).

Every attractor of proton or electron stability defines the period of a stable cycle and its angular period. As main attractors correspond with integer exponents n of the Fundamental Fractal (1), it is easy to calculate main attractor cycles:

$$t_e(n) = \tau_e \cdot e^n \qquad T_e(n) = 2\pi \cdot t_e(n)$$

$$t_p(n) = \tau_p \cdot e^n \qquad T_p(n) = 2\pi \cdot t_p(n)$$

In general, the identification of the predicted galactic cycles requires a significant increase in current data precision.

Conclusion

Within our approach, numeric attractors of stability determine the distribution of matter in space and time. Since the distribution of the attractors is fractal, the distribution of matter is also fractal. Numerical attractors cause effects known as gravity, electricity, magnetism, and nuclear forces. Numerical relationships are primary, physical effects are secondary. Numerical attractors cause the formation of matter in all scales – from the electron and proton up to planets, stars and galaxies. Interscalar cosmology [9] bases on this approach.

In particular, for maintaining stability of motion, the Sun does not have to avoid parametric resonance with every single other star on its path through the Galaxy. As this task cannot be resolved in general, the application of transcendental frequency ratios appears to be a significant alternative. As we have shown, not only stars [21], but also planets [8] make extensive use of it.

Acknowledgements

The author is grateful to Leili Khosravi, Ulrike Granögger, Michael Kauderer, Valery Kolombet, Oleg Kalinin, Viktor Bart and Viktor Panchelyuga for valuable discussions.

Eternal thanks go to the sadly deceased great scientist Simon Shnoll. He found empirical evidence of cosmophysical factors that underlie all processes in the universe. Simon Shnoll's work stimulated the development of the author's approach over many years.

Submitted on October 1, 2021

References

1. Heggie D. C. The Classical Gravitational N-Body Problem. arXiv: astro-ph/0503600v2, 11 Aug 2005.
2. Hayes B. The 100-Billion-Body Problem. *American Scientist*, v. 103, no. 2, 2015.
3. Li M. et al. Dark Energy. arXiv:1103.5870v6 [astro-ph.CO] 7 Oct 2011.
4. Einasto J. Dark Matter. arXiv:0901.0632v2 [astro-ph.CO] 19 Oct 2010.
5. Müller H. On the Cosmological Significance of Euler's Number. *Progress in Physics*, 2019, v. 15, 17–21.
6. Dombrowski K. Rational Numbers Distribution and Resonance. *Progress in Physics*, 2005, v. 1, no. 1, 65–67.
7. Müller H. The Physics of Transcendental Numbers. *Progress in Physics*, 2019, vol. 15, 148–155.
8. Müller H. Physics of Transcendental Numbers meets Gravitation. *Progress in Physics*, 2021, vol. 17, 83–92.
9. Müller H. Global Scaling. The Fundamentals of Interscalar Cosmology. *New Heritage Publishers*, Brooklyn, New York, USA, ISBN 978-0-9981894-0-6, (2018).
10. Müller H. Fractal Scaling Models of Natural Oscillations in Chain Systems and the Mass Distribution of Particles. *Progress in Physics*, 2010, v. 6, 61–66.
11. Müller H. Scale-Invariant Models of Natural Oscillations in Chain Systems and their Cosmological Significance. *Progress in Physics*, 2017, v. 13, 187–197.
12. Khintchine A.Ya. Continued fractions. University of Chicago Press, Chicago, (1964).
13. Hilbert D. Über die Transcendenz der Zahlen e und π. *Mathematische Annalen*, 1893, v. 43, 216–219.
14. Panchelyuga V.A., Panchelyuga M. S. Resonance and Fractals on the Real Numbers Set. *Progress in Physics*, 2012, v. 8, no. 4, 48–53.
15. Müller H. Global Scaling of Planetary Systems. *Progress in Physics*, 2018, v. 14, 99–105.
16. Tanabashi M. et al. (Particle Data Group), *Phys. Rev. D*, 98, 030001 (2018), www.pdg.lbl.gov
17. Astrophysical constants. Particle Data Group, pdg.lbl.gov
18. Planck M. Über Irreversible Strahlungsvorgänge. *Sitzungsbericht der Königlich Preußischen Akademie der Wissenschaften*, 1899, v. 1, 479–480.
19. Müller H. Gravity as Attractor Effect of Stability Nodes in Chain Systems of Harmonic Quantum Oscillators. *Progress in Physics*, 2018, v. 14, 19–23.
20. Catalog of Exoplanets. Observatoire de Paris, http://exoplanet.eu/
21. Müller H. Physics of Transcendental Numbers Determines Star Distribution. *Progress in Physics*, 2021, v. 17, 164–167.
22. Gies D. R., Helsel J. W. Ice age epochs and the Sun's path through the Galaxy. *The Astrophysical Journal*, 2005, v. 626, 844–848.
23. Rampino M. R., Caldeira K., Zhu Y. A pulse of the Earth: A 27.5-Myr underlying cycle in coordinated geological events over the last 260 Myr. *Geoscience Frontiers*, 2021, v. 12, 101245.

Progress in Physics is an American scientific journal on advanced studies in physics, registered with the Library of Congress (DC, USA): ISSN 1555-5534 (print version) and ISSN 1555-5615 (online version). The journal is peer reviewed and listed in the abstracting and indexing coverage of: Mathematical Reviews of the AMS (USA), DOAJ of Lund University (Sweden), Scientific Commons of the University of St.Gallen (Switzerland), Open-J-Gate (India), Referential Journal of VINITI (Russia), etc. Progress in Physics is an open-access journal published and distributed in accordance with the Budapest Open Initiative: this means that the electronic copies of both full-size version of the journal and the individual papers published therein will always be accessed for reading, download, and copying for any user free of charge.
The journal is issued quarterly (four volumes per year).

Electronic version of this journal: http://www.ptep-online.com

Postal address:
Department of Mathematics and Science, University of New Mexico,
705 Gurley Avenue, Gallup, NM 87301, USA